Strong Gravitational effects on Pulsar signals emanating from Compact Binary Systems

by

Bevan H. Tucker

Thesis presented in fulfilment of the requirements for the degree of

Master of Science in Physics

at the University of the Witwatersrand

School of Physics,
University of the Witwatersrand,
PO Box Wits, Johannesburg, 2050, South Africa

Supervisor: Dr. F. A. M. Frescura

October 2014

Contents

Declaration

By submitting this thesis electronically, I declare that the entirety of the work contained therein is my own, original work, that I am the owner of the copyright thereof (unless to the extent explicitly otherwise stated) and that I have not previously in its entirety or in part submitted it for obtaining any qualification.

Signature: .....

Initials and Surname

Date: 30 October 2014

List of Figures

List of Tables

Acknowledgements

I must thank Warren Carlson for his contribution to this work. Warren showed me how to code efficiently and effectively in C++. The OpenMPI work-flow routine and the optimized numerical integration method used in my numerical simulation were constructed collaboratively with Warren. We expect to publish work on these two developments at a later stage. Warren also helped implement the CMake build utility for my application.

The financial assistance of the South African Square Kilometre Array Project towards this research is hereby acknowledged. Opinions expressed and conclusions arrived at, are those of the author and are not necessarily to be attributed to the NRF.

Part I

Theory

Chapter 1

Introduction

The theory of General Relativity (GR) has been tested to high precision in the case of weak gravitational fields by several experimental tests within our solar system. However, such test cannot discriminate between General Relativity and competing theories of gravity. Definitive tests require strong fields, ideally the strongest fields available in nature. These are found in the vicinity of black-holes, or in black-hole/black-hole or black-hole/pulsar binaries. A way of testing the theory is by probing the motions predicted by the spacetime metric for massive and massless particles, with or without spin, in the vicinity of an object that produces a strong gravitational field. Such objects cannot be found in our solar system. Thus, tests of strong field gravity must necessarily be by the observation of signals and radiation of remote origin and containing compact objects, such as neutron stars and black holes. Observations of binary pulsar systems such as PSR B1913+16 [1] have allowed the study of stronger gravitational fields and their effect on orbital motion. Studies of the process of gravitational radiation have thus far validated General Relativity with a certainty of 0.5% [2]. The advent of the Square Kilometer Array (SKA), the first of a new generation of radio telescopes, will provide a census of pulsars within the galaxy. Of the pulsars within our galaxy which are beaming towards earth, a small number may exist in binary star systems. The most interesting of these for strong field tests are those in binary systems that contain a pulsar and a black-hole. Their number is estimated at approximately 1 in 700 observed pulsar signals, Lipunov et al. [3]. Regardless of the formation and evolution of such systems, pulsar beams propagating through the strong gravitational field region surrounding a black hole provide a test-bed for probing the metric of spacetime in the most highly curved regime.

Several models have been constructed to understand better how measurements from such

systems could provide useful tests of General Relativity. Laguna and Wolszczan [4] have used ray-tracing numerical integration methods to determine the magnitude of the time delay of pulses due to the rotation of a black-hole. The results of their simulations show a micro-second level time delay or speed up respectively for pulses travelling in counterrotating and corotating cases through the superior conjunction of the binary system. Oscoz et al. [5] have produced a theoretical model describing the timing and flux of a pulsar signal as it orbits a rotating black-hole. Their work focused principally on detecting pulses emitted just before the pulsar spirals into the black-hole and coalesces with it. Thus, their model assumes a system of small orbital radius. The flux and timing of pulses would accordingly be affected to a far greater extent by the presence of the black-hole companion than would be the case for a more representative system. Though their work is applicable in principle to the general case of black-hole/pulsar binary systems that endure for significantly longer times, providing reasonable chance of detection and observation, the physical parameters used in their models are significantly different from those used when investigating other systems. Nevertheless, the concepts examined therein is very similar and merits an in depth investigation with regards to the signal a black-hole/pulsar binary system would produce. Subsequently, Wex and Kopieken [6] studied the possibility of gaining physical information about a black-hole in a binary system by calculating analytically time delay expected in a signal due to non-zero angular momentum of the black-hole. They also discuss the possibility of determining a lower limit of the angular momentum of the black-hole by observing the strong precessional effects on the binary orbit caused by the rotation of the black-hole. Finally, they also discuss a method by which the nature of a binary pulsar's compact companion can be ascertained through simultaneous measurements of mass, spin and quadrupole moment of the companion. This could represent, if not a method for directly observing a rotating astrophysical black-hole, a method by which black-hole candidates may be eliminated.

Rafikov and Lai [7] sought to determine whether the time delay of pulses caused by rotation of the black-hole companion could be disentangled from the delay caused by the bending of space-time. Furthermore, their analysis describes effects on the pulsar signal caused by the motion of the black-hole companion as the photons propagate through the binary system. They find that direct observation of delays caused by dragging of inertial reference frames would not be sufficiently large to observe distinctly, and that the sub

micro-second level delays caused by the effect would not be distinguishable from other lensing effects. Subsequently, Wang, Jenet, Creighton and Price [8] considered the possibility of detecting strong gravitational effects on signals from pulsars orbiting supermassive black-holes in galactic centres. Their work focuses on the detection of sub-dominant pulses which could be observed as the signal from a pulsar is scattered by the supermassive black-hole. Their methods involve formulating two universal functions for obtaining the azimuthal angle and time for a photon detected by an observer at infinite radial distance from the black-hole. The analysis does simplify the system to a non-rotating black-hole, and considers the portion of the pulsar's beam within the equatorial plane of the black-hole. More recent work by Nampalliwar, Price, Creighton and Jenet [9] seeks to consider whether results such as [8] are significantly affected by considering a rotating supermassive black-hole. Their work indicates that the detectibility is not significantly affected, but the timing of pulses observed from pulsars orbiting rotating supermassive black-holes differs significantly from that in the non-rotating case.

My aim in this thesis is to lay the foundation for a numerical model for the emission of a pulsar in the vicinity of a black-hole. Theoretically, the system has been reduced to an ideal case, whereby the mass of the pulsar has been ignored, resulting in a stationary black-hole described by the Kerr geometry, with the pulsar assuming a stable circular orbit. Furthermore, the direction of emission of the conical radio-frequency beams have been constrained to the equatorial plane of the Kerr black-hole, thus making the simplification that the direction of the apex of the beam is orthogonal to the spin vector of the pulsar. The physical parameters for the system have subsequently been selected with the intention of providing pilot data generated on a single machine, with the use of a cluster or grid environment necessary for more realistic cases. Hence the numerical results presented herein are intended as a proof of principle, showing the potential of numerical simulations for the purpose of describing the effects of strongly curved space-time, in the vicinity of a black-hole, on the signal of a nearby pulsar. Theoretical work pertaining to the problem has been described and forms part I of this thesis. This includes a brief review of previous works within this field of study, mentioned above, followed by a theoretical discussion of the trajectories of photons through the Kerr space-time, central to the construction of a numerical simulation. Subsequently, a theoretical description of the orbital mechanics of compact binary systems

is performed via examination of work by Damour and Deruelle [10], to first order in v/c , and briefly work by Blanchet [11] to order 3.5 in terms of v/c . The results derived therein would constitute excellent equations for use in a numerical simulation which seeks to describe the orbital motion of the pulsar and black-hole with the necessary precision for a model which would ultimately yield results comparable with observation.

In the second part of the thesis, the formulation of the numerical simulation will be discussed in detail. The C++ model has been designed as a proof of principle, showing the potential of such methods for elucidating the true nature of the characteristic signal emitted by a pulsar in a binary system with a black-hole. Methods utilized involve the direct numerical integration of the null geodesics of the Kerr metric, using an optimized 8th/9th order Runga-Kutte-Verner method with adaptive step-size modulated by estimation of local truncation error. The ability of this method to produce truly useful physical results is made possible via the extremely precise integration method, as well as the work-flow routine, which utilizes Open-MPI to distribute the computational workload amongst parallel processes within a computing environment, both developed in collaboration with Mr. W. Carlson. The present form of simulation produces results on a single core-i7 machine, which show the aberration of pulses arriving at a distant detector as the pulsar moves through the superior conjunction. Furthermore, the time-bin averaged photon time delays caused by propagation through the strongly-curved, rotating spacetime in the vicinity of the Kerr black-hole have been plotted, corresponding to the results of the pulse profile histograms. At present the scale of the simulations, in terms of the number of photons integrated is not sufficient to generate data with a satisfactory signal to noise ratio. The intention is to run future simulations on cluster, or grid computing environments with several orders of magnitude more computing power. The results obtained thus far have been discussed in detail, including physical insights and observations, as well as comparisons with results of previous authors.

Chapter 2

Literature: Black-Hole/Pulsar Binary Systems

Black-hole / Pulsar binary systems are considered to be ideal laboratories for the study of relativistic strong gravitational fields. A number of methods have been developed to, quantify the effects of the rotating black hole on the timing of pulses as observed on earth. Identification of the emission signature for such systems would constitute a method for the detection of an astrophysical black-hole.

In this chapter, I will examine in detail the paper of Oscoz, Goicoechea, Mediavilla and Buitrago [5], as they have constructed a model similar to the one I investigate in this thesis. Following this, I will describe a numerical model constructed by Laguna and Wolszczan, detailing differences in their conceptualization of the problem as well as differences between the numerical implementation of their model and the one presented in this thesis. Finally, I review and discuss several other works that deal with black-hole + pulsar binary systems. These works include an analysis of frame-dragging and precessional effects by Wex and Kopeikin [6]; a subsequent work by Rafikov and Lai [7] on the effects of gravitational lensing and of the motion of the companion on the pulse arrival times of a binary pulsar, and finally work by Epstein [12] in which he derives an analytical formula for predicting the times of arrival of pulses in a compact binary system.

2.1 Rigorous Pulse Timing and Flux Model for a Simple System, Oscoz et al. [5]

In 1997 Oscoz, Goicoechea, Mediavilla and Buitrago [5] published a research paper that

includes a detailed description of a theoretical model for the timing and flux of pulses from a pulsar orbiting a Kerr black-hole. In chapter 11, I will compare the results obtained using my computational model with those obtained by Oscoz et al. I will also discuss the shortcomings of both models.

2.1.1 Construction of a Pulse Timing Model

The aim of Oscoz et al. was to predict the coordinate times of arrival of pulses emitted by a pulsar orbiting a black-hole. The binary system is restricted to the simplest form possible by two basic assumptions: 1. The orbit of the pulsar is circular, and 2. the binary orbital plane is "edge on" with respect to the detector, i.e. the observation point and the orbit of the pulsar lie in the equatorial plane of the Kerr geometry. They also assumed that the Pulsar is a test particle in the gravitational field of the black-hole, that the Pulsar has a constant period, and that the orbital radius of the pulsar is constant. These assumptions coincide with those of the computational model that I present in later chapters of this thesis.

Oscoz et al. define vectors and unit vectors that describe the emission of the Pulsar as it moves around the black-hole. First consider the Local Rest Frame (LRF) of the Pulsar, i.e. a frame in which the Pulsar is at rest. This reference frame has as its basis an orthonormal tetrad of unit vectors, denoted by $e_{\hat{t}}$, $e_{\hat{r}}$, $e_{\hat{\theta}}$ and $e_{\hat{\phi}}$. These vectors are connected with the coordinate basis of the Kerr geometry by means of transformations described in appendix A of paper [5]. The reference frame is a locally non-rotating frame which moves with the pulsar as it orbits.

Denote directions, in the pulsar's LRF, of the primary and secondary beams of the pulsar by **SP** and **SP′** respectively. The vector normal to these emission directions in the plane coinciding with the Kerr equatorial plane is given by $\mathbf{n}_p$, the angle between the radial unit vector $e_{\hat{r}}$ in the Pulsar's LRF $e_{\hat{r}}$ and **SP** is denoted by α_p.

The velocity of the photon is $\mathbf{V}_p = \dfrac{\mathrm{d}(\mathbf{SP})}{\mathrm{d}\hat{t}} = \Omega_p n_p$. Choose the magnitude of the space vector representing the propagation of the photons such that it is a unit vector, i.e. $|\mathbf{SP}| = |\mathbf{SP}'| = |\mathbf{n}_p| = 1$. Furthermore, $\mathbf{SP} \perp \mathbf{n}_p$ as $\mathbf{n}_p$ is the normal to $\mathbf{S}P$ in the plane spanned by $e_{\hat{r}}$ and $e_{\hat{\phi}}$. Using the pulsar's LRF coordinate system, decompose the emission vector in terms of the angle α_p and the unit vectors $e_{\hat{r}}$ and $e_{\hat{\phi}}$. This constrains the axis of the pulsar's conical emission to the equatorial plane of the black-hole. Note that indices with hats denote quantities in the pulsar's local reference frame, while indices without hats

represent the Kerr spacetime coordinates.

$$\mathbf{SP} = \cos\alpha_p e_{\hat{r}} + \sin\alpha_p e_{\hat{\phi}} \tag{2.1.1}$$

. The derivative of $\mathbf{S}P$ yields $\mathbf{V}_p$,

$$\begin{aligned}\mathbf{V}_p = \frac{\mathrm{d}\mathbf{SP}}{\mathrm{d}\hat{t}} &= \frac{\mathrm{d}}{\mathrm{d}\hat{t}}(\cos\alpha_p e_{\hat{r}} + \sin\alpha_p e_{\hat{\phi}}) \\ &= -\sin\alpha_p \frac{\mathrm{d}\alpha_p}{\mathrm{d}\hat{t}} e_{\hat{r}} + \cos\alpha_p \frac{\mathrm{d}e_{\hat{r}}}{\mathrm{d}\hat{t}} + \cos\alpha_p \frac{\mathrm{d}\alpha_p}{\mathrm{d}\hat{t}} e_{\hat{\phi}} + \sin\alpha_p \frac{\mathrm{d}e_{\hat{\phi}}}{\mathrm{d}\hat{t}}\end{aligned} \tag{2.1.2}$$

The derivatives of the unit basis vectors for the LRF of the Pulsar are given by,

$$\begin{aligned}\frac{\mathrm{d}e_{\hat{r}}}{\mathrm{d}\hat{t}} &= \frac{\mathrm{d}\phi}{\mathrm{d}\hat{t}}\frac{\mathrm{d}e_{\hat{r}}}{\mathrm{d}\phi} \\ &= \left(\frac{\mathrm{d}t}{\mathrm{d}\hat{t}}\frac{\mathrm{d}\phi}{\mathrm{d}t}\right)\frac{\mathrm{d}e_{\hat{r}}}{\mathrm{d}\phi} \\ &= \frac{\mathrm{d}t}{\mathrm{d}\hat{t}}\Omega_s e_{\hat{\phi}}\end{aligned}$$

where $e_{\hat{r}}$ is not a function of t as the spacetime is stationary. Furthermore, the selection of a stable circular orbit and restriction to the equatorial plane implies that $e_{\hat{r}}$ is only a function of ϕ. Similarly,

$$\begin{aligned}\frac{\mathrm{d}e_{\hat{\phi}}}{\mathrm{d}\hat{t}} &= \frac{\mathrm{d}\phi}{\mathrm{d}\hat{t}}\frac{\mathrm{d}e_{\hat{\phi}}}{\mathrm{d}\phi} \\ &= \left(\frac{\mathrm{d}t}{\mathrm{d}\hat{t}}\frac{\mathrm{d}\phi}{\mathrm{d}t}\right)\frac{\mathrm{d}e_{\hat{\phi}}}{\mathrm{d}\phi} \\ &= -\frac{\mathrm{d}t}{\mathrm{d}\hat{t}}\Omega_s e_{\hat{r}}\end{aligned}$$

where,

$$\Omega_s = \left(\frac{\mathrm{d}\phi}{\mathrm{d}t}\right)_s \tag{2.1.3}$$

The quantity Ω_s is thus the angular velocity of a test particle in orbit around a rotating black-hole. For a stable circular orbit of radius r_s, in the equatorial plane ($\theta = \frac{\pi}{2}$) of a black-hole of mass M and rotational parameter a, Ω_s is given by:

$$\Omega_s = \left(\frac{\mathrm{d}\phi}{\mathrm{d}t}\right)_s = \frac{M^{\frac{1}{2}}}{{r_s}^{\frac{3}{2}} + aM^{\frac{1}{2}}} \tag{2.1.4}$$

This enables us to write $\mathbf{V}_p$ as:

$$\mathbf{V}_p = \Omega_p \mathbf{n}_p = -\sin\alpha_p \frac{\mathrm{d}\alpha_p}{\mathrm{d}\hat{t}} e_{\hat{r}} + \cos\alpha_p \frac{\mathrm{d}e_{\hat{r}}}{\mathrm{d}\hat{t}} + \cos\alpha_p \frac{\mathrm{d}\alpha_p}{\mathrm{d}\hat{t}} e_{\hat{\phi}} + \sin\alpha_p \frac{\mathrm{d}e_{\hat{\phi}}}{\mathrm{d}\hat{t}}$$

$$= -\sin\alpha_p e_{\hat{r}}\left(\frac{\mathrm{d}\alpha_p}{\mathrm{d}\hat{t}}+\frac{\mathrm{d}t}{\mathrm{d}\hat{t}}\Omega_s\right)+\cos\alpha_p e_{\hat{\phi}}\left(\frac{\mathrm{d}\alpha_p}{\mathrm{d}\hat{t}}+\frac{\mathrm{d}t}{\mathrm{d}\hat{t}}\Omega_s\right)$$

Further, $\dfrac{\mathrm{d}\alpha_p}{\mathrm{d}\hat{t}}=\dfrac{\mathrm{d}t}{\mathrm{d}\hat{t}}\dfrac{\mathrm{d}\alpha_p}{\mathrm{d}t}$, so that,

$$\begin{aligned}\Omega_p\mathbf{n}_p &= -\sin\alpha_p e_{\hat{r}}\left(\frac{\mathrm{d}t}{\mathrm{d}\hat{t}}\frac{\mathrm{d}\alpha_p}{\mathrm{d}t}+\frac{\mathrm{d}t}{\mathrm{d}\hat{t}}\Omega_s\right)+\cos\alpha_p e_{\hat{\phi}}\left(\frac{\mathrm{d}t}{\mathrm{d}\hat{t}}\frac{\mathrm{d}\alpha_p}{\mathrm{d}t}+\frac{\mathrm{d}t}{\mathrm{d}\hat{t}}\Omega_s\right)\\ &= \frac{\mathrm{d}t}{\mathrm{d}\hat{t}}\left(\frac{\mathrm{d}\alpha_p}{\mathrm{d}t}+\Omega_s\right)\left(-\sin\alpha_p e_{\hat{r}}+\cos\alpha_p e_{\hat{\phi}}\right)\end{aligned}$$

This gives,

$$\Omega_p=\frac{\mathrm{d}t}{\mathrm{d}\hat{t}}\left(\frac{\mathrm{d}\alpha_p}{\mathrm{d}t}+\Omega_s\right) \tag{2.1.5}$$

since,

$$\mathbf{n}_p=-\sin\alpha_p e_{\hat{r}}+\cos\alpha_p e_{\hat{\phi}} \tag{2.1.6}$$

Finally, we need to express the term $\dfrac{\mathrm{d}\alpha_p}{\mathrm{d}t}$ in terms of more useful parameters. This is done by considering the transformation of the Pulsar period, from which:

$$\Omega_p=\frac{2\pi}{\hat{P}}=\frac{2\pi}{P}\frac{\mathrm{d}t}{\mathrm{d}\hat{t}} \tag{2.1.7}$$

Combining these expressions gives,

$$\begin{aligned}\frac{\mathrm{d}\hat{t}}{\mathrm{d}\hat{t}}\left(\frac{\mathrm{d}\alpha_p}{\mathrm{d}t}+\Omega_s\right)&=\frac{2\pi}{P}\frac{\mathrm{d}\hat{t}}{\mathrm{d}\hat{t}}\\ \Rightarrow \frac{\mathrm{d}\alpha_p}{\mathrm{d}t}&=\frac{2\pi}{P}-\Omega_s\end{aligned} \tag{2.1.8}$$

We now integrate this equation in terms of time to obtain an expression for the angle α_p in terms of the coordinate time t of an observer at $r=\infty$. Quantities with zero subscript represent the value of the quantity at $t=0$.

$$\begin{aligned}\int_{t_0}^{t_s}\frac{\mathrm{d}\alpha_p}{\mathrm{d}t}\mathrm{d}t &= \int_{t_0}^{t_s}\left(\frac{2\pi}{P}-\Omega_s\right)\mathrm{d}t\\ \Rightarrow \alpha_p-\alpha_0&=\frac{2\pi}{P}t_s-\Omega_s t_s\\ \Rightarrow \alpha_p&=\frac{2\pi}{P}t_s-\Omega_s t_s+\alpha_0\end{aligned} \tag{2.1.9}$$

Given initial conditions, the evolution of the angle α_p is given as a function of coordinate time and describes the emission of a single photon at the centre of a pulsar's beam, as the pulsar orbits the black-hole. Oscoz et al. proceed with a theoretical model that incorporates the conical beam structure of the Pulsar's emission, using a geometric optics approach.

They describe the Pulsar's emission as a primary wave-vector, which is modified by a pre-determined amount to produce a conical shape. Oscoz et al. describe the direction of primary emission, coinciding with the vector SP by a generic wave-vector $\mathbf{k} = \mathbf{k}(\lambda; q; \sigma)$, where the values of parameters λ, q and σ describe the direction of propagation and will be discussed below. To describe this wave-vector, they use the LRF of the Pulsar,

$$\mathbf{k} = k^{\hat{r}} e_{\hat{r}} + k^{\hat{\phi}} e_{\hat{\phi}} + k^{\hat{\theta}} e_{\hat{\theta}} \tag{2.1.10}$$

The four-momentum of a photon satisfies the condition $p_\mu p^\mu = 0$,

$$p^\mu = \mathbf{p} = p^{\hat{t}} e_{\hat{t}} + p^{\hat{r}} e_{\hat{r}} + p^{\hat{\phi}} e_{\hat{\phi}} + p^{\hat{\theta}} e_{\hat{\theta}}$$

Thus, we obtain the components of $\mathbf{k}$ by solving,

$$k^{\hat{\alpha}} = \frac{p^{\hat{\alpha}}}{p^{\hat{t}}} \tag{2.1.11}$$

For photons fired from an event at which at $\theta = \frac{\pi}{2}$, and $r = r_s$, in the Kerr space-time, the components of the 4-momentum are given by,

$$p_t = -E \tag{2.1.12}$$

$$p_\phi = \lambda E \tag{2.1.13}$$

$$p_\theta = qE \tag{2.1.14}$$

$$p^t = \sigma E \frac{\left((r_s{}^2 + a^2 - \lambda a)^2 - \Delta[(\lambda - a)^2 + q^2]\right)}{\Sigma} \tag{2.1.15}$$

Where E represents the photon energy, λ and q are impact parameters (q = 0 implies a photon constrained to the equatorial plane), the sign of σ defines photons moving in positive or negative radial directions (ingoing or outgoing), and the functions Δ and Σ are given by:

$$\Delta = r^2 - 2Mr + a^2 \tag{2.1.16}$$

$$\Sigma = r^2 + a^2 \cos^2 \theta \tag{2.1.17}$$

These equations of motion are written in terms of the conserved quantities of the metric, hence using the Hamilton-Jacobi formalism described in chapter 4. Below we give the non-zero components of the transformation matrix necessary to move from the pulsar's LRF to the Kerr space-time. This is for the distinct case of a point-particle Pulsar in motion around

a Kerr black-hole (rotating in a clockwise direction) along an equatorial stable circular orbit moving in a clockwise direction, as derived by Cunningham and Bardeen in 1973 [13].

$$\begin{aligned}
\Lambda_{\hat{t}}{}^{t} &= \sqrt{\frac{A}{\Sigma\Delta}}\sqrt{1-{V_s}^2} \\
\Lambda_{\hat{t}}{}^{\phi} &= \Omega_s\sqrt{\frac{A}{\Sigma\Delta}}\sqrt{1-{V_s}^2} \\
\Lambda_{\hat{\phi}\phi} &= \sin\theta\sqrt{\frac{A}{\Sigma}}\sqrt{1-{V_s}^2} \\
\Lambda_{\hat{\phi}t} &= -\Omega_s\sin\theta\sqrt{\frac{A}{\Sigma}}\sqrt{1-{V_s}^2} \\
\Lambda_{\hat{r}r} &= \sqrt{\frac{\Sigma}{\Delta}} \\
\Lambda_{\hat{\theta}\theta} &= \sqrt{\Sigma}
\end{aligned} \tag{2.1.18}$$

Where the function A is given by,

$$A = (r^2+a^2)^2 - a^2\Delta\sin^2\theta \tag{2.1.19}$$

Equations (2.1.18) allow us to solve for the impact parameters λ, q and σ, and obtain the generic wave-vector components that define the direction of propagation of the photons. The convention $c = 1$ is maintained throughout.

$$k^{\hat{\phi}} = \frac{p^{\hat{\phi}}}{p^{\hat{t}}} = \frac{-V_s + \lambda(\omega V_s + e^{\nu-\psi})}{1-\lambda\Omega_s} \tag{2.1.20}$$

$$k^{\hat{\theta}} = \frac{p^{\hat{\theta}}}{p^{\hat{t}}} = \frac{qe^{\nu-\mu}}{\gamma_s(1-\lambda\Omega_s)} \tag{2.1.21}$$

$$k^{\hat{r}} = \frac{p^{\hat{r}}}{p^{\hat{t}}} = \frac{\sigma\Lambda(\lambda,q)e^{\nu}}{\gamma_s(1-\lambda\Omega_s)} \tag{2.1.22}$$

Where,

$$e^{2\nu} = \frac{\Sigma\Delta}{A} \tag{2.1.23}$$

$$e^{2\psi} = \sin^2\theta\frac{A}{\Sigma} \tag{2.1.24}$$

$$e^{2\lambda} = \frac{\Sigma}{\Delta} \tag{2.1.25}$$

$$e^{2\mu} = \Sigma \tag{2.1.26}$$

$$\omega = \frac{2Mar}{A} \tag{2.1.27}$$

$$\gamma_s = \frac{1}{\sqrt{(1-{V_s}^2)}}. \tag{2.1.28}$$

and

$$\Lambda(\lambda, q) = \sqrt{\frac{\left((r_s{}^2 + a^2 - \lambda a)^2 - \Delta[(\lambda - a)^2 + q^2]\right)}{\Delta\Sigma}} \tag{2.1.29}$$

Oscoz et al. solve for the wave-vector components (2.1.20), (2.1.21) and (2.1.22) at $r = r_s$, $t = t_s$, and constrain the photons to the equatorial plane by setting $q = 0$, and hence $k^{\hat{\theta}} = 0$. Denote $\lambda = \lambda_p$, $\sigma = \sigma_p$ and $\Lambda(\lambda, q) = \Lambda(\lambda_p, q = 0) = \Lambda(\lambda_p)$ for this special case.

$$k^{\hat{\phi}} = \frac{p^{\hat{\phi}}}{p^{\hat{t}}} = \frac{-V_s + \lambda_p(\omega V_s + e^{\nu-\psi})}{1 - \lambda_p\Omega_s} \tag{2.1.30}$$

$$k^{\hat{\theta}} = 0 \tag{2.1.31}$$

$$k^{\hat{r}} = \frac{p^{\hat{r}}}{p^{\hat{t}}} = \frac{\sigma_p\Lambda(\lambda_p)e^{\nu}}{\gamma_s(1 - \lambda_p\Omega_s)} \tag{2.1.32}$$

Using these equations (2.1.30), (2.1.31) and (2.1.32), as well as equation (2.1.1), it is now possible to calculate λ_p and σ_p.

$$\begin{aligned}
\sin\alpha_p &= \frac{-V_s + \lambda_p(\omega V_s + e^{\nu-\psi})}{1 - \lambda_p\Omega_s} \\
\Rightarrow (1 - \lambda_p\Omega_s)\sin\alpha_p &= -V_s + \lambda_p\omega V_s + \lambda_p e^{\nu-\psi} \\
\Rightarrow \sin\alpha_p + V_s &= \lambda_p\left(\Omega_s\sin\alpha_p + \omega V_s + e^{\nu-\psi}\right) \\
\Rightarrow \lambda_p(t_s) &= \frac{V_s + \sin\alpha_p}{\omega V_s + e^{\nu-\psi} + \Omega_s\sin\alpha_p}
\end{aligned} \tag{2.1.33}$$

$$\begin{aligned}
\cos\alpha_p &= \frac{\sigma\Lambda(\lambda_p)e^{\nu}}{\gamma_s(1 - \lambda_p\Omega_s)} \\
\Rightarrow \sigma_p(t_s) &= \frac{\gamma_s(1 - \lambda_p\Omega_s)\cos\alpha_p}{\Lambda(\lambda_p)}
\end{aligned} \tag{2.1.34}$$

Similarly, the wave-vector components $\lambda_{p'}$ and $\sigma_{p'}$ for the secondary emission at $\alpha_{p'} = \alpha_p + \pi$ can be derived. Note that $q_p = q_{p'} = 0$ for emissions in the equatorial plane.

Next, choose a set of initial conditions for the model. Oscoz et. al. [5] have chosen these conditions as follows. Assuming a stable circular orbit in the Kerr space-time, the orbit is simply described by the orbital phase (azimuthal angle), denoted $\phi_s(t_s)$.

$$\phi_s(t_s) = \phi_t(t_s = 0) + \Omega_s t_s \tag{2.1.35}$$

where $\phi_t(t_s = 0)$ is the azimuthal angle at time $t_s = 0$. Equation (2.1.9) gives the angle α_p as a function of time. The observer is placed at $\phi_o = 0$ (note the subscript denotes "observer" rather than zero), and at $r_o = \infty$. Select the initial pulsar beam direction such that $\lambda_s(t_s = 0) = 0$, thus selecting $\alpha_0 = \alpha_p(t_s = 0)$, where the subscript of α_0 denotes zero,

such that $\alpha_0 = \arcsin(-V_s)$. To prove this, substitute $\lambda_s = 0$ into equation (2.1.33):

$$\begin{aligned} 0 &= \frac{V_s + \sin\alpha_p}{\omega V_s + e^{\nu-\psi} + \Omega_s \sin\alpha_p} \\ \Rightarrow 0 &= V_s + \sin\alpha_p \\ \Rightarrow \alpha_p &= \arcsin(-V_s) \end{aligned}$$

The angle describing the direction of the secondary emission is then given by:

$$\alpha_{p'} = \arcsin(-V_s) + \pi$$

Denote the position of the observer/detector in the Kerr space-time as $[t_o, r_0 = \infty, \theta_o, \phi_o]$. The trajectories of the "allowed" pulsar rays (rays reaching the observer) have been solved using the integral given in the 1983 book on black-hole Physics by Chandrasekhar [14]. Oscoz et al. used an analytical approach for this problem. They followed the work of Cunningham and Bardeen [13] for extreme Kerr black-holes ($a = 1$), and its generalization by Chandrasekhar [14]. Defining two functions as follows,

$$R(r) = (r^2 + a^2)^2 - 2a\lambda(r^2 + a^2) + a^2\lambda^2 - (r^2 - 2Mr + a^2)(q^2 + (\lambda - a)^2) \tag{2.1.36}$$

$$\Theta(\theta) = q^2 - \lambda^2 \cot^2\theta + a^2 \cos^2\theta \tag{2.1.37}$$

Chandrasekhar showed that [14]:

$$\int_{r_s}^{r_o} \frac{\mathrm{d}r}{\sqrt{R(r)}} = \int_{\theta_s}^{\theta_o} \frac{\mathrm{d}\theta}{\sqrt{\Theta(\theta)}} \tag{2.1.38}$$

Note the resemblance of this result to equation (4.2.25) derived via the Hamilton-Jacobi formalism in chapter 4. The time of arrival at the observer is given by,

$$t_o = t_s + \int_{r_s}^{r_o} \frac{\left[(r^2 + a^2)^2 - a\lambda(r^2 + a^2) + \Delta a\lambda - \Delta a^2\right]}{\Delta\sqrt{R(r)}}\mathrm{d}r + \int_{\theta_s}^{\theta_o} \frac{a^2\cos^2\theta}{\sqrt{\Theta(\theta)}}\mathrm{d}\theta \tag{2.1.39}$$

The final orbital phase of a photon is given by,

$$\phi_o - \phi_s = \int_{r_s}^{r_o} \frac{\left[(r^2 + a^2 - a\lambda)a + \Delta(\lambda - a)\right]}{\Delta\sqrt{R(r)}}\mathrm{d}r + \int_{\theta_s}^{\theta_o} \frac{\lambda\cot^2\theta}{\sqrt{\Theta(\theta)}}\mathrm{d}\theta \tag{2.1.40}$$

Using the initial conditions, in the form of the emission parameters as given by the equations (2.1.33); (2.1.34) for λ_p and σ_p ($q_p = o$), placing the observer at $r = \infty$, the final orbital phase of the photon is given by,

$$\phi_o(\lambda_p, q_p = 0, \sigma_p) = \Omega_s t_s + \int_{r_s}^{\infty} \frac{\left[(r^2 + a^2 - a\lambda_p)a + \Delta(\lambda_p - a)\right]\mathrm{d}r}{\Delta\sqrt{(r^2 + a^2 - a\lambda_p)^2 - \Delta(\lambda_p - a)^2}}\mathrm{d}r \tag{2.1.41}$$

The sign of $\dot{r}$ sets the sign of the parameter σ_p, determining whether the photon is fired towards, or away from the black-hole. The integral from r_s to r_∞ is simple to evaluate for an outward-bound photon with ($\sigma_p = 1$). For inward-bound photons, this integration must be split into two parts, firstly when $\dot{r}$ is negative, and hence $\sigma_p = -1$ for the inward motion of the photon, secondly when, $\dot{r}$ is positive; $\sigma_p = 1$ extends from the minimum radial proximity which the photon reached, to $r = \infty$. For the outward motion of a photon, all integrations over r in equations (2.1.38), (2.1.39) and (2.1.40) remain as presented above. For the inward motion, and subsequent escape to $r = \infty$, the integrals over r in equations (2.1.38), (2.1.39) and (2.1.40) become,

$$\int_{r_s}^{\infty} = -\int_{r_s}^{r_{mp}} + \int_{r_{mp}}^{\infty} \tag{2.1.42}$$

where r_{mp} denotes the minimum approach, or maximum proximity, of the photon to the black-hole. It is the point at which $\dot{r}$ changes sign for an initially inward bound photon.

The quantity r_{mp} is derived by setting $\dot{r} = 0$. Furthermore, $R(r) = 0$ at $r = r_{mp}$, for a photon in the equatorial plane (q = 0),

$$\begin{aligned} R(r_{mp}) &= 0 \qquad (2.1.43)\\ \Rightarrow 0 &= (r_{mp}^2 + a^2)^2 - 2a\lambda_p(r_{mp}^2 + a^2) + a^2\lambda_p^2 - (r_{mp}^2 - 2Mr_{mp} + a^2)((\lambda_p - a)^2)\\ \Rightarrow 0 &= r_{mp}^4 + 2r_{mp}^2a^2 + a^4 - 2a^3\lambda_p - 2r_{mp}^2a^2\lambda_p + a^2\lambda_p^2 - \Delta_{mp}(\lambda_p - a)^2\\ \Rightarrow \Delta_{mp}(\lambda_p - a)^2 &= r_{mp}^4 + 2r_{mp}^2a^2 + a^4 - 2a^3\lambda_p - 2r_{mp}^2a^2\lambda_p + a^2\lambda_p^2\\ \Rightarrow \Delta_{mp}(\lambda_p - a)^2 &= \left[r_{mp}^2 - a\lambda_p + a^2\right]^2\\ \Rightarrow \Delta_{mp}(\lambda_p - a)^2 &= \left[r_{mp}^2 - a(\lambda_p - a)\right]^2 \qquad (2.1.44) \end{aligned}$$

Define $\nu_p = \lambda_p - a$ in equation (2.1.44),

$$\begin{aligned} \Delta_{mp}\nu_p^2 &= \left[r_{mp}^2 - a\nu_p\right]^2 \qquad (2.1.45)\\ \Rightarrow r_{mp}^2\nu_p^2 - 2Mr_{mp}\nu_p^2 + \cancel{a^2\nu_p^2} &= r_{mp}^4 - 2r_{mp}^2a\nu_p + \cancel{a^2\nu_p^2}\\ \Rightarrow r_{mp}\nu_p^2 - 2M\nu_p^2 &= r_{mp}^3 - 2r_{mp}a\nu_p\\ \Rightarrow 0 &= r_{mp}^3 - (2a\nu_p + \nu_p^2)r_{mp} + 2M\nu_p^2 \qquad (2.1.46) \end{aligned}$$

Equation (2.1.45) has three solutions, with only one of these solutions representing the physical result for r_{mp}.

Finally, the pulse arrival time at the observer, for a photon fired in the equatorial plane at time t_s, is given by,

$$t_o(\lambda_p, q_p = 0, \sigma_p) = t_s + \int_{r_s}^{\infty} \frac{\left[(r^2+a^2)^2 - a\lambda_p(r^2+a^2) + \Delta a\lambda_p - \Delta a^2\right]}{\Delta\sqrt{(r^2+a^2-\lambda_p a)^2 - \Delta(\lambda_p - a)^2}}\mathrm{d}r \qquad (2.1.47)$$

Where, as previously described, the integration must be split into two parts for inward bound photons, the first being from source to r_{mp} , and the second from r_{mp} to infinity.

Oscoz et al. use this model as a starting point, with further complexifications being introduced retrospectively to describe phenomena such as the decay of the pulsar orbit due to gravitational radiation, the evolution of the pulsar period ($\dot{P} \neq 0$), as well as the effect of having a non-zero pulsar mass. Considering the pulsar as a massive body which creates its own gravitational field would cause the black-hole to orbit around the centre of mass of the system. The evolution of the pulsar period can also be considered, by modifying the parameters which select the direction in which photons are fired. Oscoz et. al. describe the evolution of the pulsar period as a function of the physical parameters of the system. The pulsar period may also be affected by electro-magnetic braking processes occuring due to electromagnetic and other radiation processes.

Oscoz et al. state that their model is only accurate for pulsar orbital phases far away from the "superior conjunction", which occurs when the pulsar is on the opposite side of the black-hole with respect to the observer. This is the region of greatest interest in this thesis, with pulses passing near the event horizon. According to Oscoz et al., the model they derive is only useful for orbital phases such that $|\phi_s - \pi| > \phi_c$, where $\phi_c = \sqrt{\frac{4M}{r_s}}$ is the "critical phase" angle and corresponds to those positions of the pulsar at which the black-hole will lens the pulsar beam to such a degree that the relative flux with respect to a beam passing through flat space-time is greatly reduced. Assuming that the model only considers pulses originating far from the superior conjunction, and that the orbital seperation is sufficiently large ($r_s >> M$), Oscoz et al. revert to the use of a simple model utilizing the Schwarzschild metric. The justification for this is that, for large enough r_s, the second order effects implicit in the metric, as well as rotational effects which scale as $\frac{1}{r^2}$, are negligable. Thus, Oscoz et al. used a result stated by an earlier (1995) paper by Goicoechea et al., given below, for the arrival times of pulses.

$$t_o^* = t_e + r_s(1-\cos\phi_s) + 2M\ln\left(\frac{2}{1+\cos\phi_s}\right) - M(1-\cos\phi_s) + r_s\left(\frac{M}{r_s}\right)^{\frac{1}{2}}\frac{P}{L}(1-\cos\phi_s)$$

$$+ M\frac{P}{L}(1-\cos\phi_s)\left(\sin\phi_s + \frac{2}{\sin\phi_s}\right) \tag{2.1.48}$$

Where $t^*{}_o$ is the time measured by the observer, t_e is the time of emission, which is given in terms of the number of pulses, N; the pulsar period, P and the rate of increase of the pulsar period, $\dot{P}$.

$$t_e = NP + \frac{1}{2}P\dot{P}N^2 \tag{2.1.49}$$

L is the orbital length, $L = 2\pi r_s$.

The sum of relativistic time delays is known as the Shapiro delay. Using a Kerr metric to derive an analogous result for a spinning black-hole would include the frame dragging effect. Oscoz et al. identify the second term of equation (2.1.48) as the "orbital delay", i.e. the time delay dependent on the position of the pulsar at the time of emission. The term with coefficient, or "amplitude" $r_s\left(\frac{M}{r_s}\right)\frac{P}{L}$ is considered to be the main aberration delay, and is caused by the curvature of spacetime. An initial orbital phase can be chosen, $\phi_s = 0$, and a train of pulses produced starting with N = 0 and allowing N to increase by half integers, corresponding to two counts per pulsar rotation. Assuming that the orbit decays and that the Pulsar period is allowed to evolve, after a substantial number N and correspondingly large time t_e, Oscoz et al. expect to see a difference between the times of arrival for the Schwarzschild and Kerr cases. The difference between the angular velocities of the pulsar in the Schwarzschild and Kerr cases is given by,

$$\Omega_s(Kerr) = \Omega_s(Schwarzschild) - \Delta\Omega_K \tag{2.1.50}$$

Where $\Omega_K = \frac{aM}{r_s^3}$. Thus Oscoz et al. state that the difference between arrival times for Schwarzschild and Kerr black-hole cases is due to a difference in the delay caused by the rotational parameter of the Kerr black hole, as well as the fact that for sufficiently large N, the Nth pulse for a Schwarzschild black-hole is emitted from a different orbital phase ϕ_s than the Nth pulse for the Kerr case. The model constructed part II of this thesis can be used to investigate numerically the difference in delay due to the rotational parameter by firing photons towards the black-hole with identical initial conditions, setting the black-hole rotational parameter to a = 0 and 0 ¡ a ¡ 1 respectively..

Oscoz et al. complexify the model by removing the assumption that the pulsar is a point particle orbiting the black-hole. Hence, the effects of the gravitational field of the pulsar on the black hole must be included. Oscoz et al. adjust the coefficients of the final two terms in equation (2.1.48). These adjustments were made retrospectively, to allow for

Newtonian effects of a finite pulsar mass, given that $M_p << M$. Higher order terms have been neglected, and it is unclear whether this model would hold true for a stellar mass black-hole only 3 to 10 times more massive than the pulsar. I do not make similar adjustments in the final model produced part II, as the numerical model is sufficiently powerful, even when executed on a single machine, to describe the ideal case of a stable circular orbit. The effect of a non-zero pulsar mass would be more completely accounted for by describing the orbits of the black-hole and pulsar via the PPN equations (first and 3.5 order) of motion described in chapter 5. These equations account for gravitational radiation as well as dragging of the black-hole by a non-zero pulsar mass.

Oscoz et al. modify the pulse arrival times to account for non-zero pulsar mass by observing changes to the physical configuration of the system. The origin of the coordinate system must be shifted to the centre of mass rather than the location of the black-hole. Furthermore, the angular velocity of the pulsar, in the case of a Schwarzschild black-hole companion, is modified from $\Omega_s(Schwarzschild) = \sqrt{\frac{M}{r_s^2}}$ to $\Omega_s(Schwarzschild) = \sqrt{\frac{(M+M_p)}{r_s^3}}$. The orbital radius of the pulsar, r_p is also altered from r_s in the original coordinate system to $\frac{Mr_s}{(M+M_p)}$. The modified arrival times are given by,

$$t_o^* = t_e + r_s(1-\cos\phi_s) + 2M\ln\left(\frac{2}{1+\cos\phi_s}\right) - M(1-\cos\phi_s) + r_p\left(\frac{M+M_p}{r_s}\right)^{\frac{1}{2}}\frac{P}{L}(1-\cos\phi_s) + M\frac{P}{L}(1-\cos\phi_s)\left(\sin\phi_s + \frac{2}{\sin\phi_s}\right). \quad (2.1.51)$$

where $\phi_s = \Omega_s t_e$. The difference between angular velocities of the pulsar in the Schwarzschild and Kerr cases is given by $\Omega_s(Kerr) = \Omega_s(Schwarzschild) - \Delta\Omega_K$, where $\Omega_s(Schwarzschild)$ is modified as above.

Oscoz et al. then use a result from a 1964 paper by Peters [15] to account for the decay of the orbit due to graviational radiation. This result yields the rate of increase of the pulsar orbital radius, $(\dot{r}_s)$, when the pulsar orbits a black hole and loses energy due to gravitational radiation.

$$\begin{aligned}\dot{r}_s &= \frac{\mathrm{d}r_s}{\mathrm{d}t} \\ &= -\frac{64c}{5}\frac{MM_p(M+M_p)}{r_s^3}\end{aligned} \quad (2.1.52)$$

Where the relation between r_s and the evolution of r_p is given by,

$$r_p(t_e) = r_p(t=0) + \dot{r}_s t_e \quad (2.1.53)$$

Note, this is denoted differently in the paper [5], with $\dot{r}_s$ written as $\dot{r}_p$.

This modification to r_p must be applied to the second term in equation (2.1.51). However, Oscoz et al. do not correct r_p in the main aberration delay, as the alteration due to orbital evolution is considered negligible when compared with the aberration delay. Despite the fact that the orbit has been altered slightly, Oscoz et al. assume that the orbit retains its circular nature, by assuming that there is no change in eccentricity: $\dot{e} = \frac{\mathrm{d}e}{\mathrm{d}t} = 0$.

Modification of the orbital radius has implications for the angular velocity of the pulsar. Furthermore, this change of angular velocity implies that the pulses will be fired from slightly different orbital phase positions. Hence, Oscoz et al. have modified both the angular velocity terms Ω_s and the phase ϕ_s in (2.1.51). Oscoz et al. quantify these modifications via the following equations.

$$\Omega_s(t_e) = \Omega_s(t = 0) + \dot{\Omega}_s t_e \tag{2.1.54}$$

Where the rate of increase of the angular velocity is given by,

$$\dot{\Omega}_s = -\frac{3}{2}\Omega_s \frac{\dot{r}_s}{r_s}. \tag{2.1.55}$$

Finally, Oscoz et al. alter the phase ϕ_s by using equations (2.1.54) and (2.1.55), as well as the following equation for the evolution of the emission phase of the pulsar.

$$\phi_s(t_e) = \Omega_s(t = 0)t_e + \frac{1}{2}\dot{\Omega}_s t_e^2 \tag{2.1.56}$$

This concludes the formulation of the basic pulse-timing model. Oscoz et al. then use it to produce plots of the signal expected at an Earth based observatory from a pulsar orbiting a black-hole. However, this model makes no attempt to compute the flux of the pulses as a function of the orbital phase of the pulsar. Oscoz et al. [5] continue to derive analytically a model that describes the flux of the main pulses (no lensed pulses were considered) as a function of the orbital phase of emission.

2.1.2 A Model to Describe Flux, Oscoz et al. [5]

Oscoz et al. calculate the relative flux detected by a distant observer, given the pulse-timing model described in the previous section. They use a theoretical approach to derive the relative flux observed by a detector of finite size situated at infinte radial distance from the black-hole. It is important to state the difficulties inherent in such a calculation. The first difficulty is the nature of the anisotropic emissions of the pulsar through two cones thought to be emitting in opposite directions along the magnetic axis of the pulsar. The study of the emission mechanism is crucial for advancements of models such as that of Oscoz et al., and the one presented in part II of this thesis. The Rotating Vector Model (RVM), described in a paper by Radhakrishnan and Cooke (1969) [16] may serve as a useful starting point. This model incorporates polarization in the analysis. Lyne and Manchester (1988) [17] discuss all prior work up to 1988 that describe beam shape and polarization. Returning to the work by Oscoz et al., their model describes a special case of simplified emission by making the assumptions previously stated.

The second difficulty inherent in the calculation of flux is the fact that the pulsar signal travels through a strongly curved spacetime near the black-hole. In superior conjunction, the beam may be scattered through large angles when compared with the incident angle. The magnification of the pulses emitted at superior conjunction could be very low, but this depends on the physical properties of the black-hole. In the case of a supermassive black-hole, Wang et al. [8] and Nampalliwar et al. [9] consider the possibility of detection of scattered pulses. Oscoz et al. assume that their model provides insufficient description of observed flux for pulses emanating at superior conjunction.

A graphical representation of quantities calculated and what these quantities represent physically is shown in Figure 2 of the paper by Oscoz et. al. [5].

Oscoz et al. place the observer at $r = \infty$ in the equatorial plane of the Kerr black-hole. The detector is circular, with radius b and area S_o. They denote the number of photons emitted per unit time in an isotropic, conical geometry of solid angle $\Delta\Omega_p$ as $\mathrm{d}N_e/\mathrm{d}t_e$. The area of the detector, from the viewpoint of the pulsar, is given by $\Delta\Omega(S_o)$. Oscoz et al. calculate the number of photons passing through the detector area S_o in a differential time $\mathrm{d}t_e$ by the following equation.

$$\mathrm{d}N_o = \mathrm{d}N_e \left[\frac{\Delta\Omega(S_o)}{\Delta\Omega_p} \right] \tag{2.1.57}$$

The red-shift factor is denoted by z, and determines the differences in emissions from points along the orbit of the pulsar, given by factors of $1+z$ and $\Omega(S_o)$.

$$\frac{\mathrm{d}t_o}{\mathrm{d}t_e} = 1+z \Rightarrow \mathrm{d}t_o = (1+z)\mathrm{d}t_e$$

where,

$$1+z = \gamma_s e^{-\nu}(1-\lambda_p \Omega_s) \tag{2.1.58}$$

and γ_s is given by equation (2.1.28).

Oscoz et al. calculate the flux, or number of photons per unit time passing the detector surface S_o, denoted $F_{\gamma o}$.

$$\begin{aligned} F_{\gamma o} &= \frac{\mathrm{d}N_o}{\mathrm{d}t_o} \\ \Rightarrow F_{\gamma o} &= \frac{\mathrm{d}N_e \left[\dfrac{\Delta\Omega(S_o)}{\Delta\Omega_p}\right]}{(1+z)\mathrm{d}t_e} \\ \Rightarrow F_{\gamma o} &= \frac{\mathrm{d}N_e}{\mathrm{d}t_e}\frac{\Delta\Omega(S_o)}{\Delta\Omega_p}\frac{1}{1+z} \\ \Rightarrow F_{\gamma o} &= F_{\gamma e}\frac{\Delta\Omega(S_o)}{\Delta\Omega_p}\frac{1}{1+z} \end{aligned} \tag{2.1.59}$$

The flux emitted by the pulsar is given by $F_{\gamma e} = \dfrac{\mathrm{d}N_e}{\mathrm{d}t_e}$. Thus, equation (2.1.59) relates the flux detected by the observer to that emitted by the pulsar by a multiplicative factor. This factor is a function of the ratio of detector solid angle as seen from the pulsar ($\Omega(S_o)$), and the solid angle subtended by the conical emission of the pulsar, $\Delta\Omega_p$. Oscoz et al. calculate the relation between the classical solid angle subtended by the detector, $\Delta\Omega_c(S_o)$, and the quantity $\Omega(S_o)$. Note that $\Delta\Omega_c(S_o)$ is the solid angle that would be seen if the observer was placed at the origin, and there was no black-hole present. The relation between the two quantities describes the distortion of the solid angle with which the pulsar sees the detector relative to the undistorted classical quantity. The classical quantity is given by,

$$\begin{aligned} \Delta\Omega_c(S_o) &= \int\int \mathrm{d}\theta_o \mathrm{d}\phi_o \\ &= \frac{\pi b^2}{r_o^2} \\ &= \pi\beta_o^2 \end{aligned} \tag{2.1.60}$$

Oscoz et al. derive a transfer function, which describes the relationship between the classical $\Delta\Omega_c(S_o)$ and the relativistic $\Delta\Omega(S_o)$. They orient the detector in a plane perpendicular to

the equatorial plane of the black-hole. They then consider an emission from the pulsar to the centre of the detector, with emission parameters given by $k(\lambda_p, q_p = 0, \sigma_p)$. Oscoz et al. use perturbation theory to describe the geometry of the beam reaching the detector. They first perturb the parameter λ such that $\lambda \to \lambda_p + d\lambda$, where $d\lambda << \lambda_p$. Making use of the fact that the perturbation is infinitesimal, expand $\mathbf{k}$ about $\lambda = \lambda_p$, keeping only terms of first order in $d\lambda$.

$$\mathbf{k}(\lambda_p + \mathrm{d}\lambda, q_p = 0, \sigma_p) = \mathbf{k}(\lambda_p, q_p = 0, \sigma_p) + \left(\frac{\partial \mathbf{k}}{\partial \lambda}\right)_p \mathrm{d}\lambda \tag{2.1.61}$$

The subscript p referrs to the values $\lambda_p, q_p = 0, \sigma_p$. These perturbations occur in specific directions in the LRF of the pulsar, relating to a change in direction in the azimuthal and polar angles with respect to a vector connecting the pulsar and the centre of the antenna. (See Figure 3 of the paper by Oscoz et al. [5]). Using the second term in equation (2.1.61), Oscoz et al. define the quantity $d\beta$,

$$\epsilon_\lambda = \left(\frac{\partial \mathbf{k}}{\partial \lambda}\right) \mathrm{d}\lambda \tag{2.1.62}$$

$$\mathrm{d}\beta = \left|\frac{\partial \mathbf{k}}{\partial \lambda}\right|_p \mathrm{d}\lambda \tag{2.1.63}$$

Equation (2.1.61) yields an alteration to the direction at which the photon is fired within the equatorial plane. To perturb the direction of propagation out of the equatorial plane, Oscoz et al. vary the impact parameter q in an analogous way.

$$\mathbf{k}(\lambda_p, q_p = 0 + \mathrm{d}q, \sigma_p) = \mathbf{k}(\lambda_p, q_p = 0, \sigma_p) + \left(\frac{\partial \mathbf{k}}{\partial q}\right)_p \mathrm{d}q \tag{2.1.64}$$

As with the perturbation in λ_p, it is useful to define the following quantities.

$$\epsilon_q = \left(\frac{\partial \mathbf{k}}{\partial q}\right) \mathrm{d}q \tag{2.1.65}$$

$$\mathrm{d}\alpha = \left|\frac{\partial \mathbf{k}}{\partial q}\right|_p \mathrm{d}q \tag{2.1.66}$$

Construct the solid angle with which the pulsar sees the detector ($\Delta\Omega(S_o)$) using these quantities, thus producing the portion of the beam which propagates to the detector. The quantities $d\alpha$ and $d\beta$ form the polar and azimuthal angles subtending the solid angle $\Delta\Omega(S_o)$, analogous to the construction of the classical solid angle subtended by the detector, given

by equation (2.1.60).

$$\begin{aligned}\Delta\Omega(S_o) &= \int\int \mathrm{d}\alpha\mathrm{d}\beta \\ &= \int\int D_k \mathrm{d}\lambda\mathrm{d}q \\ &= D_k \int\int \mathrm{d}\lambda\mathrm{d}q\end{aligned} \tag{2.1.67}$$

where,

$$D_k = \left|\frac{\partial\mathbf{k}}{\partial q}\right|_p \left|\frac{\partial\mathbf{k}}{\partial\lambda}\right|_p . \tag{2.1.68}$$

Oscoz et al. calculate the partial derivatives in equation (2.1.68) by using equations (2.1.10), (2.1.20), (2.1.21) and (2.1.22). They differentiate with respect to q first, only $k^{\hat{\theta}}$ contains q explicitly. However, the function $\Lambda(\lambda, q)$ contains q and appears in the other components of $\mathbf{k}$. Oscoz et al. overlook this by assuming $\dfrac{\partial\mathbf{k}}{\partial q} = \dfrac{\partial k^{\hat{\theta}}}{\partial q}$, i.e. only the $\hat{\theta}$ component of the wave vector $\mathbf{k}$ varies with q.

$$\begin{aligned}\left|\frac{\partial k^{\hat{\theta}}}{\partial q}\right|_p &= \left|\frac{\partial}{\partial q}\left(\frac{qe^{\nu-\mu}}{\gamma_s(1-\lambda\Omega_s)}\right)\right| \\ \Rightarrow \left|\frac{\partial k^{\hat{\theta}}}{\partial q}\right|_p &= \frac{e^{\nu-\mu}}{\gamma_s(1-\lambda_p\Omega_s)}\end{aligned} \tag{2.1.69}$$

Differentiation with respect to λ is more difficult. Although Oscoz et al. omit $k^{\hat{\theta}}$, it does contain λ. They argue that the perturbation here is explicitly in the equatorial plane: $k^{\hat{\theta}} = 0$. They make the following decomposition to perform the differentiation.

$$\left|\frac{\partial\mathbf{k}}{\partial\lambda}\right|_p = \sqrt{\left(\frac{\partial k^{\hat{r}}}{\partial\lambda}\right)_p^2 + \left(\frac{\partial k^{\hat{\phi}}}{\partial\lambda}\right)_p^2} \tag{2.1.70}$$

Differentiating $k^{\hat{\phi}}$,

$$\begin{aligned}\frac{\partial k^{\hat{\phi}}}{\partial\lambda} &= \frac{\partial}{\partial\lambda}\left(\frac{-V_s + \lambda(\omega V_s + e^{\nu-\psi})}{1-\lambda\Omega_s}\right) \\ \Rightarrow \frac{\partial k^{\hat{\phi}}}{\partial\lambda} &= \frac{1}{1-\lambda\Omega_s}\frac{\partial}{\partial\lambda}\left(-V_s + \lambda(\omega V_s + e^{\nu-\psi})\right) \\ &\quad + \left(-V_s + \lambda(\omega V_s + e^{\nu-\psi})\right)\frac{\partial}{\partial\lambda}\left(1-\lambda\Omega_s\right)^{-1} \\ \Rightarrow \frac{\partial k^{\hat{\phi}}}{\partial\lambda} &= \frac{(\omega V_s + e^{\nu-\psi})(1-\lambda\Omega_s)}{(1-\lambda\Omega_s)^2} + \frac{\Omega_s\left(-V_s + \lambda(\omega V_s + e^{\nu-\psi})\right)}{(1-\lambda\Omega_s)^2} \\ \Rightarrow \left(\frac{\partial k^{\hat{\phi}}}{\partial\lambda}\right)_p &= \frac{(\omega V_s + e^{\nu-\psi})(1-\lambda_p\Omega_s) + \Omega_s\left[-V_s + \lambda_p(\omega V_s + e^{\nu-\psi})\right]}{(1-\lambda_p\Omega_s)^2}.\end{aligned} \tag{2.1.71}$$

Differentiating $k^{\hat{r}}$,

$$\frac{\partial k^{\hat{r}}}{\partial\lambda} = \frac{\partial}{\partial\lambda}\left(\frac{\sigma\Lambda(\lambda,q)e^{\nu}}{\gamma_s(1-\lambda\Omega_s)}\right)$$

$$\Rightarrow \frac{\partial k^{\hat{r}}}{\partial \lambda} = \frac{1}{1-\lambda\Omega_s}\frac{\partial}{\partial\lambda}\frac{\sigma\Lambda(\lambda,q)e^{\nu}}{\gamma_s} + \frac{\sigma\Lambda(\lambda,q)e^{\nu}}{\gamma_s}\frac{\partial}{\partial\lambda}(1-\lambda\Omega_s)^{-1}$$

$$\Rightarrow \left(\frac{\partial k^{\hat{r}}}{\partial\lambda}\right)_p = \sigma_p \frac{e^{\nu}\left[\left(\frac{\partial\Lambda}{\partial\lambda}\right)_p(1-\lambda_p\Omega_s)+\Omega_s\Lambda_p\right]}{\gamma_s(1-\lambda_p\Omega_s)^2}. \tag{2.1.72}$$

The derivatives can be substituted into equation (2.1.67), but the result is particularly messy. Having obtained D_k, Oscoz et al. consider this formalism from the perspective of the observer. They define $\mathrm{d}\alpha$ and $\mathrm{d}\beta$ in terms of θ_o and ϕ_o as follows. Note that this definition uses classical equation (2.1.60) rather than the relativistic equation (2.1.67), and requires the use of the previously mentioned Transfer function, T_p.

$$\mathrm{d}\alpha = \left|\frac{\partial\mathbf{k}}{\partial\theta_o}\right|_p \mathrm{d}\theta_o \tag{2.1.73}$$

$$\mathrm{d}\beta = \left|\frac{\partial\mathbf{k}}{\partial\phi_o}\right|_p \mathrm{d}\phi_o \tag{2.1.74}$$

Using the classical equation (2.1.60),

$$\begin{aligned}\Delta\Omega(S_o) &= \left|\frac{\partial\mathbf{k}}{\partial\theta_o}\right|_p \left|\frac{\partial\mathbf{k}}{\partial\phi_o}\right|_p \int\int \mathrm{d}\theta_o\mathrm{d}\phi_o \\ &= T_p\pi\beta_o^2\end{aligned} \tag{2.1.75}$$

where T_p is defined in terms of partial derivatives,

$$T_p = \left|\frac{\partial\mathbf{k}}{\partial\theta_o}\right|_p \left|\frac{\partial\mathbf{k}}{\partial\phi_o}\right|_p \tag{2.1.76}$$

Applying the chain rule to relate T_p to the partial derivative equations (2.1.69), (2.1.71) and (2.1.72).

$$\left|\frac{\partial\mathbf{k}}{\partial\theta_o}\right|_p = \left|\frac{\partial\mathbf{k}}{\partial\lambda}\frac{\partial\lambda}{\partial\theta_o}\right|_p$$

similarly,

$$\left|\frac{\partial\mathbf{k}}{\partial\phi_o}\right|_p = \left|\frac{\partial\mathbf{k}}{\partial\lambda}\frac{\partial\lambda}{\partial\phi_o}\right|_p.$$

Finally, substitute into equation (2.1.76) and invert the necessary terms,

$$\begin{aligned}T_p &= \left|\frac{\partial\mathbf{k}}{\partial\lambda}\frac{\partial\lambda}{\partial\theta_o}\right|_p \left|\frac{\partial\mathbf{k}}{\partial\lambda}\frac{\partial\lambda}{\partial\phi_o}\right|_p \\ &= \frac{\left|\frac{\partial\mathbf{k}}{\partial\lambda}\right|_p \left|\frac{\partial\mathbf{k}}{\partial q}\right|_p}{\left|\frac{\partial\theta_o}{\partial q}\right|_p \left|\frac{\partial\phi_o}{\partial\lambda}\right|_p}\end{aligned} \tag{2.1.77}$$

The numerator of equation (2.1.77) is found in equations (2.1.69), (2.1.71) and (2.1.72). Oscoz et al. solve for the denominator by defining a new function $D_{\theta\phi}$.

$$\begin{aligned} T_p &= \frac{\left|\frac{\partial \mathbf{k}}{\partial \lambda}\right|_p \left|\frac{\partial \mathbf{k}}{\partial q}\right|_p}{\left|\frac{\partial \theta_o}{\partial q}\right|_p \left|\frac{\partial \phi_o}{\partial \lambda}\right|_p} \\ &= \frac{D_k}{\left|\frac{\partial \theta_o}{\partial q}\right|_p \left|\frac{\partial \phi_o}{\partial \lambda}\right|_p} \\ &= \frac{D_k}{D_{\theta\phi}} \\ \Rightarrow D_{\theta\phi} &= \left|\frac{\partial \theta_o}{\partial q}\right|_p \left|\frac{\partial \phi_o}{\partial \lambda}\right|_p \end{aligned} \tag{2.1.78}$$

The quantities $\left|\frac{\partial \theta_o}{\partial q}\right|_p$ and $\left|\frac{\partial \phi_o}{\partial \lambda}\right|_p$ must now be calculated. Oscoz et al. calculate these by using Chandrasekhar's integral equation for the trajectories of photons [14], equation (2.1.38). The integration bounds are chosen for the case of a distant observer ($r = \infty$), and a photon emission approximately in the equatorial plane ($q = \Delta q$), inward bound towards the black-hole ($\sigma_p = -1$). The integral must be split, using equation (2.1.42). Considering the radial side of equation (2.1.38), the photon propagates from the original position r_s to the minimum proximity r_mp, then outwards to r_s once more, and from there to the observer at $r = \infty$. Oscoz et al. rewrite (2.1.42) as follows.

$$\int_{r_s}^{\infty} = -\int_{r_s}^{r_{mp}} + \int_{r_{mp}}^{\infty} = 2\int_{r_{mp}}^{r_s} + \int_{r_s}^{\infty}$$

Rewrite the left hand side of equation (2.1.38) as follows.

$$\int_{r_s}^{\infty} \frac{\mathrm{d}r}{\sqrt{R(r)}} = 2\int_{r_{mp}}^{r_s} \sqrt{R(r, \lambda_p, \Delta q)}\,\mathrm{d}r + \int_{r_s}^{\infty} \sqrt{R(r, \lambda_p, \Delta q)}\,\mathrm{d}r \tag{2.1.79}$$

Denote the integral on the right hand side of equation (2.1.38) as I_θ, rewrite Chandra's result.

$$2\int_{r_{mp}}^{r_s} \sqrt{R(r, \lambda_p, \Delta q)}\,\mathrm{d}r + \int_{r_s}^{\infty} \sqrt{R(r, \lambda_p, \Delta q)}\,\mathrm{d}r = I_\theta \tag{2.1.80}$$

Oscoz et al. solve for I_θ explicitly by transforming the coordinate system, and using the small angle (θ) approximation for $\sin\theta$. They substitute $\Theta(\theta)$, given by equation (2.1.37), into equation (2.1.38). The non-zero Δq changes the direction of the photon out of the equatorial plane by an infinitesimal amount, denoted $\Delta\theta_o$. The equation for I_θ:

$$I_\theta = \int_{\frac{\pi}{2}}^{\frac{\pi}{2}+\Delta\theta_o} \frac{\mathrm{d}\theta}{\sqrt{(\Delta q)^2 - \lambda_p^2 \cot^2\theta + a^2\cos^2\theta}} \tag{2.1.81}$$

Oscoz et al. use the coordinate transformation $x = \cos\theta$, for small $\Delta\theta_o$, $\sin\Delta\theta_o \simeq \Delta\theta_o \mathrm{d}\theta \simeq \mathrm{d}x$, furthermore $\cot^2\theta \simeq x^2$. They re-write equation (2.1.81) as follows.

$$I_\theta = \int_{\frac{\pi}{2}}^{\frac{\pi}{2}+\Delta\theta_o} \frac{\frac{\Delta\theta_o}{\mathrm{d}x}}{\sqrt{(\Delta q)^2 - \lambda_p^2 x^2 + a^2 x^2}} \tag{2.1.82}$$

Equation (2.1.82) is then re-written using another coordinate transformation, $\sin y = \dfrac{\sqrt{\lambda_p^2 - a^2}\, x}{\Delta q}$,

$$I_\theta \simeq \frac{1}{\sqrt{\lambda_p^2 - a^2}} \sin^{-1}\left[\sqrt{\lambda_p^2 - a^2}\,\frac{\Delta\theta_o}{\Delta q}\right] \tag{2.1.83}$$

Taking the limit as the infinitesimal quantities on the right hand side of equation (2.1.83), Δq and $\Delta\theta_o$ tend to zero, rewrite equation (2.1.80) and solve for $\dfrac{\partial\theta_o}{\partial q}$. Evaluate $R(r)$ in equation (2.1.80) with parameter $q = 0$ rather than Δq, after taking the limit.

$$2\int_{r_{mp}}^{r_s} \sqrt{R(r,\lambda_p,q=0)}\,\mathrm{d}r + \int_{r_s}^{\infty} \sqrt{R(r,\lambda_p,q=0)}\,\mathrm{d}r = \frac{1}{\sqrt{\lambda_p^2 - a^2}} \sin^{-1}\left[\sqrt{\lambda_p^2 - a^2}\left(\frac{\partial\theta_o}{\partial q}\right)_p\right] \tag{2.1.84}$$

Solving (2.1.84) for $\left(\dfrac{\partial\theta_o}{\partial q}\right)_p$, the final result for the most general case of an inward bound photon trajectory approximately in the equatorial plane is given by the following equation. Put $R_p = R(r,\lambda_p,q=0)$. Then

$$\left(\frac{\partial\theta_o}{\partial q}\right)_p = \frac{1}{\sqrt{\lambda_p^2 - a^2}} \sin\left[\sqrt{\lambda_p^2 - a^2}\, 2\int_{r_{mp}}^{r_s} \sqrt{R_p}\,\mathrm{d}r + \int_{r_s}^{\infty} \sqrt{R_p}\,\mathrm{d}r\right] \tag{2.1.85}$$

Oscoz et al. state the result (2.1.85), with the term $2\int_{r_{mp}}^{r_s} \sqrt{R_p}\,\mathrm{d}r$ omitted, describing the radial motion of the photon from the emitter, to r_{mp} and back out to the emitter's radial distance.

Oscoz et al. calculate $\left(\dfrac{\partial\phi_o}{\partial\lambda}\right)_p$ to complete the transfer function. They use the generalization of Cunningham and Bardeen's result from [13], given by equation (2.1.40). Using this equation for a photon fired with impact parameters $q = 0$, $\lambda = \lambda_p + \Delta\lambda$ and $\sigma_p = -1$, and perturbing the final phase of the photon by an infinitesimal quantity $\Delta\phi_o$, equation (2.1.40) becomes,

$$\phi_o + \Delta\phi_o - \phi_s = 2\int_{r_{mp}(\lambda_p+\Delta\lambda,q_p=0)}^{r_s} f(r,\lambda_p+\Delta\lambda,q_p=0)\mathrm{d}r + \int_{r_s}^{\infty} f(r,\lambda_p+\Delta\lambda,q_p=0)\mathrm{d}r. \tag{2.1.86}$$

where,

$$f = \frac{\left[(r^2 + a^2 - a\lambda)a + \Delta(\lambda - a)\right]}{\Delta\sqrt{R(r,\lambda,q)}}. \tag{2.1.87}$$

Equation (2.1.86) is the result for a photon with perturbed impact parameter λ_p. The left hand side of equation (2.1.86) contains $\phi_o - \phi_s$, which is the left hand side of equation (2.1.40) for impact parameters λ_p, $q_p = 0$ and $\sigma_p = -1$. Oscoz et al. substitute this result into equation (2.1.86) to obtain the following.

$$\begin{aligned}&\Delta\phi_o + 2\int_{r_{mp}}^{r_s} f(r,\lambda_p,q_p=0)\mathrm{d}r + \int_{r_s}^{\infty} f(r,\lambda_p,q_p=0)\mathrm{d}r + \cancel{\int_{\theta_s}^{\theta_o} \frac{\lambda\cot^2\theta}{\sqrt{\Theta(\theta)}}\mathrm{d}\theta}\\ &= 2\int_{r_{mp}(\lambda_p+\Delta\lambda,q_p=0)}^{r_s} f(r,\lambda_p+\Delta\lambda,q_p=0)\mathrm{d}r + \int_{r_s}^{\infty} f(r,\lambda_p+\Delta\lambda,q_p=0)\mathrm{d}r \qquad (2.1.88)\end{aligned}$$

The integral $\int_{\theta_s}^{\theta_o} \frac{\lambda\cot^2\theta}{\sqrt{\Theta(\theta)}}\mathrm{d}\theta$ is trivially zero as this is the special case for $q_p = 0$, a photon constrained to the equatorial plane. Rearranging equation (2.1.88) accordingly yields,

$$\begin{aligned}\Delta\phi_o = 2&\left[\int_{r_{mp}(\lambda_p+\Delta\lambda,q_p=0)}^{r_s} f(r,\lambda_p+\Delta\lambda,q_p=0)\mathrm{d}r - \int_{r_{mp}}^{r_s} f(r,\lambda_p,q_p=0)\mathrm{d}r\right]\\ &+ \int_{r_s}^{\infty}\Big(f(r,\lambda_p+\Delta\lambda,q_p=0) - f(r,\lambda_p,q_p=0)\Big)\mathrm{d}r \qquad (2.1.89)\end{aligned}$$

Divide (2.1.89) through by $\Delta\lambda$ and take the limit as $\Delta\lambda$ tends to zero.

$$\begin{aligned}\left(\frac{\partial\phi_o}{\partial\lambda}\right)_p = &\lim_{\Delta\lambda\to 0}\frac{2}{\Delta\lambda}\left[\int_{r_{mp}(\lambda_p+\Delta\lambda,q_p=0)}^{r_s} f(r,\lambda_p+\Delta\lambda,q_p=0)\mathrm{d}r - \int_{r_{mp}}^{r_s} f(r,\lambda_p,q_p=0)\mathrm{d}r\right]\\ &+ \lim_{\Delta\lambda\to 0}\frac{1}{\Delta\lambda}\int_{r_s}^{\infty}\Big(f(r,\lambda_p+\Delta\lambda,q_p=0) - f(r,\lambda_p,q_p=0)\Big)\mathrm{d}r \qquad (2.1.90)\end{aligned}$$

The integral from r_s to ∞ becomes, by first principles, the partial derivative $\frac{\partial f}{\partial\lambda}$, Oscoz et al. denote $f(r,\lambda_p,q_p=0)$ by f_p. The final equation for $\left(\frac{\partial\phi_o}{\partial\lambda}\right)_p$ is given by the following.

$$\begin{aligned}\left(\frac{\partial\phi_o}{\partial\lambda}\right)_p = &\int_{r_s}^{\infty}\left(\frac{\partial f}{\partial\lambda}\right)_p \mathrm{d}r\\ &+ \lim_{\Delta\lambda\to 0}\frac{2}{\Delta\lambda}\left[\int_{r_{mp}(\lambda_p+\Delta\lambda,q_p=0)}^{r_s} f(r,\lambda_p+\Delta\lambda,q_p=0)\mathrm{d}r - \int_{r_{mp}}^{r_s} f_p\mathrm{d}r\right] \qquad (2.1.91)\end{aligned}$$

Oscoz et al. construct the transfer function by using equations (2.1.69), (2.1.71), (2.1.72), (2.1.70), (2.1.77), (2.1.85) and (2.1.91). The final result is not stated as it is a messy, path-dependant result. Oscoz et al. use the transfer function to calculate relative flux observed, given an emitted flux described by the following equation.

$$F_{\gamma stan} = \frac{F_{\gamma e}\Delta\Omega_c(S_o)}{\Delta\Omega_p} \qquad (2.1.92)$$

Finally, Oscoz et al. calculate the relative flux observed by the detector for different orbital phases of emission using equations (2.1.59), (2.1.75) and the following.

$$F^*_{\gamma o} = \frac{T_p}{1+z} \qquad (2.1.93)$$

2.2 Pulse Arrival-Times from Binary Pulsars with Rotating Black Hole Companions, Laguna and Wolszczan [4]

Laguna and Wolszczan have produced a numerical model which describes the timing residuals caused by a rotating black-hole companion in a binary system with a pulsar. In particular, the aim of their model is to identify the additional timing delay caused by black-hole rotation, which would be observed in addition to the Shapiro delay. The parameters of their system include black-hole mass, black-hole angular momentum, orbital inclination, binary orbital period and eccentricity. The approach taken differs from the numerical model in this thesis, as they specify a detector position and size, and they subsequently integrate photon trajectories along Kerr null geodesics backwards towards the binary system. They use Monte Carlo methods in conjunction with a fourth order Runge-Kutta integrator, with a simple form of adaptive stepsize scaling. They use a sample of 20000 photons to generate the timing residual data, describing the magnitude of the effect that rotation has on the timing delay measured for pulses. In this section I discuss their calculations and results.

They begin with the 1984 result presented by Dymnikova, [18], which gives the time taken for a photon travelling in the equatorial plane of the Kerr metric, to reach its maximum proximity to the black-hole:

$$t\pm = \sqrt{r^2 - d^2} + 2M_H \ln\left(\left(\frac{r + \sqrt{r^2 - d^2}}{d}\right)\right) + M_H\sqrt{\frac{r-d}{r+d}} + \frac{(15\pi - 8){M_H}^2}{4d} \mp \frac{4aM_H}{d} \tag{2.2.1}$$

where M_H is the mass of the black-hole, a is the rotational parameter, r is the point of origin for the incident photon and d its maximum proximity to the black-hole. Note that $r >> d$ for this approximate integral of the equatorial Kerr null geodesic to hold true. The $t+$ solution corresponds to the case of a photon corotating with the black-hole spin, so that the propagation time is reduced by the negative sign of the final term. The $t-$ case corresponds to a contra-rotating photon, which must move against the flow of space-time rotating about the black-hole. Accordingly the positive sign for the last term increases the propagation time to the point of maximum proximity. I have tested the numerical model in part II of this thesis against this analytical result. The comparison is discussed in chapter 9. Returning to the Laguna et al. paper, they describe the difference in propagation times on either side of the rotating black-hole. To do this, they isolate the final term in (2.2.1), which is the only term dependent on the rotational parameter of the black-hole, representing the contribution that the dragging of inertial reference frames makes to the delay or advance

of the signal. They calculate propagation times from emitter to maximum proximity, and subsequently maximum proximity to observer by using the results for $t+$ and $t-$ cases, with the result trivially just adding a multiple of the final term in (2.2.1) for each portion of photon trajectory.

$$\Delta t = \frac{16aM_H}{d} \tag{2.2.2}$$

Laguna et. al. provide an order of magnitude calculation describing system parameters which enhance the detectability of this rotational effect without reducing the probability of finding such a system too significantly. They describe an elliptical orbit which is edge-on with respect to the observer, a black-hole of mass agreeing with the literature for proposed pulsar/black-hole binary systems, quoting Narayan et al. [19]. They scale the system by choosing a value for the semi-major axis which does not reduce the lifetime of the system below 107 years before merger due to emission of gravitational radiation. The superior conjunction occurs with the pulsar at the periastron of the ellipse, minimizing distance between pulsar and black-hole to maximize relativistic effects. The size of the semi-major axis was selected to be $a_p = 5R_\odot$ and $a_p = 10R_\odot$. 20000 Photons were then integrated backwards, via 4th order Runga-Kutte (RK), from a distant detector to the plane of the pulsar's orbit. Only photons which moved within $10^{-4}a_p$ of the pulsar's orbit were analyzed, with the timing residuals formed by comparison of propagation times through flat spacetime (i.e. the first term in (2.2.1)). They reduce step size in the vicinity of the black-hole, but no details were given as to the mechanism of scaling.

Their numerical analysis uses a substantial post-processing routine. They form a uniform orbital phase grid by iterpolation of timing data, which is recorded by folding data about the azimuthal angle reached at closest approach for pair points (on either side of the blackhole) which would have identical travel times without the presence of the black-hole (flat space-time). The propagation times are then subtracted. Photons are allowed to travel slightly out of the equatiorial plane. Finally, they show that their results agree with the estimate of equation (2.2.2), after having re-formulated the impact parameter d for the case of an elliptical orbit. Note that equation (2.2.2) was derived from Dymnikova's result, and is thus specific to equatorial photons. The photon trajectories integrated numerically do however allow for slight deviation out of the equatorial plane, hence a slight discrepancy may be expected. Ultimately, their data shows micro-second level differences in the propagation delays of pulses, caused by the rotation of the black-hole. The model presented in part II

could be used, with sufficient adjustment, to replicate the measurements of Laguna et al. with even greater precision.

2.3 Frame-dragging and precessional effects, Wex & Kopeikin [6]

Wex and Kopeikin focus on the study of frame dragging and precessional effects in blackhole/ pulsar binary systems, with the hope of describing a method of directly observing a stellar-mass black-hole. They discuss the possibility of obtaining physical information from such a system, specifically with the intention of determining the properties of the blackhole. The first part of their work describes the measurement of the quadrupole moment of the black-hole, in conjunction with other physical information, to identify black-hole candidates. The quantity χ is identified as a dimensionless parameter describing the spin of an astrophysical body, coinciding with the quantity $a = M$ for the Kerr black-hole, and is governed by the following physical relationship.

$$\chi = \frac{c}{G}\frac{S}{M^2} \tag{2.3.1}$$

Here c represents the speed of light, G is the gravitational constant, S is the spin of the object and M its mass. A dimensionless parameter q can then be derived from the potentials describing a generic metric for the external geometry of a stationary, axially symmetric rotating body. They describe a relationship between the parameter q and the quadrupole moment Q, which can be obtained by a volume integral over the Newtonian mass distribution:

$$q = \frac{c^4}{G^2}\frac{Q}{M^3} \tag{2.3.2}$$

For the case of a Kerr black-hole, χ is limited to $\chi \leq 1$ by cosmic censorship (see Hawking and Ellis) [20], and the relationship between its rotational parameter and the quantity q has been described by Thorne [21] and Thorne, Price and McDonald [22], using the following equation:

$$q = -\chi^2 \tag{2.3.3}$$

Wex and Kopeikin describe the different relations governing the quantity q for other compact stellar objects. The result quoted for neutron stars via Laarakkers and Poisson [23] uses Equations of State to constrain the relation for q for neutron stars of mass $1M_{\odot}$ to $1.8M_{\odot}$:

$$q \simeq -C\chi^2 \tag{2.3.4}$$

Here $2.0 \leq C \leq 12.1$. For the case of strongly self-interacting boson stars, the expected value of χ is in the range $3.0 \leq \chi \leq 4.0$, but is not rigidly constrained to it. A complex relationship is expected between χ and q for these astrophysical objects, in particular when

χ exceeds a value of 0.2. However, a constraining inequality always holds true:

$$q \lesssim -10\chi^2 \tag{2.3.5}$$

Laguna et al. surmise that if it is possible to measure M, χ and q for the companion, then by observing the above relations, a rotating black-hole can be identified as the pulsar companion. They describe a method of determining the parameter χ for the pulsar's companion by measuring precessional effects on the binary orbit. Their analysis concludes that if the binary motion of the system is measured to high precision, it is possible to extract the values of Post Keplerian parameters for the binary orbit. This information, along with several geometric arguments and assumptions, could be used to determine the spin of the black-hole. Wex and Kopeikin analyze the magnitude of the pulse timing delay caused by the rotational parameter of the black-hole. Their findings are in agreement with Laguna et al. [4], they expect that the effect would be of the micro-second order. They argue that disentanglement from the bending delay, which has the same functional dependance on the orbital phase of the pulsar, would not be possible. Wex and Kopeikin provide an analytical description of the magnitude of the frame-dragging effect on the propagation delay of photons. They begin with the Kerr spacetime, as written with Boyer-Lindquist time t by Thorne et al. [22].

$$ds^2 = -\alpha^2 c^2 dt^2 + g_{jk}(dX^j + {}^j\, dt)(dX^k + {}^k\, dt) \tag{2.3.6}$$

Where α is the lapse function and ^{i} is the shift function, given by the following:

$$\alpha^2 = 1 + order\ O\ \frac{1}{R} \tag{2.3.7}$$

$$\beta = -\frac{2G}{c^2}\frac{\mathbf{S}\times\mathbf{X}}{R^3} + \ orderO\ \frac{1}{R^3} \tag{2.3.8}$$

$$g_{jk} = \delta_{jk} + \ orderO\ \frac{1}{R} \tag{2.3.9}$$

Where $R = |\mathbf{X}|$ is the distance from the physical black-hole singularity to the current position.

The increase due to frame-dragging in photon ($ds2 = 0$) propagation time, from emission at the pulsar position to that of the observer is then given by:

$$dt_{FD} \simeq \frac{\cdot\, d\mathbf{X}}{c^2} = -\frac{2G}{c^4}\frac{(\mathbf{S}\times\mathbf{X})\cdot d\mathbf{X}}{R^3} \tag{2.3.10}$$

Wex and Kopeikin use a coordinate system in which they denote the unperturbed (straight-line) trajectory of the photon by $\mathbf{X} = (x, 0, b)$, where b is the distance of closest approach of the photon to the black-hole. Wex and Kopeikin use the following integral equation for the time delay caused by frame-dragging.

$$\Delta_{FD} = -\frac{2G}{c^4}\frac{S_y}{b}\int_{x0}^{\infty}\frac{dx}{(x^2+b^2)^{\frac{3}{2}}} = -\frac{2G}{c^4}\frac{S_y}{b}(1-\frac{x_0}{r_0}) \tag{2.3.11}$$

The upper bound is infinity, for a distant observer, and $r_0 = |X_0|$ represents the distance between the pulsar and the black-hole. Wex and Kopeiken infer that the majority of the frame-dragging time-delay occurs as the photon travels within a few Eistein radii of the black-hole. The metric term responsible for the frame-dragging delay has a $1/R^2$ dependency, only contributing significantly for photons travelling very close to the black-hole. Note that the frame-dragging effects scale with M^2, and thus for larger black-holes ($M_H > 100M_{\odot}$), Wex et al. expect the frame-draggin delay to exceed the other propagation delay effects. This is particularly notable for supermassive black-holes, as a rapidly rotating supermassive black-hole would induce very large frame-dragging delays. Wex and Kopeikin describe the frame-dragging delay in terms of the geometric properties:

$$\Delta_{FD} = -\frac{2G}{c^4}\frac{\mathbf{S}\cdot(\mathbf{K}_0\times\mathbf{R})}{R(R-\mathbf{K}_0\cdot\mathbf{R})} \tag{2.3.12}$$

where $\mathbf{R}$ is the seperation vector between black-hole and pulsar, $\mathbf{K}_0$ is the line-of-sight vector between the observer and the black-hole. They continue with a description of the dependence of the frame-dragging delay on the geometric properties of the orbit, and the orientation of the observer. See ref [6] for details and diagrams. In this thesis I consider only an edge-on binary system with a pulsar in a stable circular orbit about a rotating black-hole. Finally, they give the maximal frame-dragging delay for the ideal edge-on, circular pulsar orbit system:

$$\Delta_{FD}(max) \approx \frac{0.0008\mu s}{|\cos i|}\big(\frac{P_b}{1day}\big)^{\frac{-2}{3}}\big(\frac{M_H}{10}\big)^{\frac{5}{3}}\chi\sin\lambda_H \tag{2.3.13}$$

where i is the angle of inclination ($\approx 90^\circ$ for an edge-on system), $\chi = a\{M_H$ is the rotational parameter of the Kerr black-hole, λ_H is the angle between the direction of the black-hole spin vector and the line of sight to the observer (90° for maximal frame-dragging effect), and P_b is the orbital period of the pulsar.

Wex and Kopeiken estimate a micro-second level framedragging delay, in agreement with the work of Laguna and Wolszczan [4] for an equivalent system. They then argue that if, serendipitously, we were to observe a black-hole/pulsar

binary system in an ideal configuration, then the delay effect could be used to determine the value of $\chi \sin \lambda_H$, setting a lower limit on the spin of the black-hole companion. A value of $\chi \geq 1$ would indicate that it cannot be a Kerr black-hole via consmic censorship conjecture [20]. It is possible that an analysis of the structure of the pulses may allow for disentanglement of this effect from the bending delay, and thus provide a direct measure of the black-hole spin, but such a procedure is subject to large uncertainties.

2.4 The Effects of Gravitational Lensing and Companion Motion on the Timing of a Binary Pulsar, Rafikov and Lai [7]

In 2005, Rafikov and Lai [24] described the magnitude of the delay caused by the gravitational field (Shapiro delay), as well as the geometric lensing delay caused by the bending of light. This work neglects rotational effects. The analysis was performed with a double pulsar system in mind, rather than a rotating black-hole/pulsar binary system. In [24]. they discuss how the pulsar's signal is magnified by the lensing effect of its companion, thus affecting the flux of the observed signal, in particular at the superior conjunction. Lai et al. give an estimate for the maximum possible lensing-corrected Shapiro delay caused by a companion, as the pulsar moves through the superior conjunction for the ideal case of an edge-on system:

$$\Delta t_{grav} = \frac{R_g}{c} \ln \left(\frac{a(1-e^2)}{R_g} \right) = 152 \mu s, \tag{2.4.1}$$

where $R_g = \frac{2GMB}{c^2}$, a is the semi-major axis of the elliptical orbit, and e its eccentricity. The unpublished paper by Rafikov and Lai (of 2006) [7] provides a detailed analysis of the measurements of distinct physical effects delaying the propagation of signals in the presence of a massive companion. They discuss their work with reference to observed binary systems containing pulsars. They mention specifically the importance of observing the magnitude of the Shapiro delay at the superior conjunction of highly inclined (edge on) systems, so as to disentangle the effects of the motion of the pulsar's companion from those of the gravitational lensing of the massive object. They also give a detailed description of the direction of emission for the pulsar's beam. In particular, they examined the longitudinal and latitudinal effects on the observed pulsar timing. They define the longitudinal and latitudinal lensing delays as the delays/shifts caused by the effect of the companion on the direction of emission of the pulsar beam. Rafikov and Lai [7] describe the pulsar beam by using the Rotating Vector Model (RVM), constructed by Radhakrishnan et al. in 1969 [16].

Implimenting such an emission model results in observable asymmetric latitudinal shifts in the pulse profiles, while the longitudinal shifts are symmetric, causing no alteration to the pulse profile, but rather shifting the pulse a certain amount in time.

Rafikov and Lai also analyze the effects of the motion of the companion on the timing of pulses. In an appendix, they derive the Shapiro Delay formula with corrections for a moving lens, to order $\frac{v}{c}$. The work could utlimately be used to quantify differences in the signal caused by companion motion. Calculation of the photon trajectories through a Kerr spacetime with a shifting origin would require a significant increase in the number of numerical operations required.

Finally, they indicate the difficulties in observing the frame-dragging time delay. They show that the magnitude of the frame dragging delay is almost an order of magnitude smaller than the delay predicted by similar calculations performed by Wex and Kopeikin [6]. An estimate of $0.15\mu s$ for the maximum magnitude of frame dragging delay implies that older detectors may not have sufficient timing accuracy at present to differentiate this effect from the lensing delay. The newer generation of telescopes would be able to resolve pulses with a tolerance in the nanosecond range.

2.5 Strong field effects on pulsar arrival times: circular orbits and equatorial beams. Wang, Jenet, Creighton and Price [8].

In this paper, Wang et al. explore the possibility that sub-dominant (reduced luminosity) pulses could be observed from pulsars orbiting supermassive black-holes. The sub-dominant pulses would be generated by a pulsar beam being deflected/scattered by the supermassive black-hole. Their findings indicate that pulses could be observable, although with reduced luminosity, and would occur at seemingly unpredictable arrival times, which would be related to the pulsar's orbital motion about the supermassive black-hole. The authors choose a non-rotating Schwarzschild black-hole, and considers only the portion of the pulsar's beam that lies in the equatorial plane. Furthermore, they assume that the pulsar orbit is circular. The chosen orbital radius is notable, as a pulsar orbiting a supermassive black-hole would be able to maintain a stable orbit at very small radial separation when compared with the stellar mass black-hole case. Wang et al. consider orbital radii of only a few multiples of the Schwarzschild radius of the black-hole, and state that the pulsar's orbit in such a case

would take many years to decay.

Wang et al. define two universal functions to describe the final phase angle (ϕ) and coordinate time for photons passing through the vicinity of the black-hole. They begin their formulation of these functions by considering a Scwarzschild black-hole.

$$\mathrm{d}s^2 = -(1 - \frac{2M}{r})\mathrm{d}t^2 + (1 - \frac{2M}{r})^{-1}\mathrm{d}r^2 + r^2(\mathrm{d}\theta^2 + \sin^2\theta\mathrm{d}\phi^2) \tag{2.5.1}$$

The pulsar emits in the equatorial plane ($\theta = \frac{\pi}{2}$), and the photon, constrained to the equatorial plane ($\mathrm{d}\theta = 0$).

$$\left(1 - \frac{2M}{r}\right)^2 \frac{\mathrm{d}t^2}{\mathrm{d}r^2}\frac{1}{r^4} = \frac{1}{r^4}\frac{\mathrm{d}r^2}{\mathrm{d}\phi^2} + \frac{1}{r^2}\left(1 - \frac{2M}{r}\right) \tag{2.5.2}$$

Wange et al. use the fact that p_ϕ and p_t are constants of the motion for the case of equatorial photons, and relate the term on the left hand side to the impact parameter b.

$$\left(1 - \frac{2M}{r}\right)^2 \frac{\mathrm{d}t^2}{\mathrm{d}r^2}\frac{1}{r^4} = \frac{1}{b^2} \tag{2.5.3}$$

giving:

$$\frac{1}{b^2} = \frac{1}{r^4}\frac{\mathrm{d}r^2}{\mathrm{d}\phi^2} + \frac{1}{r^2}\left(1 - \frac{2M}{r}\right) \tag{2.5.4}$$

Wang et al. define $\phi_{in} = \tan^{-1}(rp^\phi/p^r)$ and hence:

$$\frac{rp^\phi}{p^r} = \tan\phi_{in} \tag{2.5.5}$$

Substituting into equation (2.5.4) and setting $r = r_0$, Wang et al. obtain.

$$\frac{1}{\tan^2\phi_{in}} + 1 - \frac{2M}{r_0} = \frac{r_0^2}{b^2} \tag{2.5.6}$$

Wang et al. then give the critical value for the impact parameter, b_{crit}, for which photons must fall into the black-hole. They use this value to limit the range of ϕ_{in} in order to consider only photons not captured by the black-hole. The value of ϕ_{crit} is the root of the following equation whose value lies between π and $\frac{\pi}{2}$:

$$\tan\phi_{crit} = -\left(\frac{r_0^2}{27M^2} - 1 + \frac{2M}{r_0}\right) \tag{2.5.7}$$

When $|\phi_{in}| \geq \phi_{crit}$, the photon is captured by the black-hole. For $|\phi_{in}| \leq \phi_{crit}$, Wang et al. use their Universal functions to calculate the final phase and coordinate time of a photon at assymptotically large radial distance. They derive the functions by analytical

and curve-fitting techniques described in the appendix of their paper [8]. The Universal functions for calculating the final phase $F(\phi_{in})$ and time $T(\phi_{in})$ are:

$$F(\phi_{in}) = -\sin\phi_{in}\log\left(\left(1-|\frac{\phi_{in}}{\phi_{crit}}|\right)\right) \tag{2.5.8}$$

$$T(\phi_{in}) = r_0(1-\cos\phi_{in}) - 3\sqrt{3}\log\left(1-\frac{|\phi_{in}|}{\phi_{crit}}\right) - \frac{3\sqrt{3}}{\phi_{crit}}|\phi_{in}| \tag{2.5.9}$$

Wang et al. then proceed with a description of the directions of photon propagation for a general case. Ultimately, they consider only photons that move in the orbital plane. They have essentially simplified the problem to a plane, in which the pulsar beam emits a spinning cone of photons. They then consider the angle, at the pulsar, which subtends the detector for primary and secondary pulses. It is assumed that this angle, $\Delta\phi$ is larger for primary pulses, which reach the detector through relatively flat spacetime, and very small for secondary pulses which have been deflected by the supermassive black-hole. The size of $\Delta\phi_{secondary}$ is made even smaller since it must be divided by $\frac{\mathrm{d}F}{\mathrm{d}\phi_{in}}$, essentially accounting for the strong gravitational effects of the black-hole. Subsequent orders of pulses (tertiary, quartenary etc.) could, in theory, be observed. Wang et al. divide $\Delta\phi$ by $\frac{\mathrm{d}F}{\mathrm{d}\phi_{in}}$ an additional time for each order of pulses, i.e. $\Delta\phi_{tertiary}$ would be divided by $(\frac{\mathrm{d}F}{\mathrm{d}\phi_{in}})^2$. They then construct a system of specific orbital size, and use their formalism to produce a set of plots of pulses received at a distant observer for a given pulsar rotational period. Their discussion briefly describes how the intensity of pulses is determined by $F(\phi_{in})$, and by $\frac{\mathrm{d}F}{\mathrm{d}\phi_{in}}$ for sub-dominant pulses.

Work by Nampalliwar, Price, Creighton and Jenet, [9], seeks to expand on the work by Wang et al. [8], by considering rotating supermassive black-holes. Their work has shown that the sub-dominant deflected pulses would still be observable, and that the effects of the non-zero rotational parameter would change the timing of the secondary pulses.

2.6 Post-Newtonian Timing Effects in Binary Pulsar Systems, Epstein [12]

In a 1977 paper, Epstein [12] explores the use of pulse timing observations of pulsars in binary systems to determine post-Newtonian parameters, such as the post-Newtonian corrections to the elliptical binary orbit. By fitting a pulse-timing formula obtained from

general relativity to a set of observed pulse timing data, Epstein intends to overly constrain the system. This means that post-Newtonian parameters can be used to calculate the masses and angular momenta of both of the objects in the binary system. The pulse-timing formula was previously derived by Blandford and Teukolsky [25], for the specific purpose of comparing the predictions of GR with observational data obtained from the Hulse-Taylor binary system ,[1]. They ignore the Galilean aberration, which is caused by the fact that pulses are observed due to the pulsar spinning and emitting light rays in a manner analogous to a lighthouse. Hence, they describe the pulsar's emission by means of a cubic polynomial. Epstein provides an appendix in which he analyzed the relevence of this Galilean aberration and found it to be negligable for the type of analysis being performed. Having too much information (redundancy) describing the system permits one to check the validity of the asssumptions originally made about the system. Epstein's stated intention was to ascertain whether the assumption that the rate of periastron precession is purely due to the General Relativistic effects. The work in this thesis can test the validity of ignoring the Galilean aberration, with the spinning motion of the pulsar modelled for the simplest possible case, a pulsar rotating only in the equatorial plane of the black hole. Since it is the actual shapes and profiles of the pulses which can be analyzed using the computational model presented in part II, the Galilean aberration is important when considering how the pulsar's beam will sweep across the black-hole, creating what is hoped to be a signature pulse profile at the superior conjunction. In the future, the simulations produced by my model could be compared with the timing formulae of Epstein, as well as Blandford and Teukolsky.

I also intend to simulate the post-Newtonian dynamics of a binary system containing a pulsar and any other compact object. Pulse timing data obtained from such a simulation can be compared directly with the pulse timing formula described in Epstein's paper. Ultimately, post-Newtonian orbital parameters and pulse timing data could be used simultaneously to yield physical observables (masses and spins of each body) for the system.

2.7 Comparison of my model and the literature.

In this section, I comment on the capabilities of the numerical simulation described in part II of this thesis. The papers discussed above have given an indication of what physical effects the model should be able to simulate. A detailed description of the methods used and of the physical configuration assumed will be given in part II of this thesis. For now,

I comment only on the ability of the simulation to produce results comparable with those described in the articles discussed.

2.7.1 Oscoz et al. [5]

The model constructed in part II is similar in several ways to the model used by Oscoz et al. I will now describe the similarities, and mention any differences in application of the two models. First, the method of describing the direction of the centre of the pulsar's beam is similar. Oscoz et al. solve for the direction of the central ray of the pulsar beam in the pulsar's LRF. Their equation for the angle between the radial unit vector and the beam's direction in the LRF, (2.1.9), has also been used in my model. I have, however, used a different method to implement the transformation of this angle into the Kerr spacetime. Oscoz et al. use perturbation theory to derive an analytical result for the flux arriving at a detector as a function of the pulsar's orbital phase. They perturb the photon directions from the primary beam direction, within the LRF of the pulsar. In my model, the primary beam direction is transformed into the Kerr spacetime, this direction is then modified via a pair of coupled random numbers, resulting in a conical emission of variable apex angle. I did attempt to effect the coordinate transformation in the same way as Oscoz et al., but was not able to get a stable simulation to run, hence I applied my own method for transforming to the Kerr spacetime, as described in chapter 8. From this point I use the geodesic equations to calculate photon trajectories, whereas Oscoz et al. have used the Hamilton-Jacobi formalism to relate their trajectories and initial conditions to conserved quantites. The use of the geodesic equation allows for the possibility of using alternative spacetimes to generate photon trajectories without having to do any more theoretical work. However, using the Hamilton-Jacobi formalism does provide the advantage of being able to check the progress of the integration by monitoring the conserved quantities.

In my model, the flux of the pulsar signal at the observer is determined by time-binning of the arrival time data. The behavior of the flux seen by the observer, for different emissive pulsar orbital phases can simply be determined by placing several detectors of identical size at different locations. Oscoz et al. assume that their analysis of the relative flux seen at a detector would be inaccurate for the superior conjunction of the system. The model I describe in part II would be able to simulate observed flux for the superior conjunction, given sufficient computing resources. Oscoz et al. complexify their model by considering the decay of the pulsar's orbit due to gravitational radiation. I have not attempted to

implement modifications such as this, but intend to do so in a later phase of development of the model by using PPN equations of motion described in this thesis. The simulations would need to run over several orbital periods in order to be able to detect a change in the pulsar signal due to orbital decay. For this purpose, the model would need to be run on a cluster or on a grid computing system.

2.7 Laguna and Wolszczan [4]

Laguna and Wolszczan have used direct numerical integration of the photon geodesics to calculate the expected magnitude of the frame-dragging effect. This work could be tested using my model, by adjusting the orbital motion of the pulsar and by adding a post-processing routine to replicate their calculations (manipulate results into the same format as theirs). The analytical result by Dymnikova [18] used in their analysis has been tested agaist equatorial photon trajectories produced using my model. The timing data corresponds very well, and will be discussed in chapter 9. Their numerical model uses ray-tracing techniques similar to those implemented in my model. However, I use a higher order Runge-Kutta with adaptive step-size functioning which has been customized for the coupled differential equations being integrated. I found that using lower order RK methods as opposed to the 8th/9th order method ultimately selected, as well as setting the local truncation error tolerance to be quite large, 10^{-6} as opposed to the default setting of 10^{-9}, would allow for photons to be captured more easily/often by the black-hole event horizon. This is important, as photons which were integrated backwards could have originated from within the black-hole event horizon, implying that use of less precise methods would increase the effective size of the event horizon. Numerical experiments performed using my model showed the need for very high precision and very small step-sizes, particularly within approximately 3 multiples of the event horizon radius. I expect my model to produce photons with larger frame-dragging residuals than those indicated by Laguna and Wolszczan. Ultimately it is the time-shift of the peak of the pulse which can be measured as a timing residual, this would require significant additions in terms of post-processing procedures for my model. However, I am confident that a large-scale cluster simulation using my model would be able to produce highly detailed pulses which would display the frame-dragging effect.

2.7.3 Wex and Kopeikin [6]

Wex and Kopeikin consider the possibility of using pulsar timing to measure the semi-major axis and the longitude of the periastron of the binary system. Their aim is to measure precessional effects, including frame-dragging, by observing how the timing signal from the pulsar changes. The current version of my model uses a stable circular pulsar orbit, and is thus not suited to investigation of precessional effects of the pulsar's orbit. However, using the PPN (Parameterized Post Newtonian) equations of motion, described in chapter 5, to describe the motion of the black-hole and pulsar would make this possible. Furthermore, the pulsar's emission needs to be modelled more realistically, by using a theory such as the rotating vector model [16]. These modifications would take a substantial effort to implement, but they would not increase the computational time to the point where it is no longer viable. The modifications would need to be implemented in the distributor node of the calculation, which is a process that calculates and sends initial conditions to worker nodes so that they can perform the trajectory calculations. Hence, complexifying the emission mechanism or the pulsar position in the Kerr spacetime would not slow the most calculation intensive part of the code. If it is found that the distributor node becomes slower and cannot send information to worker nodes fast enough, the ratio of workers to distributors can be adjusted to give worker nodes more processing power. Of course, to allow precessional effects to reach a measurable size, the simulation must be allowed to run over much larger portions of the orbit than was the case for the results presented in this thesis. Run on a single CPU, the present implementation simulates only $\frac{1}{128}$ of an orbit. Hence, a cluster or grid environment is vital if this code is to produce data that are useful for the type of analysis Wex and Kopeikin discuss.

If one wishes simply to measure timing residuals caused by frame-dragging, the current version of code is sufficient. The ideal case for measuring the frame-dragging effect, as described by Wex and Kopeikin, is already modelled by my code. As with the work by Laguna and Wolszczan, post processing routines must be implemented. Specifically, the peaks of each pulse must be accurately timed, requiring far greater time binning resolution than is presently implemented in the model. To obtain reasonably large numbers of photons within each time-bin, while decreasing the pulsar period to the millisecond range, far greater numbers of photons would be required. This requires that a cluster be used.

2.7.4 Rafikov and Lai [7], [24]

As mentioned for the other articles discussed, the frame-dragging time-delay could be observed using my model. Rafikov and Lai have discussed its magnitude relative to other delays, and have noted the difficulties preventing disentanglement of the frame-dragging time delay from other delay effects. By running my model on a cluster, I would be able to identify any changes in pulse structure resulting from the rotation of the black-hole. The quantification of the peak-shift can be used to give a measure of frame-dragging delay, but the overall effect of rotation on the shape of the pulse may be more revealing than the delay itself. Curve-fitting techniques could be used to determine whether modification of the black-hole Kerr parameter causes a characteristic change of pulse shape. Figure 2 from reference [24] shows the reduction of intensity observed as an object is eclipsed in a binary system. Simulation results given in Part II of this thesis show a distinct loss of flux for pulses emanating from the superior conjunction of the system. This reduction of flux would be expected as light is bent/scattered by the black-hole, and no longer strikes the detector.

Rafikov and Lai [24] estimate a maximum gravitational delay (with lensing) of approximately $152\mu s$ for a double pulsar binary system. They also describe how including the lensing delay increases the gravitational (Shapiro) delay. In 1976 Blandford and Teukolsky [25] described the gravitational delay with an expression that did not consider lensing. Lai and Rafikov [24] have modified the expression to account for lensing, thus inflating the total delay. My model generates pulse profiles by firing large numbers of photons through the Kerr spacetime, integrating the geodesic equations to evaluate their propagation times. Hence, my model measures the time-delay of photons inclusive of all General Relativistic effects. My results show very large timing delays. This is as a result of the small orbital size of the system being modelled. The circular orbit selected for the pulsar is only at $20000M_{Hole}$, which is at least two orders of magnitude too small for a system which exhibits reasonable time before merger. Furthermore, I assume a black-hole much larger than the pulsar companions considered in [24], with $M_{Hole} = 30M_{\odot}$, leading to larger timing delays. My model must be complexified to reproduce calculations performed by Lai and Rafikov. The first and most important obstacle would be to generalize the orbit. An elliptic orbit would allow for a direct comparison of numerical results from my model and the analytical timing delays described by Rafikov and Lai. This requires a rework of the modules controlling the pulsar's orbital position at the time of emission, and of the emission process itself. The emission process used in my model is only useful for a pulsar in a stable circular orbit, a generalized

method must be implemented for future models.

Lai and Rafikov have considered the effects of companion motion on the pulsar's signal, [24]. This problem could be approached by formulating a time-dependant metric to account for the motion of the black-hole. This would result in a set of geodesic equations with more terms than the ones presently coded. This method would be more calculation intensive, and require a vast amount of processor hours to produce a good simulation.

2.7.5 Wang et al. [8] and Nampalliwar et al. [9]

These papers describe the possibility of detecting sub-dominant pulses from pulsars orbiting non-rotating and rotating supermassive black-holes respectively. Due to the relatively small scale of the systems, my model would be well suited to test this possibility numerically. Furthermore, Wang et al. have simplified their model to an ideal case of a pulsar orbiting and beaming in the equatorial plane. Altering the physical parameters and selecting an appropriately large Dyson sphere (an encapsulating spherical surface) to capture photons at a radial distance large enough to be considered assymptotic would be sufficient modification. The angular width of the pulsar's beam could also be modified to give results similar to those of Wang et al., with a cluster environment essential for producing wider pulsar beams of sufficient photon density. Photons would then be collected at the detectors and timing histograms produced, which would be comparable with the graphs produced by Wang et al. in their paper [8]. In conclusion, my model would be ideal for testing the possibility of observing sub-dominant pulses from pulsars orbiting supermassive black-holes.

Chapter 3

The Kerr Metric

3.1 The Kerr Metric

The Kerr Metric is a solution to the Einstein Field Equation that describes the spacetime in the vicinity of a rotating black-hole. It was discovered by Roy Kerr in 1963. A special case of this spacetime is the Schwarzschild metric, which was originally used to define and describe the physical concept of a black-hole. The aim is to find features in an observed pulsar signal that are evidence of the presence of a black-hole. In this chapter, I describe some of the properties of the Kerr Metric. My summary is based on Hartle [26] and the revised Project F from the book on black-holes by Taylor and Wheeler [27].

The Kerr metric in Boyer-Linquist coordinates, is given by [28]:

$$\begin{aligned} \mathrm{d}s^2 = &\left(\frac{r^2 + a^2\cos^2\theta}{r^2 - 2Mr + a^2}\right)\mathrm{d}r^2 + \left(r^2 + a^2\cos^2\theta\right)\mathrm{d}\theta^2 + \sin^2\theta\left(a^2 + r^2 + \frac{2a^2Mr\sin^2\theta}{r^2 + a^2\cos^2\theta}\right)\mathrm{d}\phi^2 \\ &- \frac{4aMr\sin^2\theta}{r^2 + a^2\cos^2\theta}\mathrm{d}\phi\mathrm{d}t - \left(1 - \frac{2Mr}{r^2 + a^2\cos^2\theta}\right)\mathrm{d}t^2. \end{aligned} \tag{3.1.1}$$

where a is the angular momentum per unit mass of the spinning black-hole, $a = \frac{J}{M}$. Setting this parameter to zero reduces the metric to the non-rotating, spherically symmetric Schwarzschild metric. Any particle which orbits a Schwarzschild black-hole remains in a plane passing through the centre of the black-hole as a result of spherical symmetry. A non-zero value of a removes this spherical symmetry. Indeed only particles in the Kerr equatorial plane, with no momentum component off of this plane, will remain in the equatorial plane, making the equatorial plane a special case for observing the simplest particle orbits about the Kerr black-hole. In this thesis, the computational model will investigate photon orbits which do not lie in the equatorial plane, with an interesting numerical simulation probing

the region that can be approached most closely by photons without being captured. The deviation from spherical symmetry in the Kerr solution is most simply seen in the coefficient of the $\mathrm{d}\phi^2$ component, given by $R^2 = \sin^2\theta\left(a^2 + r^2 + \dfrac{2a^2Mr\sin^2\theta}{r^2 + a^2\cos^2\theta}\right)$. Taylor and Wheeler [27] interpret this quantity, in the extremal spinning case of $a = M$, as the "reduced circumference" of the extreme black-hole, where its value is $R^2 = M^2 + r^2 + \dfrac{2M^3}{r}$. This quantity represents the circumference of a circle, concentric with the black-hole, and confined to the equatorial plane, divided by 2π. It replaces the r^2 coefficient of $d\phi^2$ in the case of the Schwarzschild metric, and reduces to it in the case when $a = 0$. This shows clearly the nature of the deviation from spherical symmetry.

The presence of a cross-term in the metric, $-\dfrac{4aMr\sin^2\theta}{r^2 + a^2\cos^2\theta}\mathrm{d}\phi\mathrm{d}t$ shows a further deviation from spherical symmetry, and is responsible for the effect known as "frame dragging". Taylor and Wheeler [27] describe frame dragging by analogy with the radial rocket thrust required to keep an observer from falling into the black-hole. To hold an observer at fixed coordinates $(r, \pi/2, \phi)$ in the equatorial plane, for a Schwarzschild black-hole, only a force pushing the observer radially away from the black-hole is required. For a spinning black-hole, an extra force is required in the tangential $\hat{\phi}$ direction opposite to the direction of black-hole spin. Trivially, the frame-dragging term vanishes for $a = 0$ and so it may be possible, via the numerical model constructed in part II, to disentangle the effect of frame-dragging on the pulsar's signal.

Having mentioned the extremal value of $a = M$, some clarification is necessary. Hawking and Ellis, [20] consider the case of a body described by the Kerr metric with a value of aM as a naked singularity. This is the source of the cosmic censorship conjecture, which disallows the possibility of directly observing the physical singularity at the origin of the Kerr coordinate system, and thus sets a limit of $a\ddot{M}$ for the angular momentum parameter of a spinning black-hole. The observation of a naked singularity would be possible because setting aM removes the existence of the coordinate singularity describing the event horizon of a spinning black-hole. Hence photons can escape to infinity from locations vanishingly close to the physical singularity, carrying information to distant observers and thus describing this object, which contains a space-time singularity, as something other than a black-hole. The numerical model presented in this thesis thus limits the value of the black-hole angular momentum parameter such that aM, in keeping with the cosmic censorship conjecture.

Having described the deviation from spherical symmetry, as well as the allowed values for a, the singularities of the metric can now be discussed. The singularity observed when $r^2 + a^2\cos^2\theta = 0$, and hence $r = 0$ is the physical singularity analogous to that of $r = 0$ for the Schwarzschild metric. This is a position of infinite spacetime curvature. The second singlularity occurs when $r^2 - 2Mr + a^2 = 0$, and hence $r_\pm = M \pm \sqrt{M^2 - a^2}$. The value r_+ represents the event horizon of the rotating black-hole, while the value r_- falls within the event horizon, and is called the Cauchy Horizon. Clearly, this singularity is removed by allowing $a > M$, and no event horizon can exist for this configuration of the Kerr metric, as discussed above. It is believed that the Kerr metric accurately describes the properties of spacetime for radial values beyond the Cauchy Horizon. As the r_- value is approached, the instability of space-time increases, and thus the theoretical description departs from that described by the Kerr metric. The Cauchy Horizon is also known as the "mass inflation singularity", and an object crossing it would encounter a surface of infinite mass density [27]. This constitutes what may be considered a discussion of the internal structure of a spinning black-hole, which is not important to this thesis, since I consider only photon trajectories which have not crossed the event horizon. Those that cross contribute nothing to observed signal.

The value $r_+ = M + \sqrt{M^2 - a^2}$ defines the three-surface which is the event horizon of the spinning black-hole. To show this, it is necessary to find a unique null-vector, orthogonal to two space-like vectors for this surface. This is a simple procedure. Firstly, consider the contraction of the photon four momentum for the case of a tangent vector to a three-surface of constant r, where $u^1 = u^r = 0$.

$$\mathbf{u}.\mathbf{u} = g_{\theta\theta}(u^\theta)^2 + g_{\phi\phi}(u^\phi)^2 + g_{\phi t}u^\phi u^t + g_{tt}(u^t)^2 \tag{3.1.2}$$

Which, evaluated for a null geodesic at $r = r_+$:

$$0 = \big(\frac{2Mr_+\sin\theta}{r_+^2 + a^2\cos^2\theta}\big)\big(u^\phi - \frac{a}{2Mr_+}u^t\big) + (r_+^2 + a^2\cos^2\theta)(u^\theta)^2 \tag{3.1.3}$$

This equation has a unique solution, and hence, a unique null tangent vector to the three-surface at constant $r = r_+$. This unique solution is given by $u^\theta = 0$ and $u^\phi = \frac{a}{2Mr_+}u^t$. The equation for the null tangent vector is given by (up to a multiplicative constant):

$$u^\mu = (0, 0, \Omega_H, 1) \tag{3.1.4}$$

Where $\Omega_H = \frac{a}{2Mr_+}$ is the angular velocity of photons confined to the event horizon with respect to an observer at infinity. Next, contract the unit vector with two mutually orthogonal space-like tangents ($u^t = 0$). Any tangent vectors of the form $u^\mu = (0, \mathrm{u}^\theta, u^\phi, u^t)$ would suffice. The simplest orthogonal cases are $u^\mu = (0, 1, 0, 0)$ and $u^\mu = (0, 0, 1, 0)$.

The shape of the event horizon is of particular interest in this thesis, as several plots of data points indicating where photons have struck the event horizon are used in chapter 11 in which I present data and results. The horizon of a non-rotating black-hole is spherical. In the case of the Kerr metric, however, despite the fact that the event horizon exhibits constant radial coordinate $r = r_+$, the surface does not exhibit spherical geometry. This is simply illustrated, as per [26], by selecting $r = r_+$, $dr = 0$ and choosing a constant time slice of the metric, i.e. $dt = 0$, producing a two-dimensional surface describing the event horizon.

$$d\Sigma^2 = {r_+}^2 + a^2 \cos^2\theta d\theta^2 + \frac{4M^2 {r_+}^2}{{r_+}^2 + a^2 \cos^2\theta} \sin^2\theta d\phi^2 \tag{3.1.5}$$

The metric for this surface is not the metric for a sphere. In fact, embedding this geometry in at space and producing a solid by revolution yields an oblate spheroid, which flattens increasingly in the equatorial plane as the value of a is increased. I did not attempt to use an embedding diagram to illustrate the geometry of the event horizon, but rather plotted a sphere at the radial coordinate $r = r_+$. As a is increased, a larger gap can be observed between photons striking the event horizon and the sphere. For an example, refer to Figure 11.20.

Another interesting feature of the Kerr metric is the presence of the ergosphere. This is a region with inner boundary given by the event horizon and outer boundary a surface called the static limit. It is the existence of the static limit which defines the ergosphere. Beyond the static limit, it is possible to use rocket power to counter-act the frame-dragging effect discussed above, and to hold an observer at a fixed location in the Kerr spacetime regardless of the value of a. Within the static limit, it is no longer possible to apply a tangential force which will hold the observer at fixed azimuthal position. The static limit occurs where the coefficient of dt^2 time metric vanishes, that is, where $\frac{2Mr}{r^2 + a^2 \cos^2\theta} = 1$.
Refer to [26] or [27] for a plot illustrating the shape of the ergosphere. On the equatorial

plane, the radial coordinate of the static limit is given by $r = 2M$ and coincides with the event horizon of the Schwarzschild black-hole. Within this radial value, the effect of frame dragging forces particles to be swept along in the direction of spin of the black-hole. Following Hartle [26], a stationary observer has zero four-velocity components u^r, u^θ and u^ϕ. Thus, for a massive observer, $\mathbf{u}_{obs} \cdot \mathbf{u}_{obs} = -1$, and hence for the Kerr metric we obtain $\left(1 - \frac{2Mr}{r^2 + a^2 \cos^2\theta}\right)(u^t)^2 = 1$. At the static limit, therefore, the coefficient of dt^2 (or $(u^t)^2$) vanishes. Within it, the coefficient changes sign and the above equation can no longer be satisfied. Hence an observer within the static limit cannot maintain a constant position in the Kerr spacetime. Extending this formalism to massless particles, photons are forced to change their direction of propagation within the ergosphere, light is only permitted to travel in the same direction as the spin of the black-hole. This reversal of direction can be seen in some plots shown in the chapter 11 of this thesis.

Chapter 4

Null Geodesics and Symmetry

4.1 Euler-Lagrange Formalism, Null Geodesics

The construction of a computational model for a pulsar beam moving through a black-hole spacetime requires an analysis of the geodesics of photons in the vicinity of a Black Hole. Two methods have been used to do this. The first applies the Euler-Lagrange formalism, the second, the Hamilton-Jacobi formalism. The Euler-Lagrange formalism yields the set of equations known as the *Geodesic Equation*,

$$\frac{\mathrm{d}^2 x^\alpha}{\mathrm{d}\lambda^2} = -\Gamma^\alpha{}_{\mu\nu} \frac{dx^\mu}{d\lambda} \frac{dx^\nu}{d\lambda}. \tag{4.1.1}$$

Relativistic effects on the motion of photons and particles in the vicinity of a massive (compact) body can be broken down into two categories. Firstly, effects caused by the curvature of spacetime as a result of the presence of the massive body. Secondly, effects caused by the angular momentum of the massive body. Seperation of these two effects is necessary if we are able to measure their relative magnitudes on the pulses arrival time from a binary system consisting of a black-hole and a pulsar. These effects can be investigated by modelling the spacetime in the vicinity of the Black Hole. The special case of the Kerr Metric with the rotational parameter set to zero yields the non-rotating Schwarzschild Metric. Hence, pulse structure and timing for rotating and non-rotating cases, can be compared simply by assigning a single parameter in the computational model.

Ultimately, a choice of formalism must be made for the computational model. The Hamilton-Jacobi method produces first order differential equations in terms of constants of

the motion. The theory for this method is described in the second section of this chapter. The Euler-Lagrange formalism produces a set of coupled second order ordinary differential equations. By constructing the code to solve the second order geodesic equations, it is possible, in theory, to substitute for the Kerr metric the metric of any spacetime. The theories of higher-dimensional gravity may be considered in the future, if it is possible to use them to generate sets of differential equations describing the trajectories of photons. The order, and degree of coupling of these equations may present a challenge in terms of developing algorithms to solve them numerically. The code will also consist of different modules which can be edited and swapped out as necessary, so that if it proves possible to integrate photon geodesics much faster using only first order differential equations, in conjunction with the semi-analytical methods developed by Dexter and Agol [29], for example, it would not take too much work to implement the new procedures.

Understanding the theoretical framework of both formalisms is an important step in developing a dynamic computational model. In this section, I describe the solution of the geodesic equation for the Kerr Metric using the Euler-Lagrange formalism.

In Boyer-Linquist coordinates [28], the Kerr metric is given by equation (3.1.1). In matrix form:

$$\begin{pmatrix} \frac{r^2+a^2\cos^2\theta}{r^2-2Mr+a^2} & 0 & 0 & 0 \\ 0 & r^2+a^2\cos^2\theta & 0 & 0 \\ 0 & 0 & a^2+r^2+\frac{2a^2Mr\sin^2\theta}{r^2+a^2\cos^2\theta} & -\frac{2aMr\sin^2\theta}{r^2+a^2\cos^2\theta} \\ 0 & 0 & -\frac{2aMr\sin^2\theta}{r^2+a^2\cos^2\theta} & -1+\frac{2Mr}{r^2+a^2\cos^2\theta} \end{pmatrix}$$

Note that the indices here run from 1 to 4, corresponding with r, θ, ϕ, t rather than from 0 to 3, where t would be the first variable. The Inverse metric is given by:

$$\begin{pmatrix} \frac{a^2-2Mr+r^2}{r^2+a^2\cos^2\theta} & 0 & 0 & 0 \\ 0 & \frac{1}{r^2+a^2\cos^2\theta} & 0 & 0 \\ 0 & 0 & \frac{2\left(r(-2M+r)+a^2\cos^2\theta\right)\csc^2\theta}{(a^2+r(-2M+r))\,(a^2+2r^2+a^2\cos 2\theta)} & -\frac{4aMr}{(a^2+r(-2M+r))\,(a^2+2r^2+a^2\cos 2\theta)} \\ 0 & 0 & -\frac{4aMr}{(a^2+r(-2M+r))\,(a^2+2r^2+a^2\cos 2\theta)} & -\frac{a^4+2r^4+a^2r(2M+3r)+a^2\left(a^2+r(-2M+r)\right)\cos 2\theta}{(a^2+r(-2M+r))\,(a^2+2r^2+a^2\cos 2\theta)} \end{pmatrix}$$

To make use of the Geodesic equation, we must find the Christoffel symbols (or connection coefficients) for the Kerr metric. I used the Mathematica tool that accompanies Hartle [26], written by Leonard Parker. This requires as input the components of the Metric tensor.

An example calculation of one of the Christoffel Symbols is given below, $g_{\alpha\beta}$ denotes the metric tensor, and $g^{\alpha\beta}$ its inverse.

The *Christoffel Symbols* are defined by,

$$\Gamma^{\lambda}{}_{\mu\nu} = \frac{1}{2} g^{\lambda\sigma} \left(\partial_\mu g_{\sigma\nu} + \partial_\nu g_{\sigma\mu} - \partial_\sigma g_{\mu\nu} \right) \tag{4.1.2}$$

Choose the $\Gamma^2{}_{21}$ connection, as it is the most concise result.

$$\begin{aligned}
\Gamma^2{}_{21} =& \frac{1}{2} g^{2\sigma} \left(\partial_2 g_{\sigma 1} + \partial_1 g_{\sigma 2} - \partial_\sigma g_{21} \right) \\
=& \, g^{21} \left(\partial_2 g_{11} + \partial_1 g_{12} - \partial_1 g_{21} \right) + g^{22} \left(\partial_2 g_{21} + \partial_1 g_{22} - \partial_2 g_{21} \right) \\
&+ g^{23} \left(\partial_2 g_{31} + \partial_1 g_{32} - \partial_3 g_{21} \right) + g^{24} \left(\partial_2 g_{41} + \partial_1 g_{42} - \partial_4 g_{21} \right)
\end{aligned}$$

Eliminate the components which are zero by inspecting the metric and inverse metric matrices.

$$2\Gamma^2{}_{21} = g^{22} \left(\partial_1 g_{22} \right).$$

Substituting the components and performing the differentiation yields

$$2\Gamma^2{}_{21} = (r^2 + a^2 \cos^2\theta) \left(\frac{2r}{(r^2 + a^2 \cos^2\theta)^2} \right).$$

Finally,

$$\Gamma^2{}_{21} = \frac{r}{r^2 + a^2 \cos^2\theta} \tag{4.1.3}$$

Using Mathematica, we obtain the following 20 distinct Christoffel symbols for the Kerr Metric. Due to the symmetry of the Christoffel Symbols under the interchange of lower indices, a total of 32 non-zero connections are expected. Of the 20 distinct connection coefficients obtained from Mathematica, 12 do not contain repeated lower indices, hence yielding the 12 remaining Christoffel symbols for the Kerr Metric.

The 20 distinct Christoffel Symbols for the Kerr Metric:

$$\Gamma^1{}_{11} = \frac{r(a^2 - Mr) + a^2(M - r)\cos^2\theta}{\left(a^2 + r(-2M + r)\right)\left(r^2 + a^2\cos^2\theta\right)}$$

$$\Gamma^1{}_{21} = -\frac{a^2 \cos\theta \sin\theta}{r^2 + a^2\cos^2\theta}$$

$$\Gamma^1{}_{22} = -\frac{r\left(a^2 + r(-2M + r)\right)}{r^2 + a^2\cos^2\theta}$$

$$\Gamma^1{}_{33} = -\frac{\left(a^2 + r(-2M + r)\right)\sin^2\theta \left(r^5 + a^4 r\cos^4\theta - a^2 M r^2 \sin^2\theta + \cos^2\theta(2a^2 r^3 + a^4 M \sin^2\theta)\right)}{r^2 + a^2\cos^2\theta}$$

$$\Gamma^1{}_{43} = \frac{aM\left(a^2 + r(-2M + r)\right)\left(-r^2 + a^2\cos^2\theta\right)\sin^2\theta}{\left(r^2 + a^2\cos^2\theta\right)^3}$$

$$\Gamma^1{}_{44} = -\frac{\left(a^2+r(-2M+r)\right)\left(-Mr^2+a^2M\cos^2\theta\right)}{\left(r^2+a^2\cos^2\theta\right)^3}$$

$$\Gamma^2{}_{11} = \frac{a^2\cos\theta\sin\theta}{\left(a^2+r(-2M+r)\right)\left(r^2+a^2\cos^2\theta\right)}$$

$$\Gamma^2{}_{21} = \frac{r}{r^2+a^2\cos^2\theta}$$

$$\Gamma^2{}_{22} = -\frac{a^2\cos\theta\sin\theta}{r^2+a^2\cos^2\theta}$$

$$\Gamma^2{}_{33} = -\frac{1}{(r^2+a^2\cos^2\theta)^3}[\cos\theta\sin\theta 2a^2r^2(a^2+r^2)\cos^2\theta + a^4(a^2+r^2)\cos^4\theta + r(a^2r^3+r^5+$$
$$4a^2Mr^2\sin^2\theta + 2a^4M\sin^4\theta + a^4M\sin^2 2\theta)]$$

$$\Gamma^2{}_{43} = \frac{aMr(a^2+r^2)\sin 2\theta}{\left(r^2+a^2\cos^2\theta\right)^3}$$

$$\Gamma^2{}_{44} = -\frac{2a^2Mr\cos\theta\sin\theta}{\left(r^2+a^2\cos^2\theta\right)^3}$$

$$\Gamma^3{}_{31} = \frac{4\left(r^4(-2M+r)+a^4r\cos^4\theta - a^2Mr^2\sin^2\theta + a^2\cos^2\theta\left(2r^2(-M+r)+a^2M\sin^2\theta\right)\right)}{\left(a^2+r(-2M+r)\right)\left(a^2+2r^2+a^2\cos 2\theta\right)^2}$$

$$\Gamma^3{}_{32} = \frac{\left(3a^4+8a^2Mr+8a^2r^2+8r^4+4a^2\left(a^2+2r(-M+r)\right)\cos 2\theta + a^4\cos 4\theta\right)\cot\theta}{2\left(a^2+2r^2+a^2\cos 2\theta\right)^2}$$

$$\Gamma^3{}_{41} = \frac{4aM\left(r^2-a^2\cos^2\theta\right)}{\left(a^2+r(-2M+r)\right)\left(a^2+2r^2+a^2\cos 2\theta\right)^2}$$

$$\Gamma^3{}_{42} = -\frac{8aMr\cot\theta}{\left(a^2+2r^2+a^2\cos 2\theta\right)^2}$$

$$\Gamma^4{}_{31} = \frac{2aM\left(a^4-3a^2r^2-6r^4+a^2(a^2-r^2)\cos 2\theta\right)\sin^2\theta}{\left(a^2+r(-2M+r)\right)\left(a^2+2r^2+a^2\cos 2\theta\right)^2}$$

$$\Gamma^4{}_{32} = \frac{8a^3Mr\cos\theta\sin^3\theta}{\left(a^2+2r^2+a^2\cos 2\theta\right)^2}$$

$$\Gamma^4{}_{41} = -\frac{2M(a^2+r^2)(a^2-2r^2+a^2\cos 2\theta)}{\left(a^2+r(-2M+r)\right)\left(a^2+2r^2+a^2\cos 2\theta\right)^2}$$

$$\Gamma^4{}_{42} = -\frac{4a^2Mr\sin 2\theta}{\left(a^2+2r^2+a^2\cos 2\theta\right)^2}$$

$$\Gamma^4{}_{42} = -\frac{4a^2Mr\sin 2\theta}{\left(a^2+2r^2+a^2\cos 2\theta\right)^2}$$

To obtain the equations of motion in terms of r, θ, ϕ and t, substitute the Christoffel symbols into the Geodesic equations and perform the sum. The calculation for the t component of the geodesic equation is done in full, the results for the other components are shown below.

Denote the first derivatives,

$$\frac{\mathrm{d}x^1}{\mathrm{d}\lambda} = \frac{\mathrm{d}r}{\mathrm{d}\lambda} = u^1 \tag{4.1.4}$$

$$\frac{\mathrm{d}x^2}{\mathrm{d}\lambda} = \frac{\mathrm{d}\theta}{\mathrm{d}\lambda} = u^2 \tag{4.1.5}$$

$$\frac{\mathrm{d}x^3}{\mathrm{d}\lambda} = \frac{\mathrm{d}\phi}{\mathrm{d}\lambda} = u^3 \tag{4.1.6}$$

$$\frac{\mathrm{d}x^4}{\mathrm{d}\lambda} = \frac{\mathrm{d}t}{\mathrm{d}\lambda} = u^4 \tag{4.1.7}$$

The t component of the Geodesic equation:

$$\frac{\mathrm{d}u^4}{\mathrm{d}\lambda} = -\Gamma^4{}_{\mu\nu} u^\mu u^\nu \tag{4.1.8}$$

Performing the sum over the μ index:

$$\frac{\mathrm{d}u^4}{\mathrm{d}\lambda} = -\Gamma^4{}_{1\nu} u^1 u^\nu - \Gamma^4{}_{2\nu} u^2 u^\nu - \Gamma^4{}_{3\nu} u^3 u^\nu - \Gamma^4{}_{4\nu} u^4 u^\nu$$

The sum over the ν index:

$$\begin{aligned}\frac{du^4}{d\lambda} &= -\Gamma^4{}_{11} u^1 u^1 - \Gamma^4{}_{12} u^1 u^2 - \Gamma^4{}_{13} u^1 u^3 - \Gamma^4{}_{14} u^1 u^4 \\ &- \Gamma^4{}_{21} u^2 u^1 - \Gamma^4{}_{22} u^2 u^2 - \Gamma^4{}_{23} u^2 u^3 - \Gamma^4{}_{24} u^2 u^4 \\ &- \Gamma^4{}_{31} u^3 u^1 - \Gamma^4{}_{32} u^3 u^2 - \Gamma^4{}_{33} u^3 u^3 - \Gamma^4{}_{34} u^3 u^4 \\ &- \Gamma^4{}_{41} u^4 u^1 - \Gamma^4{}_{42} u^4 u^2 - \Gamma^4{}_{43} u^4 u^3 - \Gamma^4{}_{44} u^4 u^4\end{aligned}$$

Simplify by using the list of non-zero Christoffel symbols for the Kerr Metric,

$$\begin{aligned}\frac{du^4}{d\lambda} &= -\Gamma^4{}_{13} u^1 u^3 - \Gamma^4{}_{14} u^1 u^4 - \Gamma^4{}_{23} u^2 u^3 - \Gamma^4{}_{24} u^2 u^4 \\ &- \Gamma^4{}_{31} u^3 u^1 - \Gamma^4{}_{32} u^3 u^2 - \Gamma^4{}_{41} u^4 u^1 - \Gamma^4{}_{42} u^4 u^2\end{aligned}$$

By symmetry:

$$\frac{du^4}{d\lambda} = -2\left(\Gamma^4{}_{31} u^3 u^1 + \Gamma^4{}_{32} u^3 u^2 + \Gamma^4{}_{41} u^4 u^1 + \Gamma^4{}_{42} u^4 u^2\right) \tag{4.1.9}$$

Substituting in:

$$\begin{aligned}-\frac{1}{2}\frac{du^4}{d\lambda} = &\left(\frac{2aM\left(a^4 - 3a^2r^2 - 6r^4 + a^2(a^2 - r^2)\cos 2\theta\right)\sin^2\theta}{\left(a^2 + r(-2M + r)\right)\left(a^2 + 2r^2 + a^2\cos 2\theta\right)^2}\right) u^3 u^1 \\ &+ \left(\frac{\left(3a^4 + 8a^2Mr + 8a^2r^2 + 8r^4 + 4a^2\left(a^2 + 2r(-M + r)\right)\cos 2\theta + a^4\cos 4\theta\right)\cot\theta}{2\left(a^2 + 2r^2 + a^2\cos 2\theta\right)^2}\right) u^3 u^2\end{aligned}$$

$$+\left(\frac{4aM\left(r^2-a^2\cos^2\theta\right)}{\left(a^2+r(-2M+r)\right)\left(a^2+2r^2+a^2\cos 2\theta\right)^2}\right)u^4u^1+\left(-\frac{4a^2Mr\sin 2\theta}{\left(a^2+2r^2+a^2\cos 2\theta\right)^2}\right)u^4u^2$$

After some algebra, the final equation,

$$\begin{aligned}\frac{du^4}{d\lambda}=&4M[-a(a^4-3a^2r^2-6r^4+a^2(a^2-r^2)\cos 2\theta)\sin^2\theta u^1u^3\\&-4a^3r\left(a^2+r(-2M+r)\right)\cos\theta\sin^3\theta u^2u^3\\&+\left((a^4-a^2r^2-2r^4)u^1+a^2(a^2+r^2)\cos 2\theta u^1+2a^2r(a^2-2Mr+r^2)\sin 2\theta u^2\right)u^4]\\&\frac{1}{\left(a^2+r(-2M+r)\right)\left(a^2+2r^2+a^2\cos 2\theta\right)^2}\end{aligned}\tag{4.1.10}$$

The results for the remaining three components of the equations of motion:

$$\begin{aligned}\frac{du^1}{d\lambda}=&\frac{1}{\left(r^2+a^2\cos^2\theta\right)^3}\Big[-\frac{\left(r^2+a^2\cos^2\theta\right)^2\left(r(a^2-Mr)+a^2(M-r)\cos^2\theta\right)(u^1)^2}{a^2+r(-2M+r)}\\&+2a^2\cos\theta\left(r^2+a^2\cos^2\theta\right)^2\sin\theta u^1u^2+r\left(a^2+r(-2M+r)\right)\left(r^2+a^2\cos^2\theta\right)^2(u^2)^2\\&+\left(a^2+r(-2M+r)\right)\sin^2\theta\left(r^5+a^4r\cos^4\theta-a^2Mr^2\sin^2\theta+\cos^2\theta(2a^2r^3+a^4M\sin^2\theta)\right)(u^3)^2\\&-2aM\left(a^2+r(-2M+r)\right)\left(-r^2+a^2\cos^2\theta\right)\sin^2\theta u^3u^4+\\&\left(a^2+r(-2M+r)\right)\left(-Mr^2+a^2M\cos^2\theta\right)(u^4)^2\Big]\end{aligned}\tag{4.1.11}$$

$$\begin{aligned}\frac{du^2}{d\lambda}=&\frac{1}{\left(r^2+a^2\cos^2\theta\right)^3}\Big[-\frac{a^2\cos\theta\left(r^2+a^2\cos^2\theta\right)^2\sin\theta(u^1)^2}{a^2+r(-2M+r)}\\&-2r\left(r^2+a^2\cos^2\theta\right)^2u^1u^2+a^2\cos\theta\left(r^2+a^2\cos^2\theta\right)^2\sin\theta(u^2)^2\\&+\cos\theta\sin\theta[2a^2r^2(a^2+r^2)\cos^2\theta+a^4(a^2+r^2)\cos^4\theta\\&+r(a^2r^3+r^5+4a^2Mr^2\sin^2\theta+2a^4M\sin^4\theta-a^4M\sin^2 2\theta)](u^3)^2\\&-2aMr(a^2+r^2)\sin 2\theta u^3u^4+a^2\sin 2\theta(u^4)^2\Big]\end{aligned}\tag{4.1.12}$$

$$\begin{aligned}\frac{du^3}{d\lambda}=&\frac{1}{\left(a^2+2r^2+a^2\cos 2\theta\right)^2}\\&\Big[-\frac{8\left(r^4(-2M+r)+a^4r\cos^4\theta-a^2Mr^2\sin^2\theta+a^2\cos^2\theta\left(2r^2(-M+r)+a^2M\sin^2\theta\right)\right)u^1u^3}{a^2+r(-2M+r)}\\&-\left(3a^4+8a^2Mr+8a^2r^2+8r^4+4a^2\left(a^2+2r(-M+r)\right)\cos 2\theta+a^4\cos 4\theta\right)\cos\theta u^2u^3\\&+\frac{8aM\left(-r^2+a^2\cos^2\theta\right)u^1u^4}{a^2+r(-2M+r)}+16aMr\cot\theta u^2u^4\Big]\end{aligned}\tag{4.1.13}$$

It is notable that the t and ϕ components of these equations of motion depend on the same combinations of first derivative terms. The "coefficents" of these combinations of the u^α terms differ. Similarly, the r and θ components depend on the same combinations of the u^α terms, with differing functional "coefficents". A representation of the equations, displaying these dependencies more simply is,

$$\frac{du^1}{d\lambda} = A(u^1)^2 + Bu^1u^2 + C(u^2)^2 + D(u^3)^2 + Eu^3u^4 + F(u^4)^2 \tag{4.1.14}$$

$$\frac{du^2}{d\lambda} = G(u^1)^2 + Hu^1u^2 + I(u^2)^2 + J(u^3)^2 + Ku^3u^4 + L(u^4)^2 \tag{4.1.15}$$

$$\frac{du^3}{d\lambda} = Mu^1u^3 + Nu^2u^3 + Ou^1u^4 + Pu^2u^4 \tag{4.1.16}$$

$$\frac{du^4}{d\lambda} = Qu^1u^3 + Ru^2u^3 + Su^1u^4 + Tu^2u^4 \tag{4.1.17}$$

where the "functional coefficents" A through T are all real functions of a, M, r and θ while r is greater than the event horizon.

These coupled, second order, ordinary differential equations are the equations of motion that will be integrated numerically to find the trajectories of photons in the computational model. At this point, the equations could be plotted using the Mathematica plotting tool, given a set of initial conditions. However, this is not intrinsically useful to the project, since a model for the relativistic effects on the signal emanating from a Black-Hole - Pulsar binary system would require the calculation of a very large number of photon trajectories. Hence, the numerical integration of the Geodesic Equation was completed by writing code in C++, to do so with the precision and parallelism required to form part of a working simulation. Details of the code will follow in part II of this thesis.

4.2 Hamilton-Jacobi Formalism, Conserved Quantities

The trajectories of photons can be obtained by applying the Hamilton-Jacobi formalism to the Kerr Metric. This method yields equations that are equivalent to those of the geodesic equation, as given by the Euler-Lagrange formalism. However, these equations take the form of a set of first order ordinary differential equations, this set of trajectory equations was not used in the computational model. The derivation was taken from a useful online textbook listed as being a source for a US Navy site, http://heseweb.nrl.navy.mil/gamma/ dermer/lectures/Book/Kerr.pdf. This textbook provides a concise derivation of the Carter constant of the Kerr Metric, following Carter's reasoning [30] in the process of describing the constants of motion for the Kerr metric. Following this work, begin with the Kerr metric, as given in the Boyer-Linquist coordinate system [28].

$$\mathrm{d}s^2 = \left(\frac{r^2 + a^2\cos^2\theta}{r^2 - 2Mr + a^2}\right)\mathrm{d}r^2 + \left(r^2 + a^2\cos^2\theta\right)\mathrm{d}\theta^2 + \sin^2\theta\left(a^2 + r^2 + \frac{2a^2Mr\sin^2\theta}{r^2 + a^2\cos^2\theta}\right)\mathrm{d}\phi^2 \tag{4.2.1}$$
$$- \frac{4aMr\sin^2\theta}{r^2 + a^2\cos^2\theta}\mathrm{d}\phi\mathrm{d}t - \left(1 - \frac{2Mr}{r^2 + a^2\cos^2\theta}\right)\mathrm{d}t^2$$

The Kerr Metric itself forms the Lagrangian, such that $\mathrm{d}s^2 = 2\underline{L}$. Define the Lagrangian,

$$\underline{L}(x^\mu, \dot{x}^\mu, \lambda) = \frac{1}{2}g_{\mu\nu}\dot{x}^\mu\dot{x}^\nu$$

Substitute the components of the metric tensor:

$$2\underline{L} = \left(\frac{r^2 + a^2\cos^2\theta}{r^2 - 2Mr + a^2}\right)\dot{r}^2 + \left(r^2 + a^2\cos^2\theta\right)\dot{\theta}^2 + \sin^2\theta\left(a^2 + r^2 + \frac{2a^2Mr\sin^2\theta}{r^2 + a^2\cos^2\theta}\right)\dot{\phi}^2 \tag{4.2.2}$$
$$- \frac{4aMr\sin^2\theta}{r^2 + a^2\cos^2\theta}\dot{\phi}\dot{t} - \left(1 - \frac{2Mr}{r^2 + a^2\cos^2\theta}\right)\dot{t}^2$$

Absence of the t coordinate from the Lagrangian gives. We can infer the following equation by applying standard variational calculus.

$$\frac{\partial\underline{L}}{\partial\dot{t}} = const$$

Were this equation applied to massive particles rather than to photons, E would be related to the energy per unit mass of the particle.

Explicitly,

$$E = -\left(1 - \frac{2Mr}{r^2 + a^2\cos^2\theta}\right)\dot{t} - \left(\frac{2aMr\sin^2\theta}{r^2 + a^2\cos^2\theta}\dot{\phi}\right)$$

Absence of ϕ from the Hamiltonian provides a constant for the motion, denoted by L:

$$\frac{\partial \underline{L}}{\partial \dot{\phi}} = L \tag{4.2.3}$$

Explicitly,

$$L = \sin^2\theta\left(a^2 + r^2 + \frac{2a^2Mr\sin^2\theta}{r^2 + a^2\cos^2\theta}\right)\dot{\phi} - \left(\frac{2aMr\sin^2\theta}{r^2 + a^2\cos^2\theta}\dot{t}\right)$$

These constants of the motion yield two equations fot two unknown quantities, $\dot{\phi}$ and $\dot{t}$. We solve for these first derivatives as a function of the constants. We see the relation between the ϕ and t components of these first order equations, in the previous section it was observed that the ϕ and t components of the equations of motion depended on the same mixture of first order derivatives, with different functional coefficients.

Solve for $\dot{t}$ in terms of E, L, a, M, r, and θ to obtain:

$$\dot{t} = \frac{\left((r^2 + a^2)^2 - (r^2 - 2Mr + a^2)(a^2\sin^2\theta)\right)E - 2aMrL}{(r^2 + a^2\cos^2\theta)(r^2 - 2Mr + a^2)} \tag{4.2.4}$$

Solve for $\dot{\phi}$ in terms of E, L, a, M, r, and θ to obtain:

$$\dot{\phi} = \frac{2aMrE\sin^2\theta + \left(r^2 + a^2\cos^2\theta - 2Mr\right)L}{(r^2 + a^2\cos^2\theta)(r^2 - 2Mr + a^2)\sin^2\theta} \tag{4.2.5}$$

We must now solve for the other two components. These equations are not as simple to derive, Carter first performed the work by showing that the action of our Lagrangian could be completely separated such that two more conserved quantities could be obtained. To use Hamilton's method, we must first obtain the conjugate momenta.

The generalized momenta P_μ:

$$P_\mu = \frac{\partial \underline{L}}{\partial \dot{x}^\mu} = g_{\mu\nu}\dot{x}^\nu \tag{4.2.6}$$

Define the Hamiltonian:

$$H = P_\mu\dot{x}^\mu - \underline{L} = \frac{1}{2}g^{\mu\nu}P_\mu P_\nu \tag{4.2.7}$$

The first conserved quantity is obtained from the absence of the affine geodesic parameter λ from the Hamiltonian. Hence, the Hamiltonian itself is a conserved quantity, stated:

$H = \frac{q^2}{2}$. The Hamilton-Jacobi method requires the introduction of a function, denoted S, which is a function of λ, the coordinates r, θ, ϕ and t, as well as the conserved quantities q^2, E, L, and K. The constant K is called Carter's constant.

$$S = S(\lambda, r, \theta, \phi, t, q^2, E, L, K)$$

The equations relating the conjugate momenta in the original coordinates (r, θ, ϕ, t) and the newly defined function S are given by:

$$\partial_r S = P_r, \;\; \partial_\theta S = P_\theta, \;\; \partial_\phi S = P_\phi, \;\; \partial_t S = P_t$$

Simply:

$$\partial_\mu S = P_\mu \tag{4.2.8}$$

Substituting this relation back into the definition of the Hamiltonian yields:

$$H = \frac{1}{2} g^{\mu\nu} \partial_\mu S \partial_\nu S \tag{4.2.9}$$

The Hamilton-Jacobi equation can finally be used: $\partial_\lambda S + H = 0$. Making the appropriate substitution for H and noting that here λ plays a role analogous to the time in any classical problem, we obtain:

$$\partial_\lambda S + \frac{1}{2} g^{\mu\nu} \partial_\mu S \partial_\nu S = 0 \tag{4.2.10}$$

Define:

$$\rho^2 = r^2 + a^2 \cos^2\theta$$

$$\Delta = r^2 - 2Mr + a^2$$

$$\Sigma^2 = (r^2 + a^2)^2 - \Delta a^2 \sin^2\theta$$

We now rewrite the contravariant version of the Kerr metric (the inverse) in matrix form, using these definitions to get:

$$\begin{pmatrix} \frac{\Delta}{\rho^2} & 0 & 0 & 0 \\ 0 & \frac{1}{\rho^2} & 0 & 0 \\ 0 & 0 & \frac{\Delta - a^2 \sin^2\theta}{\rho^2 \Delta \sin^2\theta} & -\frac{2aMr}{\rho^2 \Delta} \\ 0 & 0 & -\frac{2aMr}{\rho^2 \Delta} & -\frac{\Sigma^2}{\rho^2 \Delta} \end{pmatrix}$$

where $\mu = 1, 2, 3, 4$. The Hamilton-Jacobi equation now becomes.

$$2\partial_\lambda S = -\frac{\Delta}{\rho^2}(\partial_r S)^2 - \frac{1}{\rho^2}(\partial_\theta S)^2 - \frac{\Delta - a^2\sin^2\theta}{\rho^2\Delta\sin^2\theta}(\partial_\phi S)^2 + \frac{\Sigma^2}{\rho^2\Delta}(\partial_t S)^2 + \frac{4aMr}{\rho^2\Delta}\partial_t S\partial_\phi S \tag{4.2.11}$$

We look for seperable solutions of this equation. Put:

$$S = -\frac{1}{2}q^2\lambda - Et + L\phi + S_r + S_\theta \tag{4.2.12}$$

Here we have chosen the dependance of S on λ so that it satisfies identically the Hamilton-Jacobi equation.

$$\partial_\lambda S = -\frac{1}{2}q^2 = -\frac{1}{2}g^{\mu\nu}P_\mu P_\nu = -H$$

This identifies the conserved quantity q^2 as the normalization of the four-momentum. Thus $q^2 = 0$ for photons, and $q^2 = -1$ (m = 1, c = 1) for massive particles. The functions S_r and S_θ depend only on r and θ respectively, as required by the assumption of seperability. Calculating the partial derivatives of the function S:

$$\partial_\lambda S = -\frac{1}{2}q^2$$

$$\partial_r S = \frac{dS_r}{dr}$$

$$\partial_\theta S = \frac{dS_\theta}{d\theta}$$

$$\partial_\phi S = \frac{dS_\phi}{d\phi} = L$$

$$\partial_t S = \frac{dS_t}{dt} = -E$$

Substituting into the form of the Hamilton-Jacobi equation given by equation (4.2.11) yields:

$$-q^2 = -\frac{\Delta}{\rho^2}\left(\frac{dS_r}{dr}\right)^2 - \frac{1}{\rho^2}\left(\frac{dS_\theta}{d\theta}\right)^2 - \frac{\Delta - a^2\sin^2\theta}{\rho^2\Delta\sin^2\theta}L^2 + \frac{\Sigma^2}{\rho^2\Delta}E^2 - \frac{4aMr}{\rho^2\Delta}EL \tag{4.2.13}$$

This equation can be separated into two parts: the terms containing r, and those containing θ. After some algebra, the equation becomes:

$$\left[\Delta\left(\frac{dS_r}{dr}\right)^2 - \frac{C^2}{\Delta} - q^2r^2\right] = -\left[\left(\frac{dS_\theta}{d\theta}\right)^2 + \frac{D^2}{\sin^2\theta} - q^2a^2\cos^2\theta\right] \tag{4.2.14}$$

where:

$$C = C(r) = (r^2 + a^2)E - aL \tag{4.2.15}$$

$$D = D(\theta) = L - aE\sin^2\theta \tag{4.2.16}$$

We have succeeded in separating the equation, with the left hand side of (4.2.14) depending only on r, and the right only on θ. Denote the separation constant by K. Then

$$\Delta\left(\frac{dS_r}{dr}\right)^2 - \frac{C^2}{\Delta} - q^2r^2 = -K \tag{4.2.17}$$

$$\left(\frac{dS_\theta}{d\theta}\right)^2 + \frac{D^2}{\sin^2\theta} - q^2a^2\cos^2\theta = K \tag{4.2.18}$$

Rearranging:

$$\Delta^2\left(\frac{dS_r}{dr}\right)^2 = C^2 + \Delta\left(q^2r^2 - K\right)$$
$$\left(\frac{dS_\theta}{d\theta}\right)^2 = K + q^2a^2\cos^2\theta - \frac{D^2}{\sin^2\theta}$$

Define:

$$R(r) \equiv \Delta^2\left(\frac{dS_r}{dr}\right)^2 = C^2 + \Delta\left(q^2r^2 - K\right) \tag{4.2.19}$$

$$\Theta(\theta) \equiv \left(\frac{dS_\theta}{d\theta}\right)^2 = K + q^2a^2\cos^2\theta - \frac{D^2}{\sin^2\theta} \tag{4.2.20}$$

Ignoring an irrelevant additive constant, substitute these results into equation (4.2.12), we get:

$$S = -\frac{1}{2}q^2\lambda - Et + L\phi + \int\frac{\sqrt{R}}{\Delta}dr + \int\sqrt{\Theta}\,d\theta \tag{4.2.21}$$

To obtain the required results for the r and θ components of the first order derivatives, we must differentiate the function S with respect to the newly defined conserved quantities.

$$\frac{\partial S}{\partial(q^2)} = 0 = -\frac{1}{2}\lambda + \frac{\partial}{\partial(q^2)}\left(\int\frac{\sqrt{R}}{\Delta}dr\right) + \frac{\partial}{\partial(q^2)}\left(\int\sqrt{\Theta}\,d\theta\right)$$

$$\frac{\partial S}{\partial(K)} = 0 = \frac{\partial}{\partial(K)}\left(\int \frac{\sqrt{R}}{\Delta} dr\right) + \frac{\partial}{\partial(K)}\left(\int \sqrt{\Theta}\, d\theta\right)$$

So that,

$$\frac{\partial S}{\partial(q^2)} = 0 = -\frac{1}{2}\lambda + \int \frac{1}{2\sqrt{R}\Delta}\frac{\partial R}{\partial(q^2)} dr + \int \frac{1}{2\sqrt{\Theta}}\frac{\partial \Theta}{\partial(q^2)} d\theta \tag{4.2.22}$$

$$\frac{\partial S}{\partial(K)} = 0 = \int \frac{1}{2\sqrt{R}\Delta}\frac{\partial R}{\partial K} dr + \int \frac{1}{2\sqrt{\Theta}}\frac{\partial \Theta}{\partial K} d\theta \tag{4.2.23}$$

The derivatives in the integrand of (4.2.22) and (4.2.23) are given by:

$$\frac{\partial R}{\partial(q^2)} = \Delta r^2$$

$$\frac{\partial \Theta}{\partial(q^2)} = a^2 \cos^2\theta$$

$$\frac{\partial R}{\partial K} = -\Delta$$

$$\frac{\partial \Theta}{\partial K} = 1$$

Substituting:

$$\frac{\partial S}{\partial(q^2)} = 0 = -\frac{1}{2}\lambda + \int \frac{r^2}{2\sqrt{R}} dr + \int \frac{a^2\cos^2\theta}{2\sqrt{\Theta}} d\theta$$

$$\frac{\partial S}{\partial(K)} = 0 = -\int \frac{1}{2\sqrt{R}} dr + \int \frac{1}{2\sqrt{\Theta}} d\theta$$

Differentiate with respect to λ to remove the integral, we obtain:

$$\frac{1}{2} = \frac{r^2}{2\sqrt{R}}\dot{r} + \frac{a^2\cos^2\theta}{2\sqrt{\Theta}}$$

$$0 = -\frac{1}{2\sqrt{R}}\dot{r} + \frac{1}{2\sqrt{\Theta}}$$

Finally:

$$1 = \frac{r^2}{\sqrt{R}}\dot{r} + \frac{a^2\cos^2\theta}{\sqrt{\Theta}}\dot{\theta} \tag{4.2.24}$$

$$\frac{\dot{r}}{\sqrt{R}} = \frac{\dot{\theta}}{\sqrt{\Theta}} \tag{4.2.25}$$

Thus we obtain the equations for the first derivatives of r and θ with respect to λ, in terms of r, θ, a, E, L, q^2 and K:

$$\dot{r} = \pm\frac{\sqrt{\left((r^2+a^2)E - aL\right)^2 + \left(r^2 - 2Mr + a^2\right)\left(q^2r^2 - K\right)}}{r^2 + a^2\cos^2\theta} \tag{4.2.26}$$

$$\dot{\theta} = \pm\frac{\sqrt{K + q^2a^2\cos^2\theta - \dfrac{\left(L - aE\sin^2\theta\right)^2}{\sin^2\theta}}}{r^2 + a^2\cos^2\theta} \tag{4.2.27}$$

Photon world lines are null geodesics, so $q^2 = 0$, simplifying the above equations. The complete set of first derivatives are thus given by:

$$\dot{r} = \pm\frac{\sqrt{\left((r^2+a^2)E - aL\right)^2 - \left(r^2 - 2Mr + a^2\right)K}}{r^2 + a^2\cos^2\theta} \tag{4.2.28}$$

$$\dot{\theta} = \pm\frac{\sqrt{K - \dfrac{\left(L - aE\sin^2\theta\right)^2}{\sin^2\theta}}}{r^2 + a^2\cos^2\theta} \tag{4.2.29}$$

$$\dot{\phi} = \frac{2aMrE\sin^2\theta + \left(r^2 + a^2\cos^2\theta - 2Mr\right)L}{\left(r^2 + a^2\cos^2\theta\right)\left(r^2 - 2Mr + a^2\right)\sin^2\theta} \tag{4.2.30}$$

$$\dot{t} = \frac{\left((r^2+a^2)^2 - (r^2 - 2Mr + a^2)(a^2\sin^2\theta)\right)E - 2aMrL}{\left(r^2 + a^2\cos^2\theta\right)\left(r^2 - 2Mr + a^2\right)} \tag{4.2.31}$$

This formalism replaces the problem of integrating the geodesic equations, which are a set of coupled second order ODEs, by an equivalent problem that involves only a set of coupled first order ODEs.

Chapter 5

General Relativistic Orbital Mechanics

The signature emission of a Black-Hole - Pulsar binary system is a function of the orbital motion of both of the compact bodies. The celestial mechanics of the system must thus be modelled to facilitate identification of the characteristic features of the signal. Einstein's field equations are non-linear hyperbolic partial differential equation, and thus present a difficult problem. The system consists of two strongly self-gravitating bodies, which may be assumed to be widely separated. Observation of a Black-Hole/Pulsar binary in the final stages of coalescence would yield significant information useful for strong field tests of General Relativity.

5.1 Stable Circular Orbits of Test Particles in the Kerr Spacetime

As a first approximation we may model the binary system as follows. Assume the Kerr black-hole to be stationary at the origin of a coordinate system and consider the Pulsar as a test particle orbiting the black-hole along a time-like geodesic. We will consider the special case in which the pulsar orbit is a stable circular orbit. We are thus entirely neglecting the gravitational field of the Pulsar and its effect on the motion of the Black-Hole. Comparison of the signal predicted by this model with the one obtained from more complex models will give an indication of the effect of the Pulsar's gravitational field on the motions of the two bodies.

5.2 First order Parameterized Post-Newtonian Equations of Motion, as described by Damour and Deruelle, [10].

Without simplifying assumptions, the problem requires us to find equations for the orbital motion of two strongly self-gravitating objects. The result is a set of retarded-integrodifferential equations which can be converted to a set of ordinary differential equations. Restriction to low velocity then allows expansion as a power series in v/c. They neglect terms of order $(v/c)^2$ and higher, i.e. they consider only "first order" corrections to the Newtonian result. They found that these equations coincide exactly with the orbital equations of motion derived via the Post-Newtonian approximation for the case of widely separated, weakly selfgravitating, slow moving objects, and depend only on the Schwarzschild masses of the two objects. This result is, in fact, a direct consequence of the structure of Einstein's field equations, known as the "effacing principle". Below, I have followed the work of Damour and Deruelle in deriving the first order approximation to the equations of orbital motion. They begin by formulating a Lagrangian which is a function of the positions and velocities of the "centre of fields" of the two bodies, denoted r_b and r_p for the Black-Hole and Pulsar respectively, as well as v_b and v_p for their velocities. Similarly, their masses are denoted m_b and m_p. The coordinate system is chosen to be harmonic. Damour and Deruelle define:

$$\mathbf{R} = \mathbf{r}_b - \mathbf{r}_p$$

$$R = |\mathbf{R}|$$

$$\mathbf{v}_b.\mathbf{v}_b = |\mathbf{v}_b|^2 = {v_b}^2$$

$$\mathbf{v}_b.\mathbf{v}_p = (v_b v_p)$$

They define the following Lagrangian:

$$L_{PN}\big(\vec{r}_b(t), \vec{r}_p(t), \vec{v}_b(t), \vec{v}_p(t)\big) = L_N + \frac{1}{c^2} L_2 \tag{5.2.1}$$

Where the L_N denotes the Newtonian Lagrangian:

$$L_N = \frac{1}{2} m_b {v_b}^2 + \frac{1}{2} m_p {v_p}^2 + \frac{G m_b m_p}{\vec{R}} \tag{5.2.2}$$

and L2 is the Post-Newtonian correction, given by:

$$L_2 = \frac{1}{8} m_b {v_b}^4 + \frac{1}{8} m_p {v_p}^4 + \frac{G m_b m_p}{2R}\Big[3{v_b}^2 + 3{v_p}^2 - 7(v_b v_p) - (N v_b)(N v_p) - G\frac{m_b + m_p}{R}\Big] \tag{5.2.3}$$

where G is Newton's constant of universal gravitation and c is the speed of light.

Invariance of the Lagrangian under a spatial translation implies, by Noether's theorem, the conservation of linear momentum. Similarly, invariance under Lorentz boosts infers the conservation of energy, and invariance under spatial rotations implies the conservation of angular momentum. Damour and Deruelle write total momentum:

$$P_{PN} = \frac{\partial L_{PN}}{\partial \mathbf{v}_b} + \frac{\partial L_{PN}}{\partial \mathbf{v}_p} \tag{5.2.4}$$

Similarly, Damour and Deruelle state that the relativistic center of mass (centre of momentum) integral implies the following equation, the conservation of kinetic energy:

$$K_{PN} = G_{PN} - tP_{PN} \tag{5.2.5}$$

Where:

$$\begin{aligned} G_{PN} = &\Big(m_b + \frac{1}{2}\frac{m_b {v_b}^2}{c^2} - \frac{1}{2}\frac{Gm_b m_p}{Rc^2}\Big)\mathbf{r}_b \\ &+ \Big(m_p + \frac{1}{2}\frac{m_p {v_p}^2}{c^2} - \frac{1}{2}\frac{Gm_p m_b}{Rc^2}\Big)\mathbf{r}_p \end{aligned} \tag{5.2.6}$$

The next objective is to move to the inertial reference frame of the binary centre of mass, where the linear momentum and kinetic energy are both zero, i.e. $P_{PN} = K_{PN} = 0$. Damour and Deruelle achieve this by performing a Poincaré transormation, and refer to this reference frame as a post-Newtonian centre of mass frame. The concept of a centre of mass reference frame does not exist in General Relativity, only the centre of momentum reference frame could be considered in this context. They obtain the motion relative to the post-Newtonian centre of mass of the two bodies, by solving the following equations for the positions r_b and r_p:

$$0 = \frac{\partial L_{PN}}{\partial \mathbf{v}_b} + \frac{\partial L_{PN}}{\partial \mathbf{v}_p} \tag{5.2.7}$$

$$\begin{aligned} 0 = G_{PN} = &\Big(m_b + \frac{1}{2}\frac{m_b {v_b}^2}{c^2} - \frac{1}{2}\frac{Gm_b m_p}{Rc^2}\Big)\mathbf{r}_b \\ &+ \Big(m_p + \frac{1}{2}\frac{m_p {v_p}^2}{c^2} - \frac{1}{2}\frac{Gm_p m_b}{Rc^2}\Big)\mathbf{r}_p \end{aligned} \tag{5.2.8}$$

Equation (5.2.7) gives:

$$0 = m_b\mathbf{v}_b + m_p\mathbf{v}_p + \frac{1}{2c^2}m_b {v_b}^3 + \frac{1}{2c^2}m_p {v_p}^3 + \frac{Gm_b m_p}{2Rc^2}\Big[6v_b + 6v_p - 7v_b - 7v_p - (Nv_b)N - N(Nv_p)\Big] \tag{5.2.9}$$

Damour and Deruelle rearrange these equations and solve for the relative positions $\mathbf{r}_b$ and $\mathbf{r}_p$:

$$\mathbf{r}_b = \frac{\mu}{m_b}\mathbf{R} + \frac{\mu(m_b - m_p)}{2M^2c^2}\Big[V^2 - \frac{GM}{R}\Big]\mathbf{R} \tag{5.2.10}$$

$$\mathbf{r}_p = -\frac{\mu}{m_p}\mathbf{R} + \frac{\mu(m_b - m_p)}{2M^2c^2}\Big[V^2 - \frac{GM}{R}\Big]\mathbf{R} \tag{5.2.11}$$

where: $M = m_b + m_p$ is the total mass and $\mu = \dfrac{m_b m_p}{M}$ is the reduced mass. Damour and Deruelle denote $\mathbf{V} = \mathrm{d}\mathbf{R}/\mathrm{d}t$ as the "instantaneous relative velocity" of the Black-Hole and Pulsar in this frame,

$$\mathbf{V} = \frac{d\mathbf{R}}{dt} = \mathbf{v}_b - \mathbf{v}_p$$
$$V^2 = \mathbf{V}.\mathbf{V}$$

Thus it is possible to solve for the relative motion in a post-Newtonian centre of mass frame. Damour and Deruelle write the equations of motion for the motion relative to the post-Newtonian centre of mass, where the positions and velocities of the two bodies are all given by their centre of mass equations, as shown above. They introduce ν, the symmetric mass ratio: $\nu = \mu/M = m_b m_p/(m_b + m_p)^2$ and the unit vector $\mathbf{N} = \mathbf{R}/R$.

$$\begin{aligned}\frac{d\mathbf{V}}{dt} = &-\frac{GM}{R^2}\mathbf{N} + \frac{GM}{c^2R^2}\Big[\mathbf{N}\big[\frac{GM}{R}(4+2\nu) - V^2(1+3\nu) + \\ &\frac{3}{2}\nu(NV)^2\big] + (4-2\nu)\mathbf{V}(NV)\Big]\end{aligned} \tag{5.2.12}$$

In index notation, space indices only:

$$\begin{aligned}\frac{d}{dt}V_i = &-\frac{GM}{R^2}N_i + \frac{GM}{c^2R^2}\big(N_i(\frac{GM}{R}(4+\nu) - V_jV^j(1+3\nu) + \frac{3}{2}\nu(N_kV^k)^2) \\ &+ (4-2\nu)V_i(N_lV^l)\big)\end{aligned} \tag{5.2.13}$$

The value of ν may vary between 0 and 1/4 where the 0 corresponds to the case of a test particle and a massive body, and 1/4 corresponds to two bodies of equal mass. Damour and Deruelle derive the equations of motion by using two different mathematical formalisms. Firstly, the concept of the transformation of coordinates was used; secondly, standard variational calculus was applied to obtain the final equations of motion. However, these methods were applied to a general Lagrangian, in no specific frame of reference, accurate to the first order Post-Newtonian approximation. The Lagrangian does not simply describe the "relative" motion of the two bodies, but rather the general motion, whereas the equations of motion derived from it describe the relative motion in the centre of mass reference frame.

Damour and Deruelle determine whether a Lagrangian exists, from which the relative motion can be directly derived via the principles of variational calculus. This exercise

provides a surprising result: a relative Lagrangian resulting in the above equations of motion may be constructed from the original Lagrangian by replacing the positions and velocities by the expressions obtained for the relative positions and velocities as given by equations (5.2.10) and (5.2.11). Furthermore, Newtonian centre of mass expressions are sufficient to obtain the final result, equation (5.2.12). This is simply due to the fact that the resulting equations of motion are truncated to first order in terms of v/c; the relativistic corrections to the motion resulting from equations (5.2.10) and (5.2.11) are only of order $(v/c)^2$ and higher. This proceduce, known as order reduction, is widely used in work involving the dynamics of compact binary systems. It generally consists of replacing the complicated acceleration or higher order "time" derivative components in post-Newtonian terms by their explicit expressions, as found in a lower order post-Newtonian results. This is acceptable, since keeping more complicated forms usually only yields a difference in the result of higher order in (v/c) than is required. Here, Damour and Deruelle apply order reduction to a velocity term rather than to an acceleration. This order reduction is only reasonable for 1PN accurate results. Hence, they use the Newtonian expressions for the positions and velocities of both the Black-Hole and the Pulsar in the centre of mass reference frame.

$$\mathbf{r}_{b_N} = \frac{\mu}{m_b}\mathbf{R} \tag{5.2.14}$$

$$\mathbf{r}_{p_N} = -\frac{\mu}{m_p}\mathbf{R} \tag{5.2.15}$$

$$\mathbf{v}_{b_N} = \frac{\mu}{m_b}\mathbf{V} \tag{5.2.16}$$

$$\mathbf{v}_{p_N} = -\frac{\mu}{m_p}\mathbf{V} \tag{5.2.17}$$

Damour and Deruelle prove this conjecture as follows. They perform a linear transformation of the position variables in the original Lagrangian L_{PN}. Its purpose is to move from a general inertial reference frame to a centre of mass reference frame:
The transformation is:

$$(\mathbf{r}_b, \mathbf{r}_p) \rightarrow (\mathbf{R}, \mathbf{X})$$

where:

$$\mathbf{R} = \mathbf{r}_b - \mathbf{r}_p \; ; \quad \mathbf{X} = \frac{m_b\mathbf{r}_b + m_p\mathbf{r}_p}{M}$$

put:

$$\frac{d\mathbf{X}}{dt} = \mathbf{W}$$

They then write the following equations for the positions and velocities of the two bodies:

$$\mathbf{r}_b = \mathbf{r}_{b_N} + \mathbf{X} \tag{5.2.18}$$

$$\mathbf{r}_p = \mathbf{r}_{p_N} + \mathbf{X} \tag{5.2.19}$$

$$\mathbf{v}_b = \mathbf{v}_{b_N} + \mathbf{W} \tag{5.2.20}$$

$$\mathbf{v}_p = \mathbf{v}_{p_N} + \mathbf{W} \tag{5.2.21}$$

Performing the substitution explicitly, the Newtonian Lagrangian (5.2.2) becomes,

$$L_N = \frac{1}{2}m_b(\mathbf{v}_{b_N} + \mathbf{W})^2 + \frac{1}{2}m_p(\mathbf{v}_{p_N} + \mathbf{W})^2 + \frac{Gm_bm_p}{\mathbf{R}}$$
$$L_N = \frac{1}{2}m_b v_{b_N}^2 + \frac{1}{2}m_p v_{p_N}^2 + \frac{1}{2}m_b W^2 + \frac{1}{2}m_p W^2 + m_b\mathbf{v}_{b_N} + m_p\mathbf{v}_{p_N}$$

Now substitute equations (5.2.16) and (5.2.17) for the Newtonian velocity vectors $\mathbf{v}_{b_N}$ and $\mathbf{v}_{p_N}$ to get

$$L_N = \frac{1}{2}m_b(\frac{\mu}{m_b}\mathbf{V})^2 + \frac{1}{2}m_p(-\frac{\mu}{m_p}\mathbf{V})^2 + \cancel{m_b(\frac{\mu}{m_b}\mathbf{V})} + \cancel{m_p(-\frac{\mu}{m_p}\mathbf{V})} + \frac{1}{2}(m_b + m_p)W^2$$
$$L_N = \frac{1}{2}V^2\mu^2\left(\frac{1}{m_b} + \frac{1}{m_p}\right) + \frac{1}{2}MW^2$$
$$L_N = \frac{1}{2}V^2\mu^2\left(\frac{m_b + m_p}{m_bm_p}\right) + \frac{1}{2}MW^2$$
$$L_N = \frac{1}{2}V^2\mu^2(\frac{1}{\mu}) + \frac{1}{2}MW^2$$

So that finally:

$$\Rightarrow L_N = \frac{1}{2}V^2\mu + \frac{1}{2}MW^2$$

Perform the same substitution for the L_2 part of the Lagrangian, (5.2.3):

$$L_2 = \frac{1}{8}m_b{v_b}^4 + \frac{1}{8}m_p{v_p}^4 + \frac{Gm_bm_p}{2R}\left[3{v_b}^2 + 3{v_p}^2 - 7(\mathbf{v}_b\mathbf{v}_p) - (N\mathbf{v}_b)(N\mathbf{v}_p) - G\frac{m_b + m_p}{R}\right]$$

Begin with the first two terms, substitute $\mathbf{v}_b = \frac{\mu \mathbf{V}}{m_b} + \mathbf{W}$ and $\mathbf{v}_p = \frac{\mu \mathbf{V}}{m_b} + \mathbf{W}$.

$$\frac{1}{8\mu} m_b {v_b}^4 = \frac{1}{8\mu} m_b \Big[\frac{\mu^4}{{m_b}^4} V^4 + \frac{4\mu^3}{{m_b}^3} V^2 (VW) + \frac{2\mu^2}{{m_b}^2} V^2 W^2 + \frac{4\mu^2}{{m_b}^2} (VW)^2 + \frac{4\mu}{m_b} (VW) W^2 + W^4 \Big]$$

Similarly:

$$\frac{1}{8\mu} m_b {v_b}^4 = \frac{1}{8\mu} m_p \Big[\frac{\mu^4}{{m_p}^4} V^4 - \frac{4\mu^3}{{m_p}^3} (VW) V^2 + \frac{4\mu^2}{{m_p}^2} (VW)^2 + \frac{2\mu^2}{{m_p}^2} - \frac{4\mu}{m_p} (VW) W^2 + W^4 \Big]$$

Damour and Deruelle drop terms containing W, as the contributions from $\mathbf{W}$ are of the second post-Newtonian order, $\mathrm{O}(1/c^2)$.

Hence, summing terms yields:

$$\frac{1}{8\mu} m_b {v_b}^4 + \frac{1}{8\mu} m_p {v_p}^4 = \frac{1}{8\mu} \Big[\frac{\mu^4}{{m_b}^3} V^4 + \frac{\mu^4}{{m_p}^3} V^4 \Big] \tag{5.2.22}$$

Rearrange:

$$\begin{aligned}
\frac{1}{8\mu} m_b {v_b}^4 + \frac{1}{8\mu} m_p {v_p}^4 &= \frac{1}{8\mu} \Big[\frac{\mu^4}{{m_b}^3} V^4 + \frac{\mu^4}{{m_p}^3} V^4 \Big] \\
&= \frac{\mu^3}{8} \left(\frac{1}{{m_b}^3} + \frac{1}{{m_p}^3} \right) V^4 \\
&= \frac{\mu^3}{8} \left(\frac{{m_b}^3 + {m_p}^3}{{m_b}^3 {m_p}^3} \right) V^4 \\
&= \frac{\mu^3}{8} \left(\frac{M^3}{{m_b}^3 {m_p}^3} - 3 \frac{{m_b}^2 m_p + {m_p}^2 m_b}{{m_b}^3 {m_p}^3} \right) V^4 \\
&= \frac{\mu^3}{8} \left(\frac{1}{\mu^3} - 3 \frac{m_b + m_p}{{m_b}^2 {m_p}^2} \right) V^4 \\
&= \frac{\mu^3}{8} \left(\frac{1}{\mu^3} - \frac{3}{m_b m_p} \frac{1}{\mu} \right) V^4 \\
&= \frac{1}{8} \Big[1 - 3 \big(\frac{1}{m_b m_p} \frac{{m_b}^2 {m_p}^2}{(m_b + m_p)^2} \big) \Big] V^4 \\
&= \frac{1}{8} \left[1 - 3 \left(\frac{m_b m_p}{(m_b + m_p)^2} \right) \right] V^4 \\
&= \frac{1}{8} \left(1 - 3\nu \right) V^4
\end{aligned}$$

The bracketed terms of equation (5.2.3), after performing the same change of variables for the terms $3{v_b}^2 + 3{v_p}^2 - 7(v_b v_p)$, become

$$3{v_b}^2 + 3{v_p}^2 - 7(v_b v_p) = 3 \left[\big(\frac{\mu^2}{{m_b}^2} + \frac{\mu^2}{{m_b}^2} \big) V^2 + \big(\frac{2\mu}{m_b} - \frac{2\mu}{m_p} \big) (VW) + 2W^2 \right]$$

$$-7\left[(\frac{-\mu^2}{m_b m_p})V^2+\frac{\mu}{m_b}(VW)-\frac{\mu}{m_p}(VW)+W^2\right] \tag{5.2.23}$$

Omitting terms containing W, we get:

$$\begin{aligned}
3{v_b}^2+3{v_p}^2-7(v_b v_p) &= \left(3\frac{\mu^2}{{m_b}^2}+3\frac{\mu^2}{{m_p}^2}+7\frac{\mu^2}{m_b m_p}\right)V^2\\
&= \left(\frac{3\mu^2{m_b}^2+3\mu^2{m_p}^2+7\mu^2 m_b m_p}{{m_b}^2{m_p}^2}\right)V^2\\
&= \left(\frac{\mu^2}{{m_b}^2{m_p}^2}(3{m_b}^2+3{m_p}^2+7m_b m_p)\right)V^2\\
&= \left(\frac{\mu^2}{{m_b}^2{m_p}^2}(3({m_b}^2+2m_b m_p+{m_p}^2)+m_b m_p)\right)V^2\\
&= \left(\frac{\mu^2}{{m_b}^2{m_p}^2}(3(m_b+m_p)^2+m_b m_p)\right)V^2\\
&= \left(\frac{3\mu^2M^2}{{m_b}^2{m_p}^2}+\frac{\mu^2}{m_b m_p}\right)V^2\\
&= (3+\nu)\,V^2
\end{aligned}$$

Similarly, the penultimate term in equation (5.2.3), $-(Nv_b)(Nv_p)$ can be order-reduced. Note the use of the shorthand introduced earlier, $-(Nv_b)(Nv_p)=(\mathbf{N}.\mathbf{v}_b)(\mathbf{N}.\mathbf{v}_p)$.

$$-\left(\mathbf{N}.\mathbf{v}_b\right)\left(\mathbf{N}.\mathbf{v}_p\right)=-\left(\mathbf{N}.(\frac{\mu\mathbf{V}}{m_b}+\mathbf{W})\right)\left(\mathbf{N}.(-\frac{\mu\mathbf{V}}{m_p}+\mathbf{W})\right) \tag{5.2.24}$$

Manipulating the right hand side of this equation,

$$\begin{aligned}
-\left(\mathbf{N}.\mathbf{v}_b\right)\left(\mathbf{N}.\mathbf{v}_p\right) &= -\left(\frac{\mu NV}{m_b}+NW\right)\left(-\frac{\mu NV}{m_p}+NW\right)\\
-\left(\mathbf{N}.\mathbf{v}_b\right)\left(\mathbf{N}.\mathbf{v}_p\right) &= -\frac{-\mu^2(NV)^2}{m_b m_p}-\frac{\mu}{m_b}(NV)(NW)+\frac{\mu}{m_p}(NV)(NW)-(NW)^2
\end{aligned}$$

Drop terms containing W.

$$\begin{aligned}
&=\frac{(\frac{m_b m_p}{m_b+m_p})^2}{m_b m_p}(NV)^2\\
&=\frac{m_b m_p}{(m_b+m_p)^2}(NV)^2\\
&=\nu(NV)^2
\end{aligned}$$

The final term in the Lagrangian (5.2.3) is simply GM/R; Damour and Deruelle convert the coefficient of the bracketed terms to $GM/3Rc^2$. The Lagrangian describing the relative

motion of the two massive bodies at the first order post-Newtonian approximation is thus,

$$L^R_{PN} = \frac{1}{2}V^2 + \frac{GM}{R} + \frac{1}{8}(1-3\nu)\frac{V^4}{c^2} + \frac{GM}{2Rc^2}\left((3+\nu)V^2 + \nu(NV)^2 - \frac{GM}{R}\right) \quad (5.2.25)$$

This Lagrangian may now be treated using the principles of variational calculus. Damour and Deruelle indicate several different methods for the integration of the equations of motion obtained from this Lagrangian. These include methods that use the Eueler-Lagrange formalism, the Hamilton-Jacobi formalism and the Maupertius principle. However, Landau and Lifshitz [31] were more focused on the objective of describing specific relativistic effects on the motion of the two bodies. The simpler method is to exploit the symmetries present in the Lagrangian to describe the motion of the Black-Hole and the Pulsar.

The Lagrangian (5.2.25) is invariant under time translations and spatial rotations. Hence there are four first integrals, one due to the invariance under time translation, which is the total energy of the system; and three more via the invariance under spatial rotation, which are the total angular momentum of the binary system. Thus both energy and angular momentum of the system are conserved.

Damour and Deruelle first deal with the former, they denote the constant of integration E:

$$E = \mathbf{V}.\frac{\partial L^R_{PN}}{\partial \mathbf{V}} - L^R_{PN} \quad (5.2.26)$$

Differentiating with respect to $\mathbf{V}$, we get

$$\frac{\partial L^R_{PN}}{\partial \mathbf{V}} = V + \frac{1}{2}(1-3\nu)\frac{V^3}{c^2} + \frac{GM}{2Rc^2}\left[2(3+\nu)V + 2\nu N^2 V\right] \quad (5.2.27)$$

Multiply by V to get

$$\mathbf{V}.\frac{\partial L^R_{PN}}{\partial \mathbf{V}} = V^2 + \frac{1}{2}(1-3\nu)\frac{V^4}{c^2} + \frac{GM}{2Rc^2}\left[2(3+\nu)V^2 + 2\nu(NV)^2\right] \quad (5.2.28)$$

Finally, the total Noetherian energy is given by:

$$E = \mathbf{V}.\frac{\partial L^R_{PN}}{\partial \mathbf{V}} - L^R_{PN} = \frac{1}{2} + \frac{3}{8}(1-3\nu)\frac{V^4}{c^2} - \frac{GM}{R} + \frac{GM}{2Rc^2}\left((3+\nu)V^2 + \nu(NV)^2 + \frac{GM}{R}\right) \quad (5.2.29)$$

The first integral for the total angular Momentum is given by:

$$\mathbf{J} = \mathbf{R} \times \frac{\partial L^R_{PN}}{\partial \mathbf{V}} \quad (5.2.30)$$

Use equation (5.2.27) to obtain:

$$\mathbf{J} = \mathbf{R} \times \left(\mathbf{V} + \frac{1}{2}(1 - 3\nu)\frac{V^2}{c^2}\mathbf{V} + (3 + \nu)\frac{GM}{Rc^2}\mathbf{V} \right) \tag{5.2.31}$$

Thus total Noetherian angular momentum is given by:

$$\mathbf{J} = \mathbf{R} \times \mathbf{V} \left(1 + \frac{1}{2}(1 - 3\nu)\frac{V^2}{c^2} + (3 + \nu)\frac{GM}{Rc^2} \right) \tag{5.2.32}$$

From this equation, Damour and Deruelle conclude that the orbits of the Black-Hole and Pulsar in a binary system are plane. Hence, they convert to a polar coordinate system, R and Φ. Damour and Deruelle denote the azimuthal angle by Θ, where I use Φ. Then

$$V^2 = (\frac{dR}{dt})^2 + R^2(\frac{d\Phi}{dt}) \tag{5.2.33}$$

$$|\mathbf{R} \times \mathbf{V}| = R^2\frac{d\Phi}{dt} \tag{5.2.34}$$

$$(NV) = \mathbf{N}$$

$$\mathrm{V} = \frac{dR}{dt} \tag{5.2.35}$$

Finally, the equations of relative motion are obtained from the first integral equations (5.2.26) and (5.2.30). Terms of order higher than $(v/c)^2$ have been neglected. Now, $\mathrm{d}\mathbf{R}/\mathrm{d}t$ has the form

$$\left(\frac{d\mathbf{R}}{dt}\right) = A + \frac{2B}{R} + \frac{C}{R^2} + \frac{D}{R^3} \tag{5.2.36}$$

$$\frac{d\Phi}{dt} = \frac{H}{R^2} + \frac{I}{R^3} \tag{5.2.37}$$

where functional coefficients A through I are polynomials in E and $|\mathbf{J}| = J$, given by

$$A = 2E\left(1 + \frac{3}{2}(3\nu - 1)\frac{E}{c^2}\right) \tag{5.2.38}$$

$$B = GM\left(1 + (7\nu - 6)\frac{E}{c^2}\right) \tag{5.2.39}$$

$$C = -J^2\left(1 + 2(3\nu - 1)\frac{E}{c^2}\right) + (5\nu - 10)\frac{G^2M^2}{c^2} \tag{5.2.40}$$

$$D = (-3\nu + 8)\frac{GMJ^2}{c^2} \tag{5.2.41}$$

$$H = J\left(1 + (3\nu - 1)\frac{E}{c^2}\right) \tag{5.2.42}$$

$$I = (2\nu - 4)\frac{GMJ}{c^2} \tag{5.2.43}$$

Damour and Deruelle proceed to obtain explicit equations for the radial and angular motion of the two bodies. This is not necessary for this project, I have therefore omitted the second integrations.

The sixth chapter of their paper [10] describes the motion of each body explicitly at the first order post-Newtonian approximation level. This could be useful in a future application in a computational model. To implement these equations with a minimum amount of adjustment to the model, the pulsar's motion in the inertial reference frame of the black-hole must be calculated. This would allow us to solve for position of the pulsar as a function of the Kerr coordinate time, as is done in the model at present. The equations would be much more complicated, but as this calculation occurs out of the scope of the actual trajectory calculations, this would not reduce the speed of the code to a point of losing viability. These equations do not consider the rotation of the compact objects, a problem as we consider a rotating pulsar in a binary system with a rotating black-hole.

5.3 3.5 order PPN Equations of Motion

The first order post-Newtonian equations of motion derived in the previous section may be sufficient to describe the motion of black-hole and pulsar in a binary system. However, to be able to identify all signature characteristics of the signal observed, it may be necessary to describe the equations of motion to the maximum possible accuracy. A slight discrepancy in the position of the Black-Hole could have discernable effects on the flux and timing of the signal received by a distant observer, especially when considering photons passing close to the event horizon. At present, the highest degree of accuracy to which the dynamics of a compact binary system have been solved is the 3.5 order post-Newtonian level, that is, accurate to terms of order $(v/c)^7$. The 2006 paper by Luc Blanchet [11] deals with the general relativistic dynamics of compact binaries. It includes a discussion of how he formulated the Hamiltonian for the system, the 3.5PN order equations of motion expressed in the reference frame of the "centre of mass", a determination of the existence of an Innermost Stable Circular Orbit, and a criterion for the stability of stable circular orbits against gravitational perturbation.

In the second section, he derives the equations of motion themselves in a harmonic coordinate system. His starting point for this work is the 3rd order result for the same system, which he derived in 1999 [32]. First denote the following identities:

Orbital separation: $r = |\mathbf{x}|$

Relative velocity: $v^i = v_b^i - v_p^i$

$\mathbf{n} = \frac{\mathbf{x}}{r}$

$\dot{r} = \mathbf{n}.\mathbf{v}$

Total mass: $m = m_b + m_p$

Mass difference: $\delta m = m_b - m_p$

Reduced mass: $\mu = \frac{m_b m_p}{m}$

Symmetric mass ratio: $\nu = \frac{\mu}{m}$

Blanchet obtained the following equations of motion by translating the result for the 3PN accurate equations from reference [32] to the centre of mass frame by imposing $G_i = 0$, where G_i denotes the vector position of the centre of mass. This is analogous to the procedure followed when deriving the 1PN equations of motion in the previous section, where the symmetry of the Lagrangian under Lorentz boosts yields equations (5.2.4) and (5.2.5). In the 3.5PN case, the Lagrangian used is accurate to terms of $(v/c)^7$, and yields a much more

complicated set of equations. These are

$$\frac{dv^i}{dt} = \frac{Gm}{r^2}\left[(1+\Omega)n^i + \Upsilon v^i\right] \tag{5.3.1}$$

The first term represents the Newtonian result. The terms including Ω and Υ represent the post-Newtonian corrections to order $(v/c)^7$. The quantities Ω and Υ are given by

$$\begin{aligned}
\Omega =& \frac{1}{c^2}[-\frac{3\dot{r}^2\nu}{2} + v^2 + 3\nu v^2 - \frac{m}{r}(4+2\nu)] \\
&+ \frac{1}{c^4}[\frac{15\dot{r}^4\nu}{8} - \frac{9\dot{r}^2\nu v^2}{2} + 6\dot{r}^2\nu^2 v^2 + 3\nu v^4 - 4\nu^2 v^4 \\
&+ \frac{m}{r}(-2\dot{r}^2 - 25\dot{r}^2\nu - 2\dot{r}^2\nu^2 - \frac{13\nu v^2}{2} + 2\nu^2 v^2) + \frac{m^2}{r^2}(9 + \frac{87\nu}{4})] \\
&+ \frac{1}{c^5}[-\frac{24\dot{4}\nu v^2}{5}\frac{m}{r} - \frac{136\dot{r}\nu}{15}\frac{m^2}{r^2}] \\
&+ \frac{1}{c^6}[-\frac{35\dot{r}^6\nu}{16} + \frac{175\dot{r}^6\nu^2}{16} - \frac{175\dot{r}^6\nu^3}{16} + \frac{15\dot{r}^4\nu v^2}{2} \\
&- \frac{135\dot{r}^4\nu^2 v^2}{4} + \frac{255\dot{r}^4\nu^3 v^2}{8} - \frac{15\dot{r}^2\nu v^4}{2} + \frac{237\dot{r}^2\nu^2 v^4}{8} \\
&- \frac{45\dot{r}^2\nu^3 v^4}{2} + \frac{11\nu v^6}{4} - \frac{49\nu^2 v^6}{4} + 13\nu^3 v^6 \\
&+ \frac{m}{r}(79\dot{r}^4\nu - \frac{69\dot{r}^4\nu^2}{2} - 30\dot{r}^4\nu^3 - 121\dot{r}^2\nu v^2 + 16\dot{r}^2\nu^2 v^2 \\
&+ 20\dot{r}^2\nu^3 v^2 + \frac{75\nu v^4}{4} + 8\nu^2 v^4 - 10\nu^3 v^4) \\
&+ \frac{m^2}{r^2}(\dot{r}^2 + \frac{32573\dot{r}^2\nu}{168} + \frac{11\dot{r}^2\nu^2}{8} - 7\dot{r}^2\nu^3 + \frac{615\dot{r}^2\nu\pi^2}{64} - \frac{26987\nu v^2}{840} \\
&+ \nu^3 v^2 - \frac{123\nu\pi^2 v^2}{64} - 110\dot{r}^2\nu\ln\left(\frac{r}{r'_0}\right) + 22\nu v^2\ln\left(\frac{r}{r'_0}\right)) \\
&+ \frac{m^3}{r^3}(-16 - \frac{437\nu}{4} - \frac{71\nu^2}{2} + \frac{41\nu\pi^2}{16})] \\
&+ \frac{1}{c^7}[\frac{m}{r}(\frac{366}{35}\nu v^4 + 12\nu^2 v^4 - 114 v^2\nu\dot{r}^2 - 12\nu^2 v^2\dot{r}^2 + 112\nu\dot{r}^4) \\
&+ \frac{m^2}{r^2}(\frac{692}{35}\nu v^2 - \frac{724}{15}v^2\nu^2 + \frac{294}{5}\nu\dot{r}^2 + \frac{376}{5}\nu^2\dot{r}^2) \\
&+ \frac{m^3}{r^3}(\frac{3956}{35}\nu + \frac{184}{5}\nu^2)]
\end{aligned} \tag{5.3.2}$$

$$\begin{aligned}
\Upsilon =& \frac{1}{c^2}[-4\dot{r} + 2\dot{r}\nu] \\
&+ \frac{1}{c^4}[\frac{9\dot{r}^3\nu}{2} 3\dot{r}^3\nu^2 - \frac{15\dot{r}\nu v^2}{2} - 2\dot{r}\nu^2 v^2 + \frac{m}{r}(2\dot{r} + \frac{41\dot{r}\nu}{2} + r\dot{r}\nu^2)] \\
&+ \frac{1}{c^5}[\frac{8\nu v^2}{5}\frac{m}{r} + \frac{24\nu}{5}\frac{m^2}{r^2}] \\
&+ \frac{1}{c^6}[-\frac{45\dot{r}^5\nu}{8} + 15\dot{r}^5\nu^2 + \frac{15\dot{r}^5\nu^3}{4} + 12\dot{r}^3\nu v^2 \\
&- \frac{111\dot{r}^3\nu^2 v^2}{4} - 12\dot{r}^3\nu^3 v^2 - \frac{65\dot{r}\nu v^4}{8} + 19\dot{r}\nu^2 v^4 + 6\dot{r}\nu^3 v^4
\end{aligned} \tag{5.3.3}$$

$$
\begin{aligned}
&+\frac{m}{r}[\frac{329\dot{r}^3\nu}{6}+\frac{59\dot{r}^3\nu^2}{2}+18\dot{r}^3\nu^3-15\dot{r}\nu v^2-27\dot{r}\nu^2v^2-10\dot{r}\nu^3v^2]\\
&+\frac{m^2}{r^2}[-4\dot{r}-\frac{18169\dot{r}\nu}{840}+25\dot{r}\nu^2+8\dot{r}\nu^3-\frac{123\dot{r}\nu\pi^2}{32}+44\dot{r}\nu\ln\left(\frac{r}{r'_0}\right)]]\\
&+\frac{1}{c^7}[\frac{m}{r}[-\frac{626}{35}\nu v^4-\frac{12}{5}\nu^2v^4+\frac{678}{5}\nu v^2\dot{r}^2+\frac{12}{5}\nu^2v^2\dot{r}^2-120\nu\dot{r}^4]\\
&+\frac{m^2}{r^2}[\frac{164}{21}\nu v^2+\frac{148}{5}\nu^2v^2-\frac{82}{3}\nu\dot{r}^2-\frac{848}{15}\nu^2\dot{r}^2]\\
&+\frac{m^3}{r^3}[-\frac{1060}{21}\nu-\frac{104}{5}\nu^2]]
\end{aligned}
$$

Where r'_0 is an arbitrary gauge constant, occuring in the logarithmic terms in the expressions for both Ω and Υ, and which may be removed by a change of variables. However, this change of variables may place constraints on any quantities calculated in this coordinate system, so it is better to retain the original coordinate system. The gauge constant can be selected accordingly.

These equations can be used to simulate physically realistic systems in future numerical models. The use of such large and messy equations may not even inhibit the performance of a massively parallelized code calculating extremely large numbers of photon trajectories. Realistically, it would take a finite amount of time for the photon to traverse the system. Hence this is a static approximation, as the black-hole and pulsar are considered to be stationary throughout calculation of the photon trajectory. Considering the motion of black-hole and pulsar within the trajectory calculations would imply an increase in computational load, as the positions of black hole and pulsar would have to be recalculated at each integration step of the photon's trajectory. Hence the more complicated the equations used to describe the binary motion, the more difficult this would become. Such a complexification would be the final step of developement of the numerical model, and considering the time-scale of a photons traversal through the system, shifts in timing, frequency and polarization of photons would only be expected for geodesics which pass relatively close (within 10 multiples of the event horizon) to the black hole. Analytical work by Rafikov and Lai, [7] discusses the effect of companion motion on the pulsar's signal. A numerical model to account for this effect is still a distant possibility, and requires the succesful construction of a static approximation model.

Ultimately, the approximations could be dropped altogether and the full General Relativistic equations of motion for compact binaries derived using Mathematica. These retarded-integro-differential equations could be used in a computational model such as the one pre-

sented in part II of this thesis, although the ramifications on the computational time might jeopardize the viability of the simulation. The process of incorporating more advanced orbital mechanics into the simulation would thus be an iterative one, starting with the stable circular orbit modelled in this thesis, and moving on to more advanced equations of motion. The results could be compared with each revision of the code, ultimately building up a profile of the effects of orbital dynamics on the pulsar signal.

Part II

A Numerical Model for the Emission of a Pulsar orbiting a Black Hole

Chapter 6

Introduction to Part II

The purpose of the computational model presented in this part of the thesis is to predict the pulse arrival times and the pulse shape of a signal from a binary system consisting of a stellar mass black-hole and a pulsar. The model is designed to explore the effects of the strong gravitational field, such as Shapiro Delay and frame dragging, on the propagation of the pulsar signal. These effects are expected to leave a characteristic trace in the arrival times of the pulsar signal at the observation point.

The present version of the model records the time-binned photon counts and bin-averaged photon timing residuals for a theoretically ideal system. The angular momentum parameter has been varied to generate a parameter set which shows that it may be possible, in principle, to use such results to disentangle the frame-dragging delay from the Shapiro delay. A single CPU was used to produce the data presented in this part of the thesis. In future the code should be executed on a cluster to obtain vastly superior results. In the following chapters, the methodology, assumptions and simplifications necessary to produce the simulation will be described.

In the process of constructing the simulation, many numerical results and graphical outputs were produced which do not relate directly to the black-hole/pulsar binary system, but rather to the behaviour of photons in the vicinity of a black-hole. These results, and the data plots representing them, will be discussed in chapter 11. In the final chapter of this thesis, I will discuss what can be gained from the computational results.

Chapter 7

Assumptions and Simplifications

To proceed, a description of the assumptions and cases considered is necessary. Firstly, this model fires photons from a point source at a specified location in the Kerr spacetime. Although this is not a realistic mechanism of emission for a pulsar, it is a simplification which is necessary to proceed with the construction of a computational model. Secondly, the effect of the curvature and rotation of spacetime in the vicinity of the pulsar on the path of the conical beam has been neglected. This simplification is motivated by two factors; the first of which is a necessity to construct a computational model which begins with the simplest cases, at a later point complexifying as the numerical methods utilized are improved and revised. The second reason is that the spacetime curvature and rotation in the vicinity of the pulsar does not change significantly on the timescale of a single orbit. Although the sum of the precessional effects (geodetic [**?**]; Lense-Thirring [**?**]; Thomas [**?**]) would modify the spin of the pulsar as it orbits the black hole, these effects would only significantly affect the arrival times of pulses on the timescale of several orbits and more. Furthermore, this model has been constructed specifically to probe the very strongly curved spacetime in the vicinity of the black hole. As such, the variation in the pulsar emission as a result of the physical properties of the pulsar itself, can be removed, as the intention is to compare emissions at different pulsar orbital positions within the binary system.

The third simplification to the computational model is the choice of a stable circular orbit for the pulsar. The work reviewed in the chapter entitled "General Relativistic Orbital Mechanics" described the orbital motion of a binary star system comprised of two compact objects. Ultimately, this work must be applied to the computational model, such

around the black hole without perturbing its position, it is a somewhat more difficult problem first to solve for the positions of black hole and pulsar in the centre of mass reference frame, and then transform the results to the Kerr metric. A perfect model would solve for the trajectories of the photons through the spacetime of a kerr black hole which is not stationary for the duration of the photon's flight through the strong gravitational field region. More simply, the trajectories of the photons would depend on the relative positions of both black-hole and pulsar throughout their path from source to detector. Although this discrepancy may be small for black hole more than ten times the mass of its pulsar companion, the slight perturbation in its position from the time of firing of a photon, to its detection may have a discernable affect on which photons actually reach the detector, and the times at which they do. For the model described in this thesis, this effect is ignored as it would greatly increase the computational overhead inherent in the calculation. Analytically, the concept of a moving lens modulating the signal of a pulsar in a binary system has been discussed by Rafikov and Lai [7].

A further simplification made in this model is that of the reduction of the geometry of the system to an ideal case. Theoretically, it is desirable to place the detector on the equatorial plane of the black hole, with the spin vector of the black-hole orthogonal to the orbital plane of the pulsar. Hence, the binary system is edge on ($i = 90°$) with respect to the detector, the equatorial plane of the Kerr metric coincides with the orbital plane of the pulsar. This case would best yield the most information and elucidate the effects of the strong gravitational field on the propagation of photons. It corresponds to the case selected by Wex and Kopeiken, [6], to maximize the effect of frame-dragging on the signal. Difficulty in producing a useful simulation arises in the choice of radial separation between black hole and detector. The solid angle subtended by a realistic detector (on earth) at the position of the black hole, where the binary system is chosen to be at an arbitrary position between the earth and the central bulge of the galaxy, would be far too tiny to select an accurate radial distance for the position of the detector, as well as its size. Hence, a detector has been chosen to be relatively close and subtend a larger solid angle in the sky of the black hole. For this thesis, the number of cores and time constraints on the numerical simulation force the choice of detector which is notably larger and much closer than the theoretical ideal. However, the data representing the arrival time of pulses is valid, in that the detector

has been placed sufficiently far from the black hole, so as to reside within assymptotically flat spacetime. Thus the effects of the presence of the black hole on the propagation of the pulsar beam have already been accounted for to sufficient accuracy, before detection. Photons which have passed close to the black hole are of greatest interest, and, a sufficiently high number of photons must be fired in order to ensure that "scattered" photons contribute a sufficient number of detector hits to contribute useful data to the histogram for a given detector size. The issue is visibilty. An analysis of the flux of scattered pulses may yield insight into the possibility of detecting photons which have essentially passed closest to the black-hole event horizon. Wang et al. [8] have studied the possibility of observing secondary (scattered) pulses from pulsars that orbit non-rotating supermassive black-holes, with the generalization to the rotating case made by Nampalliwar et al. [9]. For the case of stellar mass black-holes, it is expected that scattered pulses would not be sufficiently bright for observation with current technology, although it is possible that, as the pulsar approaches superior conjunction, the luminosity of such pulses would increase sufficiently for detection. My model indicates that edge on systems with maximally rotating black-holes would have an increased chance of detection, with the pulsar's beam compressed towards the equatorial plane by the rotation of the black-hole. As regards to the final choice of detector size, the concept of "post processing" was used to remove the dependancy of numerical results on detector size and location. A Dyson sphere was selected to record the coordinate time, azimuthal and polar angles of photons when they cross a predetermined value of r, the radial coordinate. Once this data has been recorded for a suitable choice of input parameters and initial conditions, another C++ sub-routine was used to process the data, and generate graphical data for any configuration of detector size and location.

With the choice of a system which is edge-on, and with the equatorial plane coincident with the orbital plane, an additional assumption must be stated. A rotating black-hole would be expected to have an accretion disk in the equatorial plane, and consisting of dense matter or plasma. The matter orbits the black-hole in pseudo-circular, stable orbits before plunging in to the event horizon after moving beyond the radial distance of the last stable circular orbit. A pulsar emitting in the equatorial plane of a black-hole, would thus have its signal obscured by the accretion disk as it moves towards the superior conjunction of the orbit, and indeed for a brief period before and after, depending on the size of the disk. This would interfere with the emitted signal. For the purpose of this thesis, the assumption was

made that the black-hole has no accretion disk.

Simplifications made so far improve the performance of the code. Some further assumptions are necessary to constrain the parameter space, as regards the physical parameters of the system being modelled. For example, the model assumes that each gaussian cone of photons, representing an emission at a particular instance in time, is fired in a way so as to mimic the spinning motion of the pulsar. Selecting a relatively long pulsar period is beneficial, since it increases the number of photons which are fired during a single pulsar rotation. This ensures a high density of photons for a conical pulsar emission at any given point in the simulation, thus generating better statistical data for the tiny fraction of photons which are actually scattered by the black hole. For this model to reach a state comparable with analytical predictions or observational data, timing data must be accurately binned in the nano-second range. At present, with only a single CPU, this is not possible as too many bins reduces the number of counts seen when a pulse sweeps past the detector. For results presented in this thesis, 50000 time-bins have been used, for a simulation spanning approximately 25s, implying that although timing of photons is recorded with great precision, the data is recorded with bin-width of 5×10^4s. At least three orders of magnitude better time-binning is necessary to observe deviations of a tenth of a micro-second.

List of simplifications:

- The pulsar is assumed to be a point source.
- The pulsar is assumed to be massless.
- The pulsar travels on a stable circular orbit.
- The orbit is in the equatorial plane of the black-hole.
- Pulses are emitted perpendicular to the spin axis of the pulsar.

Chapter 8

Solving Ordinary Differential Equations

The trajectories of photons we solved using the geodesic equation as described in chapter 4. Hence, photons are fired into the spacetime of a Kerr black-hole by solving the set of four coupled second order ordinary differential equations (4.1.11), (4.1.12), (4.1.13) and (4.1.10) with sufficient accuracy. To perform the calculation, a method for solving differential equations numerically must be used. The method selected is known as an embedded Runge-Kutta-Verner solver. This solver is a numerical predictor-corrector method based on a perturbation theory expansion, correct to 8th order, with 9th order error estimation. A high-order method was selected to avoid numerical instabilities suffered by lower order numerical integrators, of particular importance when a photon approaches the event horizon of a black hole. The cost of using the 8th order solver, as opposed to the more common 4th order Runge-Kutta, is the increase in computational overhead. The increased number of calculations implicit in the higher order method was of serious concern when considering that the simulation requires a large number of photons to produce statistically useful data. A generic 4th/5th order embedded Runge-Kutta was constructed in order to provide a direct comparison, ultimately leading to the selection of a numerical integration algorithm.

Before a direct comparison can be made, a brief comment must be made on the operation of higher (than 4th order) order Runge-Kutta solver methods . Embedded Runge-Kutta methods provide an estimate for the error, in a given integration step, by evaluating the final value using numerical coefficients for 8th (assuming the 8th/9th order method), and then 9th

order expansions, and then observing the difference between the two results. Theoretically, the 9th order final value is more accurate than the 8th order value, the difference between the two forming what is termed the "local truncation error". This error estimate only really describes the amount of truncation error incurred between the 8th and 9th order results. As the order increases, the magnitude of successive terms decreases, and the discrepancy between successive orders tends assymptotically to zero. However, the concept of "diminishing returns" comes into play, whereby the drastic increase in the number of calculations required for each successive order approximation is simply not worth the reduction in the rapidly diminishing truncation error. It is thus implicitly clear that the difference in final values at 4th and 5th order is greater than the difference between 8th and 9th order final values.

At this point it is necessary to consider the concept of adaptive step-size scaling. At the end of each integration step, a set of eight error estimates is calculated, supplying the local truncation error for r, θ, ϕ and t, as well as $\dot{r}$, $\dot{\theta}$, $\dot{\phi}$ and $\dot{t}$. These values are then summed to obtain total error value, which is then compared against an a priori choice of desired error. Thus the quantities described, in the code, as the "errorfactor" and "pre-errorfactor" are generated, and used to scale the step-size such that the error in the next step is pushed towards the desired error value. If the desired error is exceeded by any given step, that step is repeated with a rescaled step-size, proportional to how much excess error was incurred in the previous calculation.

Having established a method by which to scale integration stepsize, it is now possible to compare trajectories as calculated by 8th/9th order, against 4th/5th order. I found that the higher order method performed the trajectory calculations with greater efficiency than the lower order method, despite having 10 more calculation steps to complete, per integration step, per variable. The result is illustrated by the figure below. It is clear that the higher order method requires fewer steps to calculate trajectories to the same accuracy than the lower order method.

With the selection of a Runge-Kutta solver, it is necessary to discuss the method by which initial values for this set of ODE's were generated. The objective was to select a set of initial coordinate parameters, r, θ, ϕ, t, $\dot{r}$, $\dot{\theta}$, $\dot{\phi}$ and $\dot{t}$, for each photon so as to describe the conical beam emission of the pulsar. This is done by a simple algorithm, using three numer-

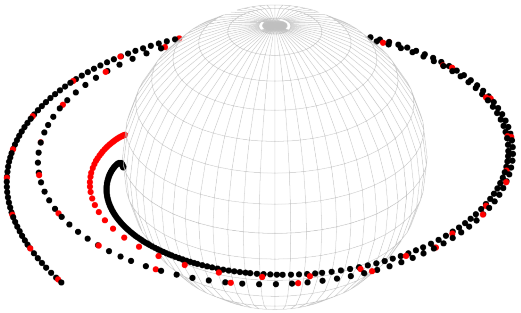

Figure 8.1: Trajectories calculated with 8th/9th order (red) and 4th/5th order (black) Runga- Kutte methods.

ically generated random numbers, in conjunction with several equations. Once the physical parameters have been chosen, i.e. pulsar orbital radius, pulsar period, black hole mass and black hole Kerr parameter, the bounds of the simulation must be defined. These bounds are encoded into parameters which include orbital fraction (the portion of the orbit that the pulsar will traverse during the simulation), initial orbital phase (value of ϕ at t = 0), gaussian width (controlling factor for the angular spread of the pulsar beam), as well as the total number of photons constituting the run. It is important to note the dependence of these secondary parameters on the choices made for the physical parameters. The total

number of photons required to produce good statistical data scales directly with the choice of pulsar orbital radius, as well as pulsar rotational period. Simply put, the further the beam must travel before reaching the black hole, the more photons are required to describe the cone. Similarly, increasing the rotational period of the pulsar requires that the total number of photons be increased proportionally, so as to maintain a constant number of photons per rotation. The choices made for each simulation run will be discussed in chapter 10.

I can now describe the generation of the individual photon initial conditions. This process begins by using the selected parameters to generate necessary physical quantities which are used in selecting initial conditions. Firstly, the orbital radius and orbital fraction are used to calculate the range of initial coordinate time values for photons. This is possible due to the fact that a stable circular orbit for a given orbital radius maintains an angular velocity given by the following equation, from Oscoz et al. [5].

$$\Omega = \frac{d\phi}{dt} = \frac{\sqrt{M}}{r^{\frac{3}{2}} + a\sqrt{M}} \tag{8.0.1}$$

Integrate this equation, with i subscripts denoting initial values and f subscripts denoting final values, obtain the following:

$$\phi_f - \phi_i = (t_f - t_i)\left(\frac{\sqrt{M}}{r^{\frac{3}{2}} + a\sqrt{M}}\right) \tag{8.0.2}$$

The quantity of interest is the final time at which photons are emitted given a particular orbital fraction of the simulation. The symmetry of the system allows for the setting of the initial orbital phase ϕ_i to zero, regardless of where the actual orbit will start and terminate in the simulation. Having obtained t_f, assuming that $t_i = 0$, the range 0 to t_f now spans the entire range of time for which pulsar emissions occur. Multiply t_f by a random number from a flat distribution spanning $[0, 1]$ to obtain a random time of emission for any photon. Given this coordinate time value, it is trivial to substitute this quantity into equation (8.0.2) in order to obtain the orbital phase (ϕ) of the pulsar at the time of emission. This time value is then substituted into the following equation, from [5], to obtain the direction of the centre of the pulsar's conical beam in the local reference frame of the pulsar. The subscript s is

used by Oscoz et al., and denotes the "starting point" for integration of photon trajectories.

$$\alpha_p = \frac{2\pi}{P} t_s - \Omega_s t_s + \alpha_0 \tag{8.0.3}$$

Thus the initial position and direction of a photon may be randomly assigned by a time value "seed". The next step is to translate this direction into components of the four-momentum of the photon, in the coordinate system of the black hole. Were the system being modelled more complex to allow for the pulsar to spin out of the equatorial plane, or to allow for a non-circular orbit, the next step would be to use a transformation of coordinates, given by Chandrasekhar [14], or by Cunningham and Bardeen in the case of an extremally rotating black hole [13]. However, it is important to reduce the number of computations in the simulation to a minimum. For the case of a stable circular orbit, given a pulsar rotating in the equatorial plane of the black hole, it is sufficient to perform a simple calculation to test the bounds of the components of the four-velocity in the inertial reference frame of the black hole. The Kerr metric may be written

$$\begin{aligned}\frac{\mathrm{d}s^2}{\mathrm{d}\lambda^2} = &\left(\frac{r^2 + a^2\cos^2\theta}{r^2 - 2Mr + a^2}\right)\frac{\mathrm{d}r^2}{\mathrm{d}\lambda^2} + \left(r^2 + a^2\cos^2\theta\right)\frac{\mathrm{d}\theta^2}{\mathrm{d}\lambda^2} + \sin^2\theta\left(a^2 + r^2 + \frac{2a^2MR\sin^2\theta}{r^2 + a^2\cos^2\theta}\right)\frac{\mathrm{d}\phi^2}{\mathrm{d}\lambda^2} \\ &- \frac{4aMr\sin^2\theta}{r^2 + a^2\cos^2\theta}\frac{\mathrm{d}\phi}{\mathrm{d}\lambda}\frac{\mathrm{d}t}{\mathrm{d}\lambda} - \left(1 - \frac{2Mr}{r^2 + a^2\cos^2\theta}\right)\frac{\mathrm{d}t^2}{\mathrm{d}\lambda^2}\end{aligned} \tag{8.0.4}$$

Rename the first order derivatives:

$$\begin{aligned}\frac{\mathrm{d}r}{\mathrm{d}\lambda} &= u^1 \\ \frac{\mathrm{d}\theta}{\mathrm{d}\lambda} &= u^2 \\ \frac{\mathrm{d}\phi}{\mathrm{d}\lambda} &= u^3 \\ \frac{\mathrm{d}t}{\mathrm{d}\lambda} &= u^4\end{aligned}$$

Numerical values for these quantities must be found, so as to form initial values for the set of ODEs. First, a choice for the time component u^4 must be made. This determines

the frequency, up to a factor, of the photon being fired at the black hole and should be a function of the pulsar's motion, as implied in the papers by Oscoz et al. [5] and Wang et al. [8]. Since the trajectory through the Kerr spacetime is not a function of the frequency of the photon, and we are not interested in the initial and final frequencies of photons at present, the numerical value $u^4 = 1$ was selected for simplicity. The azimuthal component of the photon four-momentum is the quantity which will effectively control the direction of the pulsar beam in the Kerr spacetime, as the polar component is constrained such that the centre of the beam (primary direction) lies within the equatorial plane, i.e. $u^2 = 0$. Furthermore, the magnitude of the gaussian modification applied to the polar and azimuthal components is scaled so that a narrow cone is formed. This negates the need to be concerned that modifying the polar component may cause it to require a change of sign of the radial component. By setting the radial component, u^1 to zero, the magnitude of the azimuthal component, u^3, corresponding to a direction tangential to the circular orbit of the pulsar, can be obtained by substitution into the above equation (8.0.4). A null geodesic is selected by setting $\mathrm{d}s^2 = 0$. Performing the calculation:

$$\begin{aligned} 0 =& \cancel{\left(\frac{r^2 + a^2\cos^2\theta}{r^2 - 2Mr + a^2}\right)(0)} + \left(r^2 + a^2\cos^2\theta\right)(u^2)^2 + \sin^2\theta\left(a^2 + r^2 + \frac{2a^2MR\sin^2\theta}{r^2 + a^2\cos^2\theta}\right)(u^3)^2 \\ & - \frac{4aMr\sin^2\theta}{r^2 + a^2\cos^2\theta}(u^3)(u^4) - \left(1 - \frac{2Mr}{r^2 + a^2\cos^2\theta}\right)(u^4)^2 \end{aligned} \tag{8.0.5}$$

Finally:

$$\begin{aligned} 0 =& \left[\left(r^2 + a^2\cos^2\theta\right)(u^2)^2 - \left(1 - \frac{2Mr}{r^2 + a^2\cos^2\theta}\right)(u^4)^2\right] \\ & - \left[\frac{4aMr\sin^2\theta}{r^2 + a^2\cos^2\theta}u^4\right](u^3) \\ & + \left[\sin^2\theta\left(a^2 + r^2 + \frac{2a^2MR\sin^2\theta}{r^2 + a^2\cos^2\theta}\right)\right](u^3)^2 \end{aligned} \tag{8.0.6}$$

Apply the quadratic formula in terms of u^3 to obtain the following result:

$$
\begin{aligned}
u^3_{\pm critical} = & \frac{r^2 + a^2\cos^2\theta}{2((r^2+a^2)^2 - (r^2 - 2Mr + a^2)a^2\sin^2\theta)\sin^2\theta} \\
& \Big[\frac{4Mra\sin^2\theta u^4}{r^2 + a^2\cos^2\theta} \pm \Big(\big(\frac{4Mra\sin^2\theta u^4}{r^2 + a^2\cos^2\theta}\big)^2 \\
& - 4\big(\frac{[(r^2+a^2)^2 - (r^2 - 2Mr + a^2)(a^2\sin^2\theta)]\sin^2\theta}{r^2 + a^2\cos^2\theta}\big) \\
& \big([-1 + \frac{2Mr}{r^2 + a^2\cos^2\theta}](u^4)^2 + [r^2 + a^2\cos^2\theta](u^2)^2\big)\Big)^{\frac{1}{2}}\Big]
\end{aligned} \tag{8.0.7}
$$

These quantities represent the largest possible value of the ϕ component of the four-velocity of a photon in the Kerr metric, given a particular orbital radius, Kerr parameter, etc. Multiply the sine of the angle described by equation (8.0.3), by the appropriate value given by the above equations (8.0.7). For photons tangential to the pulsar's orbit, fired in the same direction as the rotation of the black hole, the larger value must be used. For photons fired in the oppposite direction to the spin of the black hole, the smaller value must be used. In this manner, the azimuthal directions of photons in the Kerr metric are determined, with only the calculation of radial component, u^1, remaining. Having already determined the other three first order derivatives, the radial component can be found by using the metric in the form given by (8.0.4). By setting $\mathrm{d}s^2 = 0$ and substituting the values of the other components, as well as the pulsar's orbital radius, the component u^1 can be found. The sign of u^1 must be determined to choose correctly whether the photon initially moves towards, or away from the black hole. Noting that the pulsar emits conical beams in opposite directions, this problem is dealt with by evaluating the reference angle, α as described by equation (8.0.3), such that every second photon has π added to the calculated α_p. The sign of the azimuthal component, u^3, is then calculated by observing the sign of $\sin(\alpha_p)$. If this quantity is positive, u^3 is positive and is calculated by multiplying the larger critical value, as given above (8.0.7), by $\sin(\alpha_p)$. If the sign of $\sin(\alpha_p)$ is negative, the photon is moving in a direction opposite to the rotation of the black hole, hence the smaller critical value given by equation (8.0.7) is used, multiplied once again by $\sin(\alpha_p)$ to obtain the magnitude of the u^3 component in the Kerr spacetime. For both cases, the sign of the radial component, u^1, is determined by observing the sign of $\cos\alpha_p$.

Having constructed a method by which the direction of the centre of the pulsar's beam is calculated for any coordinate time along the pulsar's orbit, the next task is to use this

"primary" direction to generate a conical beam to mimic a pulsar emission. This is done by modifying the quantities u^2 and u^3 by two random numbers of suitable sizes. To produce a beam of the correct conical geometry, a specific pair of coupled pseudo-random numbers must be produced, using a distribution known as a bivariate Gaussian. The first pseudo-random number describes the magnitude of the deviation from the centre of the cone, and is selected from a Gaussian distribution, so as to achieve greatest density in the centre, the second selects a position along a circle which is projected by sweeping the first modification around the initial, unmodified, primary direction. A brief mathematical description is given below, where $R1$ and $R2$ represent the modifications to u^2 and u^3 respectively, ρ and σ represent pseudo-random numbers generated via STL (Standard Template Library) or GSL (Gnu Scientific Library) routines. More specifically, ρ is a pseudo-random number generated from a gaussian distribution, of a specified width which must be scaled according to the size of the system and the desired width of the cone. The number σ is simply a pseudo-random number generated from a flat distribution, of interval $[0:1]$.

$$\rho = gslrangaussian(rng_gen, width)$$

$$\sigma = 2\pi gslranflat(rng_gen, 0.0, 1.0)$$

$$R1 = \rho\cos\sigma$$

$$R2 = \rho\sin\sigma$$

I will now discuss how these pseudorandom numbers were used. Since the primary direction (beam centre) of the conical emission lies within the equatorial plane of the black hole, the polar angular componant u^2 may be modified first, as a small modification in this direction has no chance of changing the sign of the radial component, u^1. Having modified the u^2 component via the quantity $R1$, such that $u^2 \to u^2 + R1$, the modification to the azimuthal component, u^3 may be performed. This modification must be performed with more care, as it is possible for the pulsar's primary direction to be extremely close to the critical value of u^3, as described by (8.0.7). In this case, it is important to observe the change in sign of u^1 which occurs when the additive modification in u^3 exceeds the critical value. As such, an algorithm has been constructed to take, as inputs, the primary beam direction, as well as the modified $u^2 \to u^2 + R1$. This algorithm re-calculates the critical

value of u^3, given that u^2 has become non-zero; the modification to the original u^3 component is then made such that $u^3 \rightarrow u^3 + R2$. The new value of u^3 is then compared with the critical value, and if it is exceeded, the sign of u^1 is changed and component u^3 is then modified by subtracting from the critical value of u^3 the amount by which it was exceeded, thus maintaining the magnitudes of the modifications. Ultimately, once u^2 and u^3 have been modified, and the sign of u^1 determined, the magnitude of u^1 is solved for, as before, by normalizing the photon trajectory to correspond to a null geodesic ($\mathrm{d}s^2 = 0$).

This completes the description of the method by which initial conditions are generated. In the code, these quantities are then parsed to an algorith designed to numerically integrate the trajectories of the photons.

Chapter 9

Shortcomings of the Numerical Model

In this chapter, I look critically at the numerical model I have constructed and discuss its deficiencies, and the problems which affect the quality of its numerical output.

The first issue affecting the ability of the model to produce good output is its dependance on computing resources. The data produced for this thesis was done in a limited amount of time, using only one CPU. As more time, funding and infrastructure becomes available, the code will be able to produce results far superior to those presented here. This problem is common to all computational physics research projects. The remainder of this chapter will discuss the problems specific to this numerical model.

The use of a Runge-Kutta procedure introduces a measure of uncertainty into the results obtained. An adaptive step-size mechanism was developed specifically for the purpose of having strict control over the error implicit in each integration step. Ultimately, a choice must be made regarding an acceptable value for desired error. In programming terms, choosing this value becomes what is known as a "magic number", meaning that it is not calculated, nor based on any physical reasoning. The choice is made simply by trial and error. The only way in which an acceptable choice for this quantity can be made, is by comparing an analytical result with a result generated numerically. Since the arrival time of photons at the detector is of prime importance to the numerical model, it follows that the result which should be scrutinised is that of the propagation time of the photon. Thus, by selecting identical parameters for both analytical calculation and numerical simulation, a measure of the accuracy of the code can be made. An expression for the propagation time

of photons from a source to the minimum radial distance to the black-hole, in the equatorial plane, has been found by Dymnikova [18], given by equation (2.2.1) in this thesis. Of course, the results will only agree to a certain precision, as the numerical methods constitute an approximation of limited accuracy. Tests performed thus far indicate agreement to within 0.01% for photons allowed to within three multiples of the event horizon radius. This agreement improves to 0.001% outside of four multiples of the event horizon radius. When photons move closer to the event horizon, the error in the propagation time increases rapidly. The reason for this disagreement with the analytical result is probably not a problem with the algorithm itself, but rather a fact of machine precision. Photons which are fired within the equatorial plane should remain in that plane. In the numerical model, they deviate from the plane by an extremely small deviation. This is due to numerical uncertainty, and I must note that the use of conserved quantities to describe the photon trajectories may have assisted in alleviating this problem. When the photon gets very close to the event horizon, an oscillation has been observed, whereby the photon oscillates by a tiny amount about the polar angle $\theta = \pi/2$. Within three multiples of the event horizon this effect becomes substantially more pronounced, with the out-of-plane propagation of the photon contributing an additional value to the propagation time. Hence, this deviation from the analytical comparison can be considered a result of the numerical approximation, but not necessarily a source of large numerical uncertainity. It is possible that setting more stringent numerical error constraints, i.e. smaller desired error would reduce the magnitude of this effect, but it is also possible to re-run the calculations with an extra constraint by setting the θ component out of the equatorial plane to zero. Alternatively, timing data for photons passing too close to the event horizon could be excluded. Furthermore, a more complex analytical test of accuracy could be used to test propagation times for photons out of the equatorial plane. Chandrasekhar's integral [14] could be used for this purpose.

The most notable shortcoming of this computational model arises because of the need to contract the components of the photon four-momentum correctly. This must be done to guarantee that they fall upon null geodesics. A superior method is that in which all four components of the photon four-momentum are calculated in the local reference frame of the pulsar, and then projected via a non-trivial coordinate transformation onto the Kerr Metric. However, due to the calculational intensity of these transformations, coupled with the

need to be able to fire as many photons as possible to produce useful data, this method has been avoided, resulting in a numerical deficiency. This deficiency occurs for conical emissions approaching tangents to the circular orbit of the pulsar. Tangential photons exhibit a vanishingly small radial four-momentum component (u^1), which coupled to the fact that photons are normalized via calculating u^1 such that $\mathrm{d}s^2 = 0$, causes a numerical precision error, whereby photon directions cannot be modified close enough to the perfect tangent vector. Thus, "tangential" cones, which trivially do not interact with the spacetime in the vicinity of the black hole, have a decreased density of photons along the conical axis. This discrepancy is predictable, as a tangential beam direction is encountered once per pulsar rotation, thus implying a predictability in the missed counts that will be observed at distant detectors. Although this problem can be solved, I felt it was unnecessary to spend too much time to such an endeavour. This problem generates an error which does not contribute to the bulk of the results of interest. Nevertheless, this problem should be addressed in future versions of the code.

Chapter 10

Simulation Parameters

Having described the construction of the numerical model, a choice must now be made for the physical parameters of the simulations. The system considered has already been restricted to an ideal case. Due to the limited resources available for the simulation, very specific choices must be made for the physical parameters. Furthermore, it is possible to gain more undestanding of the system by varying the length of time (coordinate time) of each simulation, and by focusing on the most interesting aspects. For example, a run can be set up to simulate 1/16th of a full pulsar orbit around the black hole. This simulation will involve a pre-determined number of photons, and hence a specific number of photons per pulsar rotation. This will generate output of a particular resolution, limited by the fact that the number of photons per rotation may not be sufficiently high to capture all of the desired detail. It is then possible to isolate a specific portion of the original $\frac{1}{16}$th orbit, possibly even just a single rotation thereof, and evaluate that part of the orbit with a far higher number of photons per rotation. Numerically, the start and end points of the simulation can be adjusted to do exactly this, the idea being to use a much greater number of photons to generate more detailed output, particularly when the pulsar reaches the superior conjunction with respect to the detector. Thus a multi-layered simulation is ideal, since by exploiting the symmetry of the system, the selection of many localized detectors in the sky of the black hole allows a full orbit to be simulated by a small portion of a simulated orbit, thus generating a pulse timing histogram which details the behaviour of the pulses received by a distant, stationary observer, as the pulsar orbits the black hole. Finer detail can be added by re-running a much smaller fraction of the simulation while mainitaining all physical parameters, yielding a much better description of what a detector would see at the

superior conjunction.

A brief mention of the detectors was made above. I will now discuss this point in more detail. Attempting to simulate an entire pulsar orbit would require a large number of processor hours. Selecting the ideal case of a stable, circular, equatorial orbit makes it possible to generate the data for a whole orbit by simulating only a small fraction thereof, but having many detectors placed at different locations on the Dyson sphere encapsulating the system. The ideal location for an observer is on the equatorial plane of the black hole, at a sufficiently large distance from the black-hole for the space in the vicinity to be considered "assymptotically flat". Firstly, a size must be chosen for the detector. For the purposes of this thesis, it is reasonable to select a detector which is substantially larger than the solid angle subtended by the earth in the sky of the black hole, but which collects useful arrival time data. At present, detectors have been placed at equatorial positions in the black hole sky, with centres at phase angles of multiples of $\pi/4$. Hence, a total of 8 detectors capture arrival time data for photons, and produce a histogram unique to their location. This enables the code to generate data describing the behaviour of the signal received by observers at different azimuthal locations. Numerically this is performed simultaneously via 8 conditional photon capture statements. The symmetry of the Kerr metric then allows for the analyses of these histograms such that timing data is essentially equivalent to allowing the simulation to run over an entire pulsar orbit, with just a single detector at a selected position. Of course, this may not be necessary for all parameter sets, as it may be sucient to simply generate a single set of data of this nature, and observe the behaviour of the signal for an entire orbit; then assume that the same trends would be expected for all possible data sets of equivalent scale. Due to the fact that detectors capture data by means of conditional tests of output data, limiting the number of if statements to a minimum is necessary for the code to operate at the desired speeds. Furthermore, selecting a single detector, placed such that the pulsar reaches the superior conjunction halfway through the portion of the orbit simulated, presents a method for observing the behaviour of pulses travelling through the most rapidly rotating and highly curved spacetime only, allowing for much more detailed histogram data. It is thus clear that for each set of physical parameters to be simulated, several different simulations can be run, the composition which will comprise a detailed description of the entire system.

The selection of physical parameters for simulation runs must now be discussed. Although the aims of this project were originally specific to the case of a stellar mass black hole with a pulsar companion, the numerical code does not experience any sort of slow-down with respect to an increase in the mass of the black-hole, largely due to the intelligence of the adaptive step-size adjusting sub-routine. Furthermore, as mentioned by Wang et al., [8], the size of the pulsar's orbit, in terms of multiples of the black-hole mass, can be very small for a supermassive black-hole, allowing for dense pulses of photons moving past the event horizon without scaling the number of photons up. The interaction between the pulsar's conical beam and a supermassive black hole may yield distinct different results, as the scale of the pulsar's beam with respect to the size of the event horizon would be vastly different when compared to the stellar mass case. Hence it would be intersting to generate a set of results for the case of a pulsar orbiting (in close proximity) a supermassive black-hole, even though it is not feasible to measure any signal from the galactic centre with great accuracy due to the interference ineherent at the galactic hub. My model is ideal for simulation of such cases, as the relatively small orbital radius of the system would allow for very high photon density as pulses sweep across the event horizon. The assumption of a stationary black-hole also makes more sense, as the pulsar would be of negligible mass when compared with a supermassive black-hole. It is, however, far more likely that a pulsar orbiting a supermassive black hole at relatively small orbital separation ($r_{orbit} \leq 10000 M_{black-hole}$) would assume an eccentric orbit, with the pulsar possibly achieving relativistic velocities. For the purposes of this thesis, a stable circular orbit is sufficient. Complexification to an elliptical orbit must be done at a later point, when more computational resources are available. I was not able to run the code for a pulsar orbiting a supermassive black-hole. Running such simulations would require a simple adjustment of several physical parameters within the code. This will be done at a later stage.

Returning to the selection of physical parameters of simulations presented in chapter 11, Table 10.1 describes the parameter set generated. The pulsar's period was set to a very slow $10s$ rotation, much slower than would be necessary to describe a realistic system. This simplification was forced to ensure sufficient photon density for each rotation so as to observe a reasonable number of scattered photons. Once the code is run on a cluster, an increase in photon density of several orders of magnitude is possible, parameters can be selected to represent more realistic systems, as described by Lipunov et al., [3].

Table 10.1: Parameter space of simulations run on a single machine.

Black-hole Mass ($M_\odot$)	Kerr parameter	Orbital Separation (M_{BH})	Pulsar Period (ms)
30	0.000	20000	10000
30	±0.250	20000	10000
30	±0.500	20000	10000
30	±0.999	20000	10000

Table 10.2: Parameter space proposed for future simulations.

Black-hole Mass ($M_\odot$)	Kerr parameter	Orbital Separation (M_{BH})	Pulsar Period (ms)
30/100	0.000	50000/100000/200000	1/100
30/100	±0.100	50000/100000/200000	1/100
30/100	±0.200	50000/100000/200000	1/100
30/100	±0.300	50000/100000/200000	1/100
30/100	±0.400	50000/100000/200000	1/100
30/100	±0.500	50000/100000/200000	1/100
30/100	±0.600	50000/100000/200000	1/100
30/100	±0.700	50000/100000/200000	1/100
30/100	±0.800	50000/100000/200000	1/100
30/100	±0.900	50000/100000/200000	1/100
30/100	±0.999	50000/100000/200000	1/100
1e6/1e9	0.000	100/1000/10000	1/100
1e6/1e9	±0.100	100/1000/10000	1/100
1e6/1e9	±0.200	100/1000/10000	1/100
1e6/1e9	±0.300	100/1000/10000	1/100
1e6/1e9	±0.400	100/1000/10000	1/100
1e6/1e9	±0.500	100/1000/10000	1/100
1e6/1e9	±0.600	100/1000/10000	1/100
1e6/1e9	±0.700	100/1000/10000	1/100
1e6/1e9	±0.800	100/1000/10000	1/100
1e6/1e9	±0.900	100/1000/10000	1/100
1e6/1e9	±0.999	100/1000/10000	1/100

Chapter 11

Simulation Results and Interpretations

The results presented in this chapter have been generated with a preliminary version of the code. This version has been optimized to run on a single CPU with four cores and eight virtual processing threads. All output generated thus far represents only preliminary results that indicate how the code can generate physically useful results, i.e a proof of principle. For superior data, the code will be run on a much larger scale using, firstly, the computing cluster at the University of Johannesburg, and subsequently the South African National Grid (via Dr.Bruce Becker and Mr.Warren Carlson). The code is currently being finalised for use on this scale. Despite the limited computing resources used to generate the output presented in this chapter, the effects of the black hole on the propagation times of photons were clearly discernable. The systems simulated were constructed as a set of ideal cases, and would not represent realistic black-hole/pulsar binary systems. They were constructed to maximise the magnitude of the strong gravitational field effects on the pulsar's signal, as well as to maximise the ability of the present version of the numerical application to produce useful output. The simulation produces several types of data which are useful to gain an understanding of the effects of highly curved, rapidly rotating spacetime. This consists of: single and multiple photon trajectory plots; Dyson sphere captured scatter plots; scatter projections (Hammer plots); detector specific pulse arrival histograms with corresponding bin averageed photon propagation time residuals and event-horizon strike plots.

I have plotted the trajectories of photons as they travel through the vicinity of a black-hole. Plots have been generated to illustrate how altering the mass and angular momentum of the black hole affects the trajectories of photons propagation. This has been achieved

by setting the coordinate time-range of the simulation to a vanishingly small quantity, essentially selecting the emission of the pulsar at a particular moment in time, and thus, the centre of the beam is confined to a distinct direction. The source is placed at a constant radial distance from the black hole, an initial direction is then chosen and the photon is fired into the Kerr spacetime, it's trajectory plotted for differing values of black hole mass and angular momentum.

The first cases presented are those of photons which are fired within the equatorial plane of the Kerr geometry. Confining the initial conditions of a photon to the equatorial plane is a necessary and sufficient condition for the photons to remain within it. An interesting exercise illustrates the effect of increasing the Kerr parameter of the black hole on the motion of a single photon. The nearest approach to the black-hole event horizon of a photon in the equatorial plane was plotted via trial and error. The angle in the local reference frame of the pulsar, between the initial photon direction and a radial unit vector was recorded and compared for different values of "a". Since each simulation of this nature entails only the integration of the geodesic equations for a single photon, it is possible to force an extremely tiny error without losing viability. A value of 10^{-12} was selected for this purpose, although a maximum integration step limit of 30000 was enforced, to prevent the photon from being stuck in a loop of diminishing returns at a small distance from the event horizon in the case of it being captured by the black-hole. The maximum proximity for corotating and contra-rotating photons were considered. Select an orbital radius of $r_{pulsar} = 20000M_{BH}$ for the pulsar, where $M_{BH} = 30M_{\odot}$. The following figures are plots of "nearest miss" photons, The cyan filled circle centered at the origin represents the event horizon of the black hole. The photon is incident from the bottom left of the image, line colour represents its frequency (to a factor) as it falls in towards the black hole. The number of rotations of each photon, and the magnitude of the angle between the photon's initial direction and a radial unit vector at the pulsar are stated in each image caption.

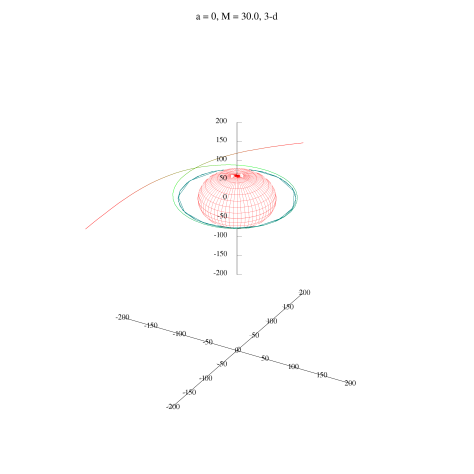

Figure 11.1: Rotations about black hole = 4.641330722760045347612123389 78. Magnitude of local reference frame angle between radial unit vector and initial direction of propagation = 2.5979461082499953508 6e-4 rad. Case: a = 0

The non-rotating case presented on the left can be used to calculate the solid angle subtended by the event horizon of black hole, as viewed by the pulsar. This is due to the spherical symmetry of the Schwarzschild metric. This calculation becomes considerably more difficult when the Kerr parameter deviates from zero, as the spherical symmetry is broken by the rotation of the black hole.

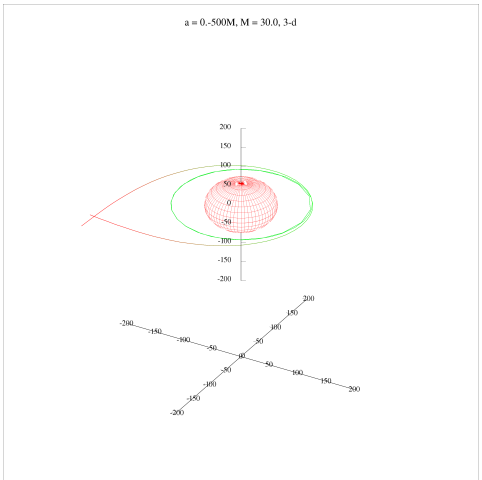

Figure 11.2: Rotations about black hole = 3.28243456888529956216697669458. Contrarotating case. Magnitude of local reference frame angle between radial unit vector and initial direction of propagation = 3.0688992202626969938 0e-4 rad. Case: a = 0.5M

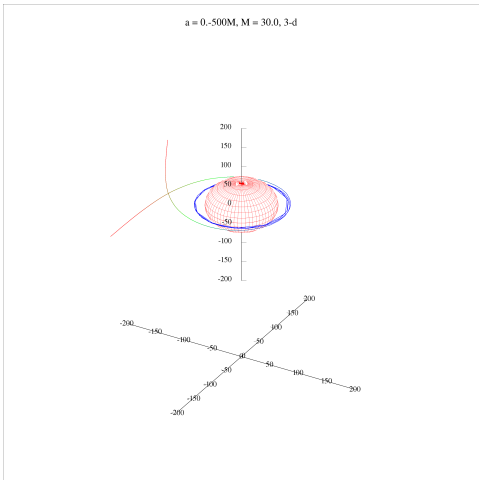

Figure 11.3: Rotations about black hole = 5.42614892392993316888247234964. Corotating case. Magnitude of local reference frame angle between radial unit vector and initial direction of propagation = 2.0480557386018504036 9e-4 rad. Case: a = -0.5M

These results illustrate the effect of rotation on the ability of the black-hole to capture photons. Theoretically, the event horizon radius decreases by a small amount as the black hole begins to rotate. From the point of view of the pulsar source, the rotation causes an increase in effective horizon size in the contrarotating case, and a decrease in the corotating case. We can infer this by observing the magnitude of the angle of minimun approach given in the above figures, and comparing the rotating cases with the non-rotating case. This angle was 18.127901519% larger than the non-rotating value for a contrarotating photon; the photon then orbited the black hole 3.282 times before escaping to infinity, a decrease from 4.641 rotations for the Scwarzschild black hole. For the corotating photon the angle was decreased by 21.166350137% with respect to the non-rotating case and the number of rotations performed was increased to 5.426 as the photon was "helped around" the black hole by the rotation of spacetime. The overall affect of this phenomenon is that the angle which subtends the event horizon in the equatorial plane of a black-hole is shifted by a notable percentage (20% of the non-rotating case for this particular set of parameters)

towards the contrarotating side of the black hole. Another interesting point is that of the amount of time which a photon may spend performing these very-near to circular orbits around the black hole. If a black-hole is placed in an environment within a galaxy, implying the incidence of photons from all possible directions, the finite amount of time which a tiny fraction of photons spends orbiting the black hole may give rise to a field of temporarily captured photons around a characteristic radius distinct to the physical parameters of the black-hole. The energy contained in this field of photons could also give rise to, or simply contribute to the existence certain quantum effects, such as particle creation and destruction, forming Hawking radiation near the event horizon of the black hole. Similar numerical simulations out of the equatorial plane would be necessary to ascertain what shape this "field" could form around the event horizon. Between the outer pseudo-stable circular orbits for a contra-rotating case, and the corresponding inner orbits for the corotating case, the deviation from a spherical shape for the Schwarzschild case could be observed with incremental increase in black hole angular momentum. The difference in radial size between contra-rotating and corotating pseudo-circular photon orbits is indicated clearly by the colour of the lines. Corotating photons, which reach their innermost point exhibiting a blue colour have fallen much closer to the black-hole and have been blue-shifted substantially more by the gravitational potential. The contra-rotating photons orbit further away from the black-hole, and exhibit a green colour. If the contra-rotating photon does spiral into the event horizon, it is interesting to note that its direction of travel around the black-hole is completely reversed as it reaches the static limit and is forced to reverse its direction (see Figure 11.7).

While these results are interesting, the truly chaotic orbits which photons may assume in the vicinity of a rotating black hole are those which move out of the equatorial plane of the Kerr geometry. The initial phases of the construction of the numerical model included a fortran simulation which was only sufficiently powerful to simulate the pulse arrival times in the equatorial plane, with the entire system, including the detector forming part of a $2+1$ dimensional plane. Although this model could have provided intersting results in its own right, it was deemed insufficient, as future versions of the code would be required to model realistic pulsar beams which do not have their beam axis constrained to the equatorial plane. To illustrate the effect on a beam of photons fired towards the black-hole, I have produced several plots of thirty photons. The photons were fired towards the black hole, with the polar and azimuthal components of the photon four-momentum randomized as discussed in

chapter 8, so as to produce 30 arbitrary photon orbits in the near vicinity of the black hole. For this purpose, the error tolerance of the simulation was set to the default value of $1.0e-9$. The relaxed error constraint causes a slightly more jagged appearance for the photon trajectories, as gnuplot must essentially "connect the dots" between wider spaced data points. The images below consist of three different points of view of the same 30 photons moving through the immediate vicinity of a 30 solar mass black hole, for a non-rotating case, and the case $a = 0.500M$. The modifications to the photon trajectories to form random orbits were sufficiently small for the majority of photons to hit the event horizon. Once again, the colour of the lines indicate the magnitude of the temporal component of the photon four-momentum. This illustrates the gravitational blueshift of incident photons, as well as the subsquent redshift of those which do not hit the event horizon, and move off to infinity.

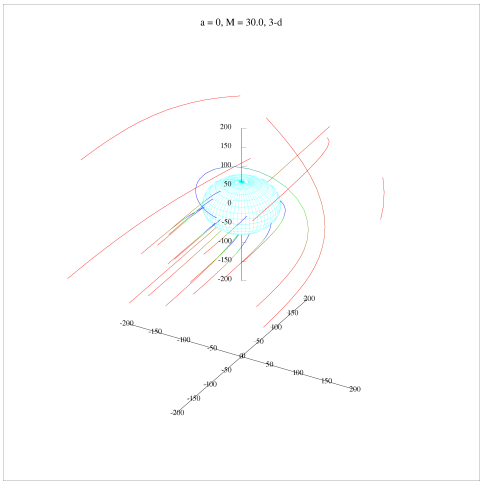

Figure 11.4: Three dimensional view. Case a = 0.

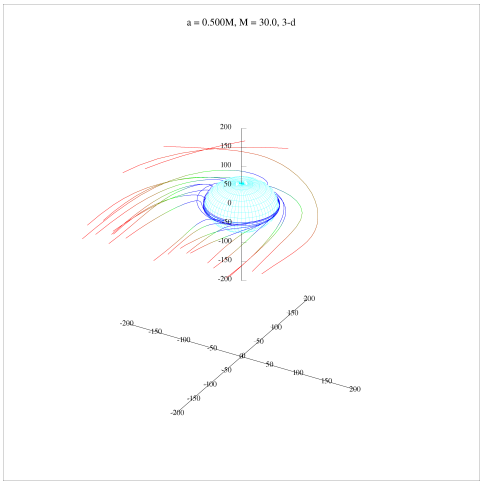

Figure 11.5: Three dimensional view. Case a = 0.500M.

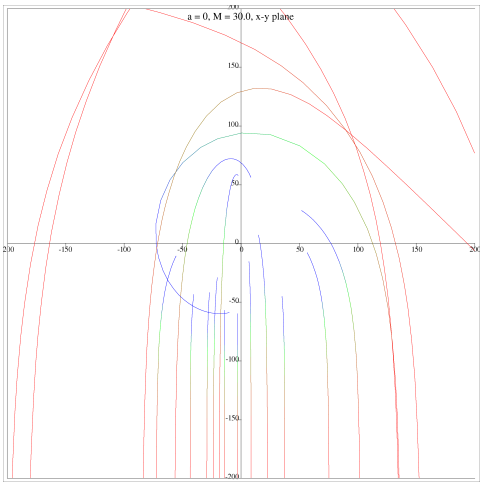

Figure 11.6: View of the x-y plane, looking down onto the black hole. Case a = 0.

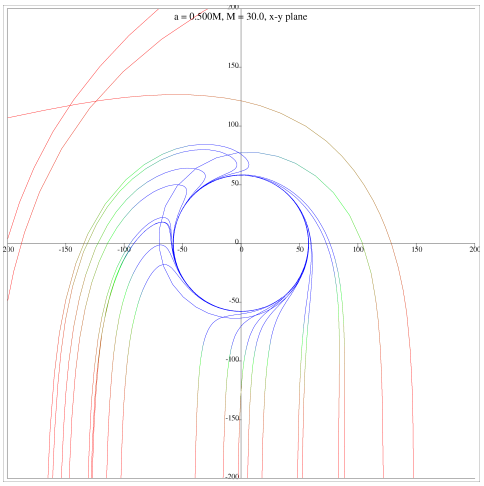

Figure 11.7: View of the x-y plane, looking down onto the black hole. Case a = 0.500M.

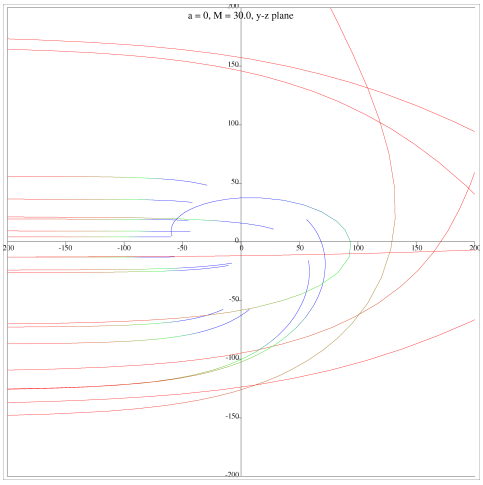

Figure 11.8: View of the y-z plane, the beam is incident from the left of the image. Case a = 0.

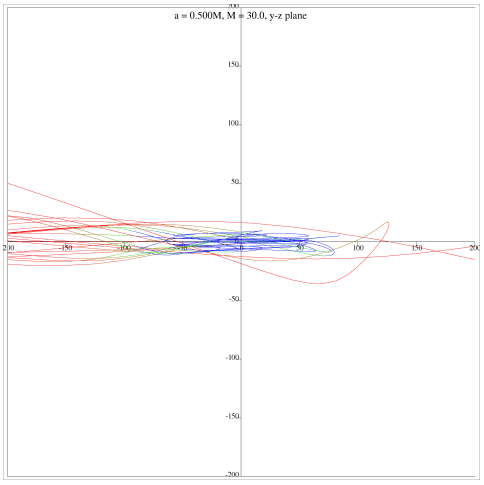

Figure 11.9: View of the y-z plane, the beam is incident from the left of the image. Case a = 0.500M.

These images provide an iteresting look at how the photons move very near to the black-hole. Most notably, increasing the rotational parameter forces incident photons much closer to the equatorial plane as they move towards the black-hole. I intended to provide trajec-

tory plots for conical emissions of up to 100000 photons fired in a beam similar to the above setup. Such images provide insight into how the photons are scattered by the black-hole, and interesting features forming within the spacetime as a result. However, I do not presently have computing resources capable of producing these plots. I have stored several older images generated for this purpose. Once new computing resources have been secured, these types of plots can be produced.

The production of very large numbers of photons for recording statistical data, such as timing residual and histogram plots was achieved by eliminating the need to store each integration point of each photon trajectory as data. The data was captured by placing a Dyson sphere at a radius of two orders of magnitude larger than the pulsar's orbital radius about the black-hole. The integration step-size was adjusted in the vicinity of the Dyson sphere, so that the final step integrates the photon trajectory to terminate within a specified tolerance of the Dyson sphere radius. This tolerance was chosen to be 0.01 units, as it is important to measure the photon propagation time to this point with great accuracy. To put this value in context, the simulation runs for histogram and residual data were performed for a black-hole of thirty solar masses, with a pulsar orbiting at a radius of 6×10^5. The parameters of quasi-coalescent binary systems have been discussed in the model by Oscoz et al. [5]. These systems may have orbital seperations as small as $r_s = 200M_{BH}$, before the pulsar spirals in and coalesces with the black-hole. Their work also describes a "detached" binary system consisting of a pulsar and a black-hole of mass $10M_{\odot}$, with orbital separation of $r_s = 2 \times 10^5 M_{BH}$. This is an order of magnitude larger than the system simulated. More computational power would allow for useful results to be generated for realistic detached binary systems. The photon density produced by my CPU was not sufficient to gain useful data on this scale, hence requiring the selection of a relatively small orbital radius.

Before discussing histogram outputs, we must observe the manner in which large numbers of photons are scattered by the black-hole, as the pulsar spins along its orbit. For this purpose, simulations of varying photon number and pulsar orbital radius have been produced to illustrate the scattering effect of black-holes on the pulsar's beam. Unfortunately, due to present computational restrictions they cannot be incorporated into this document. For this reason, I have stored data in a repository for potential future publications. Returning to a verbal descriptions of the nature of the results, it has become evident that a rotating

black hole scatters the conical beam of a nearby pulsar in a predictable fashion. As the beam sweeps across the black-hole, the scattering pattern varies with the Kerr parameter. If the pulsar was isolated, the scatter of its radio-frequency emissions as it rotates forms a highly predictable band in the sky. The earth must fall within this band of emission for the pulsar to be visible. However, as the beam sweeps across a rotating black hole, photons are scattered and may form sub-dominant pulses [8], of lower flux when compared with the primary beam emissions of the pulsar. If the earth falls within the scattered emission band, but not the primary emission band, for a sufficiently bright and nearby black-hole/pulsar binary system, it may be possible to detect only the scattered pulses. This would present an interesting transient system whereby the black-hole itself would appear to be a weak pulsar, with the flux of pulses received increasing as the pulsar moves towards the superior conjunction with respect to the earth. This is similar to the concept of sub-dominant pulses being detected from a pulsar orbiting a supermassive black-hole, as discussed by Wang et al. [8] and Nampalliwar et al. [9].

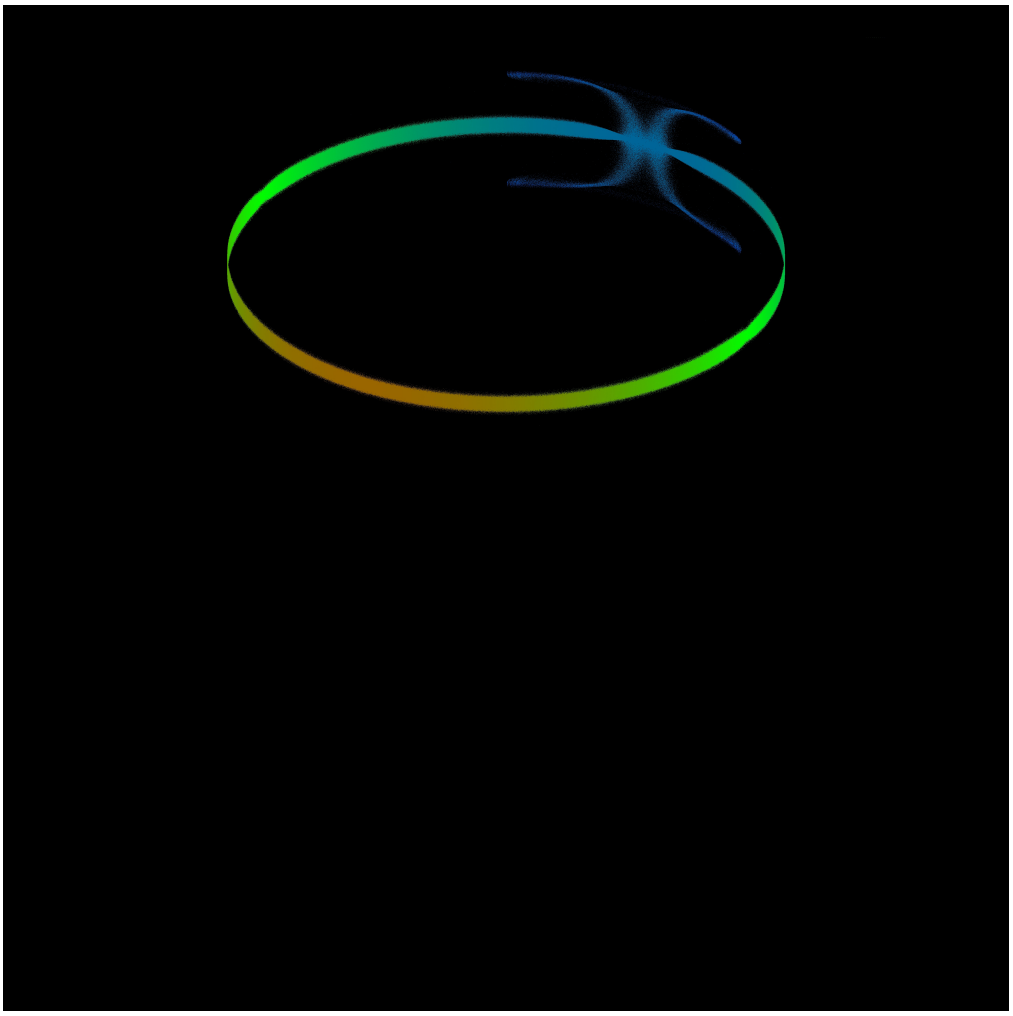

Figure 11.10: This scatter image was produced by simulating 12.5 million photons, similar to the production runs generating histogram and residual data, but with a significantly wider pulsar beam. The pulsar moved through $\frac{1}{128}$ of an orbit; with a very slow 10s rotational period. The scattering pattern behind the black-hole gives rise to a band of scattered emissions. The black-hole was rotating slowly ($a \approx 1/30M$). Plot cannot be cropped with current machine.

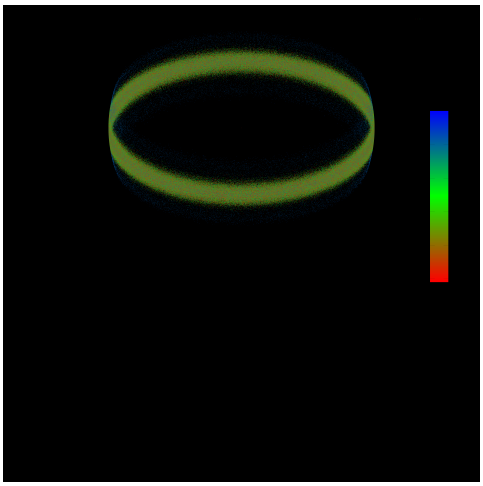

Figure 11.11: Plot of all photon strikes at a Dyson Sphere. Pulsar was allowed to complete a full orbit, with a wide beam, 1 million photons present. Blue dots above/below the dense band indicate scattered emissions. The black-hole was rotating slowly ($a \approx 1/30M$).

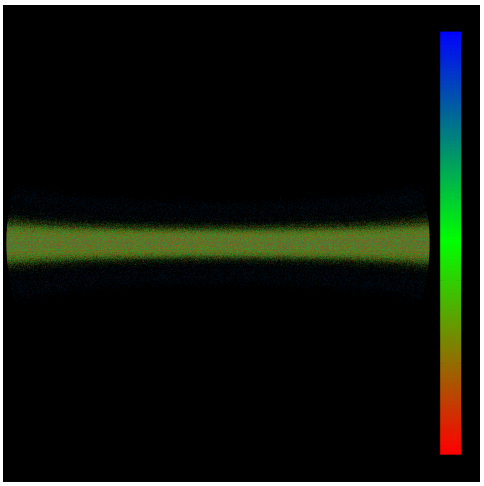

Figure 11.12: Corresponding Hammer projection plot of all photon strikes at a Dyson Sphere. System properties: $M_{BH} = 10M_{Solar}$; $a = 0.999M$; $r_s = 1e4M_{BH}$. Plots cannot be cropped with current machine. The black-hole was rotating slowly ($a \approx 1/30M$).

I can now discuss the statistical results generated by the largest, most complete simulation runs. These production runs took approximately eight hours to complete 12.5 million photon trajectories using my original Core-i7 CPU. Results were produced fastest with 23 worker threads and a single distributor thread after simple comparitive tests running different Open-MPI configurations. I intended to include the scatter and hammer plots for each simulation, however, computational resources do not allow for this contingency. Below I present the histogram and timing residual data generated by placing eight detectors, with centres in the equatorial plane, as described in chapter 10. I must discuss the method of capture of this statistical output beforehand.

The range of time for which detectors may receive signals from the pulsar needs to be divided into a suitably large number of bins, in order to represent the nature of the pulses with sufficient resolution. Preliminary configuration simulations were run with a small fraction of the photons to record the earliest possible time of detection at any of the

detectors, as well as the latest possible time of detection. This allows for a choice of time range for the time-binning subroutine. A total of 50000 time bins were selected subsequent to a process of trial and error to yield reasonable pulse shapes, without reducing counts per bin to an unacceptably small number. Residual timing data was produced by subtraction of the propagation time of photons through flat spacetime from the propagation time through the Kerr metric . This simply yields a number for each photon, and so, a method must be used to generate useful graphs which correspond to the histogram plots. I did this by averaging timing residual results for each time-bin. Firstly, the code must ascertain whether a photon has struck one of the detectors. This is determined by setting a detector centre at a particular rotation in the Hammer-projection of the black-hole sky. The Hammer projection maps the azimuthal and polar angles of the black-hole sky to a two-dimensional plane in such a way as to preserve the area element. This implies that selecting a certain value for the area of a detector in the Hammer projection, allows for the possibility of moving the detector around to different locations in the projection, while maintaining that the area at each different detector location in the original parameter space is identical. To obtain the Hammer projection values for the coordinates of each photon as it strikes the Dyson sphere, several transformations/normalizations must take place. Firstly, the polar coordinate in the Kerr spacetime is measured from the "North" pole downwards, with the equatorial plane taking a value of $\theta = \pi/2$. This must be transformed such that the equatorial plane takes a value of $\theta = 0$, and the poles $\pm\pi/2$. This is performed by a case-wise algorithm, if $\theta \leq \frac{\pi}{2}$, $\theta \rightarrow \frac{\pi}{2} - \theta$ and if $\theta \geq \frac{\pi}{2}$, $\theta \rightarrow -(\theta - \frac{\pi}{2})$. The azimuthal coordinate of the Kerr geometry needs to be normalized, as for a correct hammer projection, this angle must fall within the range $-\pi : \pi$. This is accomplished by a simple angular normalization procedure, given by $\phi \rightarrow ((\phi+\pi)\ mod\ \pi)-\pi$. The projection to a Hammer plot is then achieved by the following equations, where x and y are the Hammer coordinates and z is the intermediate variable used in their calculation. Note that this projection is only used for azimuthal coordinates at the Dyson sphere, in asymptotically at spacetime.

$$z = \sqrt{1 + \cos\theta * \cos(\frac{\phi}{2})} \tag{11.0.4}$$

$$x = \frac{\cos\theta \sin(\frac{\phi}{2})}{z} \tag{11.0.5}$$

$$y = \frac{\sin\theta}{z} \tag{11.0.6}$$

Thus photons are assigned an x and y Hammer coordinate value, which are then compared with each detector area on the Hammer plane. If a photon is designated as having struck a detector, the detector number is recorded, along with the residual time value for the photon and the time bin into which it fell. This information is then sent back to the distributor process, where the detector number determines to which histogram data array the count is added for the assigned time bin. The array storing the timing residual data then has the photon's residual value added to the bin corresponding to the time bin. Once all photon trajectories have been completed, a loop averages the timing residual information in each bin by dividing it by the number of counts obtained for bin. In this way, an average timing residual can be plotted as a histogram correlating with the photon count histogram. This yields valuable information, as it may indicate the nature in which the black-hole increases propagation times of photons that move through its vicinity. Increased propagation times also indicate a greater degree of scattering, and a reduction in photon flux for time-bins of high photon residuals can be expected. Plots of the detector strikes indicate a problem with this normalization for a detector placed at $\phi = \pi$. The pulsar is selected to complete $\frac{1}{128}$ of an orbit, with the centre of this orbital fraction at $\phi = \frac{3\pi}{2}$. Hence, the directions of the pulsar beam tangent to the circular orbit point towards $\phi = \pi$ and $\phi = 2\pi$ and these detectors experience an aberration in the number of counts received as a result. The detectors important to this analysis are those placed at $\phi = \frac{\pi}{2}$(superior conjunction) and $\phi = \frac{3\pi}{2}$ (inferior conjunction). This completes the description the system, it is now possible to present the output obtained from a series of simulation runs, each comprised of 12.5 million photons. The first data presented are the scatter and horizon strike plots for the cases $a = 0$; $a = 0.250M$; $a = 0.500M$; $a = 0.720M$ and $a = 0.998M$. The horizon strike plots illustrate how increasing the rotational parameter of the Kerr black-hole forces photons incident from a distant source towards the equatorial plane. For the extremal case of $a = 0.998M$, photons have struck the event horizon within a vanishingly small distance from the equatorial plane. This is an interesting result, and may explain why the centre of the galaxy produces a large amount of radio-frequency interference, perhaps the result of photons being scattered preferentially into the galactic disk, relatively close to the equatorial plane of the inferred supermassive black-hole present within there. Whether these photons impart any angular momentum to particles within the galactic disk may pose an interesting

question. Returning to the discussion of results, only the positive values of a are presented, as the direction of rotation is unimportant for the purpose of these images.

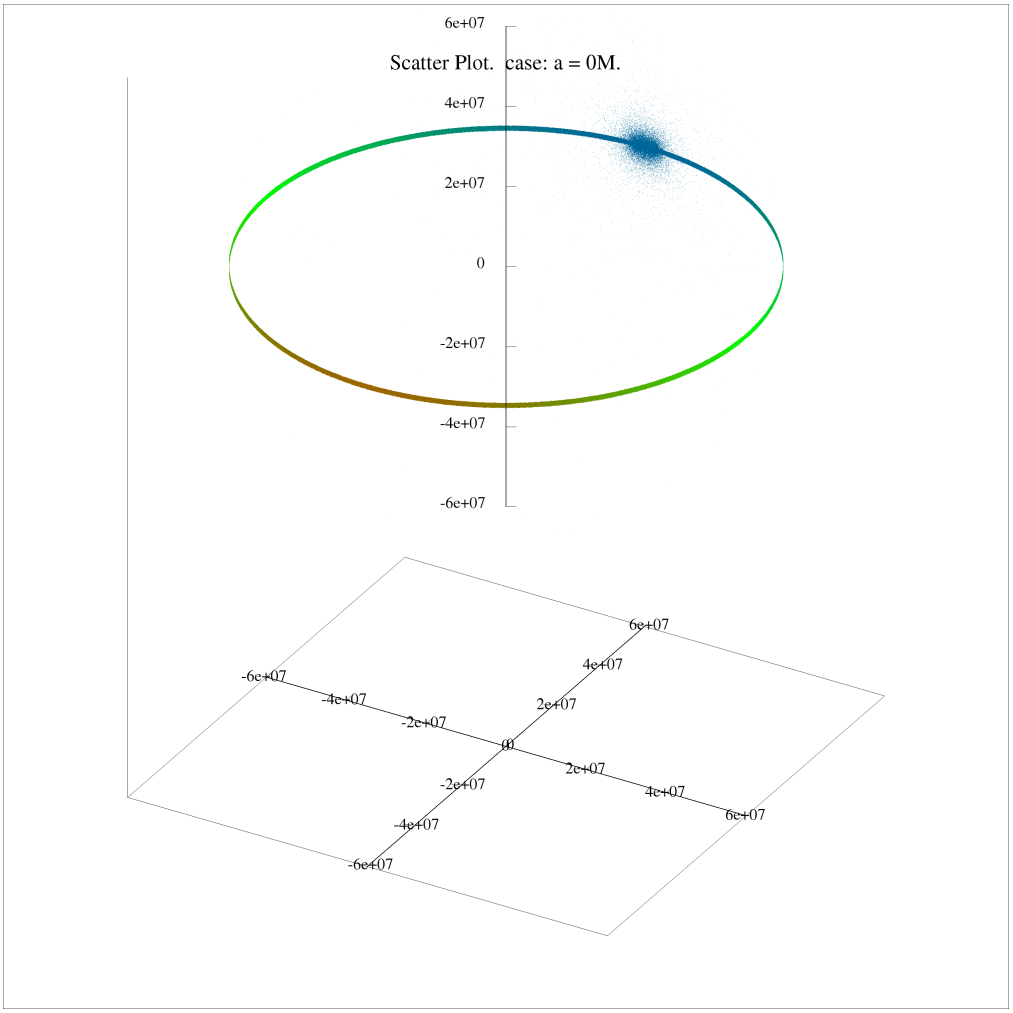

Figure 11.13: Scatter Plot, case: a = 0.

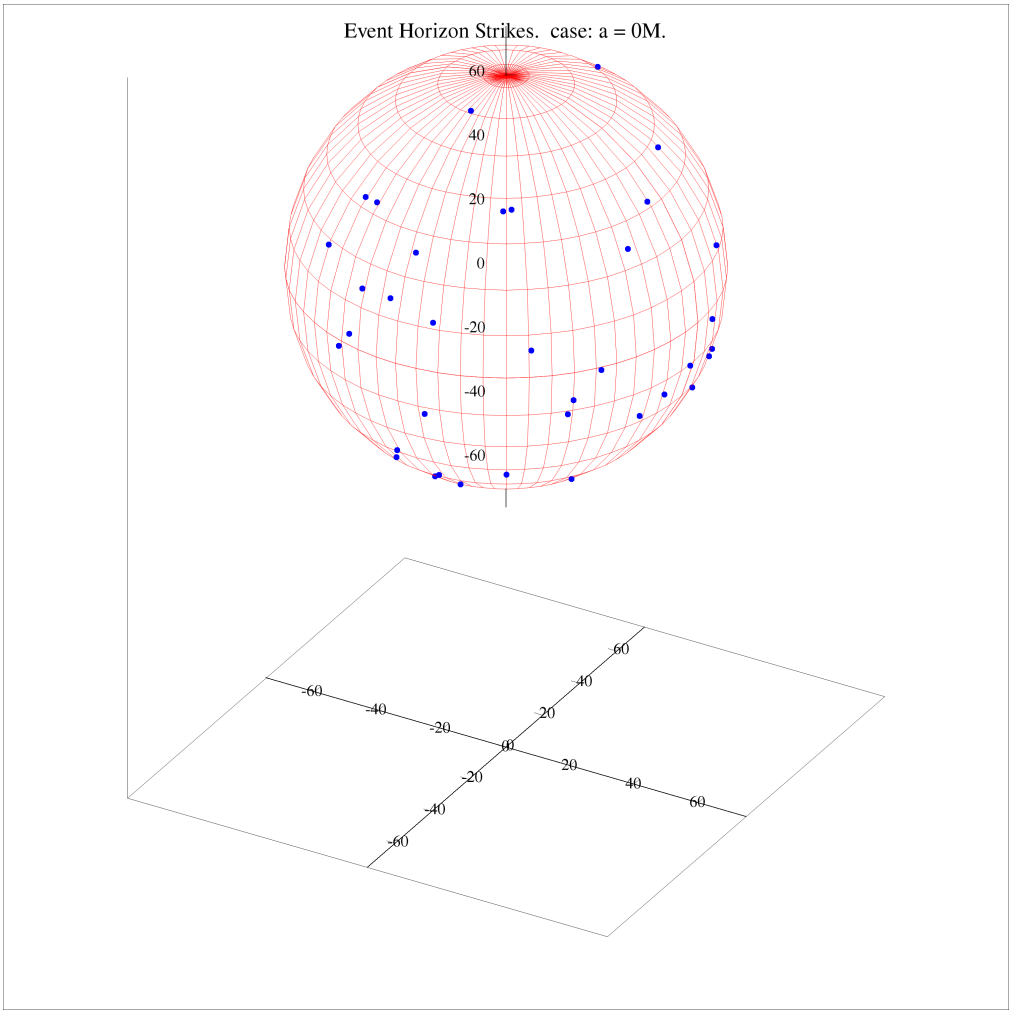

Figure 11.14: Horizon Strike plot, case: a = 0.

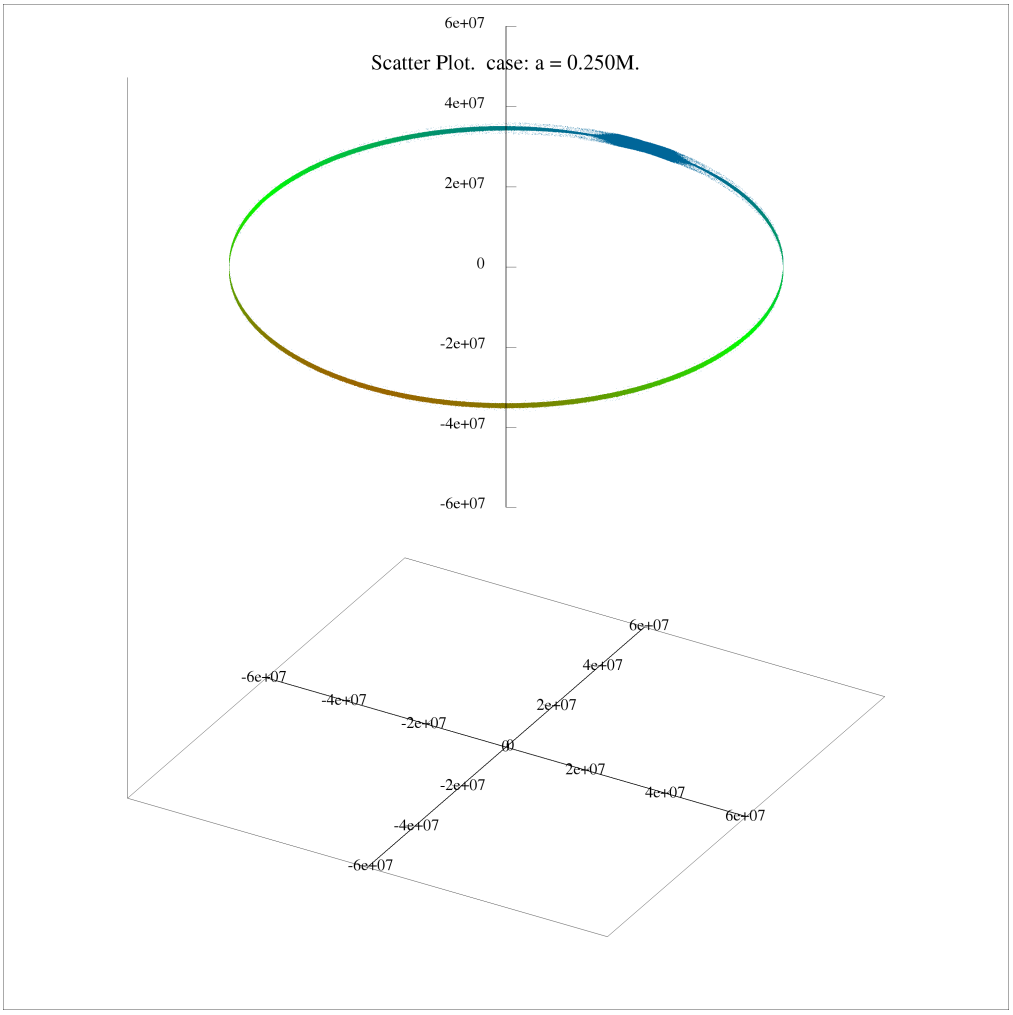

Figure 11.15: Scatter Plot, case: a = 0.250M.

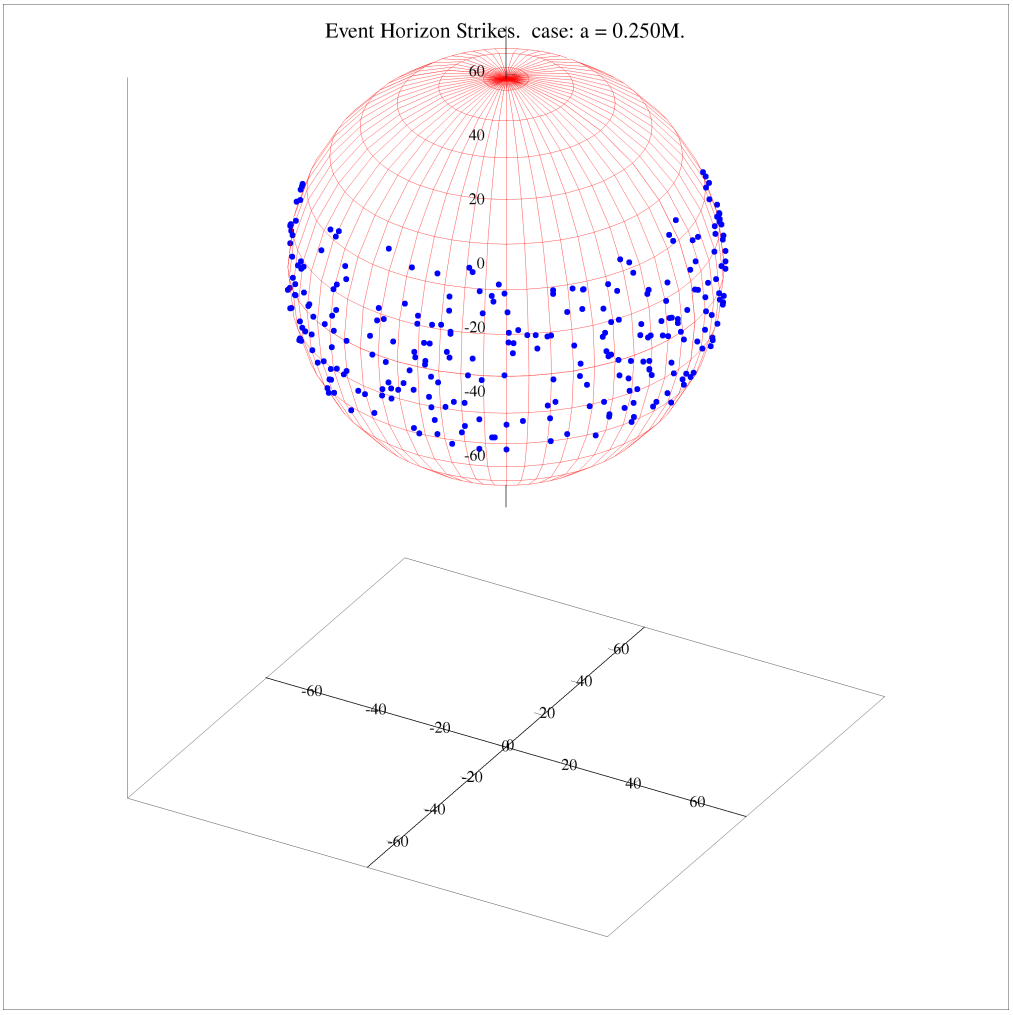

Figure 11.16: Horizon Strike plot, case: a = 0.250M.

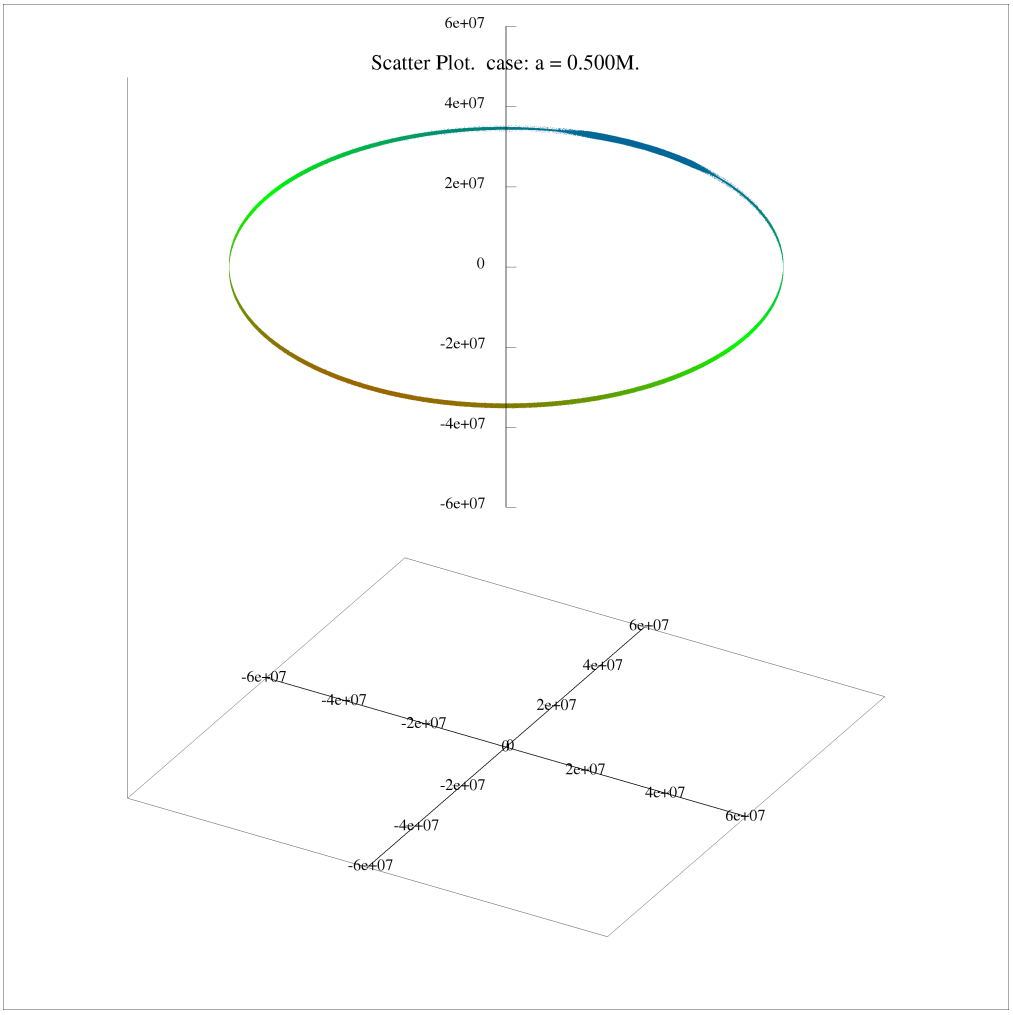

Figure 11.17: Scatter Plot, case: a = 0.500M.

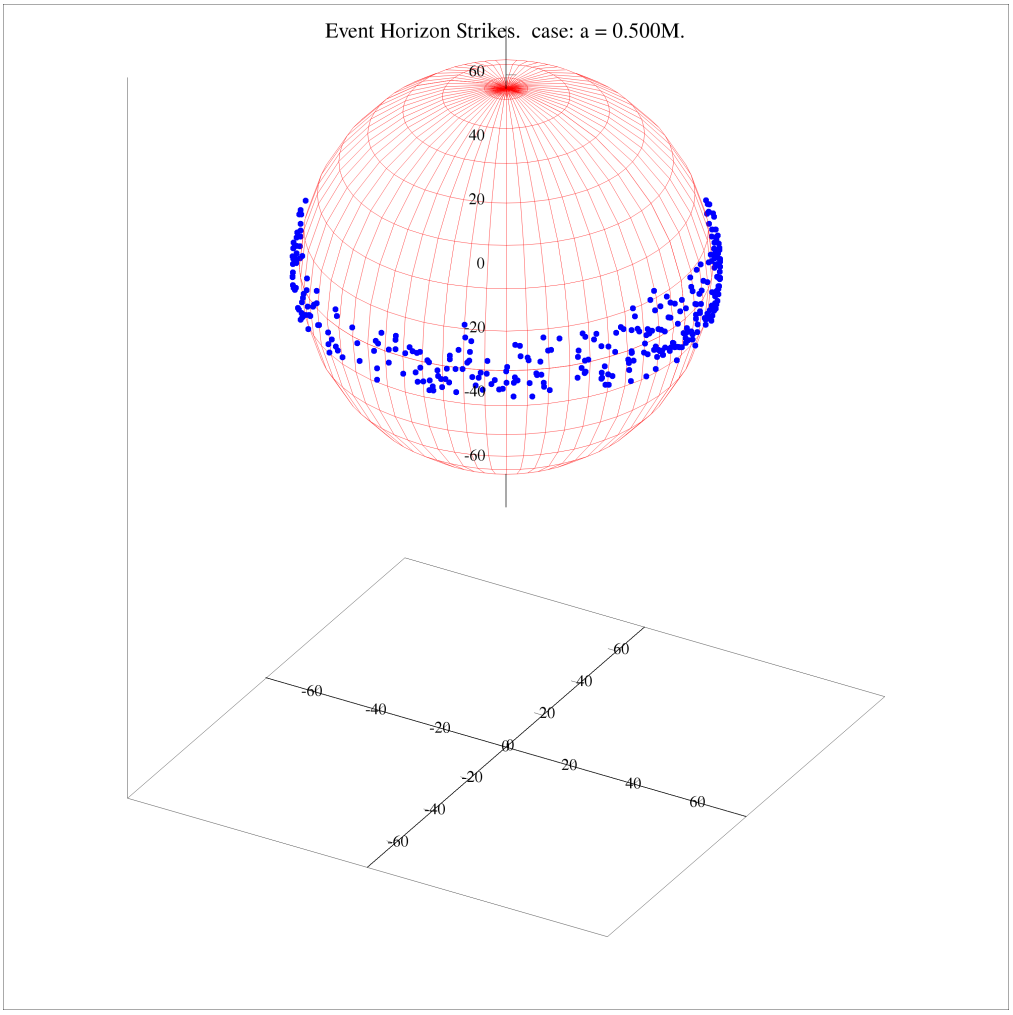

Figure 11.18: Horizon Strike plot, case: a = 0.500M.

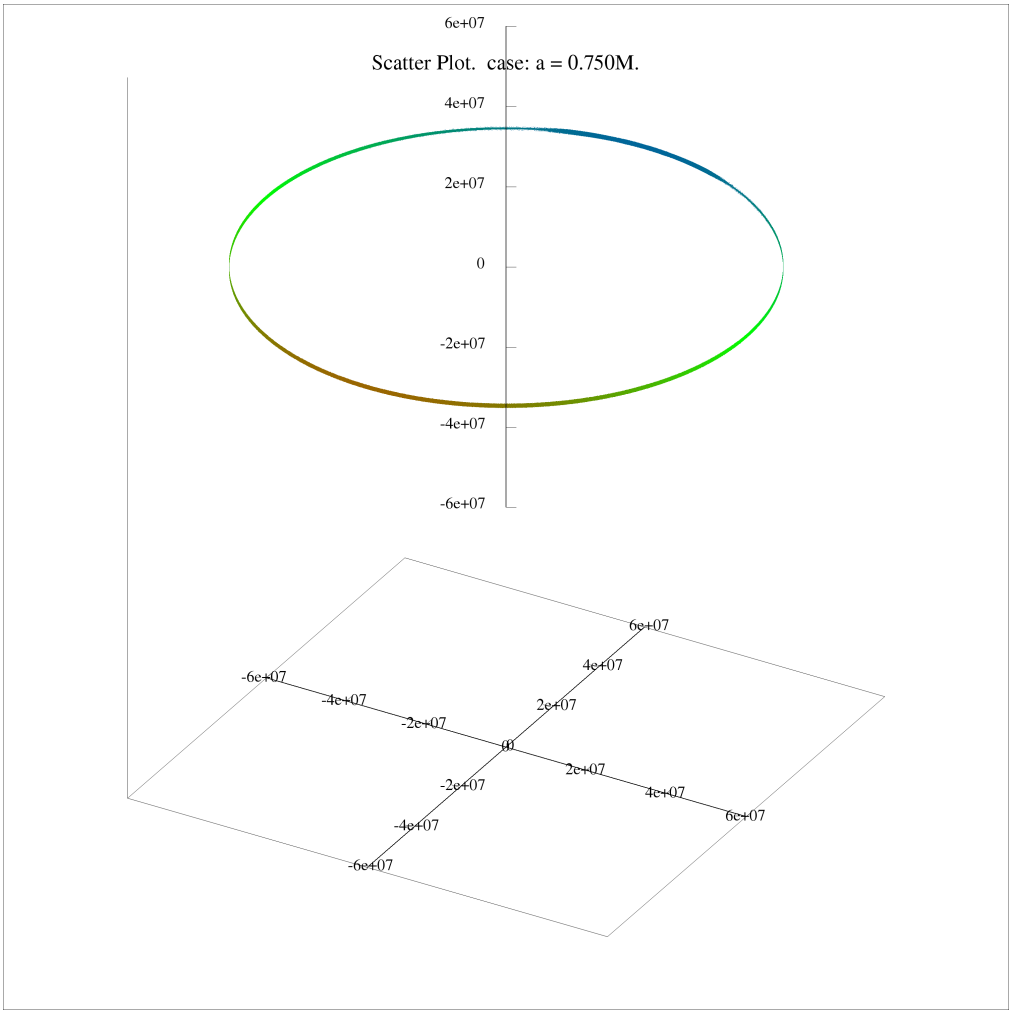

Figure 11.19: Scatter Plot, case: a = 0.750M.

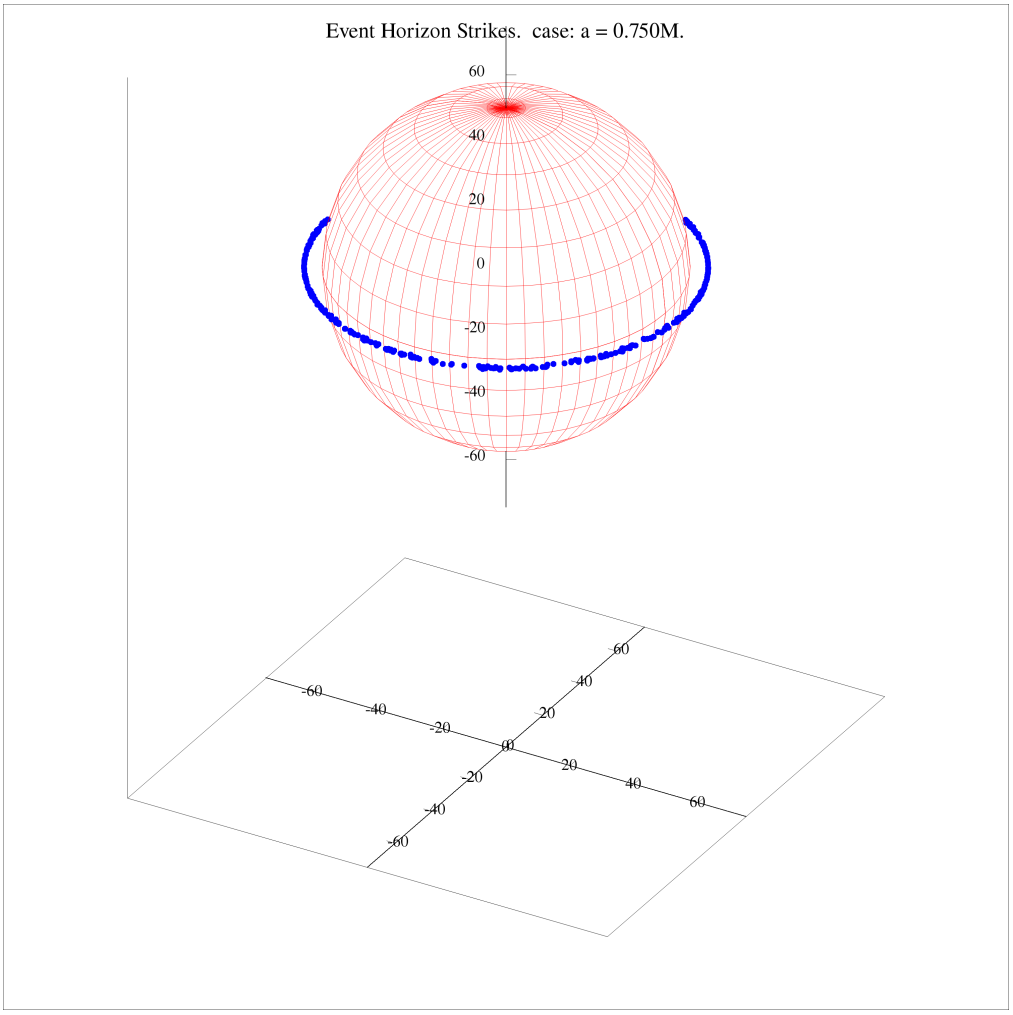

Figure 11.20: Horizon Strike plot, case: a = 0.750M.

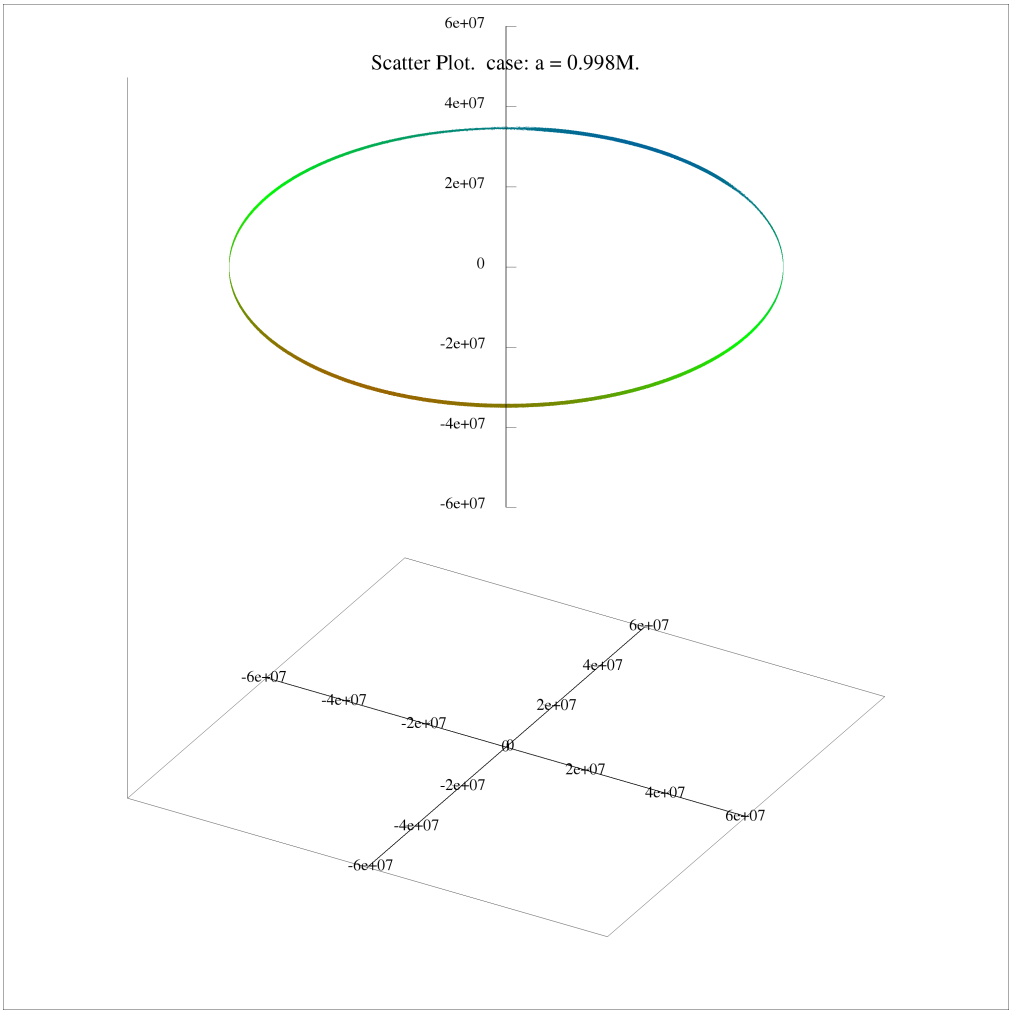

Figure 11.21: Scatter Plot, case: a = 0.998M.

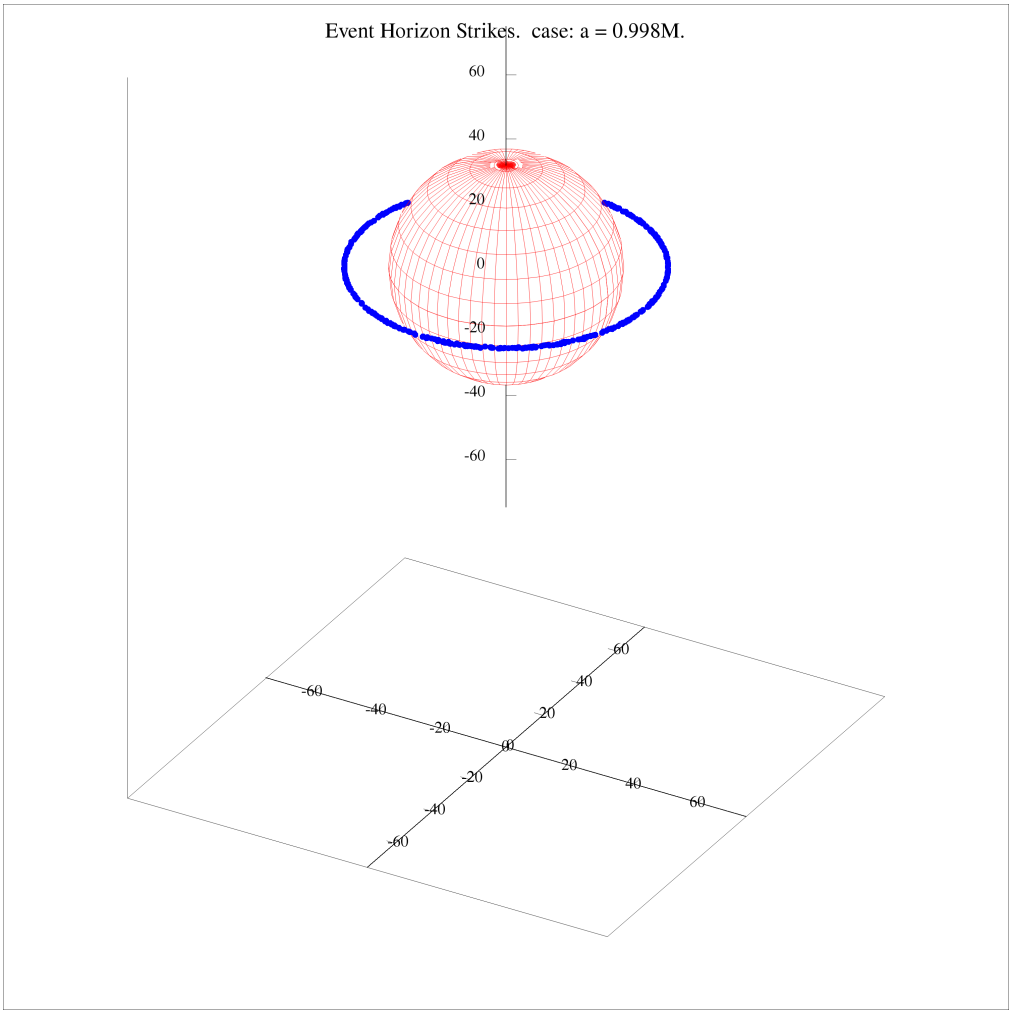

Figure 11.22: Horizon Strike plot, case: a = 0.998M.

The histogram and corresponding residual graphs are given in pairs. First, the overall data showing all pulses. See the caption for details. Inferior conjunction data contributes a reference of pulses which have travelled through relatively flat spacetime to the detector, the non-zero residual data does, however, indicate the effect of the photons "climbing out" of the gravitational potential created by the black-hole. Detector number and positions are given as follows. Ultimately it would be useful to generate photon count and timing residual histograms for a vast array of detectors placed at many locations in the black-hole sky, giving an indication of what the emissions of the pulsar would look like for an entire orbit by exploiting the symmetry of the system. These simulations could not be run due to the

increase in computational time experienced by introducing too many detectors at present. Fluxes of pulses captured by the two detectors at the superior and inferior conjunctions have been compared.

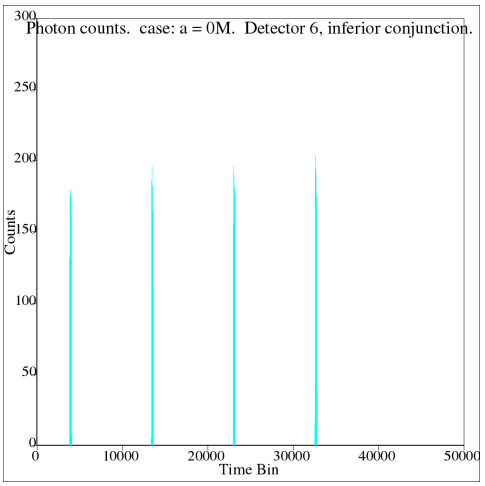

Figure 11.23: Non-rotating case: a = 0. Inferior conjunction photon counts.

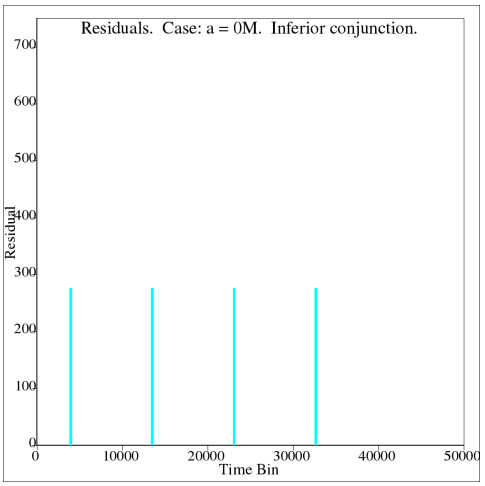

Figure 11.24: Non-rotating case: a = 0. Inferior conjunction photon timing residuals. Note the scattered photon received late, with very high residual.

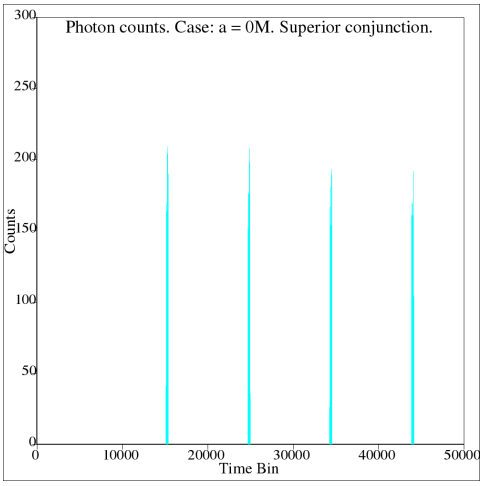

Figure 11.25: Non-rotating case: a = 0. Superior conjunction photon counts.

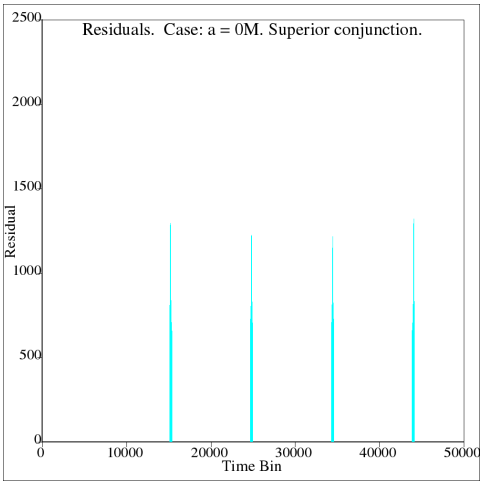

Figure 11.26: Non-rotating case: a = 0. Superior conjunction photon timing residuals.

The difference in pulse shape, as well as the corresponding residual measurements is shown above, but to really see the effect of the black-hole on the pulses which have moved through its vicinity, a more detailed view of each distinct pulse is necessary. Below are presented single pulse close-ups for the same case of $a = 0$. A direct comparison is made between photon count histograms for individual pulses, for the inferior and superior conjunction detectors.

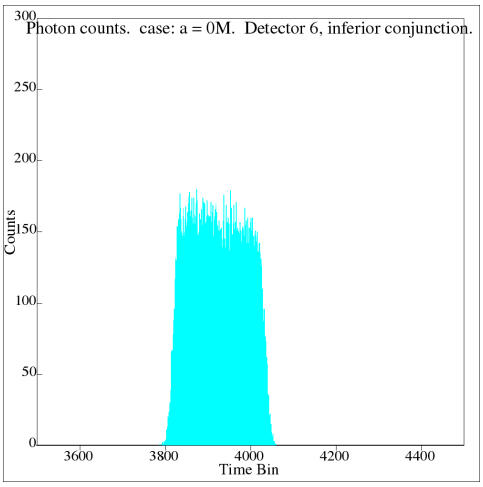

Figure 11.27: Non-rotating case: a = 0. Inferior conjunction photon counts, first pulse.

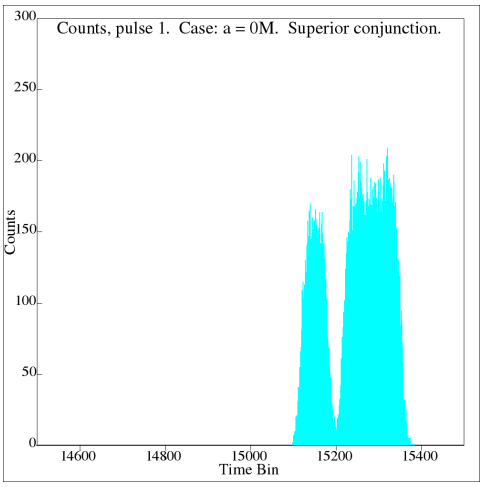

Figure 11.28: Non-rotating case: a = 0. Superior conjunction photon counts, first pulse.

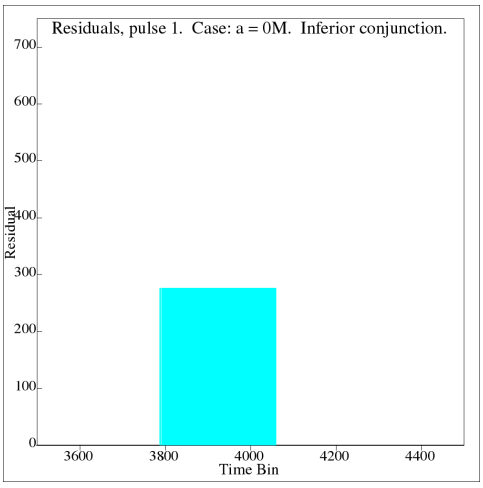

Figure 11.29: Non-rotating case: a = 0. Inferior conjunction photon timing residuals, first pulse.

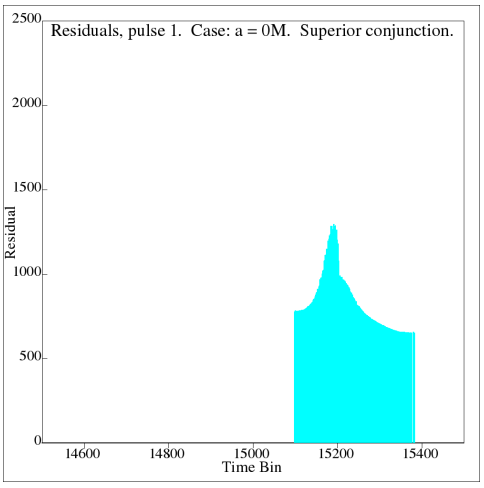

Figure 11.30: Non-rotating case: a = 0. Superior conjunction photon timing residuals, first pulse.

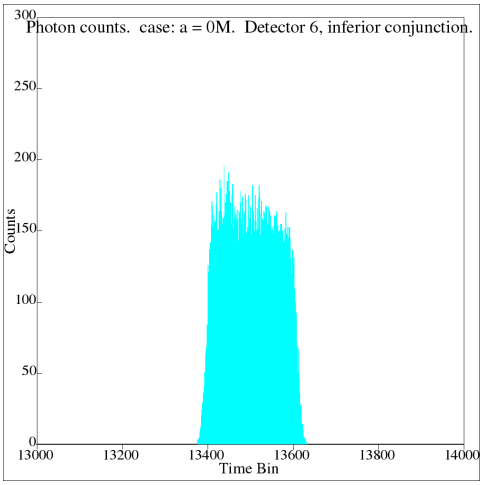

Figure 11.31: Non-rotating case: a = 0. Inferior conjunction photon counts, second pulse.

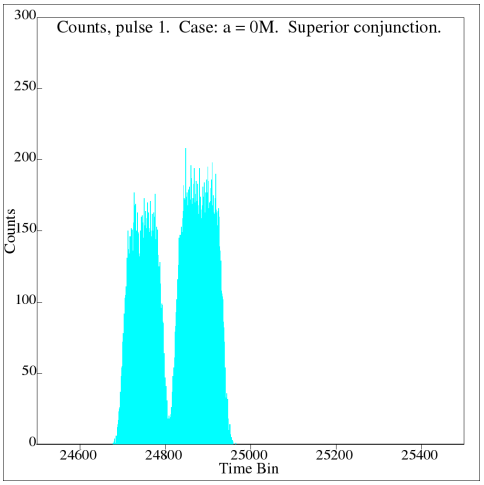

Figure 11.32: Non-rotating case: a = 0. Superior conjunction photon counts, second pulse.

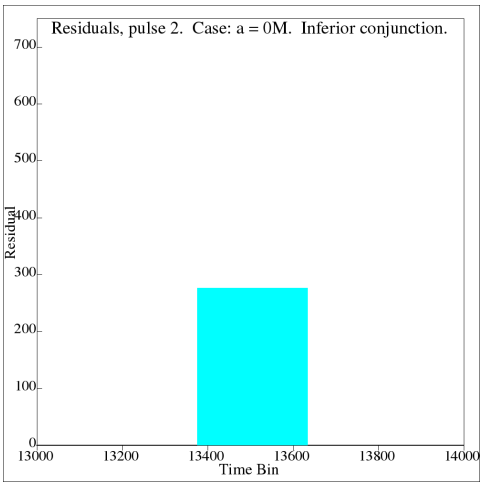

Figure 11.33: Non-rotating case: a = 0. Inferior conjunction photon timing residuals, second pulse.

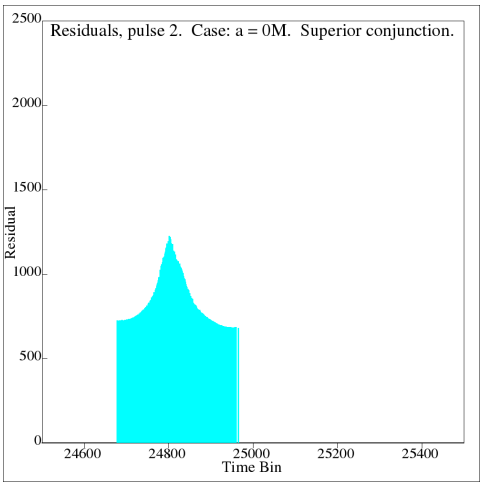

Figure 11.34: Non-rotating case: a = 0. Superior conjunction photon timing residuals, second pulse.

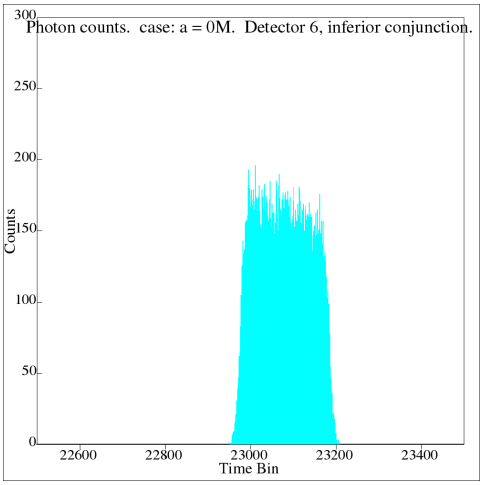

Figure 11.35: Non-rotating case: a = 0. Inferior conjunction photon counts, third pulse.

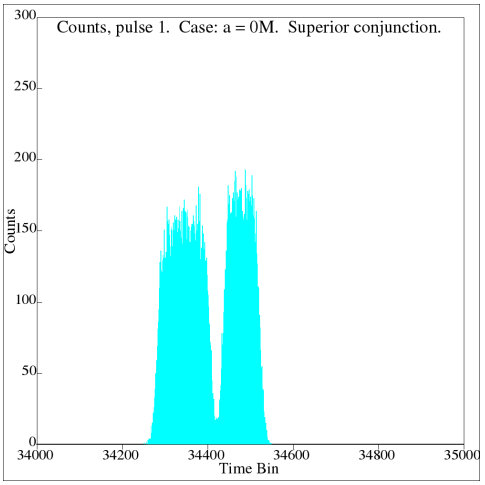

Figure 11.36: Non-rotating case: a = 0. Superior conjunction photon counts, third pulse.

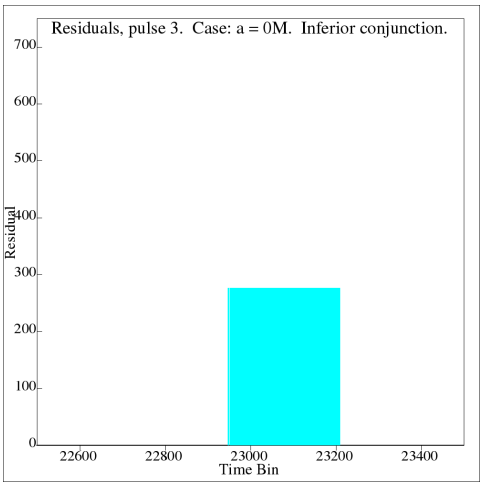

Figure 11.37: Non-rotating case: a = 0. Inferior conjunction photon timing residuals, third pulse.

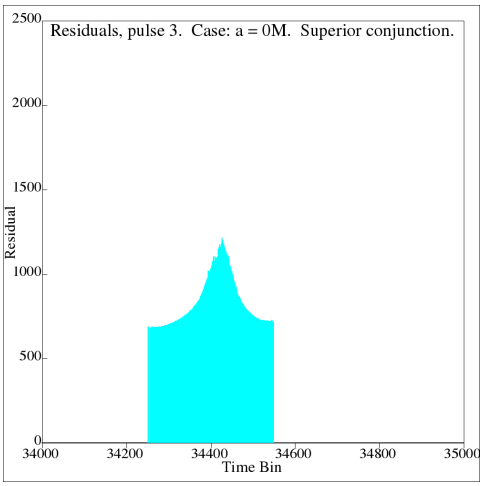

Figure 11.38: Non-rotating case: a = 0. Superior conjunction photon timing residuals, third pulse.

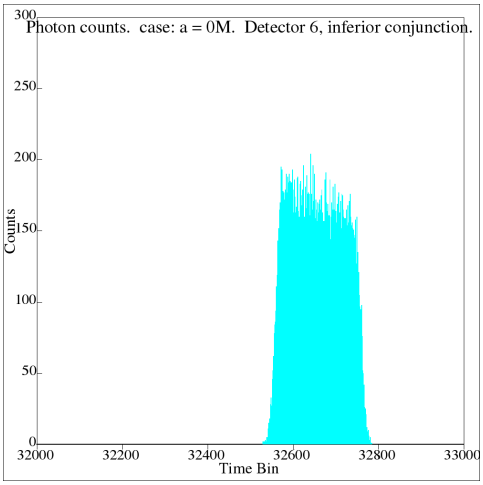

Figure 11.39: Non-rotating case: a = 0. Inferior conjunction photon counts, fourth pulse.

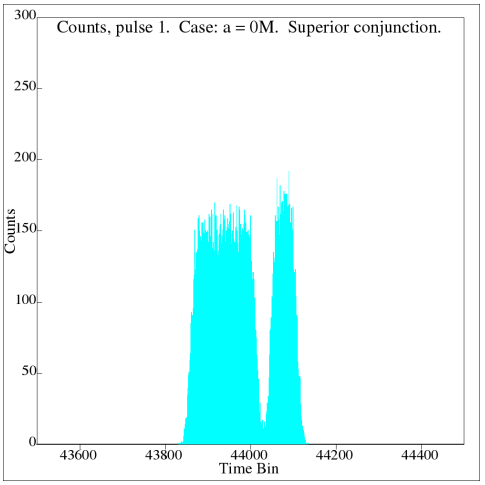

Figure 11.40: Non-rotating case: a = 0. Superior conjunction photon counts, fourth pulse.

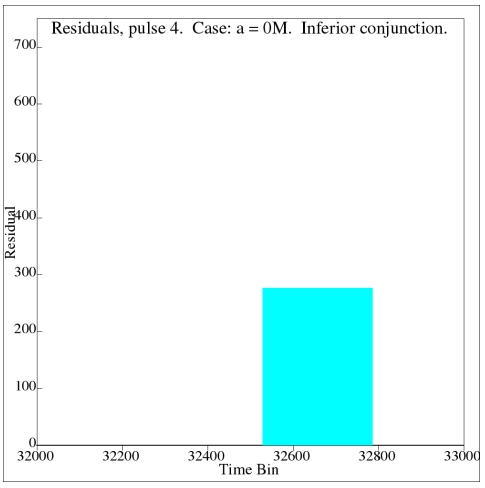

Figure 11.41: Non-rotating case: a = 0. Inferior conjunction photon timing residuals, fourth pulse.

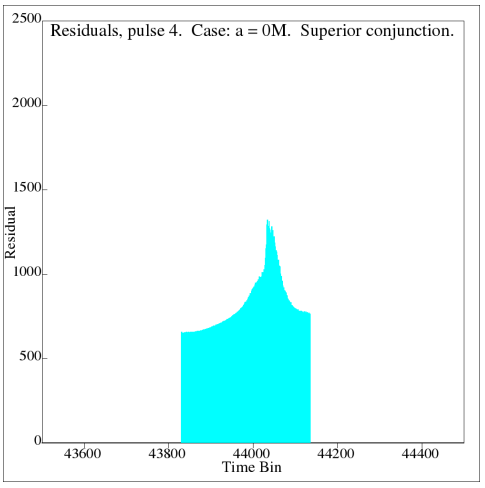

Figure 11.42: Non-rotating case: a = 0. Superior conjunction photon timing residuals, fourth pulse.

This concludes the presentation of photon count and timing residual histograms for the Schwarzschild case of $a = 0$. The effects of the black-hole on the flux of each pulse, and the delay of photons constituting each pulse, is clearly discernable. A trough is experienced for each pulse originating from the superior conjunction of a black-hole pulsar binary system, with the orientation of the trough dependent on whether the pulsar was approaching or receding from superior conjunction. This is useful as it can indicate the direction of rotation of the pulsar around the black-hole. The residual data is not something which could be observed, but it does give some insight into how photons have been delayed and scattered by the black-hole. Indeed, the troughs within each superior conjunction pulse correspond to large photon residual measurements. This indicates that photons have been scattered by the black-hole, and those which have been scattered to final angles within the detector's area have experienced substantial propagation time delays. The very large delays observed for this system were caused by the toy-model selection of parameters, whereby the orbital separation of the system is one to two orders of magnitude too small, furthermore, the black-hole is of mass $30M_{\odot}$. In comparison with observed shapiro delays for known pulsar binary systems, which have delays in the $100\mu s$ range for high companion mass binaries, the delays generated by the numerical model are approximately 50 multiples too large. Nonetheless, the increase is consistent throughout all simulations, and is not due to numerical inaccuracy

of the code. The conversion of units of time for this data is given by: $1unit = 4.925e-6s$. To be able to determine whether other physical parameters of black-hole pulsar binary systems can be extrapolated from pulse timing data such as the above, a large number of parameter sets would need to be run, using large numbers of photons. The results presented below were generated for the same physical system as the above results, with the exception of the variation of the Kerr parameter of the black-hole. Thus the effect of rotation on the signal can be observed, although perhaps with insufficient detail to disentangle it from other strong-field effects. Each set of superior conjunction outputs will be presented alongside inferior conjunction outputs; however, for the rotating cases, the results for positive and negative rotational parameters will be presented simultaneously. The first rotating cases considered were those of black-holes with rotational parameters set to $a = \pm 0.250M$.

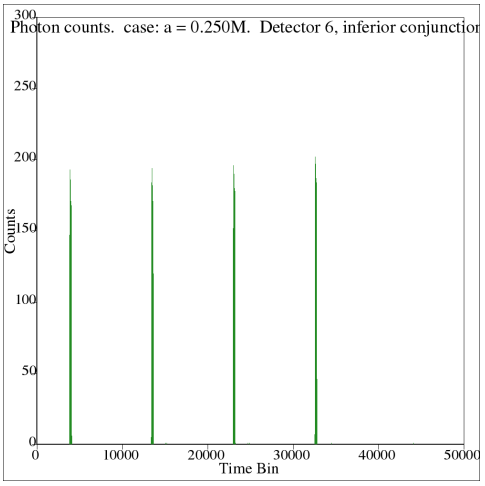

Figure 11.43: Case: a = 0.250M. Inferior conjunction photon counts.

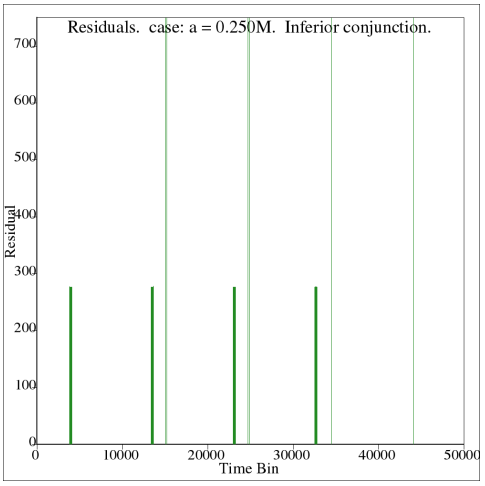

Figure 11.44: Case: a = 0.250M. Inferior conjunction photon timing residuals.

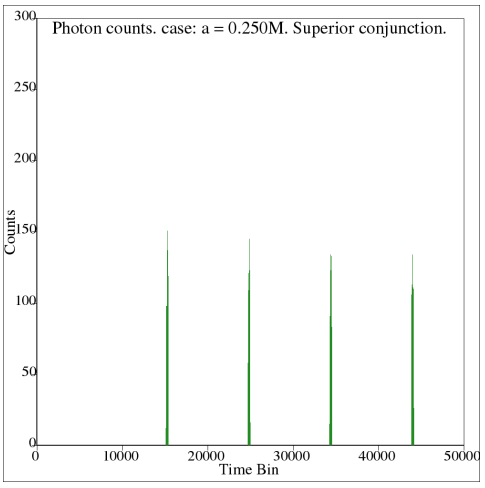

Figure 11.45: Case: a = 0.250M. Superior conjunction photon counts.

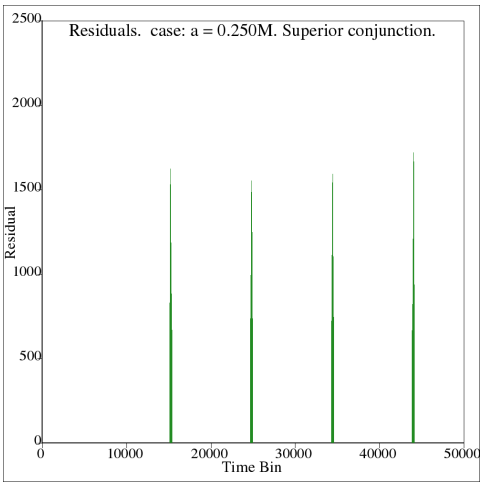

Figure 11.46: Case: a = 0.250M. Superior conjunction photon timing residuals.

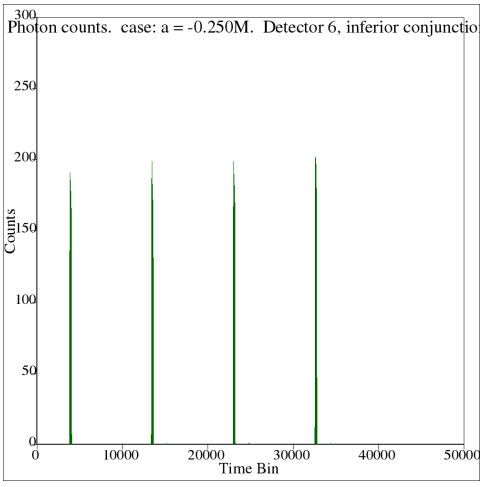

Figure 11.47: Case: a = -0.250M. Inferior conjunction photon counts.

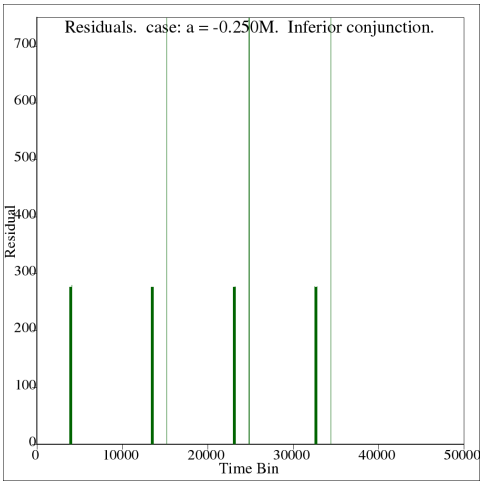

Figure 11.48: Case: a = -0.250M. Inferior conjunction photon timing residuals.

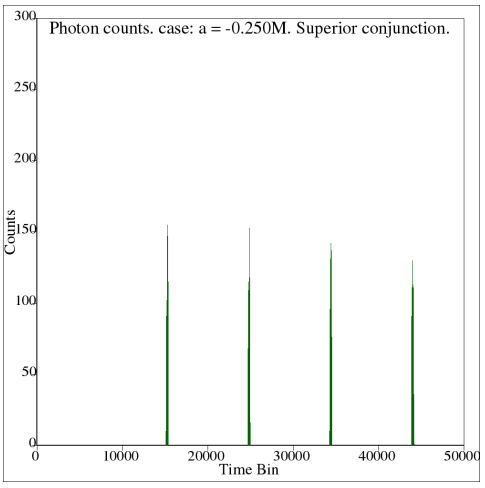

Figure 11.49: Case: a = -0.250M. Superior conjunction photon counts.

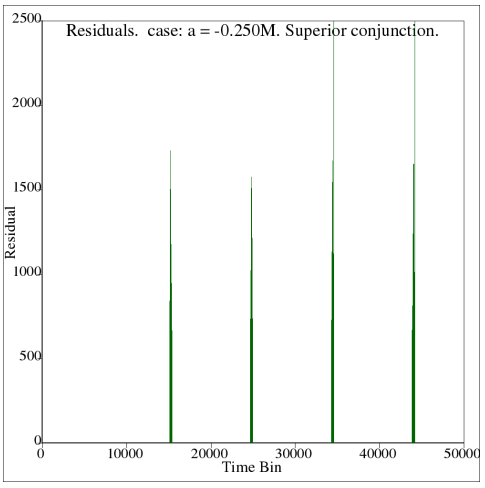

Figure 11.50: Case: a = -0.250M. Superior conjunction photon timing residuals.

Individual pulse close-up data for the cases $a = \pm 0.250M$ is presented below.

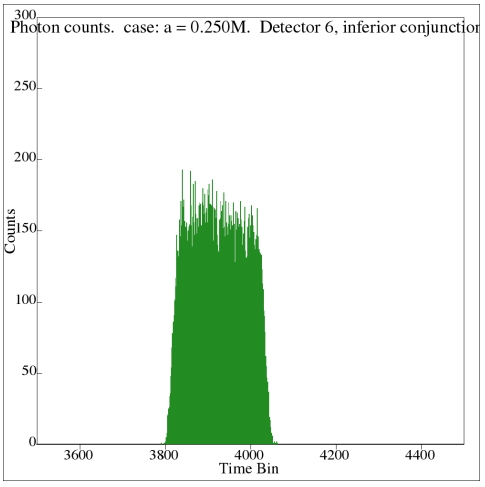

Figure 11.51: Case: a = 0.250M. Inferior conjunction photon counts, first pulse.

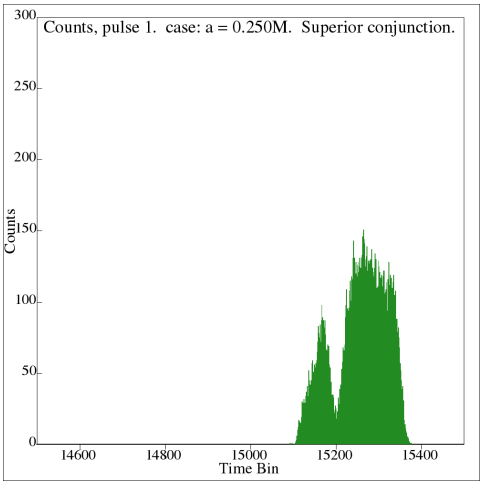

Figure 11.52: Case: a = 0.250M. Superior conjunction photon counts, first pulse.

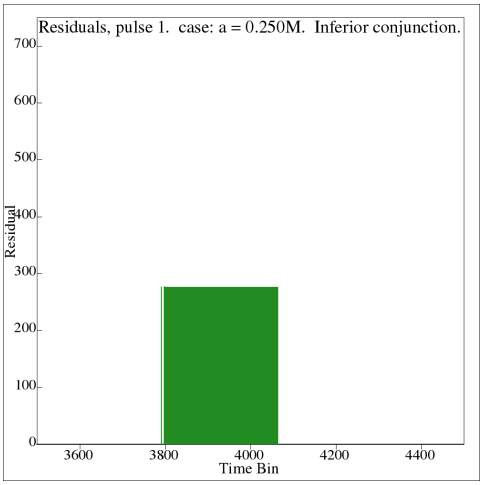

Figure 11.53: Case: a = 0.250M. Inferior conjunction photon timing residuals, first pulse.

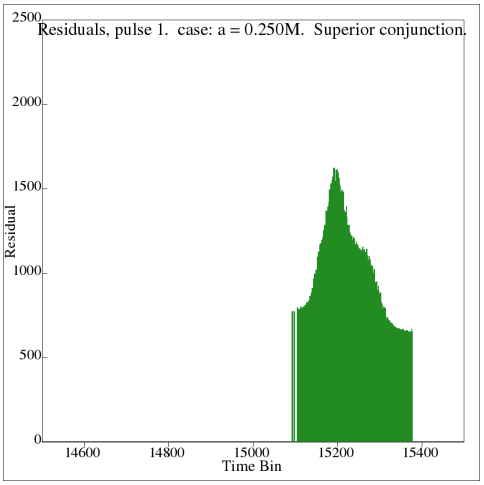

Figure 11.54: Case: a = 0.250M. Superior conjunction photon timing residuals, first pulse.

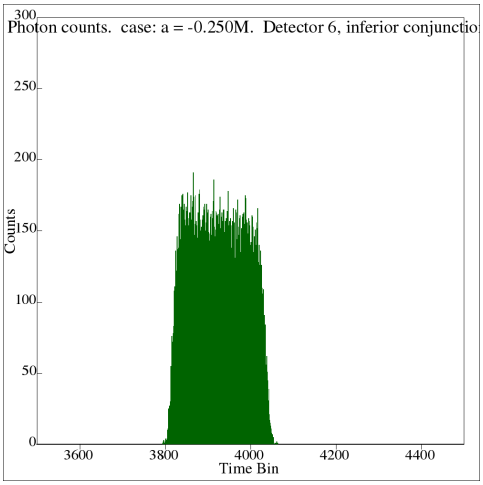

Figure 11.55: Case: a = -0.250M. Inferior conjunction photon counts, first pulse.

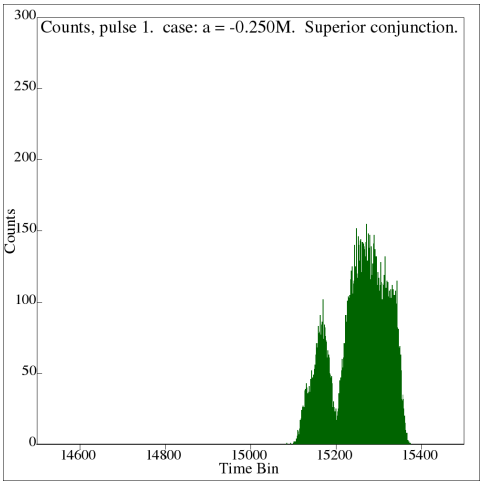

Figure 11.56: Case: a = -0.250M. Superior conjunction photon counts, first pulse.

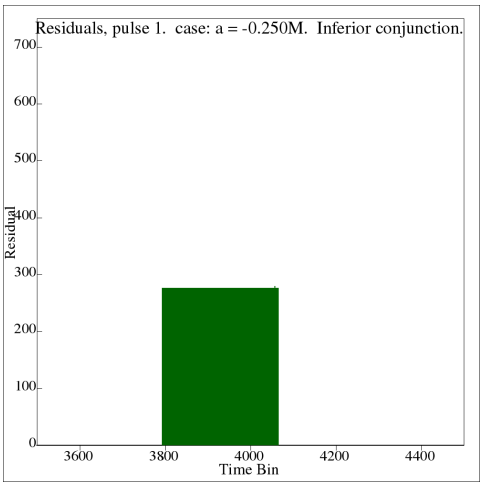

Figure 11.57: Case: a = -0.250M. Inferior conjunction photon timing residuals, first pulse.

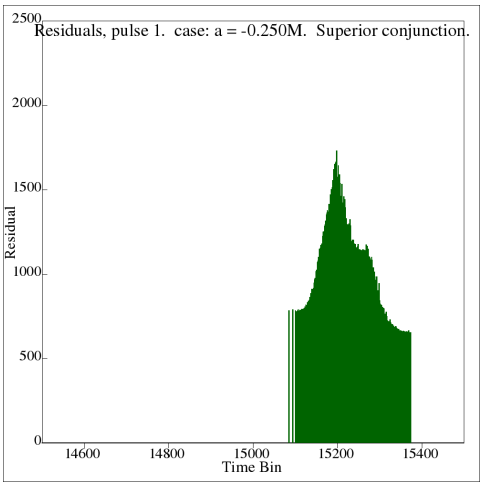

Figure 11.58: Case: a = -0.250M. Superior conjunction photon timing residuals, first pulse.

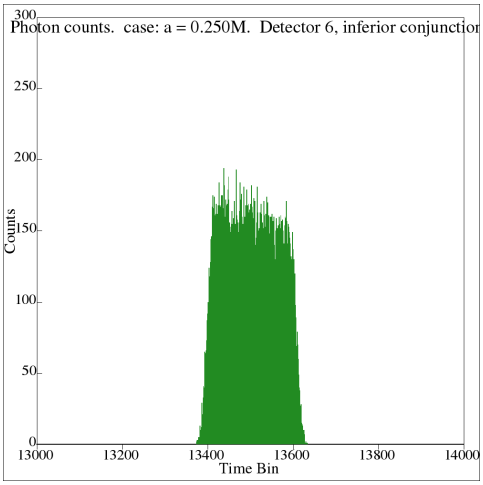

Figure 11.59: Case: a = 0.250M. Inferior conjunction photon counts, second pulse.

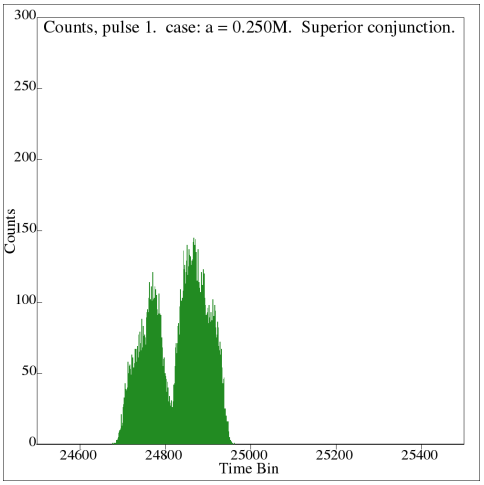

Figure 11.60: Case: a = 0.250M. Superior conjunction photon counts, second pulse.

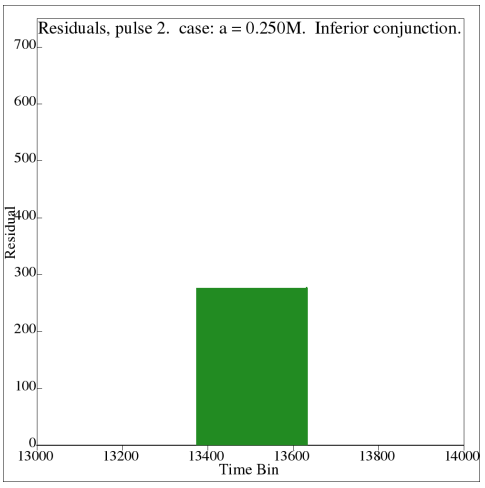

Figure 11.61: Case: a = 0.250M. Inferior conjunction photon timing residuals, second pulse.

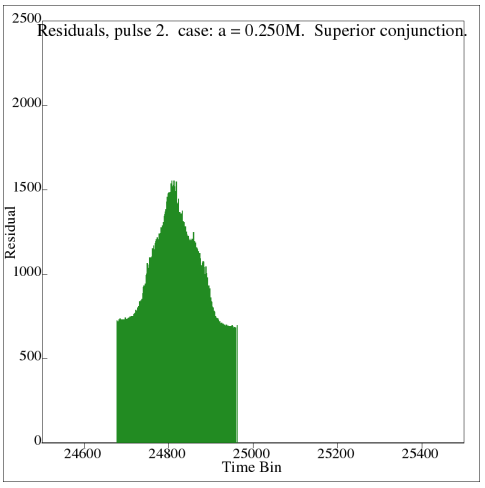

Figure 11.62: Case: a = 0.250M. Superior conjunction photon timing residuals, second pulse.

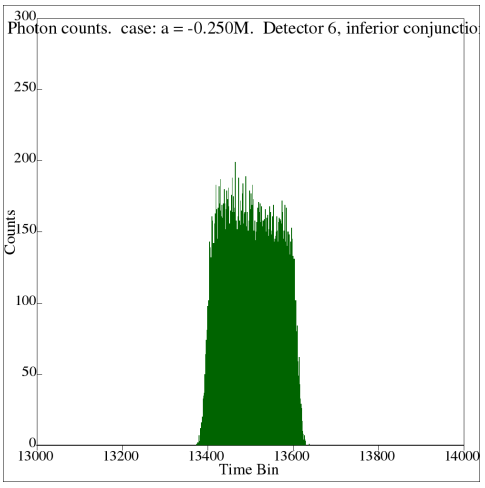

Figure 11.63: Case: a = -0.250M. Inferior conjunction photon counts, second pulse.

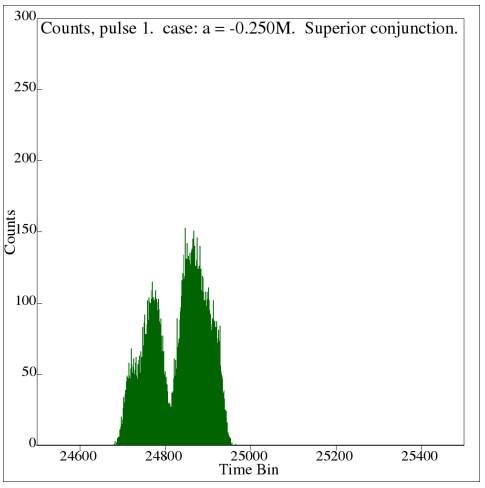

Figure 11.64: Case: a = -0.250M. Superior conjunction photon counts, second pulse.

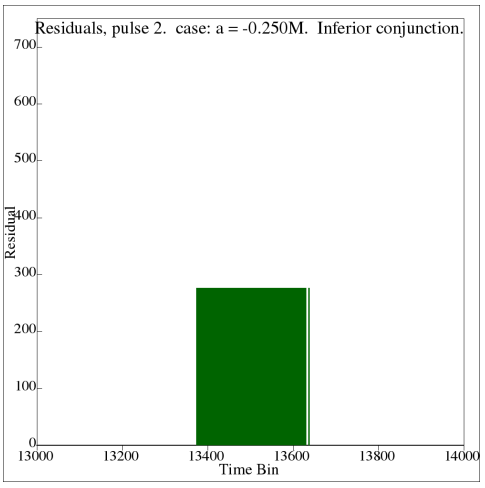

Figure 11.65: Case: a = -0.250M. Inferior conjunction photon timing residuals, second pulse.

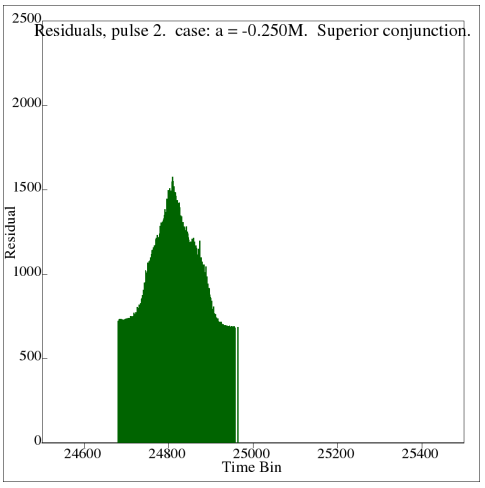

Figure 11.66: Case: a = -0.250M. Superior conjunction photon timing residuals, second pulse.

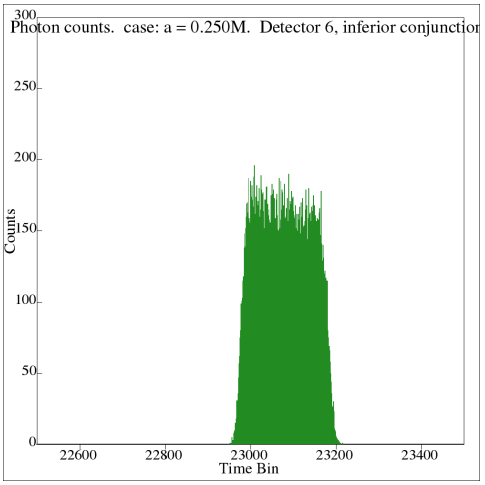

Figure 11.67: Case: a = 0.250M. Inferior conjunction photon counts, third pulse.

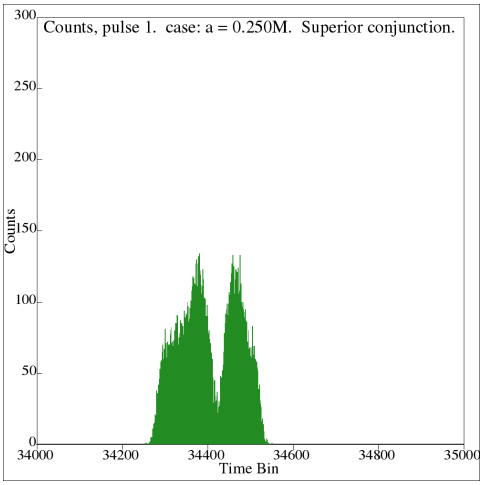

Figure 11.68: Case: a = 0.250M. Superior conjunction photon counts, third pulse.

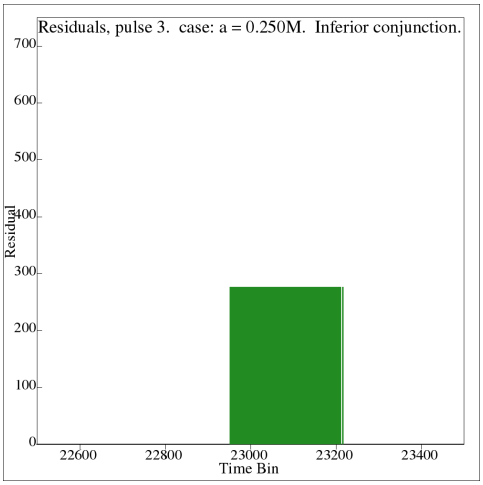

Figure 11.69: Case: a = 0.250M. Inferior conjunction photon timing residuals, third pulse.

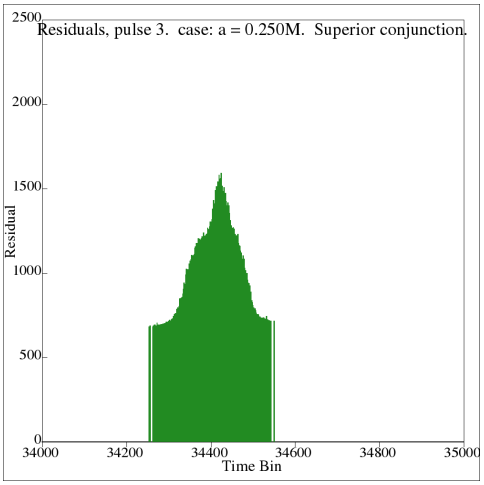

Figure 11.70: Case: a = 0.250M. Superior conjunction photon timing residuals, third pulse.

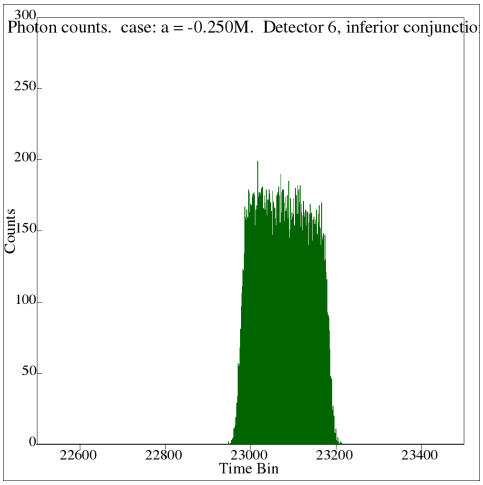

Figure 11.71: Case: a = -0.250M. Inferior conjunction photon counts, third pulse.

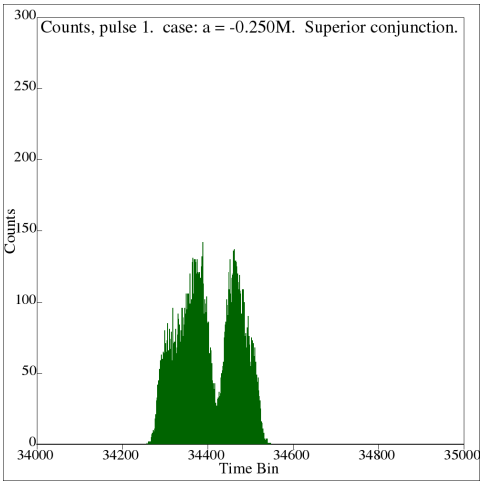

Figure 11.72: Case: a = -0.250M. Superior conjunction photon counts, third pulse.

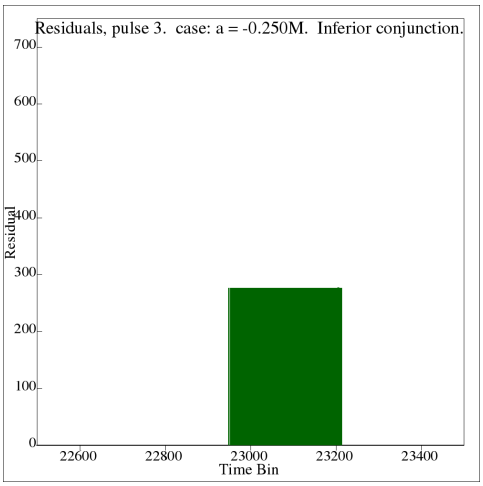

Figure 11.73: Case: a = -0.250M. Inferior conjunction photon timing residuals, third pulse.

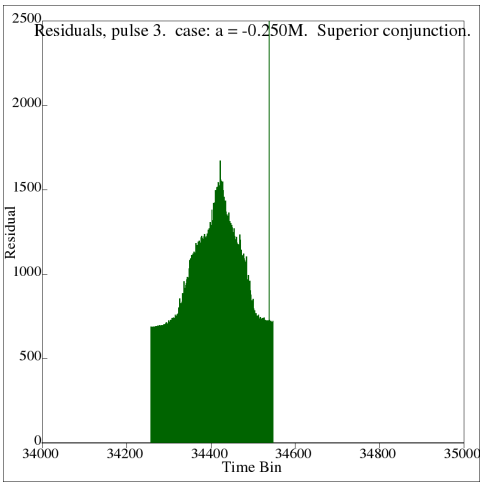

Figure 11.74: Case: a = -0.250M. Superior conjunction photon timing residuals, third pulse.

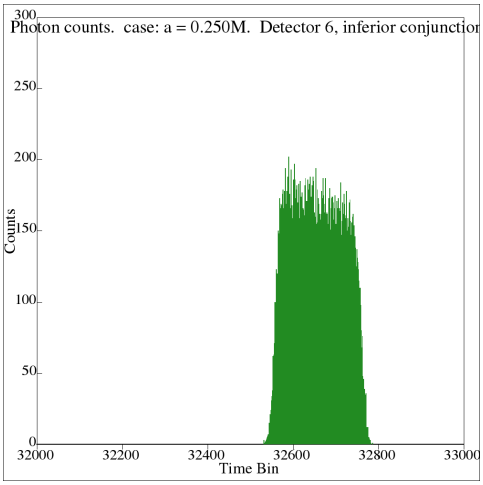

Figure 11.75: Case: a = 0.250M. Inferior conjunction photon counts, fourth pulse.

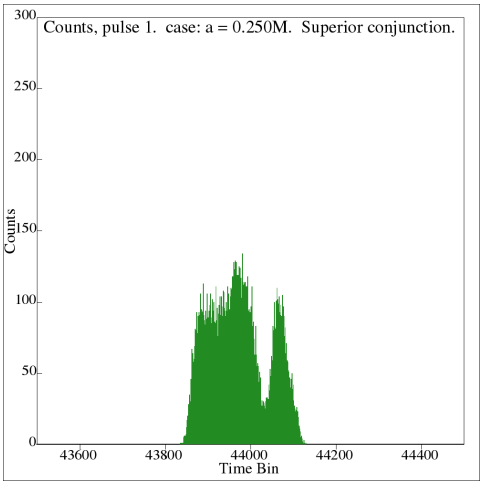

Figure 11.76: Case: a = 0.250M. Superior conjunction photon counts, fourth pulse.

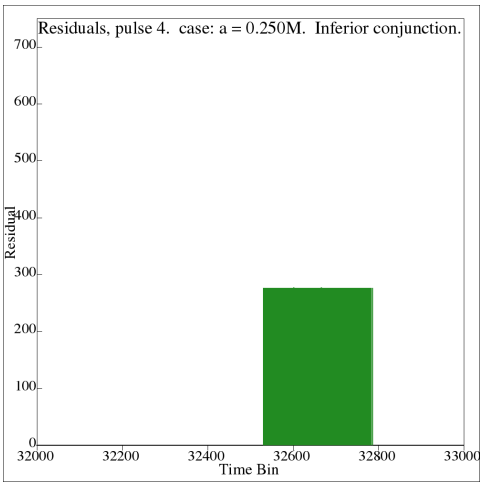

Figure 11.77: Case: a = 0.250M. Inferior conjunction photon timing residuals, fourth pulse.

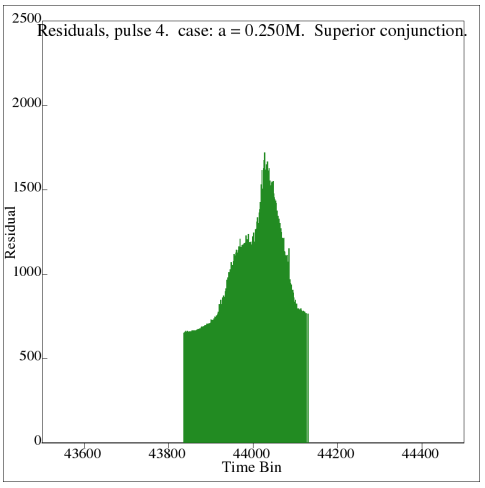

Figure 11.78: Case: a = 0.250M. Superior conjunction photon timing residuals, fourth pulse.

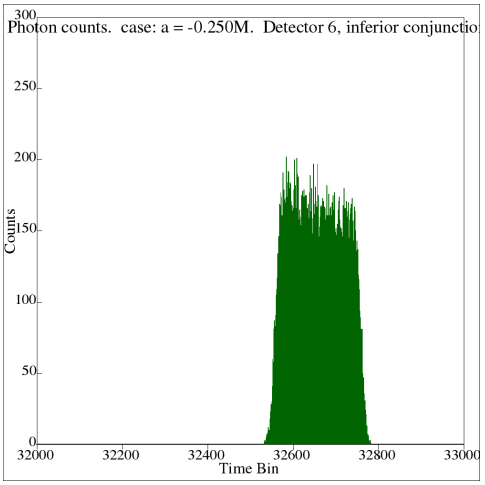

Figure 11.79: Case: a = -0.250M. Inferior conjunction photon counts, fourth pulse.

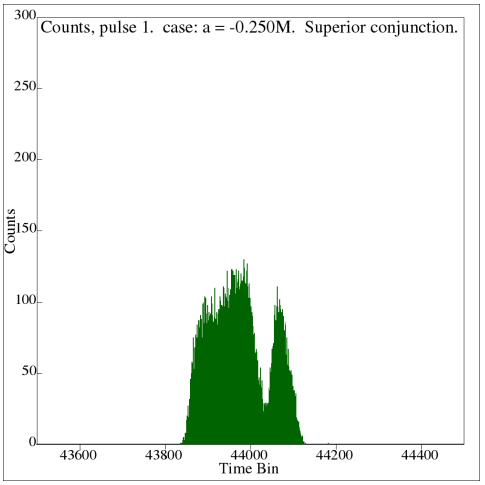

Figure 11.80: Case: a = -0.250M. Superior conjunction photon counts, fourth pulse.

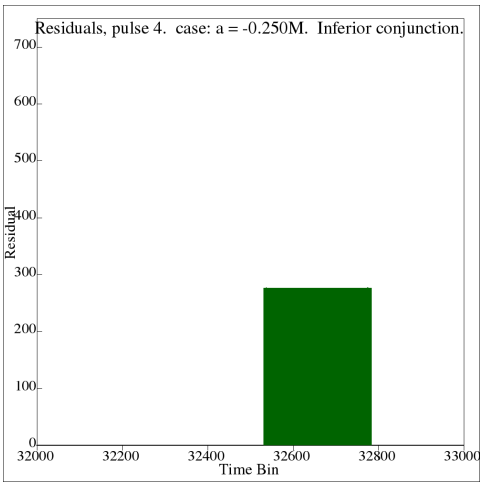

Figure 11.81: Case: a = -0.250M. Inferior conjunction photon timing residuals, fourth pulse.

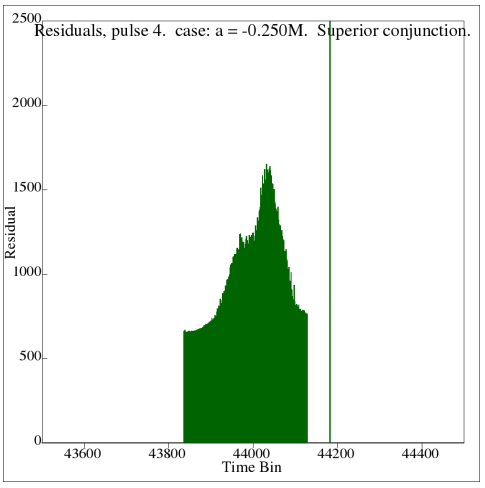

Figure 11.82: Case: a = -0.250M. Superior conjunction photon timing residuals, fourth pulse.

This concludes the presentation of photon count and timing residual output for the cases $a = \pm 0.250M$. The next cases to be presented are those of $a = \pm 0.500M$.

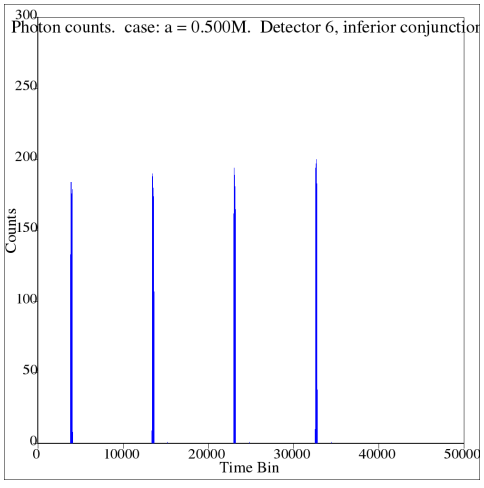

Figure 11.83: Case: a = 0.500M. Inferior conjunction photon counts.

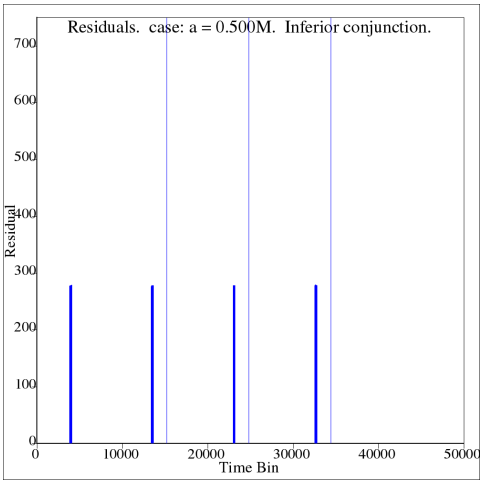

Figure 11.84: Case: a = 0.500M. Inferior conjunction photon timing residuals.

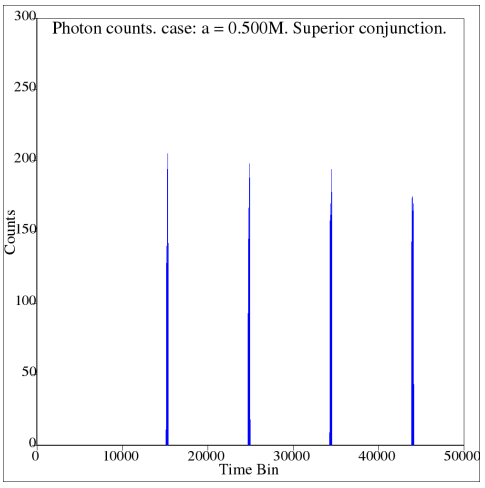

Figure 11.85: Case: a = 0.500M. Superior conjunction photon counts.

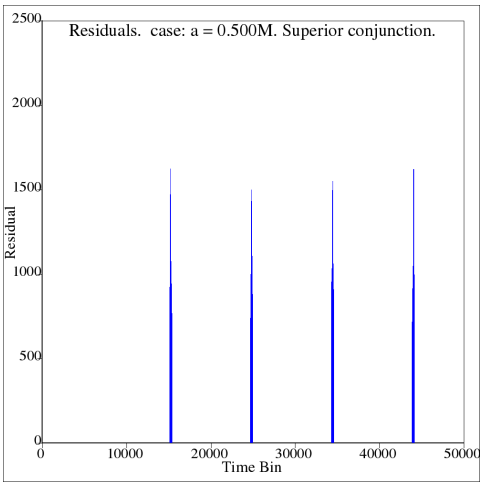

Figure 11.86: Case: a = 0.500M. Superior conjunction photon timing residuals.

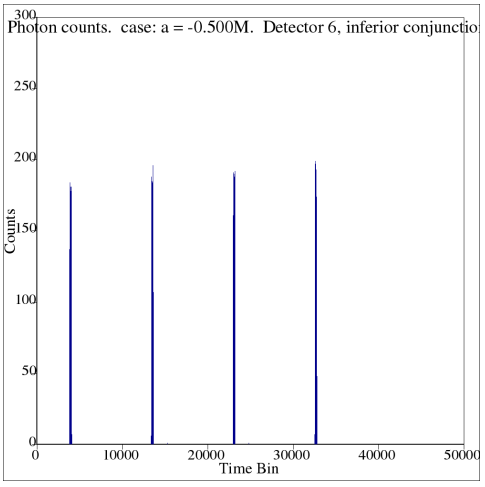

Figure 11.87: Case: a = -0.500M. Inferior conjunction photon counts.

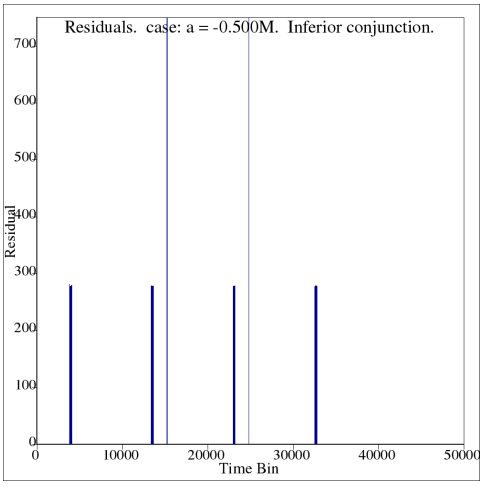

Figure 11.88: Case: a = -0.500M. Inferior conjunction photon timing residuals.

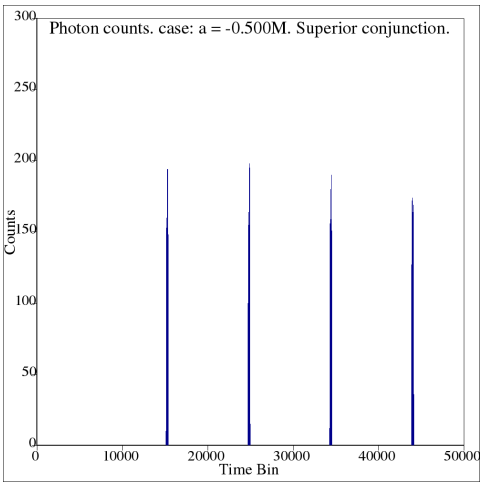

Figure 11.89: Case: a = -0.500M. Superior conjunction photon counts.

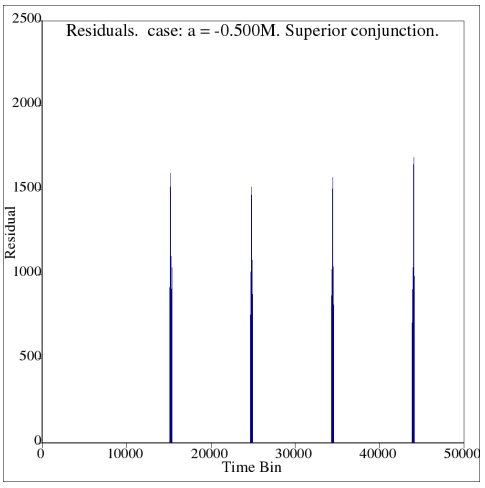

Figure 11.90: Case: a = -0.500M. Superior conjunction photon timing residuals.

Individual pulse close-up output for the cases $a = \pm 0.500M$ is presented below.

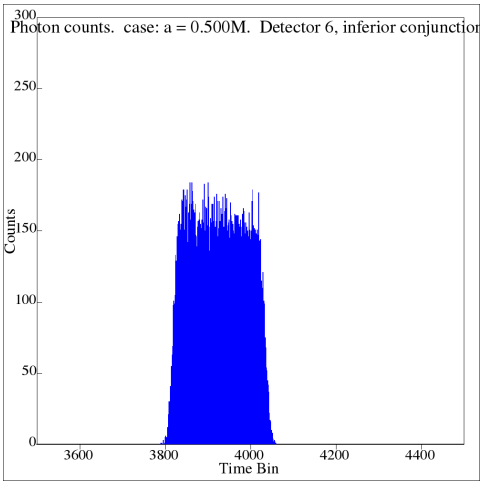

Figure 11.91: Case: a = 0.500M. Inferior conjunction photon counts, first pulse.

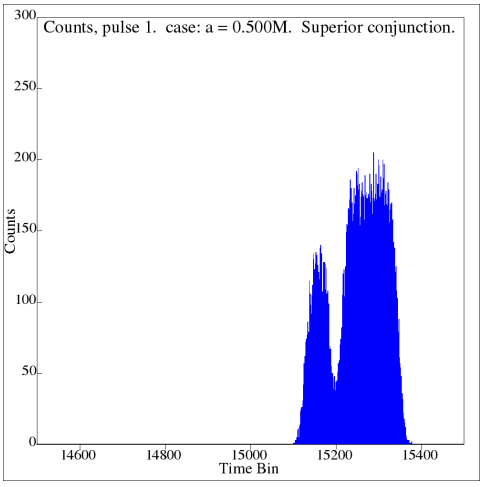

Figure 11.92: Case: a = 0.500M. Superior conjunction photon counts, first pulse.

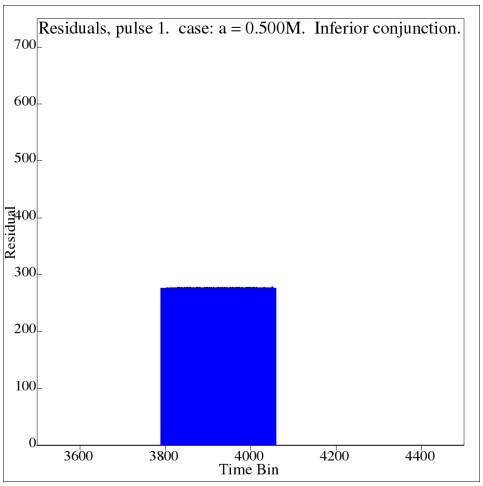

Figure 11.93: Case: a = 0.500M. Inferior conjunction photon timing residuals, first pulse.

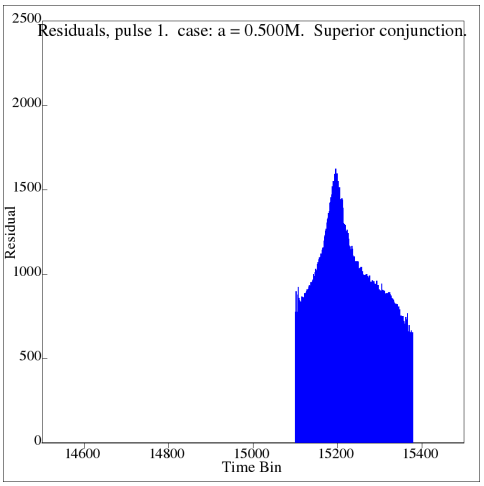

Figure 11.94: Case: a = 0.500M. Superior conjunction photon timing residuals, first pulse.

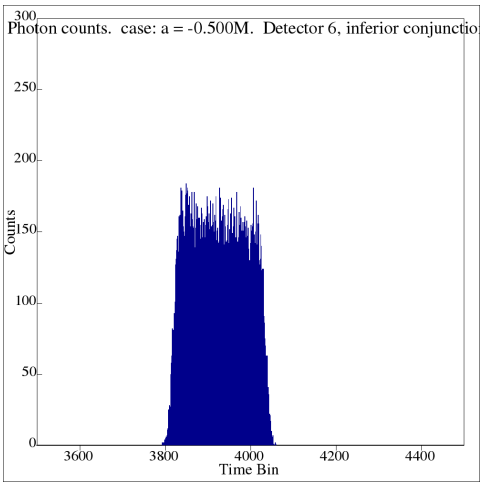

Figure 11.95: Case: a = -0.500M. Inferior conjunction photon counts, first pulse.

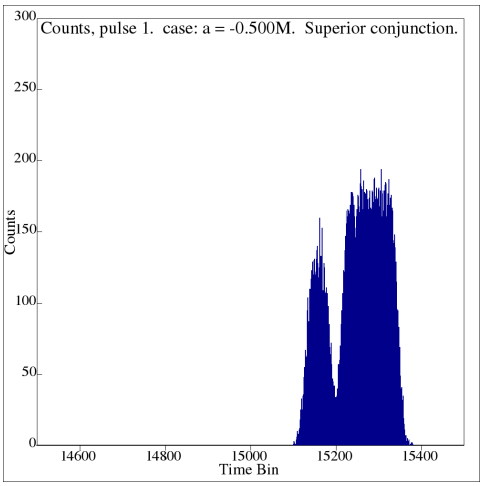

Figure 11.96: Case: a = -0.500M. Superior conjunction photon counts, first pulse.

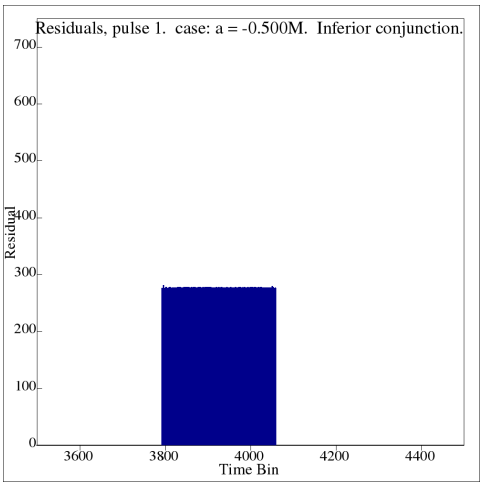

Figure 11.97: Case: a = -0.500M. Inferior conjunction photon timing residuals, first pulse.

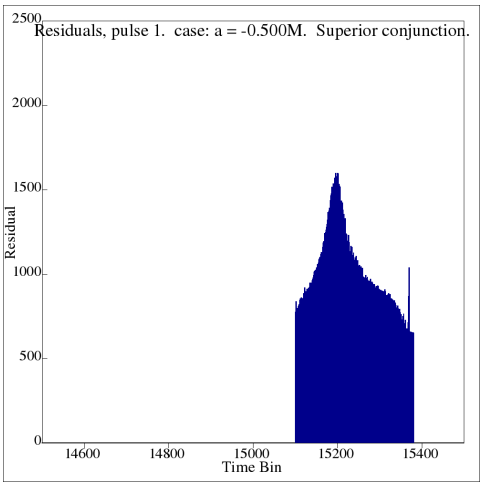

Figure 11.98: Case: a = -0.500M. Superior conjunction photon timing residuals, first pulse.

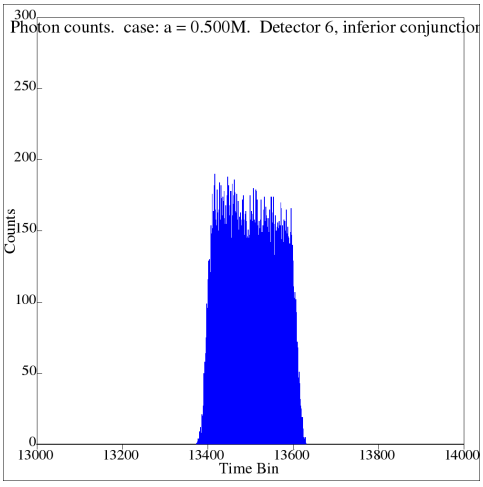

Figure 11.99: Case: a = 0.500M. Inferior conjunction photon counts, second pulse.

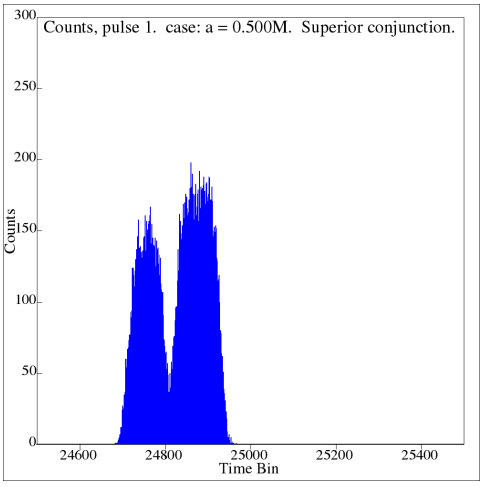

Figure 11.100: Case: a = 0.500M. Superior conjunction photon counts, second pulse.

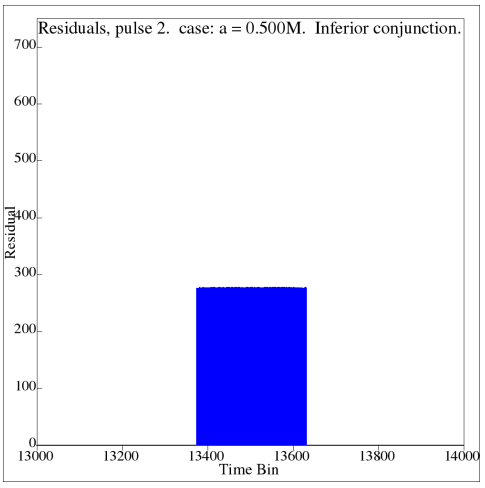

Figure 11.101: Case: a = 0.500M. Inferior conjunction photon timing residuals, second pulse.

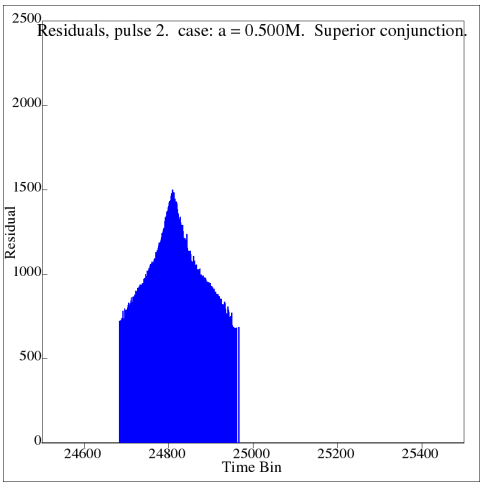

Figure 11.102: Case: a = 0.500M. Superior conjunction photon timing residuals, second pulse.

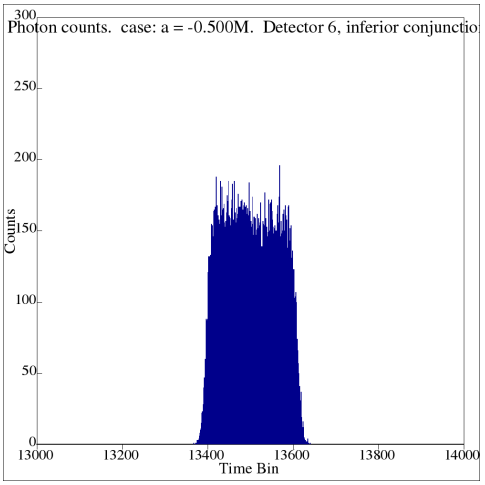

Figure 11.103: Case: a = -0.500M. Inferior conjunction photon counts, second pulse.

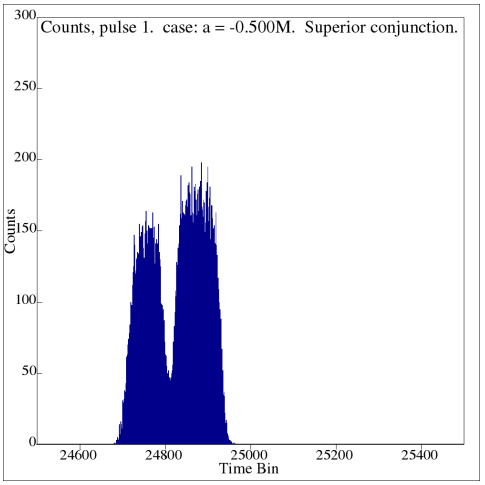

Figure 11.104: Case: a = -0.500M. Superior conjunction photon counts, second pulse.

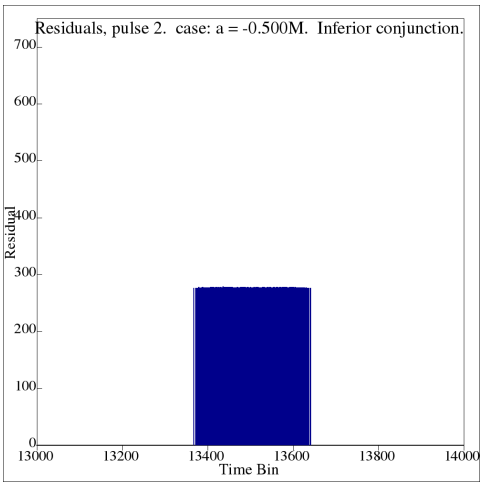

Figure 11.105: Case: a = -0.500M. Inferior conjunction photon timing residuals, second pulse.

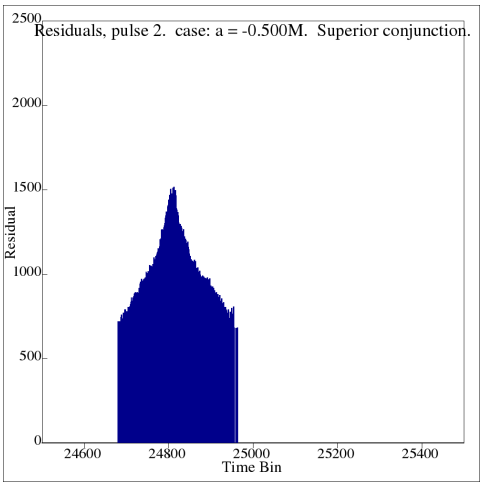

Figure 11.106: Case: a = -0.500M. Superior conjunction photon timing residuals, second pulse.

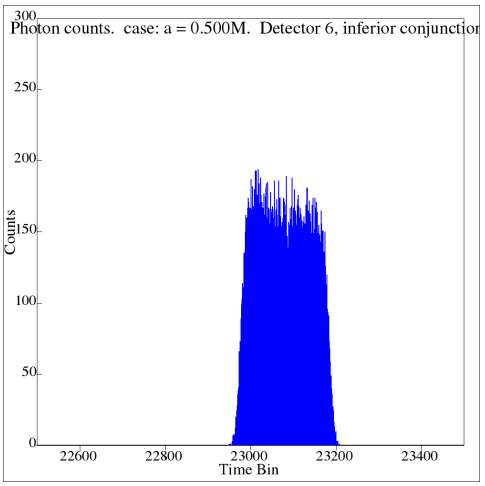

Figure 11.107: Case: a = 0.500M. Inferior conjunction photon counts, third pulse.

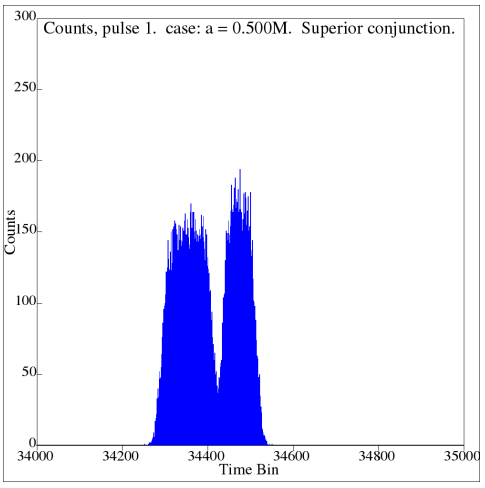

Figure 11.108: Case: a = 0.500M. Superior conjunction photon counts, third pulse.

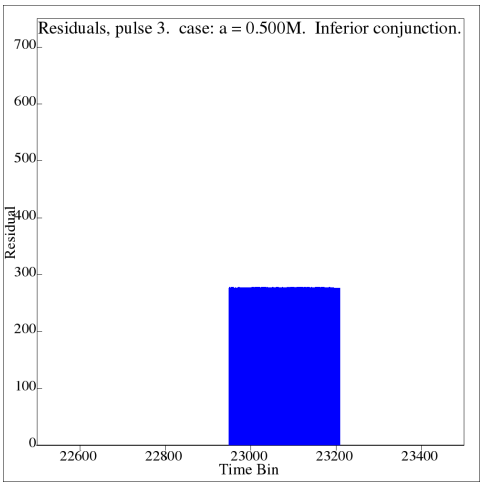

Figure 11.109: Case: a = 0.500M. Inferior conjunction photon timing residuals, third pulse.

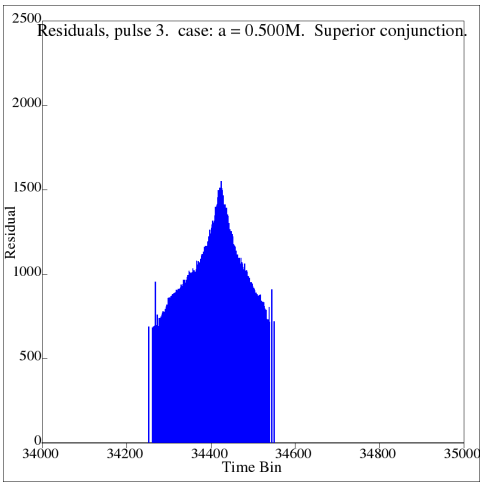

Figure 11.110: Case: a = 0.500M. Superior conjunction photon timing residuals, third pulse.

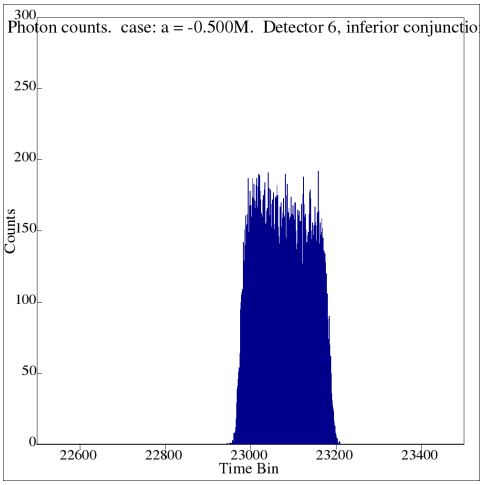

Figure 11.111: Case: a = -0.500M. Inferior conjunction photon counts, third pulse.

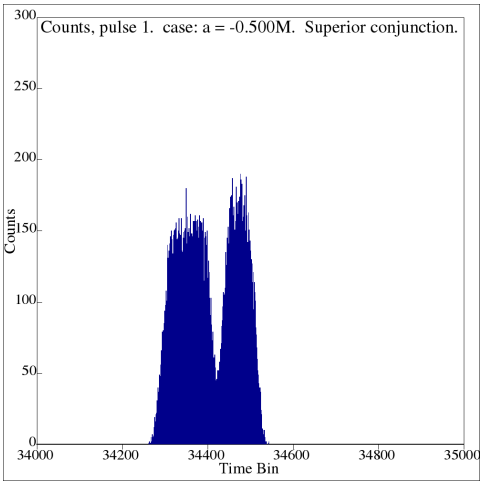

Figure 11.112: Case: a = -0.500M. Superior conjunction photon counts, third pulse.

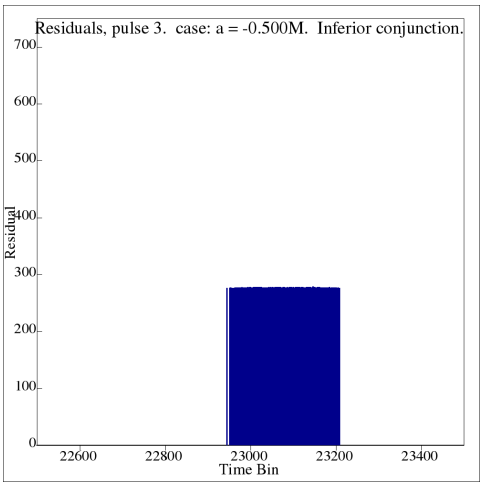

Figure 11.113: Case: a = -0.500M. Inferior conjunction photon timing residuals, third pulse.

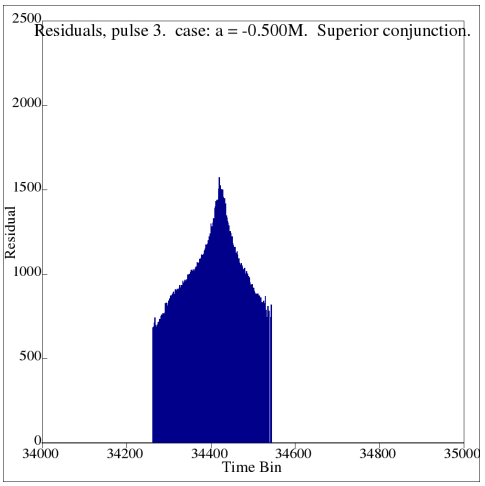

Figure 11.114: Case: a = -0.500M. Superior conjunction photon timing residuals, third pulse.

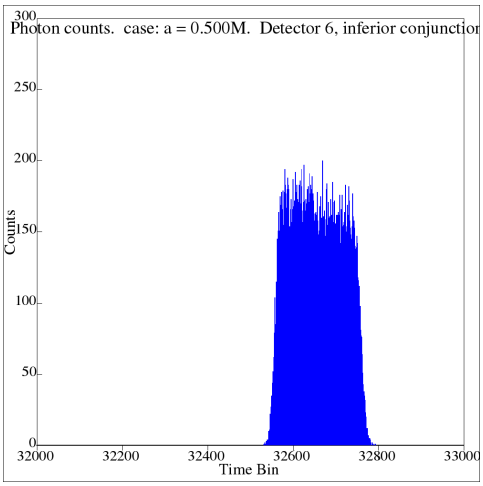

Figure 11.115: Case: a = 0.500M. Inferior conjunction photon counts, fourth pulse.

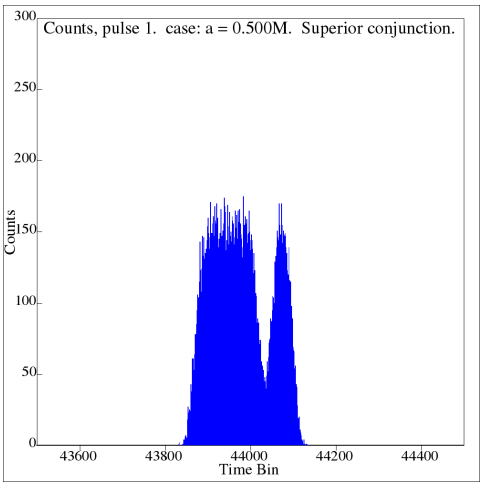

Figure 11.116: Case: a = 0.500M. Superior conjunction photon counts, fourth pulse.

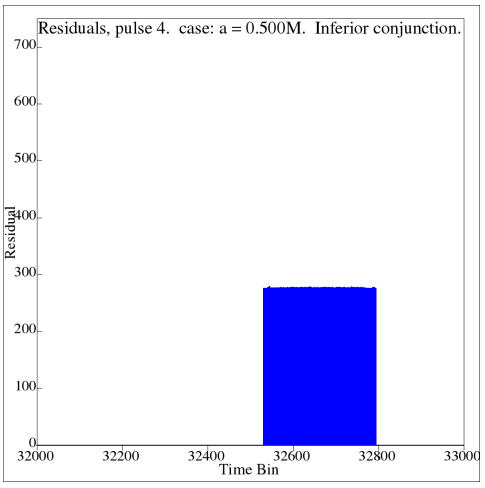

Figure 11.117: Case: a = 0.500M. Inferior conjunction photon timing residuals, fourth pulse.

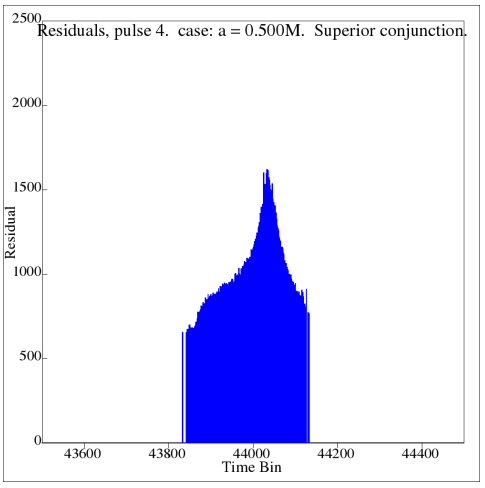

Figure 11.118: Case: a = 0.500M. Superior conjunction photon timing residuals, fourth pulse.

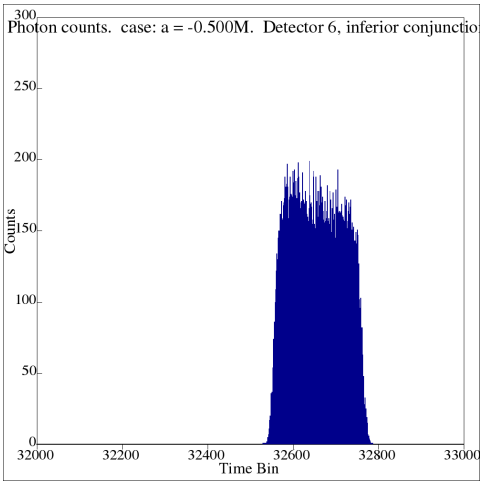

Figure 11.119: Case: a = -0.500M. Inferior conjunction photon counts, fourth pulse.

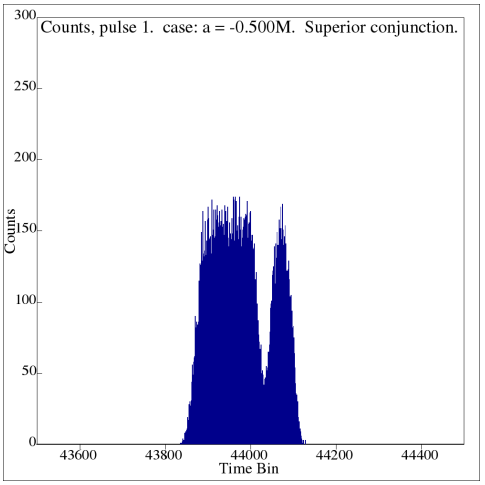

Figure 11.120: Case: a = -0.500M. Superior conjunction photon counts, fourth pulse.

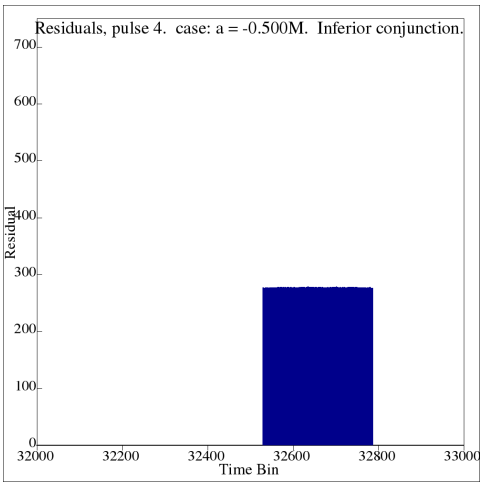

Figure 11.121: Case: a = -0.500M. Inferior conjunction photon timing residuals, fourth pulse.

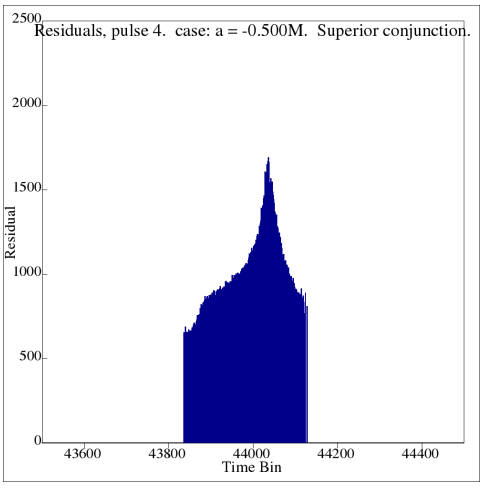

Figure 11.122: Case: a = -0.500M. Superior conjunction photon timing residuals, fourth pulse.

This concludes the presentation of photon count and timing residual output for the cases $a = \pm 0.500M$. The next cases to be presented are those of $a = \pm 0.750M$.

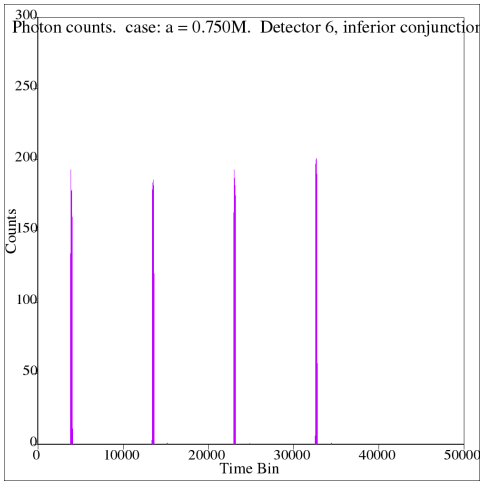

Figure 11.123: case: a = 0.750M. Inferior conjunction photon counts.

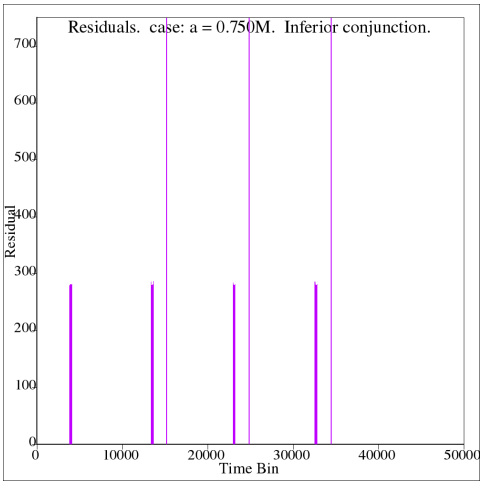

Figure 11.124: case: a = 0.750M. Inferior conjunction photon timing residuals.

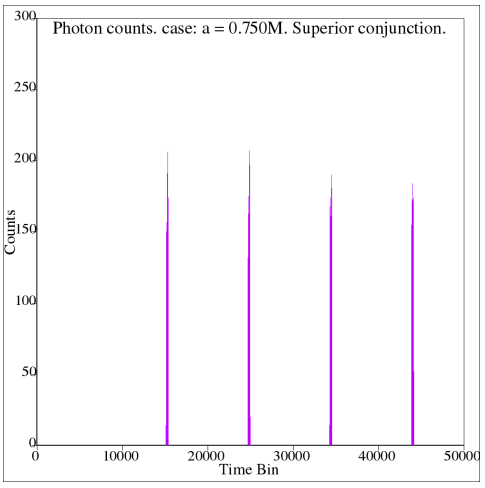

Figure 11.125: case: a = 0.750M. Superior conjunction photon counts.

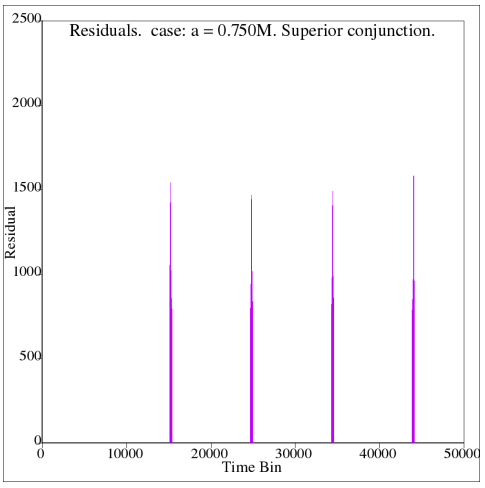

Figure 11.126: case: a = 0.750M. Superior conjunction photon timing residuals.

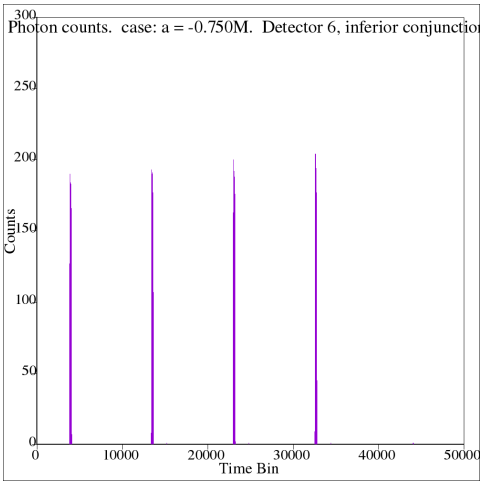

Figure 11.127: case: a = -0.750M. Inferior conjunction photon counts.

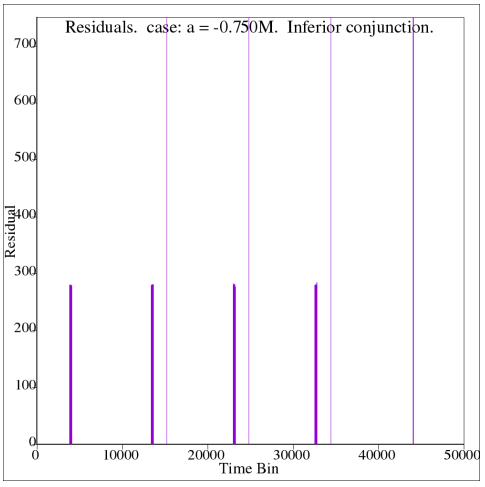

Figure 11.128: case: a = -0.750M. Inferior conjunction photon timing residuals.

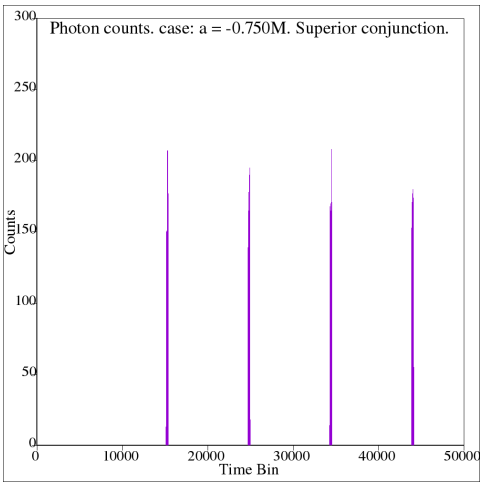

Figure 11.129: case: a = -0.750M. Superior conjunction photon counts.

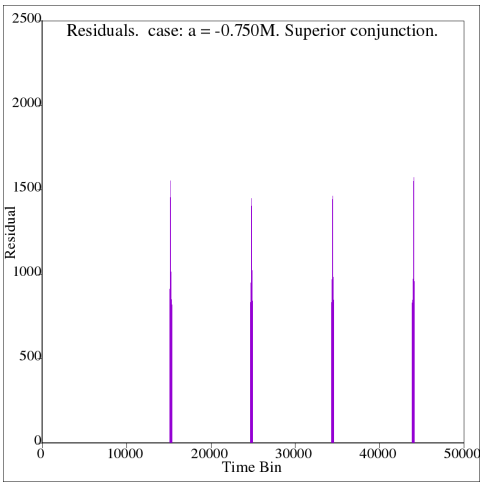

Figure 11.130: case: a = -0.750M. Superior conjunction photon timing residuals.

Individual pulse close-up output for the cases $a = \pm 0.500M$ is presented below.

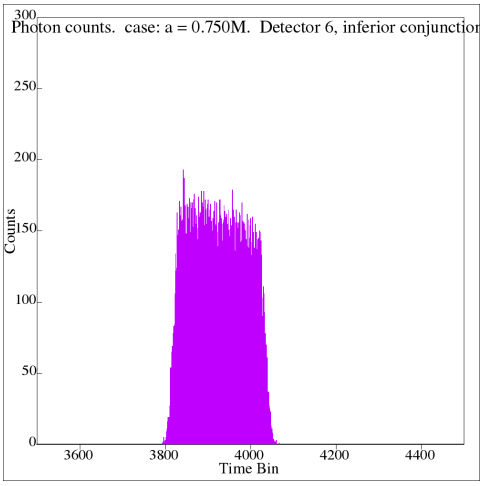

Figure 11.131: case: a = 0.750M. Inferior conjunction photon counts, first pulse.

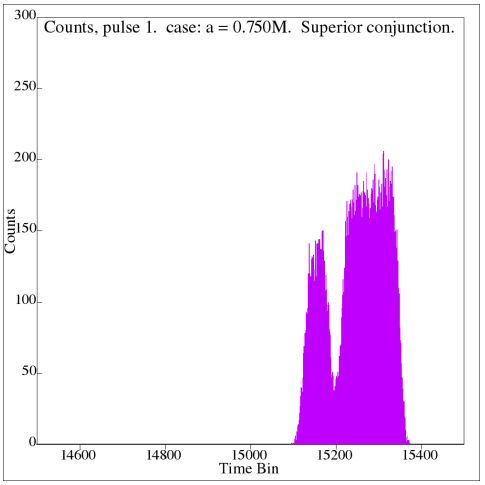

Figure 11.132: case: a = 0.750M. Superior conjunction photon counts, first pulse.

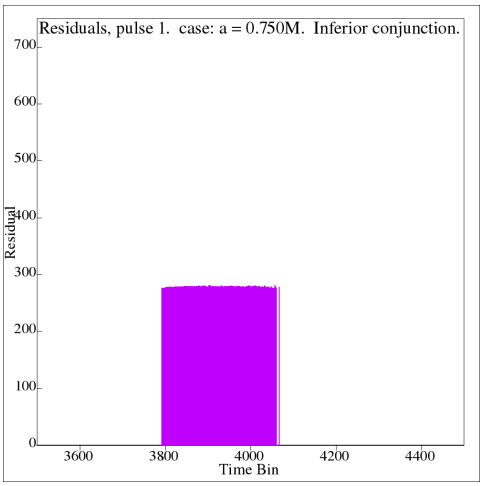

Figure 11.133: case: a = 0.750M. Inferior conjunction photon timing residuals, first pulse.

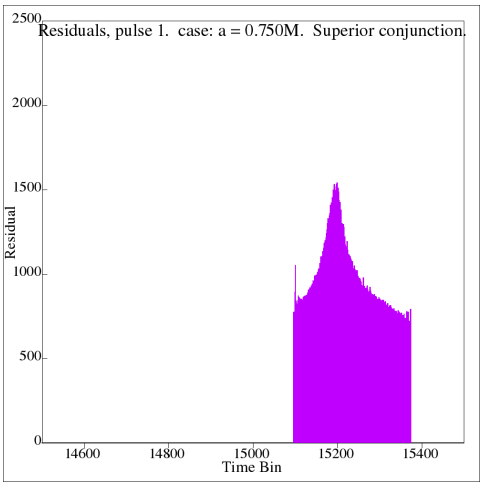

Figure 11.134: case: a = 0.750M. Superior conjunction photon timing residuals, first pulse.

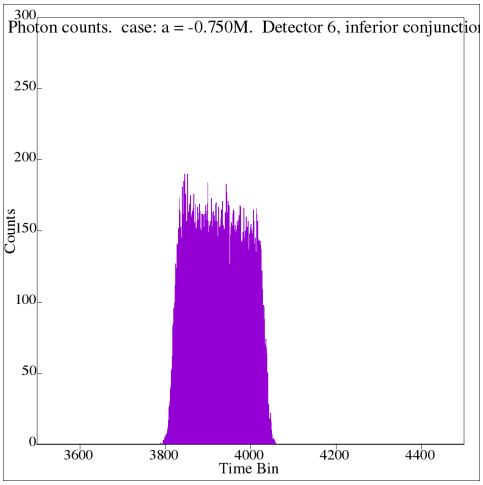

Figure 11.135: case: a = -0.750M. Inferior conjunction photon counts, first pulse.

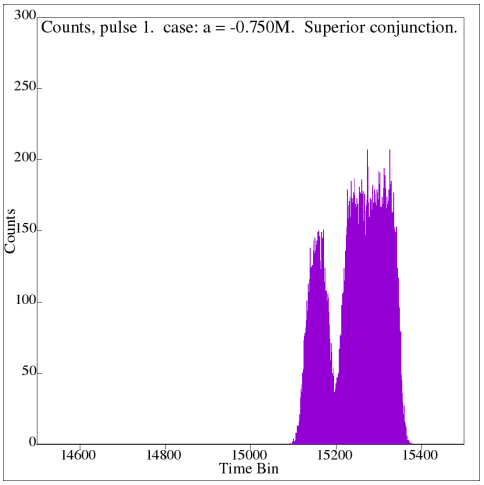

Figure 11.136: case: a = -0.750M. Superior conjunction photon counts, first pulse.

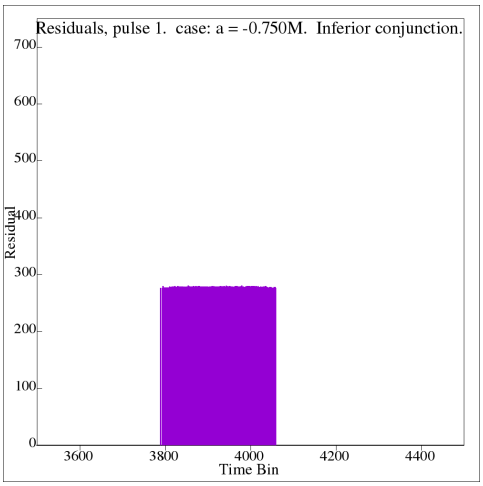

Figure 11.137: case: a = -0.750M. Inferior conjunction photon timing residuals, first pulse.

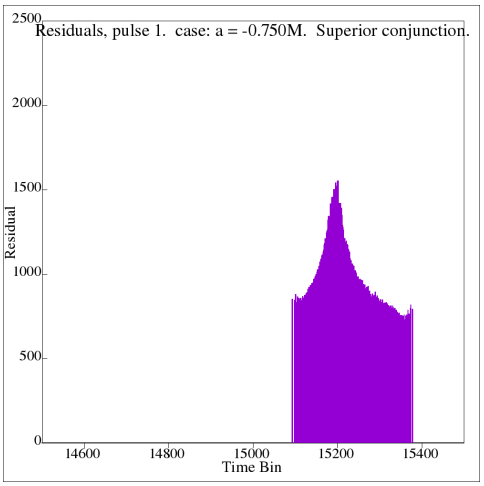

Figure 11.138: case: a = -0.750M. Superior conjunction photon timing residuals, first pulse.

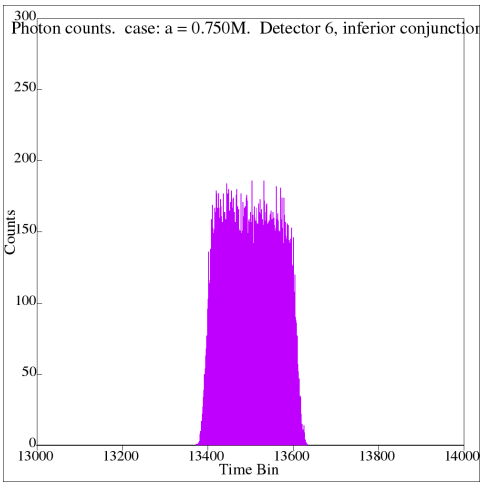

Figure 11.139: case: a = 0.750M. Inferior conjunction photon counts, second pulse.

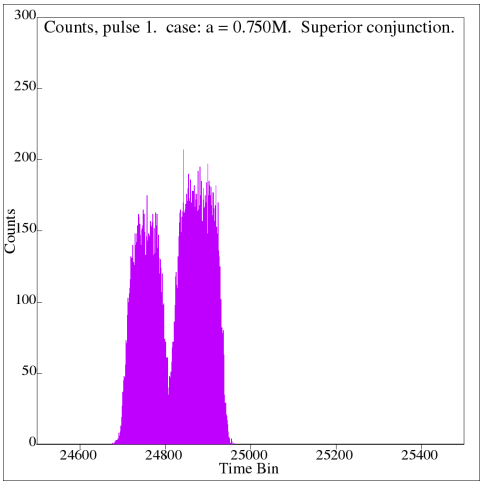

Figure 11.140: case: a = 0.750M. Superior conjunction photon counts, second pulse.

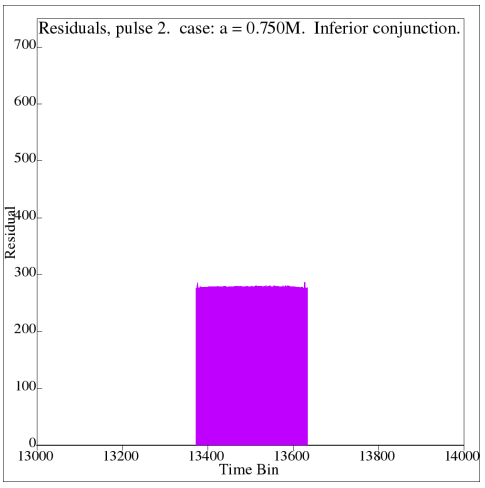

Figure 11.141: case: a = 0.750M. Inferior conjunction photon timing residuals, second pulse.

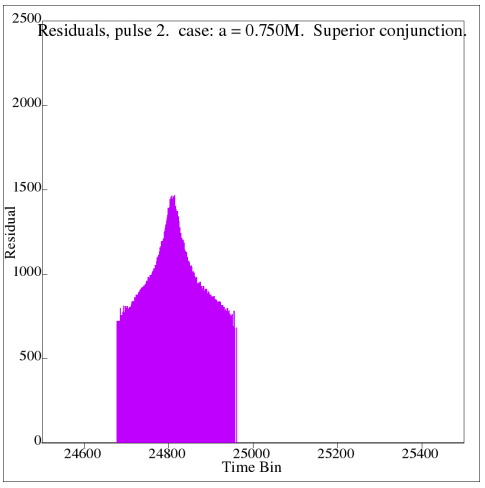

Figure 11.142: case: a = 0.750M. Superior conjunction photon timing residuals, second pulse.

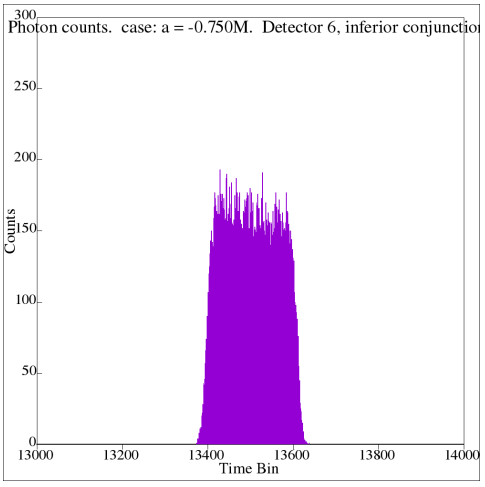

Figure 11.143: case: a = -0.750M. Inferior conjunction photon counts, second pulse.

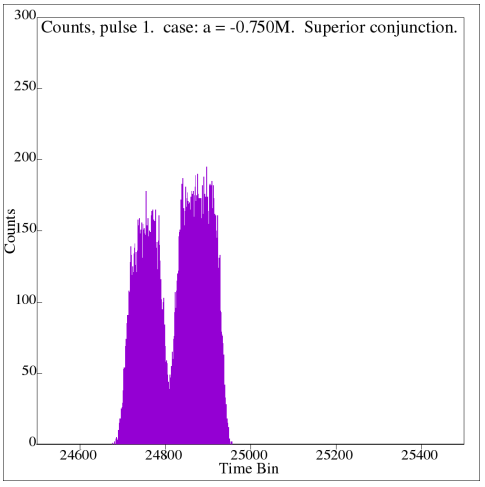

Figure 11.144: case: a = -0.750M. Superior conjunction photon counts, second pulse.

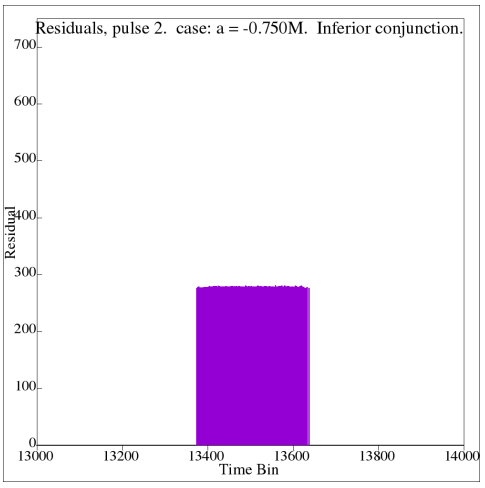

Figure 11.145: case: a = -0.750M. Inferior conjunction photon timing residuals, second pulse.

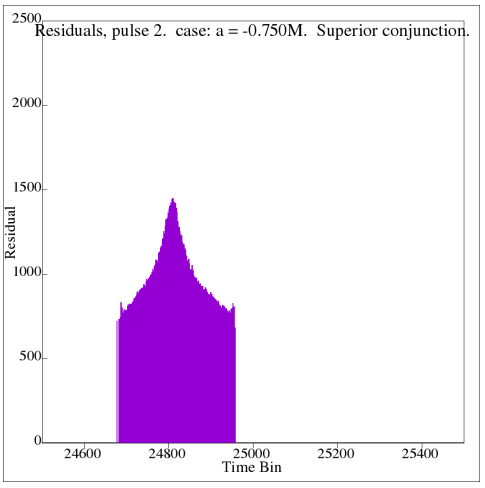

Figure 11.146: case: a = -0.750M. Superior conjunction photon timing residuals, second pulse.

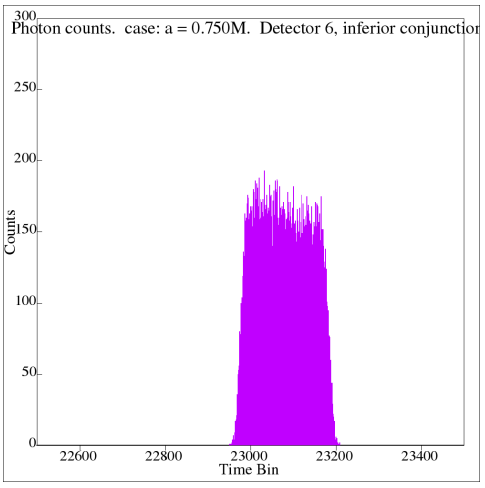

Figure 11.147: case: a = 0.750M. Inferior conjunction photon counts, third pulse.

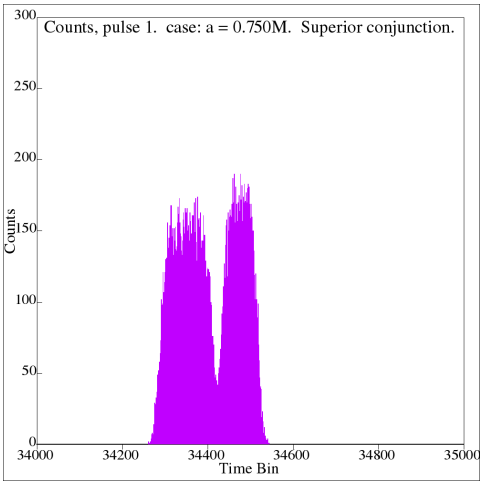

Figure 11.148: case: a = 0.750M. Superior conjunction photon counts, third pulse.

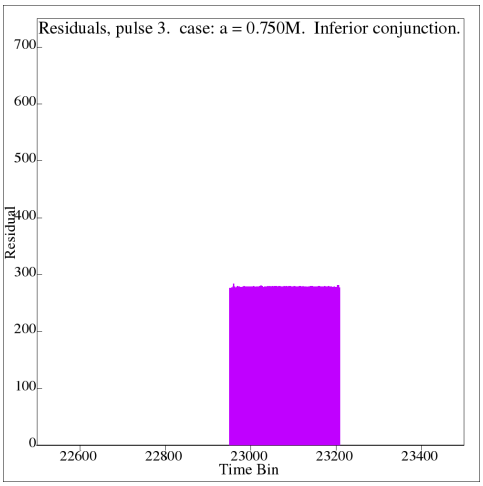

Figure 11.149: case: a = 0.750M. Inferior conjunction photon timing residuals, third pulse.

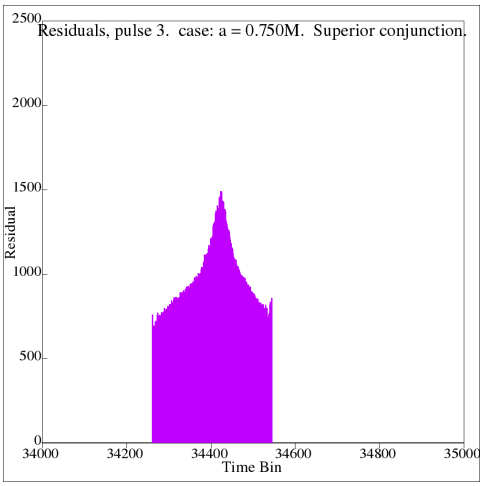

Figure 11.150: case: a = 0.750M. Superior conjunction photon timing residuals, third pulse.

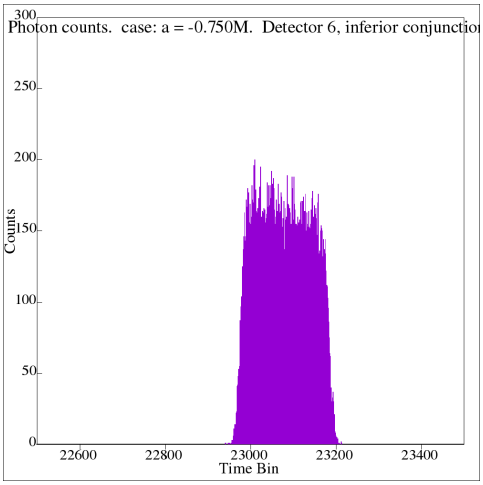

Figure 11.151: case: a = -0.750M. Inferior conjunction photon counts, third pulse.

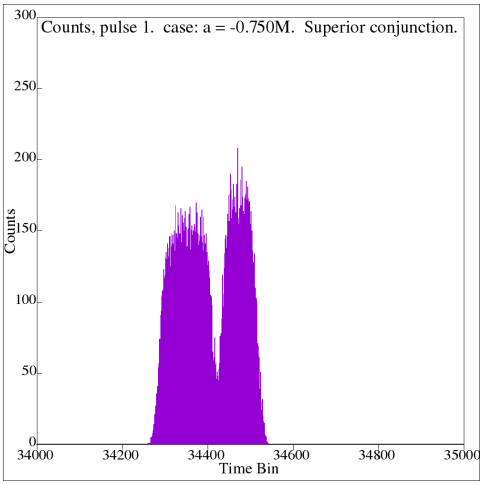

Figure 11.152: case: a = -0.750M. Superior conjunction photon counts, third pulse.

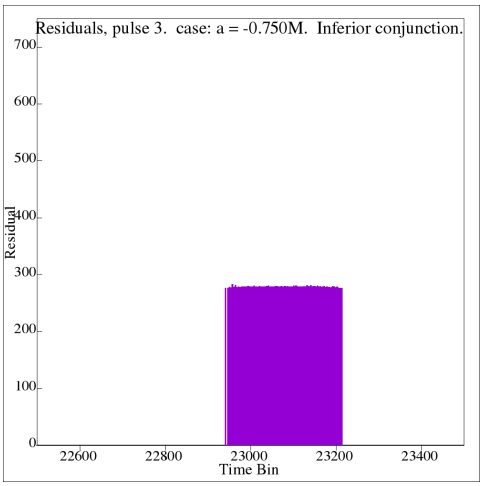

Figure 11.153: case: a = -0.750M. Inferior conjunction photon timing residuals, third pulse.

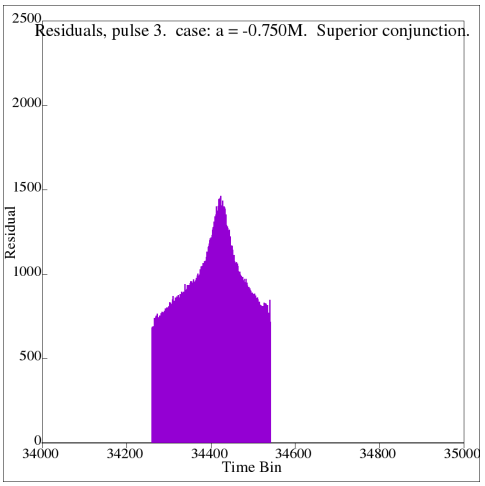

Figure 11.154: case: a = -0.750M. Superior conjunction photon timing residuals, third pulse.

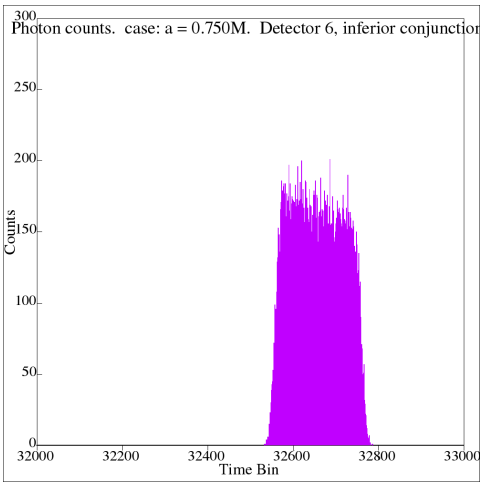

Figure 11.155: case: a = 0.750M. Inferior conjunction photon counts, fourth pulse.

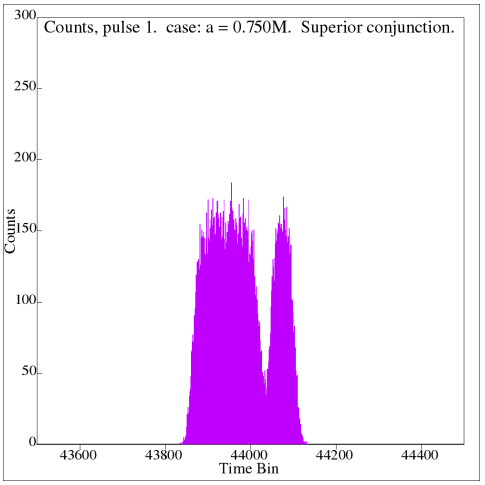

Figure 11.156: case: a = 0.750M. Superior conjunction photon counts, fourth pulse.

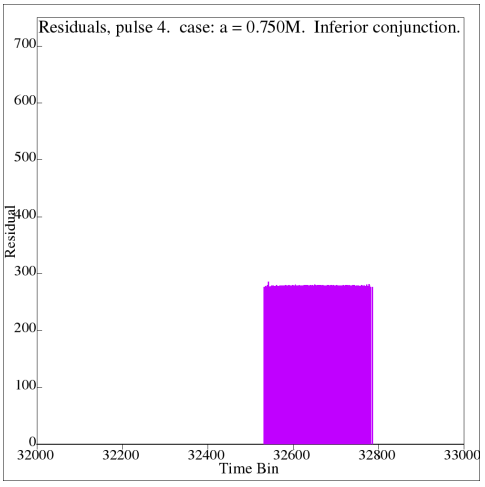

Figure 11.157: case: a = 0.750M. Inferior conjunction photon timing residuals, fourth pulse.

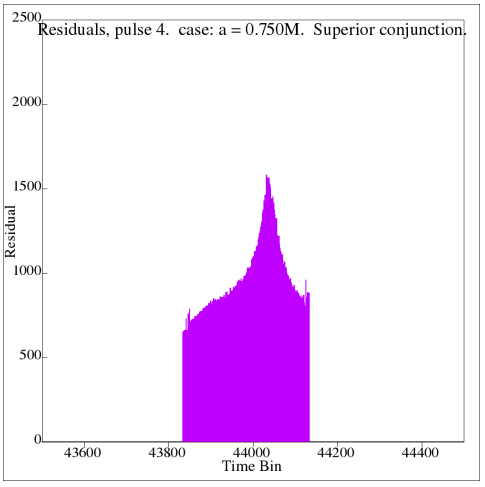

Figure 11.158: case: a = 0.750M. Superior conjunction photon timing residuals, fourth pulse.

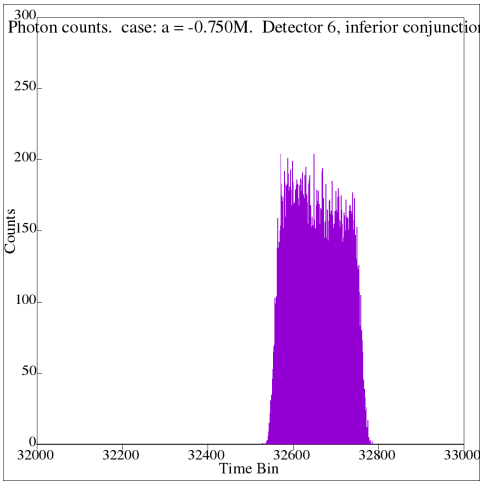

Figure 11.159: case: a = -0.750M. Inferior conjunction photon counts, fourth pulse.

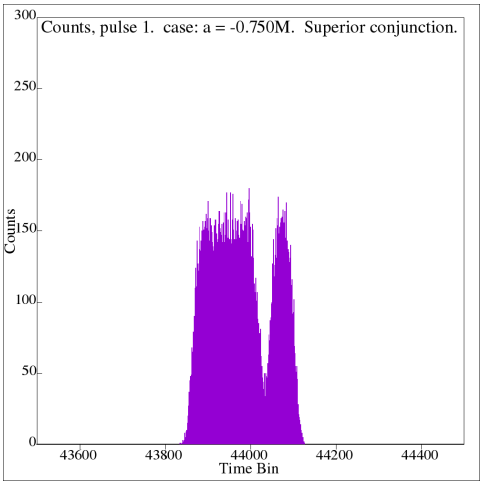

Figure 11.160: case: a = -0.750M. Superior conjunction photon counts, fourth pulse.

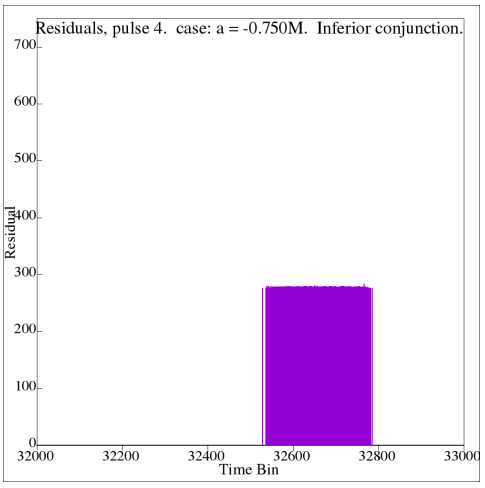

Figure 11.161: case: a = -0.750M. Inferior conjunction photon timing residuals, fourth pulse.

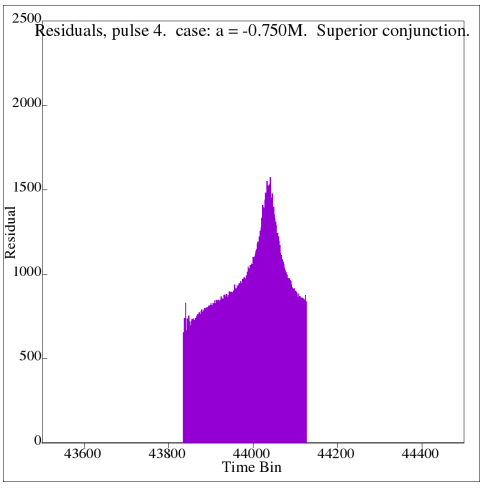

Figure 11.162: case: a = -0.750M. Superior conjunction photon timing residuals, fourth pulse.

This concludes the presentation of photon count and timing residual output for the cases $a = \pm 0.750M$. The next cases to be presented are those of the extremal rotation cases: $a = \pm 0.998M$.

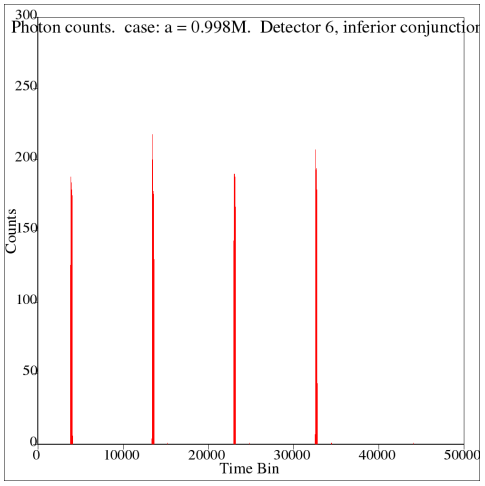

Figure 11.163: case: a = 0.998M. Inferior conjunction photon counts.

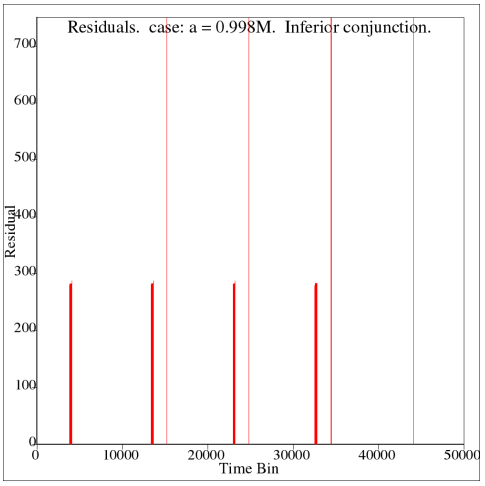

Figure 11.164: case: a = 0.998M. Inferior conjunction photon timing residuals.

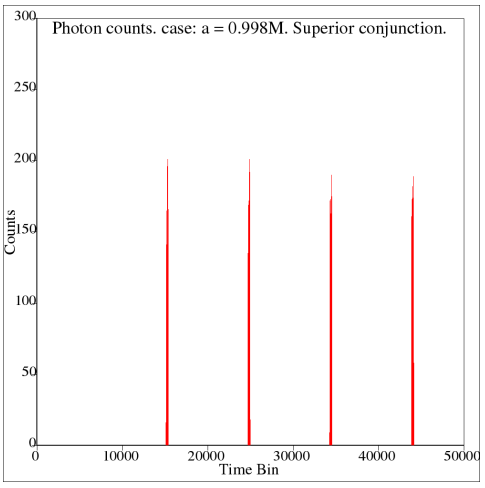

Figure 11.165: case: a = 0.998M. Superior conjunction photon counts.

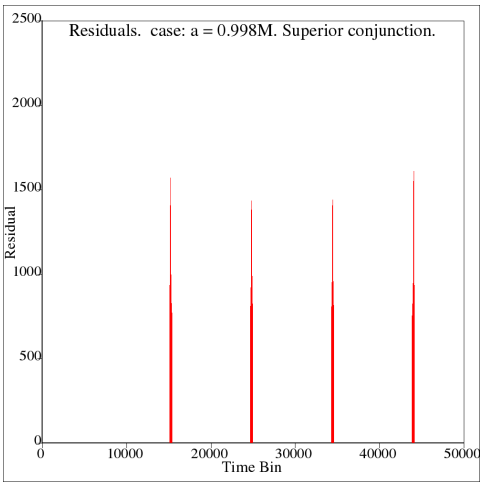

Figure 11.166: case: a = 0.998M. Superior conjunction photon timing residuals.

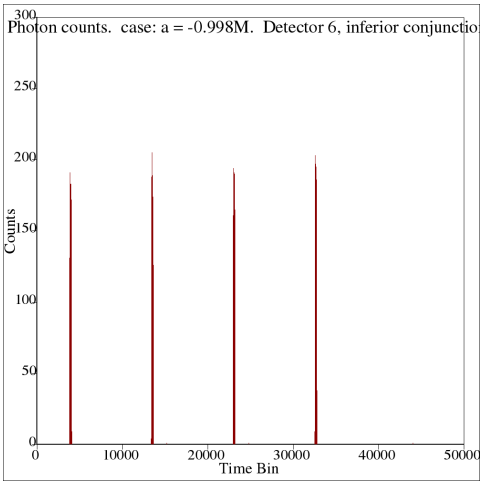

Figure 11.167: case: a = -0.998M. Inferior conjunction photon counts.

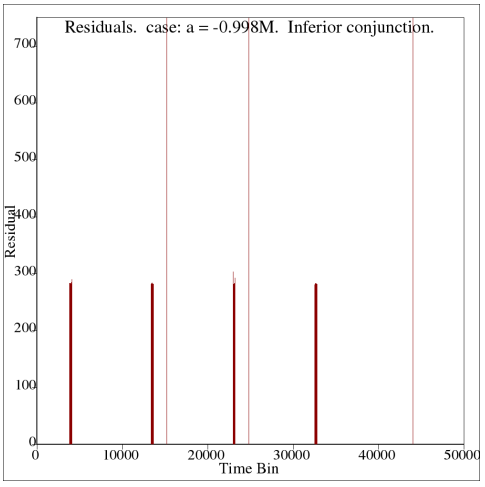

Figure 11.168: case: a = -0.998M. Inferior conjunction photon timing residuals.

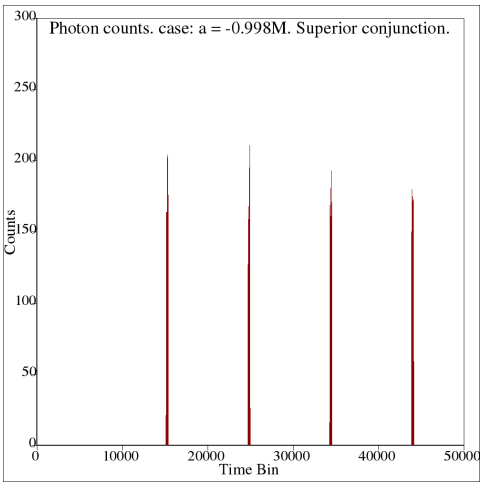

Figure 11.169: case: a = -0.998M. Superior conjunction photon counts.

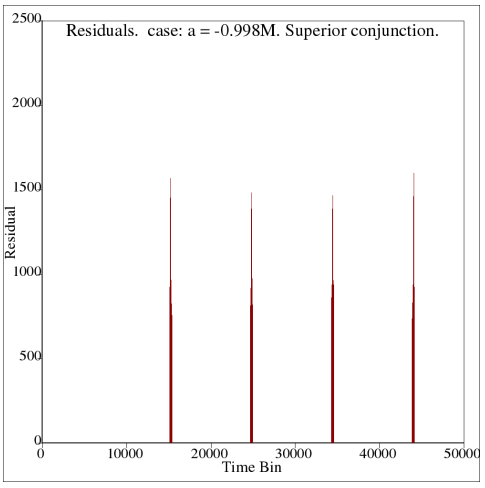

Figure 11.170: case: a = -0.998M. Superior conjunction photon timing residuals.

Individual pulse close-up output for the extremal rotational cases $a = \pm 0.998M$ is presented below.

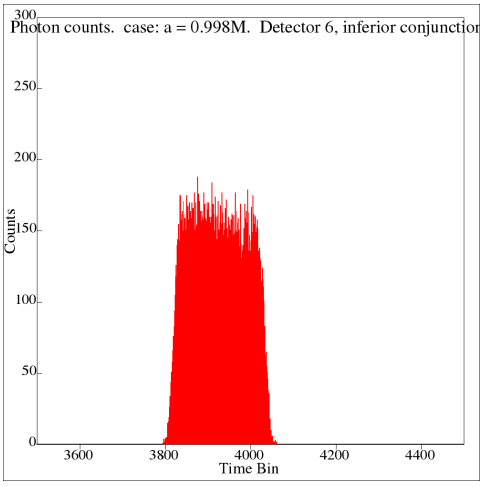

Figure 11.171: case: a = 0.998M. Inferior conjunction photon counts, first pulse.

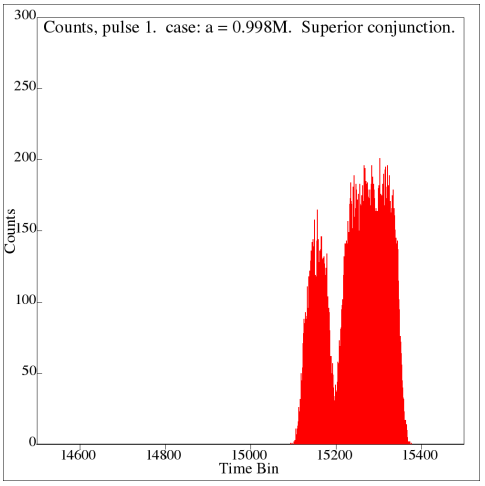

Figure 11.172: case: a = 0.998M. Superior conjunction photon counts, first pulse.

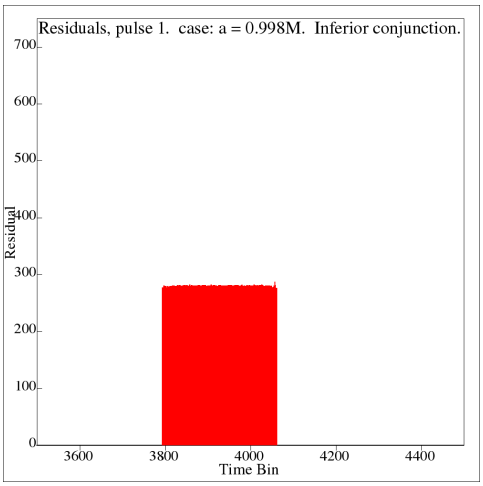

Figure 11.173: case: a = 0.998M. Inferior conjunction photon timing residuals, first pulse.

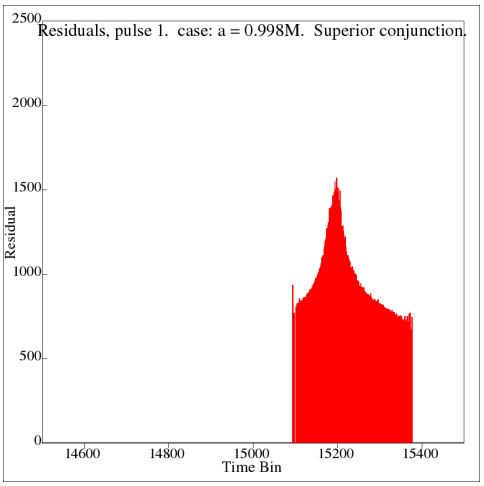

Figure 11.174: case: a = 0.998M. Superior conjunction photon timing residuals, first pulse.

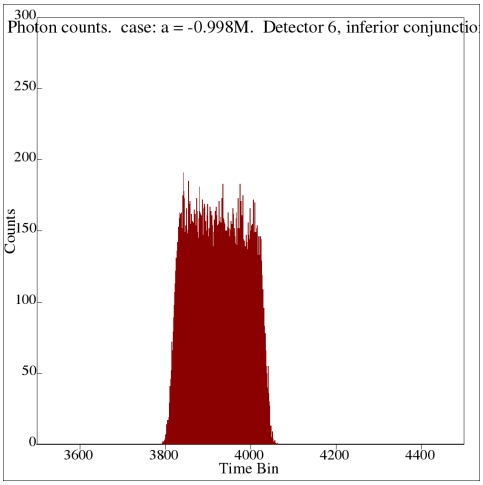

Figure 11.175: case: a = -0.998M. Inferior conjunction photon counts, first pulse.

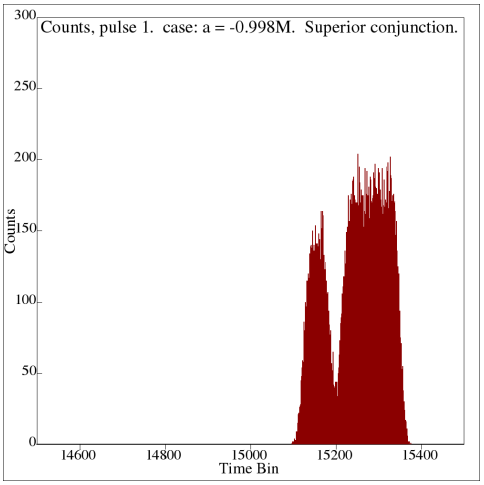

Figure 11.176: case: a = -0.998M. Superior conjunction photon counts, first pulse.

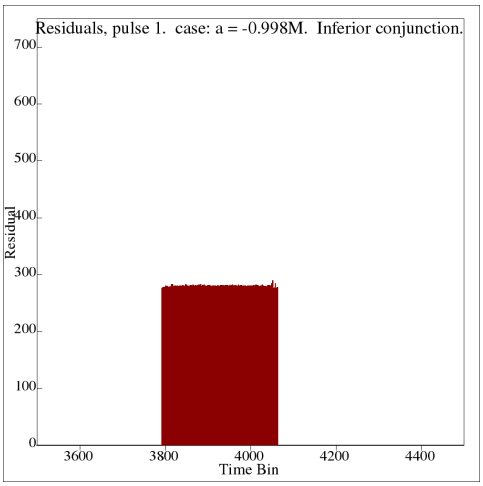

Figure 11.177: case: a = -0.998M. Inferior conjunction photon timing residuals, first pulse.

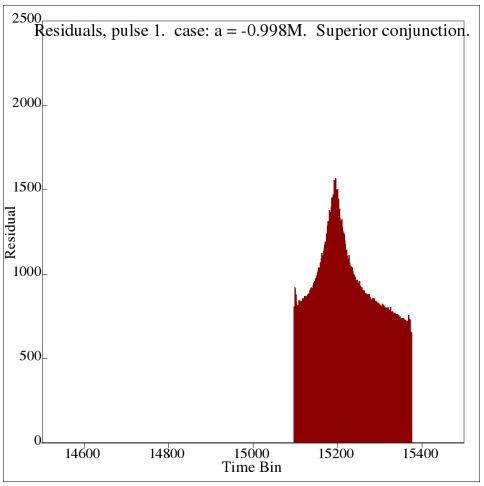

Figure 11.178: case: a = -0.998M. Superior conjunction photon timing residuals, first pulse.

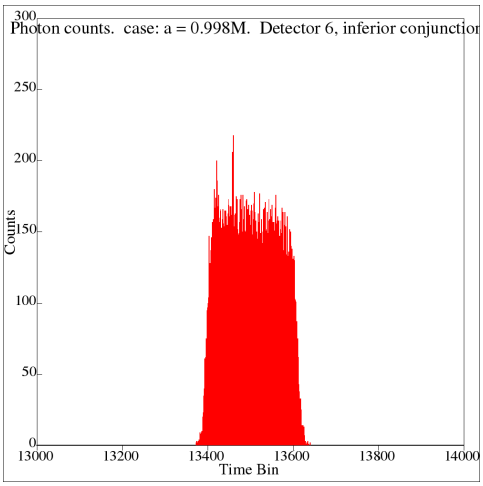

Figure 11.179: case: a = 0.998M. Inferior conjunction photon counts, second pulse.

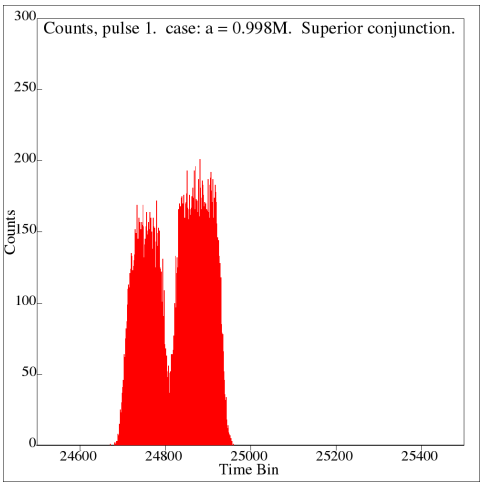

Figure 11.180: case: a = 0.998M. Superior conjunction photon counts, second pulse.

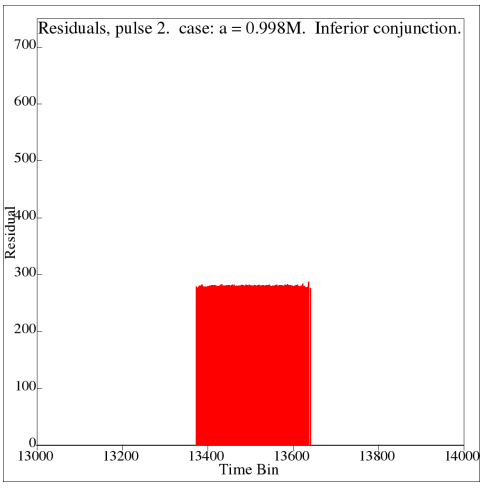

Figure 11.181: case: a = 0.998M. Inferior conjunction photon timing residuals, second pulse.

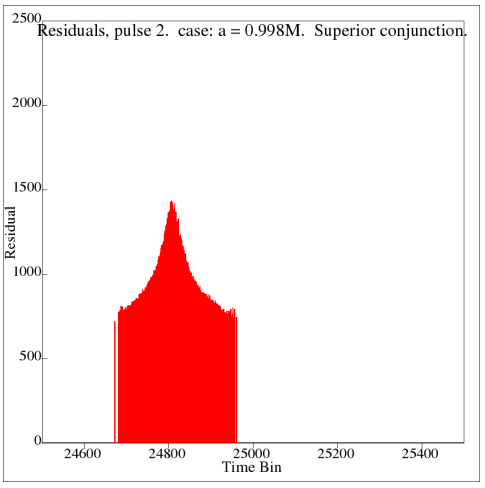

Figure 11.182: case: a = 0.998M. Superior conjunction photon timing residuals, second pulse.

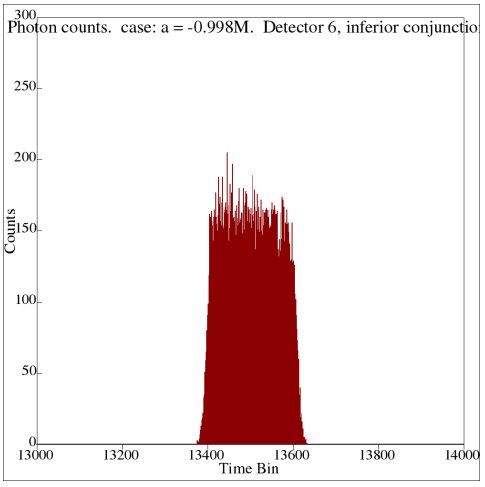

Figure 11.183: case: a = -0.998M. Inferior conjunction photon counts, second pulse.

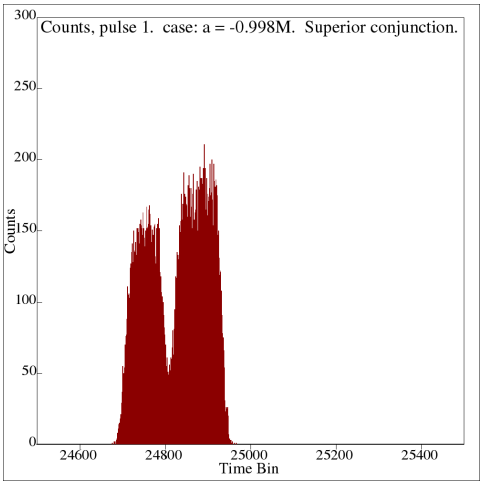

Figure 11.184: case: a = -0.998M. Superior conjunction photon counts, second pulse.

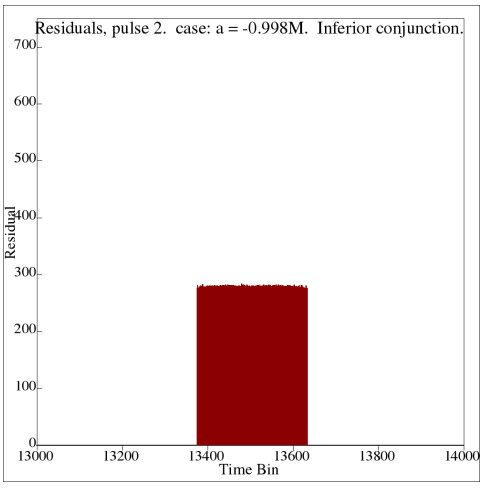

Figure 11.185: case: a = -0.998M. Inferior conjunction photon timing residuals, second pulse.

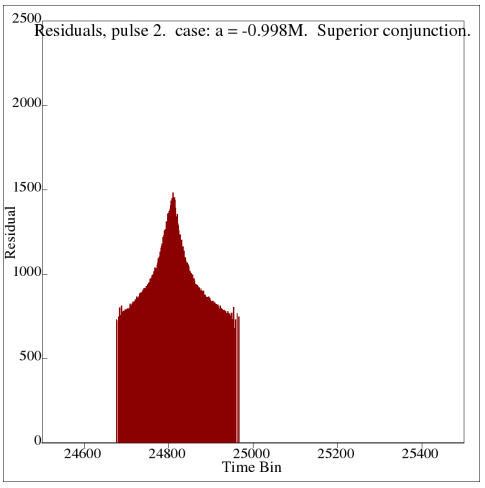

Figure 11.186: case: a = -0.998M. Superior conjunction photon timing residuals, second pulse.

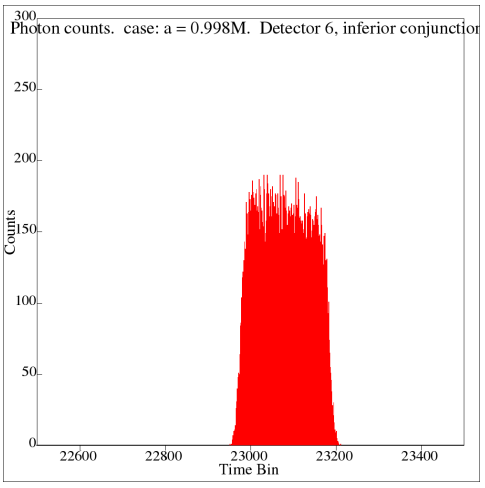

Figure 11.187: case: a = 0.998M. Inferior conjunction photon counts, third pulse.

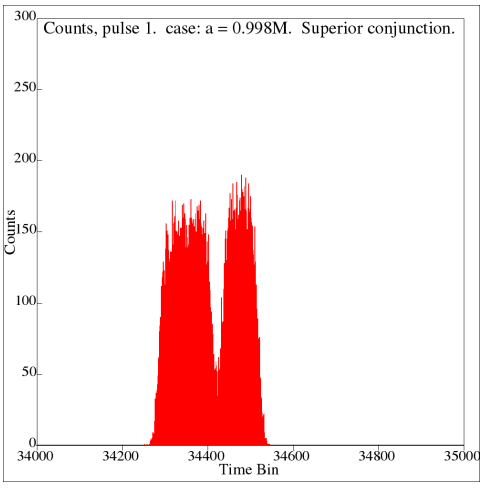

Figure 11.188: case: a = 0.998M. Superior conjunction photon counts, third pulse.

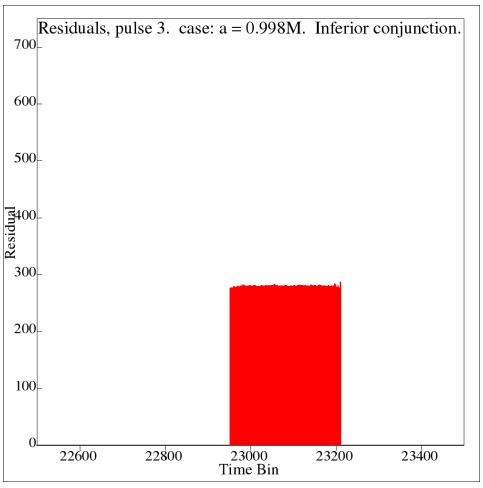

Figure 11.189: case: a = 0.998M. Inferior conjunction photon timing residuals, third pulse.

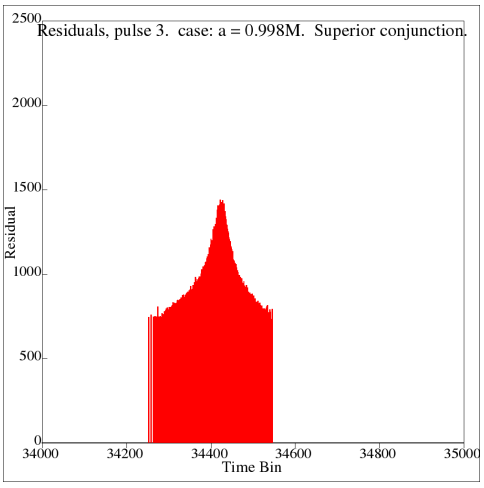

Figure 11.190: case: a = 0.998M. Superior conjunction photon timing residuals, third pulse.

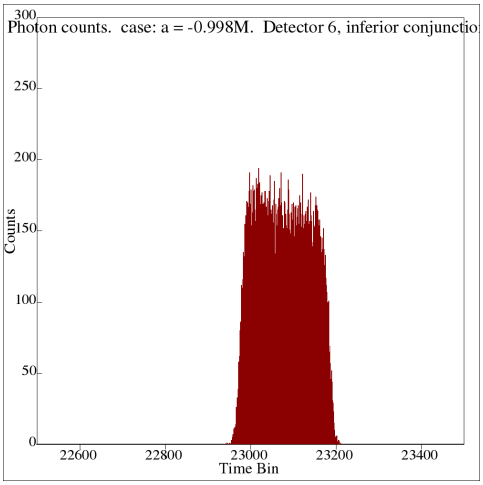

Figure 11.191: case: a = -0.998M. Inferior conjunction photon counts, third pulse.

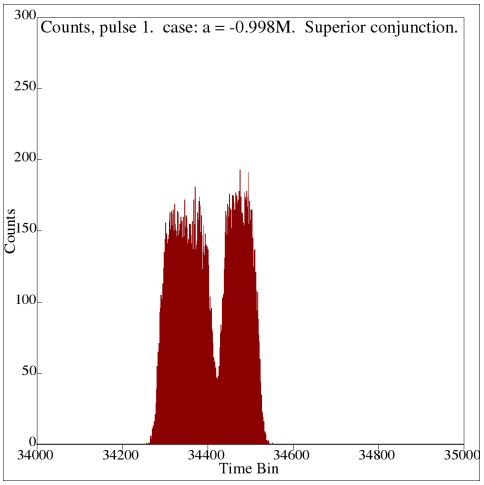

Figure 11.192: case: a = -0.998M. Superior conjunction photon counts, third pulse.

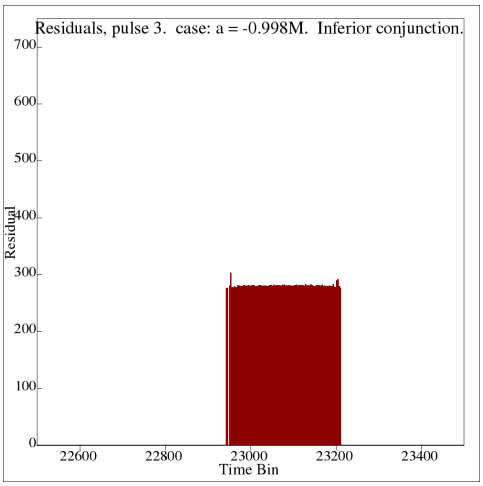

Figure 11.193: case: a = -0.998M. Inferior conjunction photon timing residuals, third pulse.

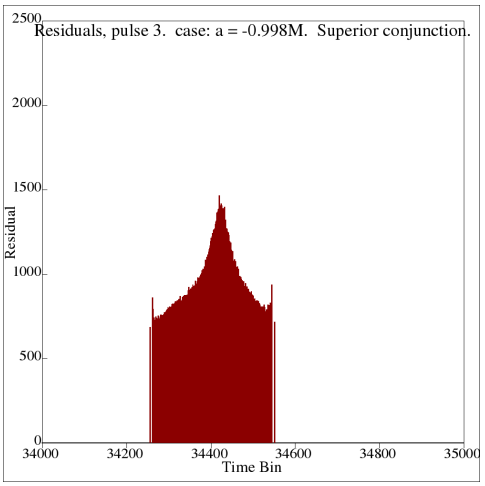

Figure 11.194: case: a = -0.998M. Superior conjunction photon timing residuals, third pulse.

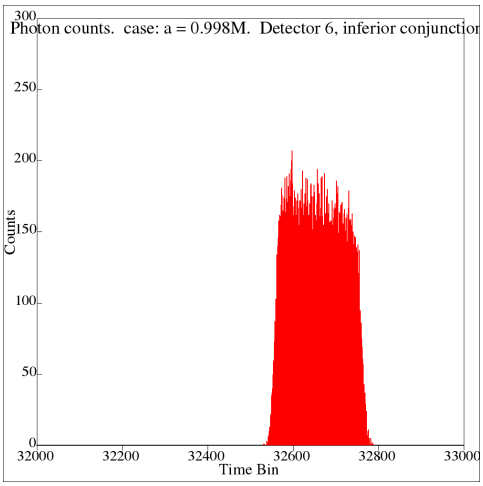

Figure 11.195: case: a = 0.998M. Inferior conjunction photon counts, fourth pulse.

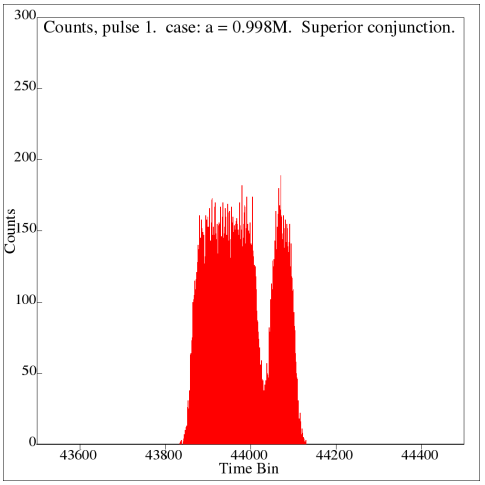

Figure 11.196: case: a = 0.998M. Superior conjunction photon counts, fourth pulse.

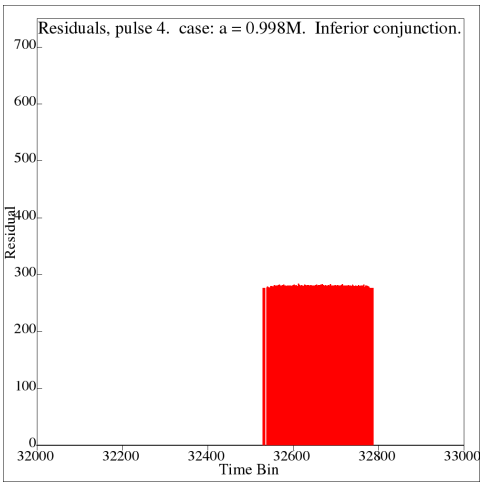

Figure 11.197: case: a = 0.998M. Inferior conjunction photon timing residuals, fourth pulse.

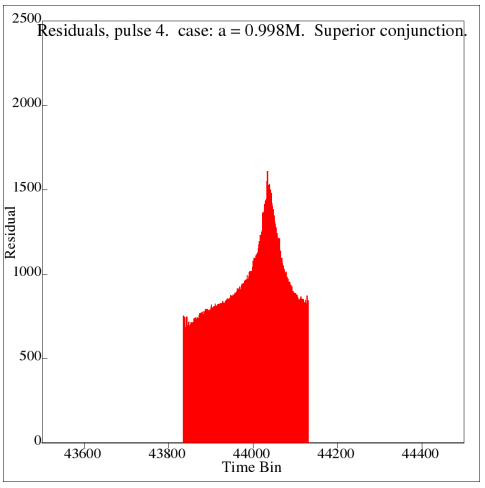

Figure 11.198: case: a = 0.998M. Superior conjunction photon timing residuals, fourth pulse.

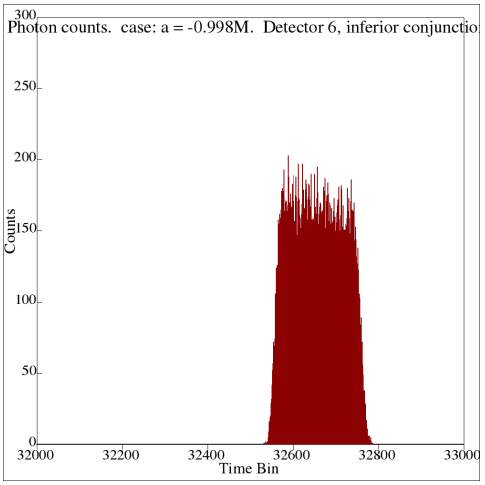

Figure 11.199: case: a = -0.998M. Inferior conjunction photon counts, fourth pulse.

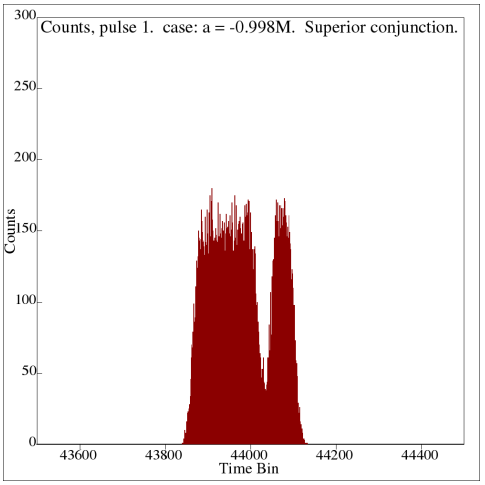

Figure 11.200: case: a = -0.998M. Superior conjunction photon counts, fourth pulse.

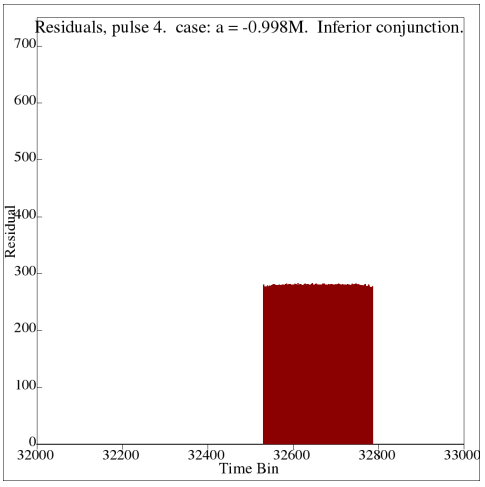

Figure 11.201: case: a = -0.998M. Inferior conjunction photon timing residuals, fourth pulse.

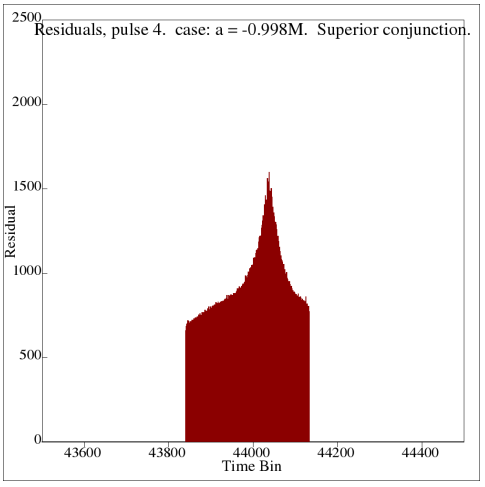

Figure 11.202: case: a = -0.998M. Superior conjunction photon timing residuals, fourth pulse.

Direct comparisons of pulse data are perhaps the best way of observing the effect of increasing black-hole rotational parameter. Superior conjunction data was compared for different cases. The second pulse was selected for comparison, both photon count and timing residual data was used. The first comparison made was between the non-rotating case, and that of the extremally rotating case, since this should illustrate the maximal possible effect of rotation.

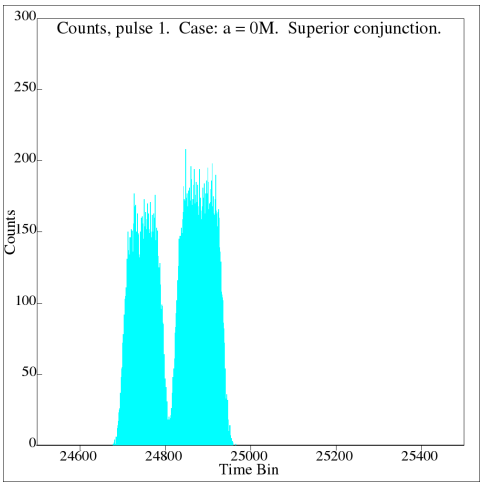

Figure 11.203: Non-rotating case: a = 0. Superior conjunction photon counts, second pulse.

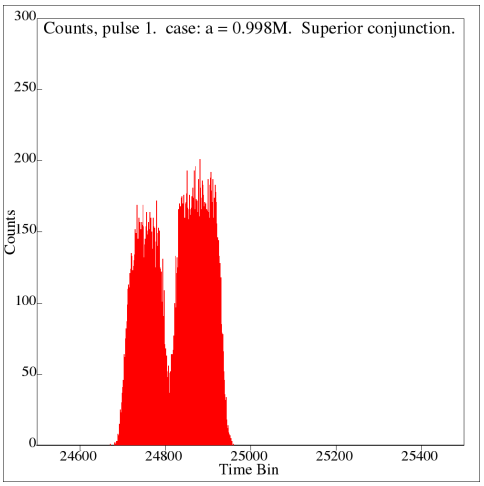

Figure 11.204: case: a = 0.998M. Superior conjunction photon counts, second pulse.

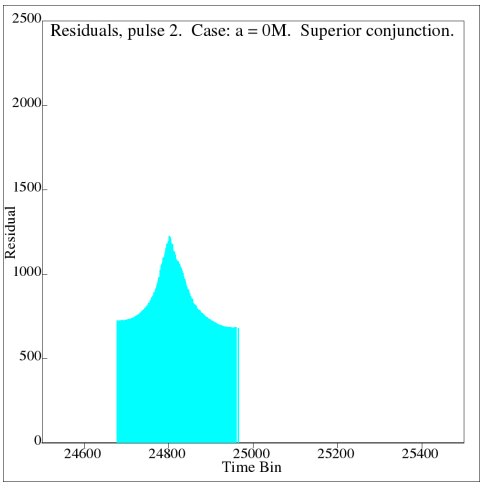

Figure 11.205: Non-rotating case: a = 0. Superior conjunction photon timing residuals, second pulse.

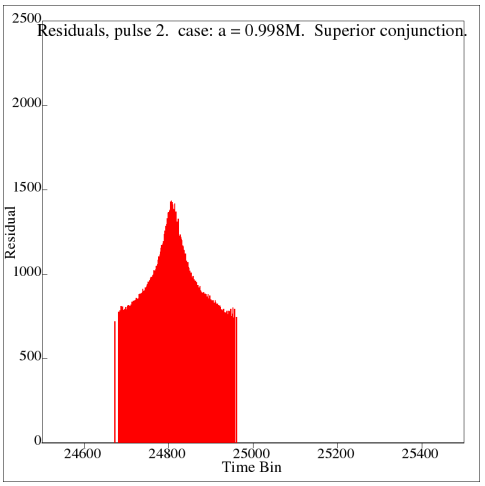

Figure 11.206: case: a = 0.998M. Superior conjunction photon timing residuals, second pulse.

The data above indicates that the width of the trough within the pulse was increased by increasing the rotational parameter of the black-hole. The shape of the residual histogram was only slightly augmented, the magnitude of timing residuals for the maximally rotating case were slightly increased with respect to the Schwarzschild case. The next step is to compare identical black-holes rotating in opposite directions. Two comparisons were made: firstly, the cases $a = \pm 0.500M$ were compared; subsequently the extremal case was used for comparison, as it should emphasize the differences in the data, if any are descernable.

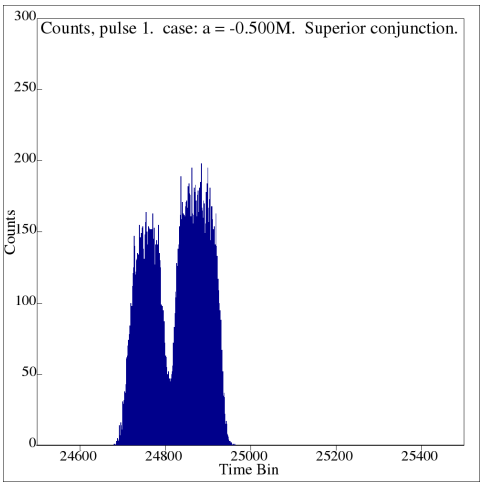

Figure 11.207: Case: a = -0.500M. Superior conjunction photon counts, second pulse.

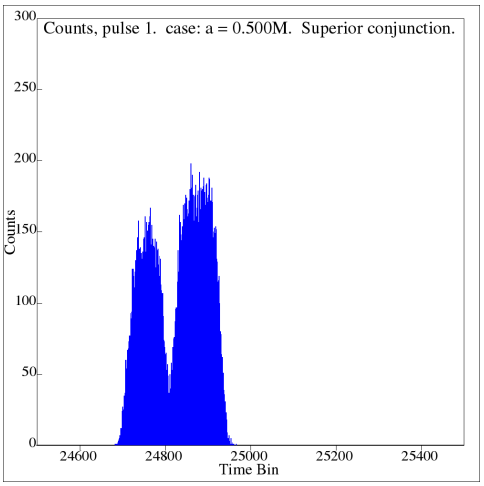

Figure 11.208: Case: a = 0.500M. Superior conjunction photon counts, second pulse.

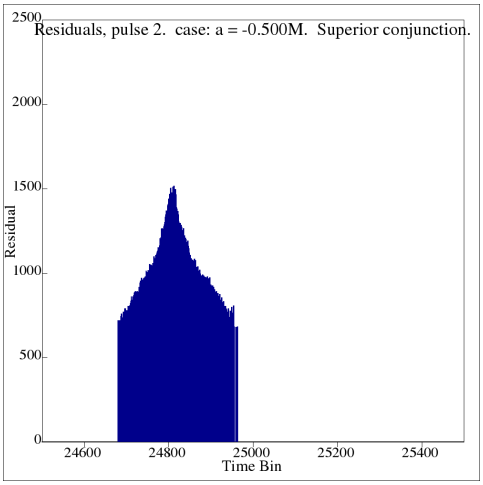

Figure 11.209: Case: a = -0.500M. Superior conjunction photon timing residuals, second pulse.

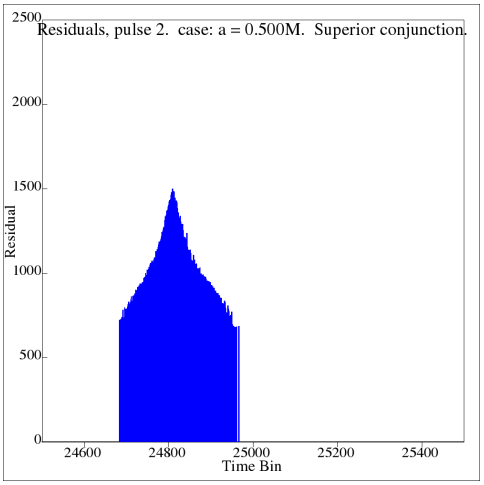

Figure 11.210: Case: a = 0.500M. Superior conjunction photon timing residuals, second pulse.

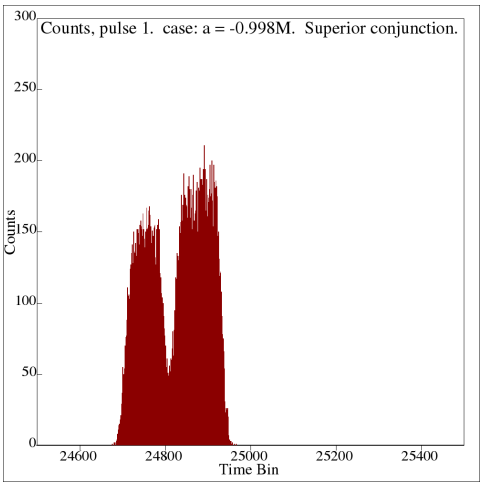

Figure 11.211: case: a = -0.998M. Superior conjunction photon counts, second pulse.

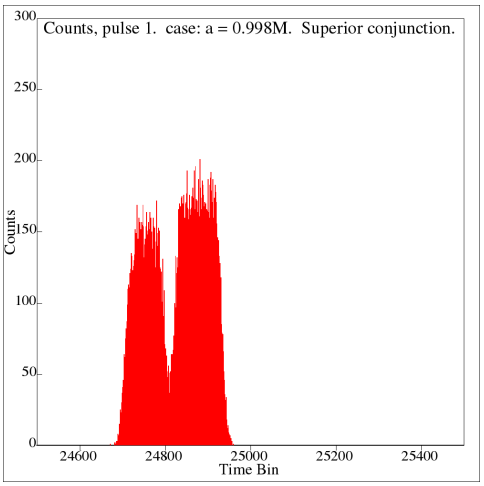

Figure 11.212: case: a = 0.998M. Superior conjunction photon counts, second pulse.

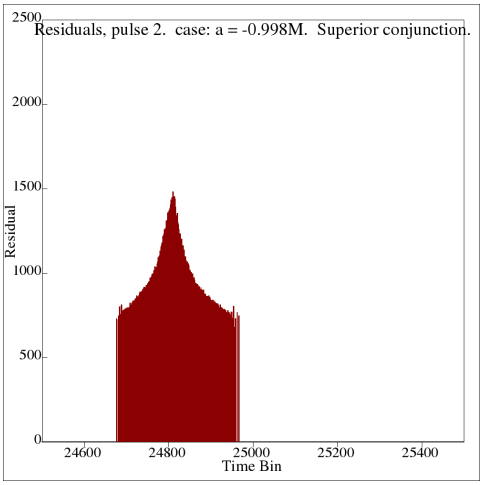

Figure 11.213: case: a = -0.998M. Superior conjunction photon timing residuals, second pulse.

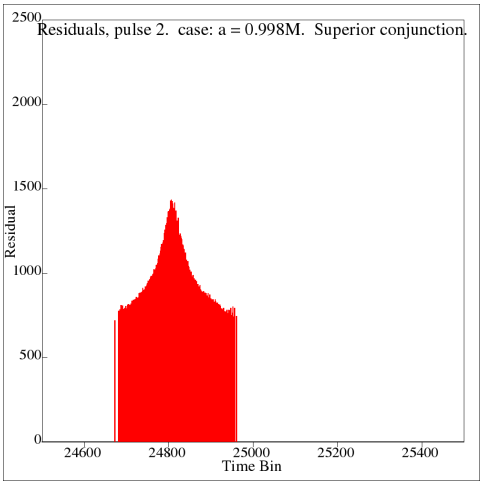

Figure 11.214: case: a = 0.998M. Superior conjunction photon timing residuals, second pulse.

The two comparisons above do not yield any discernable difference between output for black-holes rotating in opposite directions. The shapes of the pulses on either side of the trough do appear to be slightly different, but these results lack sufficient resolution for fur-

ther comment. If such a difference exists, it would be useful in determining the direction of rotation of the black-hole. Results obtained using this code on a cluster with a far greater number of cores may be able to produce results useful for this purpose. An attempt at improving the quality of the output produced was made by decreasing the magnitude of the modifications to the polar and azimuthal components of the photon four-momentum. A single simulation was produced for the case $a = -0.998$, where the factor controlling the size of the perturbations was reduced by a multiple of five. Ultimately, this could constitute a simulation for a pulsar with an extremely narrow conical radio-frequency emission. Alternatively, this data could be considered to be a simulation of increased density at the centre of the beam for the the original simulation. The results will be compared against the original simulation for the same case, giving an indication of the necessity of increasing the density of photons.

Comparitive outputs are presented below, indicating the reduced width of the pulses, and increased resolution of the superior conjunction output representing scattered photons. The superior conjunction output was compared against the original simulation run with wider pulses, although representation of inferior conjunction output is necessary simply to indicate the change in pulse width in a simple manner. The inferior conjunction histograms and residual outputs have simply been presented alongside equivalent results from the corresponding wider pulse simulation.

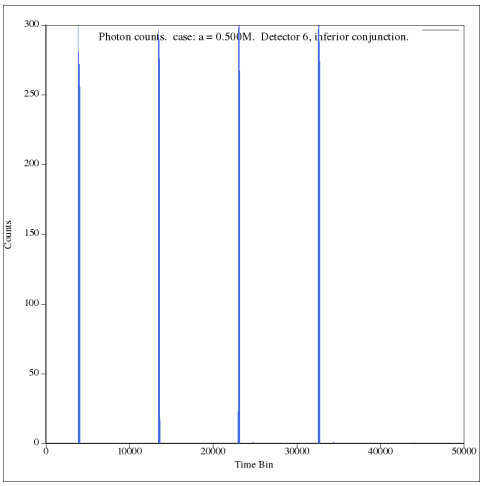

Figure 11.215: Reduced pulse-width. case: a = -0.998M. Inferior conjunction photon counts.

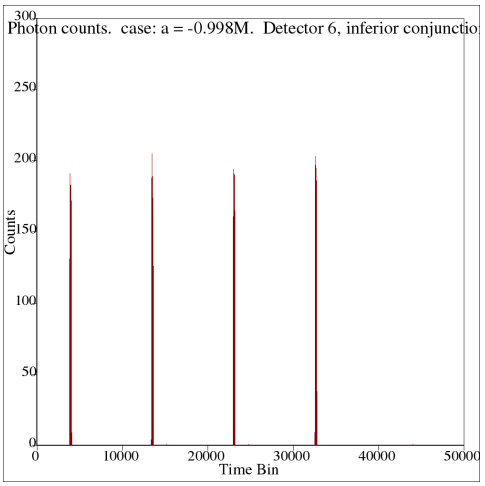

Figure 11.216: Original pulse-width. case: a = -0.998M. Inferior conjunction photon counts.

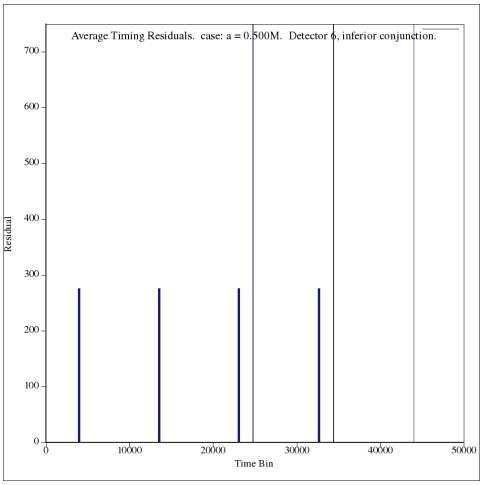

Figure 11.217: Reduced pulse-width. case: a = -0.998M. Inferior conjunction photon timing residuals.

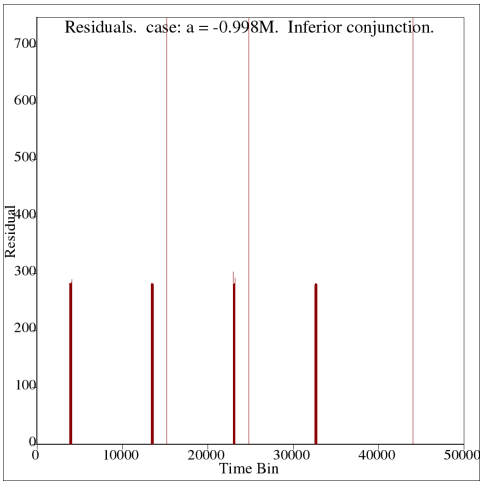

Figure 11.218: Original pulse-width. case: a = -0.998M. Inferior conjunction photon timing residuals.

A single instance of an individual pulse close-up output is presented for the inferior conjunction data. The second pulse was selected.

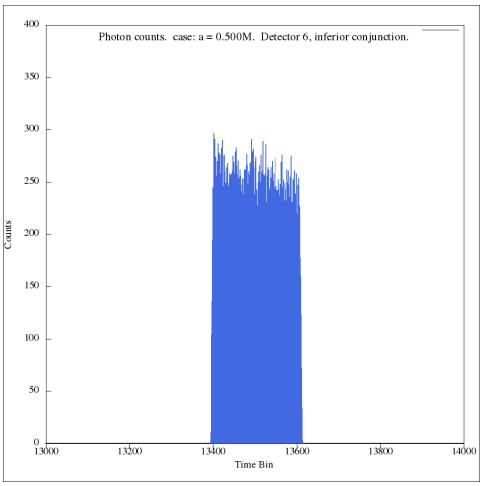

Figure 11.219: Reduced pulse-width. case: a = -0.998M. Inferior conjunction photon counts, second pulse.

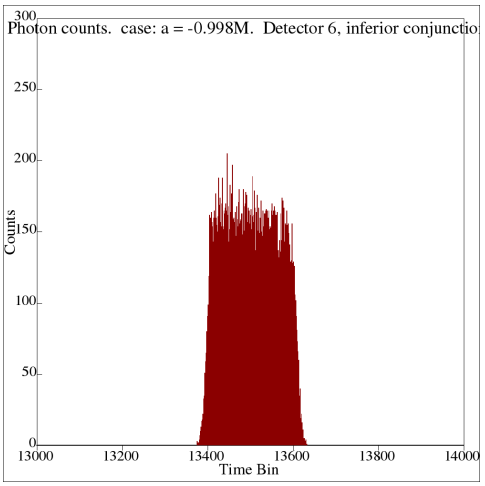

Figure 11.220: Original pulse-width. case: a = -0.998M. Inferior conjunction photon counts, second pulse.

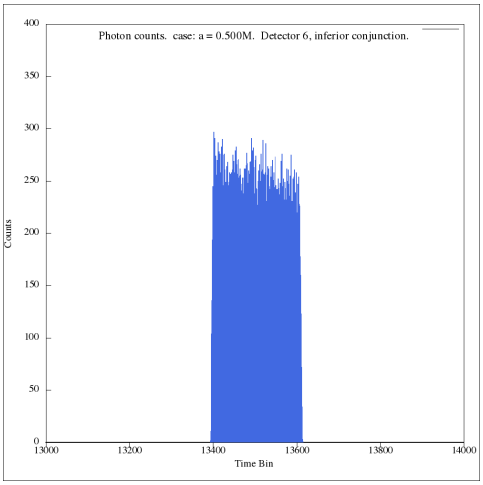

Figure 11.221: Reduced pulse-width. case: a = -0.998M. Inferior conjunction photon timing residuals, second pulse.

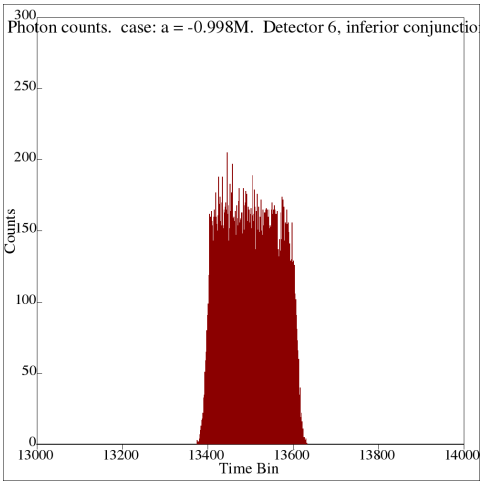

Figure 11.222: Original pulse-width. case: a = -0.998M. Inferior conjunction photon timing residuals, second pulse.

With a reference to the less interesting case of the inferior conjunction complete, the comparison of reduced pulse-width output with original output for the superior conjunction detector can now be presented.

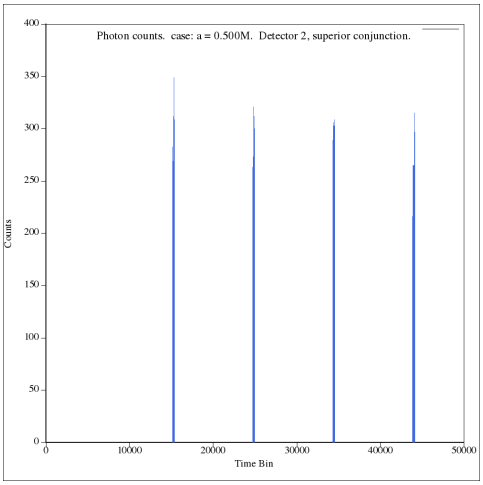

Figure 11.223: Reduced pulse-width. case: a = -0.998M. Superior conjunction photon counts.

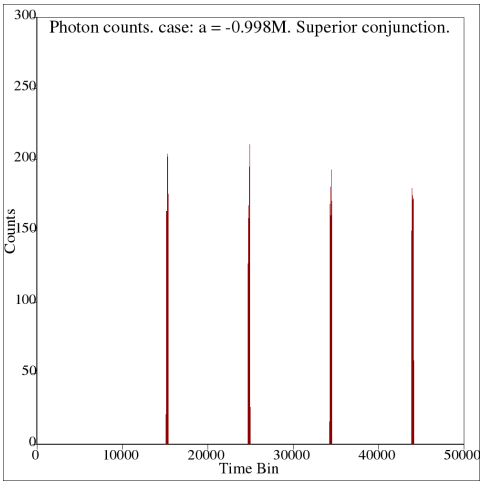

Figure 11.224: Original pulse-width. case: a = -0.998M. Superior conjunction photon counts.

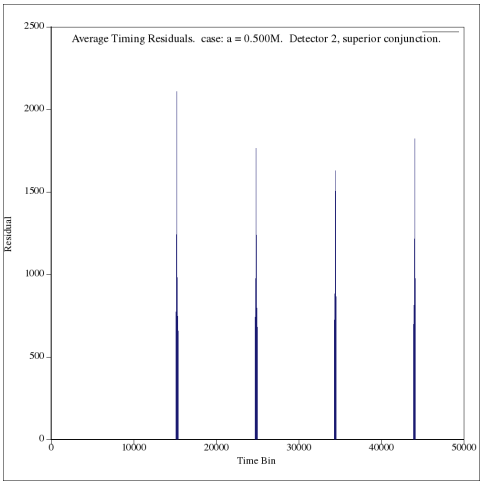

Figure 11.225: Reduced pulse-width. case: a = -0.998M. Superior conjunction photon timing residuals.

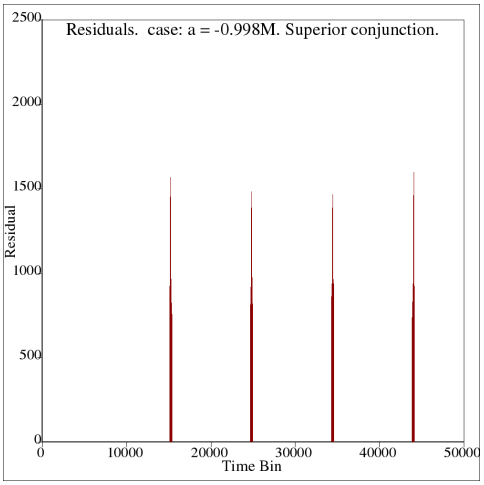

Figure 11.226: Original pulse-width. case: a = -0.998M. Superior conjunction photon timing residuals.

Individual pulse close-up output for pulse-width comparison of case $a = -0.999$ is presented below.

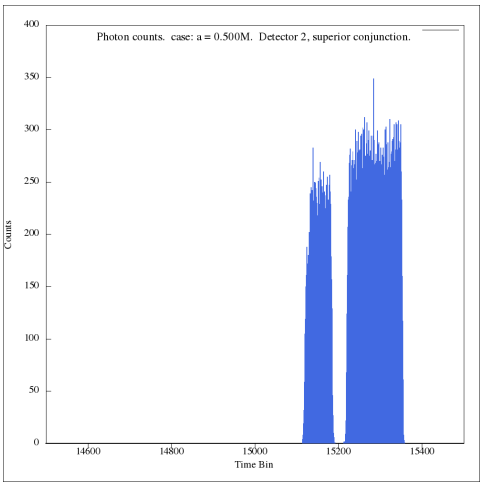

Figure 11.227: Reduced pulse-width. case: a = -0.998M. Superior conjunction photon counts, first pulse.

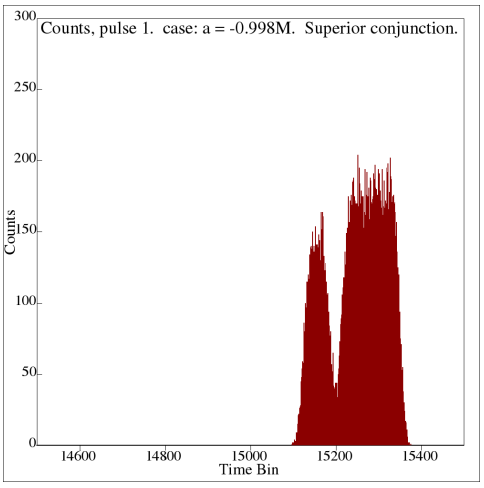

Figure 11.228: Original pulse-width. case: a = -0.998M. Superior conjunction photon counts, first pulse.

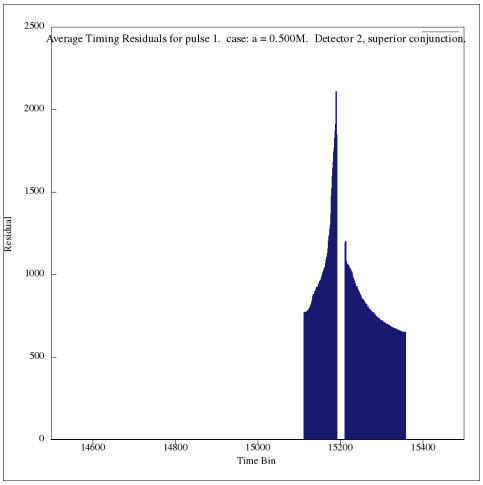

Figure 11.229: Reduced pulse-width. case: a = -0.998M. Superior conjunction photon timing residuals, first pulse.

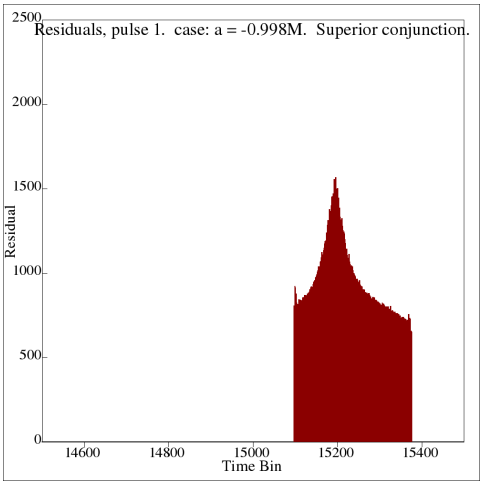

Figure 11.230: Original pulse-width. case: a = -0.998M. Superior conjunction photon timing residuals, first pulse.

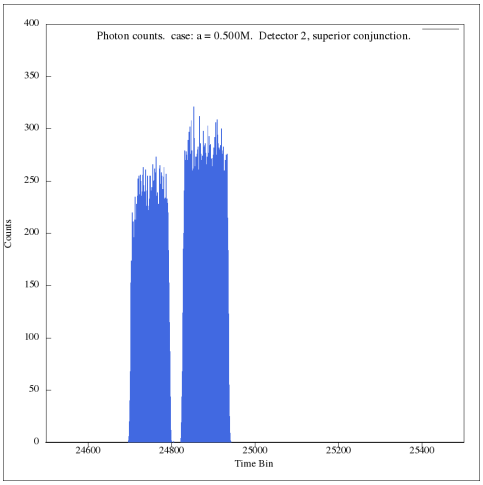

Figure 11.231: Reduced pulse-width. case: a = -0.998M. Superior conjunction photon counts, second pulse.

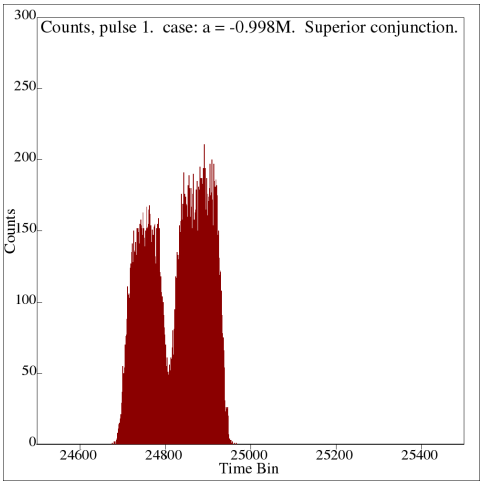

Figure 11.232: Original pulse-width. case: a = -0.998M. Superior conjunction photon counts, second pulse.

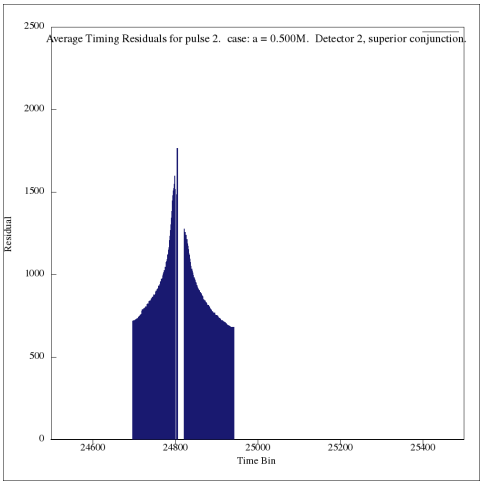

Figure 11.233: Reduced pulse-width. case: a = -0.998M. Superior conjunction photon timing residuals, second pulse.

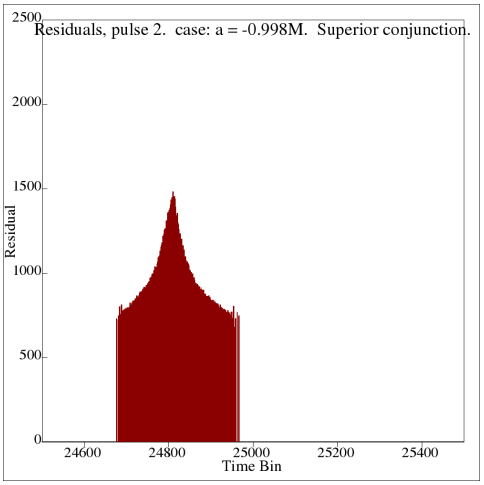

Figure 11.234: Original pulse-width. case: a = -0.998M. Superior conjunction photon timing residuals, second pulse.

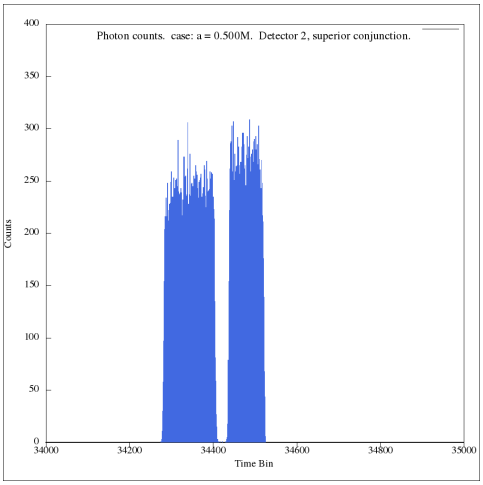

Figure 11.235: Reduced pulse-width. case: a = -0.998M. Superior conjunction photon counts, third pulse.

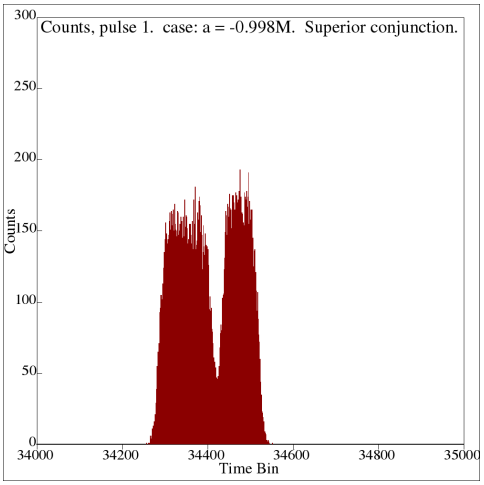

Figure 11.236: Original pulse-width. case: a = -0.998M. Superior conjunction photon counts, third pulse.

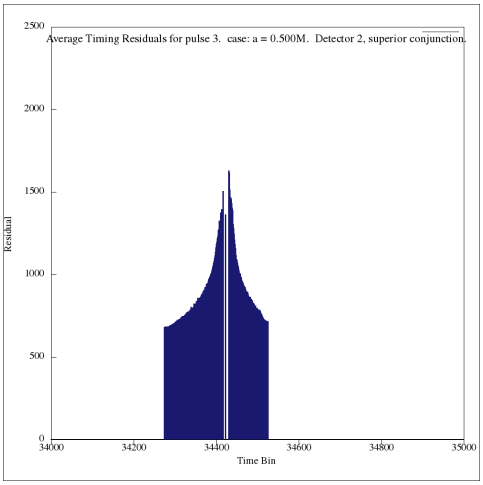

Figure 11.237: Reduced pulse-width. case: a = -0.998M. Superior conjunction photon timing residuals, third pulse.

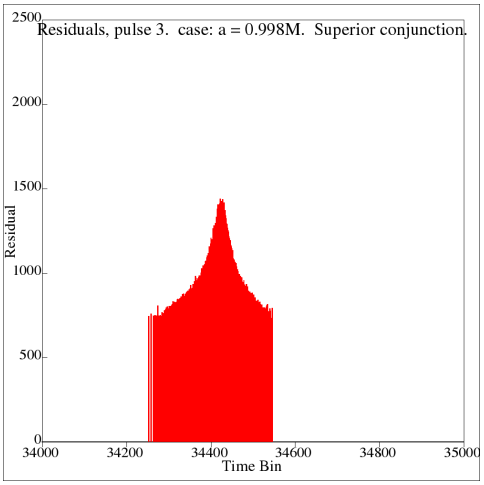

Figure 11.238: Original pulse-width. case: a = -0.998M. Superior conjunction photon timing residuals, third pulse.

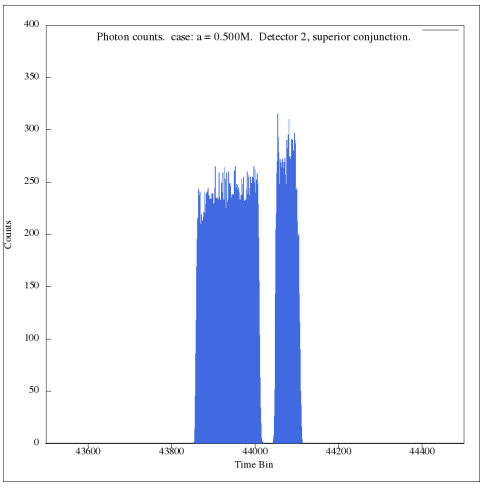

Figure 11.239: Reduced pulse-width. case: a = -0.998M. Superior conjunction photon counts, fourth pulse.

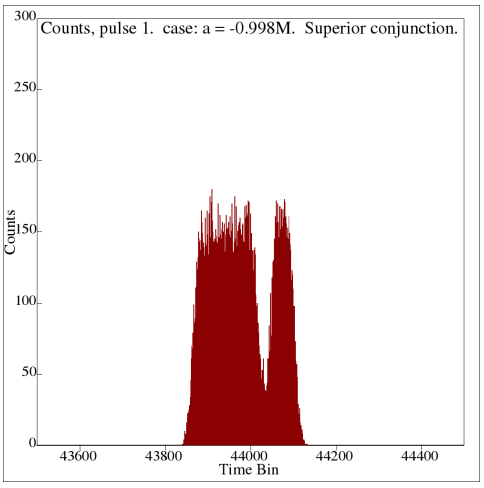

Figure 11.240: Original pulse-width. case: a = -0.998M. Superior conjunction photon counts, fourth pulse.

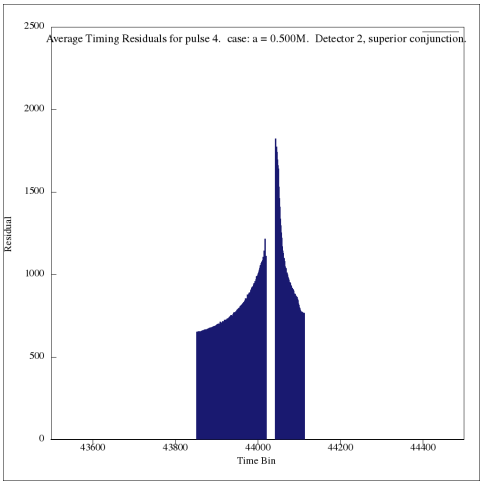

Figure 11.241: Reduced pulse-width. case: a = -0.998M. Superior conjunction photon timing residuals, fourth pulse.

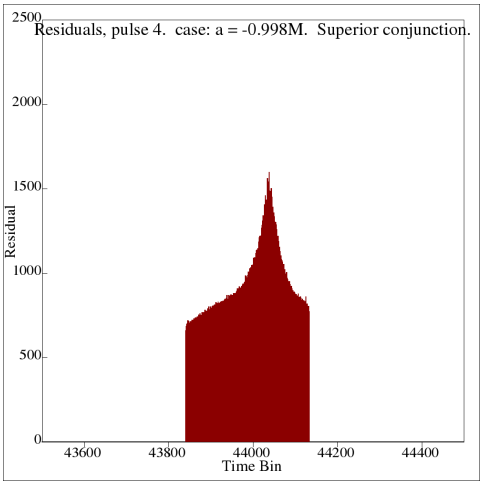

Figure 11.242: Original pulse-width. case: a = -0.998M. Superior conjunction photon timing residuals, fourth pulse.

This comparison illustrates the need for a much greater density of photons to simulate the pulsar's emission. It is notable that the width of the photon count pulses, as seen by the detector, were not greatly reduced by reducing the width of the pulses by a factor

of 5. This may be due to the fact that the time for which pulses are observable is more dependant on the pulsar rotation period than the width of the actual pulses, especially when the detector is of much larger area than a realistic case. Selecting a detector smaller in terms of area would allow for pulse count histograms with much more distinctive gaussian shape. Furthermore, using the GSL gaussian random number generator (rather than the STL version) to produce the conical beam shape has been shown to produce pulses with greater photon density near the cone axis, which would be an improvement. The most interesting outcome of the reduced pulse-width simulation is the region, within each pulse, where the number of photons striking the detector was reduced to zero. This corresponds to even greater timing residual measurements near this empty zone. This indicates that the beam was so narrowly focused, that there was a period of time for which all photons sweeping across the event horizon were scattered through large angles when compared with the incident beam. A portion of the photons struck the event horizon. Ultimately, a decent simulation would require photon density sufficient to reproduce, and even amplify these effects, while still allowing the total beam width to represent a realistic radio-frequency pulsar emission. Such simulations are possible for simple cases, such as the above data-sets, by use of a cluster to increase total photon count by several orders of magnitude. Ultimately it would also be more interesting to simulate a realistic pulsar, with rotational period in the millisecond range. A much faster rotating pulsar would exhibit different superior conjunction pulse behavior, something which this model would be able to explore. It is clear that for the section of orbit modelled in the presented output the black-hole did have a discernable affect on the pulsar's signal. The orbital fraction simulated would also be increased for cluster runs, in order to see the progression from unaffected pulses to pulses with large aberration caused by the presence of the black-hole. This concludes the presentation results for the simulations produced by my model.

Chapter 12

Conclusions

In this chapter I discuss the conclusions that can be drawn from the simulation results, as well as some theoretical and numerical considerations relevant to future versions of the model. The discussion is in three parts. First, I will interpret the simulation results. Then I will discuss numerical revisions which might improve the results for the idealized model considered in this thesis. Finally, I will discuss possible revisions to the theoretical content of the model, with a view to obtaining more realistic simulations in the future.

12.1 Discussion of Simulation Results

The aim of the present simulation was to determine whether it is possible to identify a characteristic signature in the signal emanating from a pulsar orbiting a stellar mass black-hole. A further aim was to determine whether information about physical properties of the black-hole could be obtained by observation of the pulsar signal. The system modelled was an ideal case in which the binary system is seen edge-on and in which the pulsar is in a stable circular orbit in the equatorial plane of the Kerr black-hole. The pulsar was assumed to rotate slowly, with the axis of the conical emission constrained to the equatorial plane of the Kerr geometry.

The simulation results indicate that the pulsar signal is affected in a predictable manner as it passes through the superior conjunction of the system with respect to a distant observer. A single pulse was found to be split into two peaks, more or less distinct. The shape of the split pulse is sensitive to whether the pulsar is approaching or receding from

the superior conjunction. Similar pulse-splitting was observed in the simulation of Oscoz et al., [5]. An analysis of the periodicity of a pulse-timing profile such as this would indicate a deviation from the expected pulsar period as the pulsar nears the superior conjunction of the system. This phenomenon may provide a basis for identifying a signature emission from a black-hole/pulsar binary systems. A real pulsar rotates in general much more rapidly than was assumed in this model in which I used only single machine simulations. This would need to be corrected in future simulations.

In the present simulation, no effect on the pulse profile was observed as the sense and magnitude of rotation was changed. There was a discernable difference in the shapes of the split pulses in the non-rotating and extreme rotating cases, but the effect was not strong enough to draw any meaningful conclusions. However, obtaining some slight discrepancy in pulse shapes is an exciting result, since it suggests that simulations with photon numbers larger by several orders of magnitude may be more successful in extracting such information.

The simulations also display other forms of interesting phenomena. Many interesting images of the scatter of photons from a black-hole have been obtained. However, they cannot be presented in this thesis due to the inability to effectively crop and edit them with my present machine. I have stored many graphical representations of the trajectories of photons through the Kerr-geometry in a data repository. These include plots describing the scatter of large numbers of photons by a slowly rotating black-hole, in which the pulsar is allowed to complete a full orbit. These reveal the net effect of the presence of the black-hole in the form of a band of scattered photons above and below the primary band formed by the beam of the pulsar as it sweeps through relatively flat spacetime. This suggests that it may be possible to detect the scattered emission from a very luminous pulsar, whose primary beam emission is not incident on the earth. The observed pulses for such a system would be low in flux, but with a spread larger than the pulsar beam since they consist of photons scattered over a large number of possible trajectories, each with a different propagation delay. The observed emission from such a pulsar would constitute a transient source since scattering into Earth direction occurs only near the superior conjunction. The model developed here can be used to explore transients of this kind by creating a large array of virtual detectors at different locations in the sky of the black-hole, and exploring the features of the detected signals in greater detail.

As the rotation rate of the black-hole is increased, the size of the scattered band (for a system where the orbital plane coincides with the equatorial plane) decreases, with photons being increasingly more focused towards the black-hole equatorial plane. Given an inclined system with a pulsar not beaming towards earth, it is possible that the beam could be observed by earth subsequent to being focused into the equatorial plane of the black-hole, as described by scatter images presented in chapter 11. Selecting a detector location which falls within the scattered band may yield interesting pulse profiles. However, this was not explored in this thesis.

The simulation could also test the hypotheses of Wang et al. [8] and Nampalliwar et al. [9] regarding the detection of highly deflected pulses from pulsars orbiting supermassive black-holes.

Plots using extremely small time step size (for pulsar motion and rotation) yield effectively "single-cone" data which helps to illustrate the effect of the black-hole on the beam of the pulsar. The trajectory data for each photon was recorded and plotted. However this procedure generates a large amount of data and considerably extends the computational time. The simulation is thus capable of producing very detailed representations of the scattering effect of the rotating black-hole. Computers with considerably larger data storage capability and RAM would enable one to plot these very large data files, allowing graphical representation of strong-field effects on a pulsar beam. I have several single-cone images stored in a data repository. With the limited computing facilities abailable to me, I was able to save only the scatter information as recorded at the Dyson Sphere. This information indicates clearly the substantial effect which black-holes have on the pulsar signal.

The code has been set up specifically for the simulation of black-hole pulsar binary systems. However, with alteration of only a few constituent modules, a vast number of different simulations mapping the effects of highly curved spacetime on photons can be performed. Maximum proximity tests were performed at high precision for only a small set of parameters, yielding interesting results. The most notable was the ability of a black-hole to capture a photon, for a finite amount of time, in a pseudo-circular orbit. The prospect of a stellar mass black-hole within the galactic disk would imply that the black-hole would be

subject to an incidence of radiation from all directions. The short-lived capture of a tiny fraction of this radiation implies that black-holes could maintain a field of photons at a radial distance specific to its physical properties and location. These photons would be particularly high in energy as they had been gravitationally blue-shifted upon their descent towards the black-hole, and thus, a population of high-energy photons could exist, and be constantly scattered about the black-hole. A field of high-energy photons in the highly-curved space-time around a black-hole could give rise to quantum field effects, such as particle creation. Increasing the angular momentum of the black-hole results in the preferential scattering of photons in the equatorial plane (perpendicular to the spin axis). With particular reference to the inferred supermassive black-hole at the centre of our galaxy, incident light from galactic and inter-galactic space would be scattered with much greater luminosity in and about the black-hole's equatorial plane, thus affecting the manner in which radiation permeates outwards. This could explain the immense electromagnetic interference seen from the galactic hub. If black-holes are present in sufficient numbers and with a sufficiently isotropic distribution about the galaxy, the manner in which they scatter incident radiation as a function of their angular momentum could have far-reaching consequences. Ultimately, I would like to simulate a black-hole at a particular location within a galaxy of a specific geometry, and determine the resulting influx and scatter of photons by the black-hole for an extended period of time. The results may provide insight into how the presence of an anomylous distribution of black-holes throughout a galaxy would affect the dynamics thereof.

12.2 Future Developments, Numerical and Theoretical.

12.2.1 Numerical revisions necessary for further developement.

- Detector size must be reduced as the present size does not allow for pulses to produce the correct gaussian shape when considering the photon count histograms.
- The simulation must be configured to represent known physical cases, so as to test the numerical operation against known physical results, such as the magnitude of the Shapiro delay for a known binary pulsar system.
- Sufficient processing resources must be used to produce reasonable simulation data.

This is only possible by making use of cluster computing system, and subsequently a grid infrastructure incorporating several clusters. Ultimately, the aim is to produce simulations which incorporate the trajectories of at least 10^11 photons, thus producing far superior statistical data. Photon numbers must be increased to enable the reduction of time-bin size to a scale comparable with current antenna sensitivity.

- A more advanced version of the Runge-Kutta subroutine has been written, but not implemented. This version uses several loops to generate the necessary intermediate terms and stores them within a predefined array, which updates the necessary entry with each loop iteration. The use of this subroutine would reduce the memory requirement of the most calculation intensive part of the code, possibly allowing for the entire calculation to occur within the cache memory for much faster processing of information.

12.2.2 Theoretical generalizations and extensions.

- Photon four-momentum components must be calculated in the local reference frame of the pulsar. This calculation must incorporate the contraction of the four-momentum such that a null geodesic is selected, after which the components must be calculated in the Kerr metric by use of the necessary transformations. This theoretical developement also solves the numerical deficiency of insufficient photon density of pulsar beam directions tangential to the circular orbit. Furthermore, the time component of the photon four-momentum must be solved explicitly, rather than be set to a constant.

- The rotational period of the Pulsar must be reduced to the millisecond range, so as to simulate a real millisecond pulsar emission. Ultimately pulsars can be modelled to fall within physical parameter ranges as specified by Lipunov et al. [3].

- The pulsar's orbit must be generalized. This may occur in various phases, beginning with simply altering the eccentricity of the orbit for an ellipse, and subsequently taking into account phenomena such as the decay of the orbit via gravitational radiation. Ultimately the most accurate possible description of the orbital mechanics of a compact binary system must be utilized, hence the discussion of the PPN equations of motion for such systems within this thesis. The asymmetry (variability of the radial separation) of the pulsar's orbit as it passes through the superior conjunction of the system with respect to a distant observer would cause a certain amount of asymmetry

in the histogram of photon counts, as the pulsar was nearer to the black hole on one side of the superior conjunction and further on the other.

- Orbits of different inclinations need to be considered. The orbital plane coinciding with the equatorial plane of the Kerr geometry is an ideal situation. However, the black-hole can be expected to have an accretion disk in its equatorial plane which would disrupt the pulsar's signal. For such situations, one needs to consider a model in which the orbital plane of the binary system is inclined with respect to the equatorial plane of the Kerr black-hole.

- The motion of the black-hole requires revision of the theory on which the model is constructed. The null geodesics of the photons must be calculated in the spacetime resulting from an overlay of the Kerr geometry, and the geometry of the pulsar. The correct approach would be to formulate a time-dependant metric which takes into account the motion of the black-hole, as well as the non-zero pulsar mass. For photons travelling close to the event horizon, a slight shift in the position of the black-hole would have a strong effect on the direction of scatter. The sensitivity of input direction used for the maximum proximity tests described in chapter 11 illustrates this scenario very well, with the adjustment of the input four-momentum initial conditions, even at the 20th decimal place having a drastic affect on the final phase angle of the photon when it hits the Dyson Sphere. Ultimately the work must be comparable with analytical studies such as the one performed by Rafikov and Lai, [7], describing the effect of a moving lens on the propagation of the pulsar's signal.

- The precession of the spin axis of the pulsar due to the Lense Thirring [**?**] effect needs to be taken into account. Such theoretical considerations have been made by Wex and Kopeikin [6], as they seek to obtain physicical information by studying the precessional effects on the pulsar's signal.

- Polarization data represents an additional method of obtaining useful information from black-hole/pulsar binary systems. This is a difficult problem, due to the presence of both black-hole and pulsar magnetospheres. Hence a net effect of Faraday rotation through the magnetospheres, as well as the effect of the highly-curved, rotating spacetime on the relativistic polarization four-vector, ought to be calculated. The numerical implementation of these calculations would not be difficult, but the theoretical framework regarding the physical properties of the pulsar magnetosphere must

be studied in detail. The present simulation models the pulsar's beam orthogonal to the spin axis, thus describing a specific case of pulsar magneto-electrodynamics, the orthogonal rotator, see Michel et al.[33].

- The relation between the physical properties of a pulsar and its resulting radio-frequency emission must be studied in detail, so as to implement more realistic models of photon emission from the pulsar. A starting point may be the implementation of the Rotating Vector Model, by Radhakrishnan et al. [16], and work by Lyne and Manchester [17].

- The dependance of the signal on the interstellar distance it must travel from the pulsar to earth has not been taken into account. Models exist to describe the effect that this journey would have on the signal, and should be implemented to generate more realistic simulations for comparison with observation.

- The effect of the motion of the solar system relative to the black-hole/pulsar binary system must be considered. Although the time-scale of the simulation is relatively tiny when compared with the motion of each stellar system, in the context of the present simulation, this could be accounted for by making necessary adjustments to the size and position of the detector in the sky of the black-hole. Theoretical methods must therefore be developed to perform this calculation.

In conclusion, the results presented in this thesis indicate the possibility of direct detection of the presence of a black-hole in a binary system with a pulsar, with subsequent studies representing the possibility of gaining useful physical information describing the properties of the two compact objects comprising the system. Although the model is only capable of simulating the ideal case scenarios as described in this thesis, the revision and generalization of the simulations described by the above points is a possibility which could yield exciting results. Comparison of the simulation results with observation may provide a conclusive test-bed for the validation of General Relativity in its most extreme regime of highly-curved and rapidly rotating spacetime. The potential of the model presented in this thesis is vast, and the scale of the project required to bring the work to a level whereby realistic results can be produced is substantial. I hope to be able to develop this method further, and produce more interesting results in the future.

Bibliography

[1] Hulse, R.A. and Taylor, J.H.: Discovery of a pulsar in a binary system. *The Astrophysical Journal*, vol. 195, no. 2, pp. L51–L53, 1975.

[2] Taylor, J.H. and Weisberg, J.M.: A new test of general relativity: Gravitational radiation and the binary pulsar psr 1913+16. *The Astrophysical Journal*, vol. 253, pp. 908–920, 1982.

[3] Lipunov, V.M., Postnov, K.A., Prokhorov, M. and Osminkin, E.Y.: Binary radiopulsars with black holes. *The Astrophysical Journal*, vol. 423, pp. L121–L124, 1994.

[4] Laguna, P. and Wolszczan, A.: Pulse arrival-times from binary pulsars with rotating black hole companions. *Astroph. J. Lett.*, vol. 486, p. 27, 1997.

[5] Oscoz, A., Goicoechea, L.J., Mediavilla, E. and Buitrago, J.: Light-curve models for a pulsar orbiting a kerr black hole. *Monthly Notes of the Royal Astronomical Soceity*, vol. 285, pp. 413–426, 1997.

[6] Wex, N. and Kopeikin, S.M.: Frame dragging and other precessional effects in black hole pulsar binaries. *The Astrophysical Journal*, vol. 514, pp. 388–401, 1999.

[7] Rafikov, R.R. and Lai, D.: Effects of gravitational lensing and companion motion on the binary pulsar timing. *See arXiv:astro-ph/0512417v2 21 Feb 2006*, vol. -, pp. –, 2006.

[8] Wang, Y., Jenet, F.A., Creighton, T. and Price, R.H.: Strong field effects on pulsar arrival times: Circular orbits and equatorial beams. *Preprint, See arXiv:0812.2302v1 [astro-ph] 12 Dec 2008*, vol. -, pp. –, 2008.

[9] Nampalliwar, D., Price, R.H., Creighton, T. and Jenet, F.A.: Detection of pulsar beams deflected by the black hole in sgr a*: Effects of black hole spin. *The Astrophysical Journal*, vol. 778, p. 145, 2013.

[10] Damour, T. and Deruelle, N.: General relativistic celestial mechanics of binary systems i. the post-newtonian motion. *Annales de l' I.H.P., Section A*, vol. 43, No.1, no. 1, pp. 107–132, 1985.

[11] Blanchet, L.: General relativistic dynamics of compact binary systems. *See arXiv:gr-qc/0611142v1 27 Nov 2006*, vol. -, pp. –, 2006.

[12] Epstein, R.: The binary pulsar: Post-newtonian timing effects. *The Astrophysical Journal*, vol. 216, pp. 92–100, 1977.

[13] Cunningham, C.T. and Bardeen, J.M.: The optical appearance of a star orbiting an extreme kerr black hole. *The Astrophysical Journal*, vol. 183, pp. 237–264, 1973.

[14] Chandrasekhar, S.: *The Mathematical Theory of Black Holes*. Clarendon Press, Oxford, Oxford, 1983.

[15] Peters, P.: Gravitational radiation and the motion of two point masses. *Phys. Rev.*, vol. 136, pp. B1224–B1232, 1964.

[16] Radhakrishnan, V. and Cooke, D.J.: Magnetic poles and the polarization structures of pulsar radiation. *Ap. Letters*, vol. 3, p. 225, 1969.

[17] Lyne, A.G. and Manchester, R.M.: The shape of pulsar radio beams. *Mon. Not. R. Astr. Soc.*, vol. 234, pp. 477–508, 1988.

[18] Dymnikova, I.: Effect of relative time delay of rays focused by a rotating massive body. *Soviet Physics JETP*, vol. 59, p. 223, 2013.

[19] Narayan, R., Piran, T. and Shemi, A.: Neutron star and black hole binaries in the galaxy. *The Astrophysical Journal*, vol. 379, pp. L17 – L20, 1991.

[20] Hawking, S.W. and Ellis, G.F.R.: *The Large Scale Structure of Space-Time*. Cambridge University Press, Cambridge, 1973.

[21] Thorne, K.S.: Multipole expansion of gravitational radiation. *Reviews of Modern Physics*, vol. 52, pp. 299–340, 1980.

[22] Thorne, K.S., Price, R.H. and Macdonald, D.M.: *Black Holes: The Membrane Paradigm*. Yale University Press, New Haven, CT, 1986.

[23] Laarakkers, W.G. and Poisson, E.: Quadrupole moments of rotating neutron stars. *The Astrophysical Journal*, vol. 512, p. 282, 1999.

[24] Lai, D. and Rafikov, R.R.: Effects of gravitational lensing in the double pulsar system j0737-3039. *The Astrophysical Journal*, vol. 621, pp. L41 – L44, 2005.

[25] Blandford, R. and Teukolsky, S.A.: Arrival-time analysis for a pulsar in a binary system. *The Astrophysical Journal*, vol. 205, pp. 580–591, 1976.

[26] Hartle, J.B.: *Gravity. An Introduction to Einstein's General Relativity.* Addison-Wesley, San Fransisco, CA, 2002.

[27] Taylor, E.F. and Wheeler, J.A.: *Exploring Black Holes, Sample Chapters: Project F.* Addison Wesley Longman, Boston, MA 02116 USA, 2008.

[28] Boyer, R.H. and Lindquist, R.W.: Maximal analytic extension of the kerr metric. *Journal of Mathematical Physics*, vol. 8, pp. 265–281, 1967.

[29] Dexter, J. and Agol, E.: A fast new public code for computing photon orbits in a kerr spacetime. *The Astrophysical Journal*, vol. 696, pp. 1616–1629, 2009.

[30] Carter, B.: Global structure of the kerr family of gravitational fields. *Physical Review*, vol. 174, no. 5, pp. 1559–1571, 1968.

[31] Landau, L.D. and Lifshitz, E.M.: *The Classical Theory of Fields.* Addison-Wesley, Reading, Mass, 1971.

[32] Blanchet, L.: Equations of motion of compact binaries at the third post-newtonian order. *PRAMANA*, vol. 53, no. 6, pp. 1–15, 1999.

[33] Michel, F.C. and Li, H.: Electrodynamics of neutron stars. *Physics Reports*, vol. 318, pp. 227–297, 1999.